UNIVERSITÀ DELLA CALABRIA

Dipartimento di Ingegneria Meccanica, Energetica e Gestionale (DIMEG)

Dottorato di Ricerca in

Ingegneria Civile e Industriale

Ciclo

XXIX

Shape Memory Alloy connectors for Ultra High Vacuum applications: a breakthrough for accelerator technologies

Settore scientifico disciplinare

ING-IND/14

Coordinatore: Ch.mo Prof. Franco Furgiuele
Firma:__________________________

Supervisori/Tutor: Ch.mo Prof. Franco Furgiuele (UNICAL)
Firma:_____________________

Ch.mo Dott. Cedric Garion (CERN)
Firma:_____________________

Dottorando: Dott. Fabrizio Niccoli
Firma:_______________________

ABSTRACT

The design of tight connections for ultrahigh-vacuum (UHV) systems is a key subject for vacuum technology. Design requirements become even more stringent when dealing with UHV beam-pipe coupling in high-energy particle accelerators, where reliability and safety are core issues. For this specific application, additional needs often arise: strict geometrical and/or space limitations, connection of dissimilar materials and installation in restricted access areas. The latter constraint is of major concern, especially in the new generation of high-energy particle accelerators such as the HL-LHC (High Luminosity Large Hadron Collider), which will be operational at CERN (European Organization for Nuclear Research) in 2026. Owing to the increased proton-beam intensity and luminosity of the HL-LHC, radioactivity will be higher at some points than in the present LHC. The radiation exposure time of the technical personnel in some critical areas will be strictly controlled and minimized. The use of standard ConFlat® flanges (CF) or quick connect ConFlat® flanges (QCF) could result in significant design and operational/maintenance limitations. In particular, the mounting and dismounting of CFs are time-consuming due to the high number of bolts and lead to significant radiation doses incurred by operators. Conversely, QCFs can be installed more quickly, but they suffer from the requirement of more space and are unwieldy components comprising heavy stainless-steel chain clamps.

Within this framework, Shape Memory Alloys (SMAs) offer a unique possibility to generate tight connections and fast clamping/unclamping by remotely changing the temperature of the SMA junction unit; at the microscopic scale this occurs trough a reversible solid-state transformation between the parent austenitic phase and the product martensitic one. In this PhD work, SMAs were used to develop a new generation of vacuum tightening systems for accelerator beam-pipe coupling by exploiting their shape recovery capabilities and actuation principles. The proposed coupling system consists of a SMA ring and a sealing element to be placed at the SMA-vacuum chambers interface, *i.e.* a copper coating or a thin cylindrical aluminum/copper gasket. Commercial NiTiNb rings and NiTi sleeves *ad-hoc* developed by Intrinsic Devices Inc. (USA) based on CERN technical constraints were properly investigated. The rings show two-way shape memory effect "remembering" a contracted austenitic shape and an enlarged martensitic one. The thermomechanical properties of the selected SMAs were measured experimentally. The tightening performance of SMA rings, was studied for different values of the initial clearance between the SMA ring and the vacuum pipe. The contact pressure was estimated by both strain gauge (SG) measurements and by Digital Image Correlation (DIC), using an *ad-hoc* developed numerical procedure. A novel design method was proposed that involves numerical results, obtained from Finite Element (FE) simulations and a literature vacuum sealing model. Leak tightness tests were carried out to assess the sealing performance of the of SMA-based prototype UHV chambers even after ageing at room temperature and repeated thermal cycles. Irradiation tests on SMA-based prototype vacuum chambers (SMA absorbed dose > 100 kGy) was performed at CHARM (Cern High energy AcceleRator Mixed field) facility at CERN and the functional and leak tightness performance of the couplings was successfully verified afterwards.

The main results revealed that the contact pressure is not significantly affected by the initial SMA ring-pipe assembly clearance due to the plateau in the stress-strain response of the material. Thermal dismounting and subsequent re-clamping is obtained by exploiting the two-way shape memory recovery capabilities of the alloys. Leak rate measurements showed that the constraints for UHV applications could be easily satisfied (leak rate < 10^{-10} mbar l s^{-1}) even after multiple thermal cycles; this opens the possibility of remotely clamping/unclamping the tight couplers by well-defined temperature variations.

The proposed SMA-based beam-pipe couplers can be installed without using any connection flange. They are smaller and lighter than CF and QCF devices currently used in UHV systems at CERN. These bolt-free SMA-based connectors could provide significant benefits in terms of installation-dismounting time, space occupancy, bi-material joining and, above all, possible remote thermal activation, obtainable, for example, with removable heating/cooling collars.

Based on these results, possible applications in CERN accelerators have already been identified. A first use has been proposed for the ISOLDE (Isotope Separator On Line DEvice). A second application is the vacuum system of the Large Hadron Collider (LHC) between the two high-luminosity experiments (ATLAS and CMS) and the beam focusing-defocusing quadrupole magnets (frequently called inner triplets). Moreover, particle collimators are also critical devices of accelerator equipment. In all these applications, high-energy particles induce a large radioactivity and, consequently, personnel access is restricted. The use of SMA rings with remote clamping-unclamping features could be beneficial to avoid contamination and irradiation of technical personnel. Finally, SMA coupling installations are already planned in the CLEAR test facility at CERN, which provides the electron beam for the Compact Linear Collider (CLIC) study.

SOMMARIO

La progettazione di dispositivi di collegamento meccanico per applicazioni in sistemi di ultra-alto vuoto (Ultra High Vacuum - UHV) è particolarmente complessa. I vincoli di progettazione diventano ulteriormente stringenti nel caso di sistemi di accoppiamento per i tubi a vuoto utilizzati negli acceleratori di particelle ad elevata energia, quale il Large Hadron Collider (HLC) del CERN, in cui affidabilità e sicurezza rappresentano requisiti fondamentali. In particolare, in queste applicazioni occorre spesso considerare le seguenti esigenze progettuali: vincoli di ingombro, connessioni multi-materiale e installazione in aree ad accesso limitato. Quest'ultima peculiarità diventa sostanziale in vista di una nuova generazione di acceleratori di particelle, l'HL-LHC (High Luminosity Large Hadron Collider), che sarà operativa al CERN nel 2026. HL-LHC è un progetto volto all'incremento della luminosità di LHC di un fattore 10 rispetto al valore di progetto. L’aumento dell’intensità del fascio e del numero di collisioni delle particelle permetterà misure più accurate e l'osservazione di processi fisici rari, che avvengono al di sotto del livello di sensibilità della macchina attuale. Sfortunatamente, la radioattività sarà significativamente più alta in alcune aree critiche. Il tempo di esposizione alle radiazioni del personale tecnico dovrà essere strettamente controllato e limitato. Per queste ragioni, l'utilizzo di flange convenzionali ConFlat® (CF) o di flange a collegamento rapido (Quick ConFlat, QCF) potrebbe causare importanti limitazioni sia nella progettazione dei sistemi UHV oltre che nelle operazioni di manutenzione in esercizio. In particolare, il montaggio e lo smontaggio di delle flange CF richiedono molto tempo a causa dell'elevato numero di bulloni; ne conseguono dosi di radiazione per i tecnici significativamente elevate. I sistemi QCF, invece, possono essere installati più velocemente, ma si tratta di componenti realizzati mediante pesanti catene in acciaio e, pertanto, risultano molto ingombranti.

In questo contesto, le leghe di memoria di forma (Shape Memory Alloys - SMAs) offrono la possibilità unica di generare connessioni di tenuta caratterizzate da montaggio/smontaggio rapido sfruttando un recupero di forma vincolato attivabile termicamente da remoto. Su scala microscopica, questo avviene attraverso una trasformazione reversibile allo stato solido tra la struttura austenitica e martensitica, nota come trasformazione martensitica termo-elastica.

Nell’ambito delle attività di dottorato, le SMAs sono state utilizzate per sviluppare una nuova generazione di sistemi di serraggio per i tubi a vuoto degli acceleratori del CERN, sfruttando le loro capacità di recupero di forma e i peculiari principi di attuazione. Il sistema di accoppiamento proposto è costituito da un anello SMA e da un elemento deformabile con funzione di tenuta da collocare all'interfaccia tra l’anello SMA e le camere da vuoto; questo può essere un rivestimento in rame o una guarnizione cilindrica sottile in alluminio/rame. Lo studio è stato condotto sia su anelli commerciali in lega nichel-titanio-niobio (NiTiNb) che su manicotti in lega nichel-titanio (NiTi) sviluppati *ad-hoc* da Intrinsic Devices Inc. (USA) in accordo ad opportune specifiche funzionali definite dal CERN. Gli anelli investigati manifestano memoria di forma a due vie “ricordando” una geometria contratta in fase austenitica ed una espansa in fase martensitica. Le proprietà termomeccaniche delle leghe selezionate sono state misurate sperimentalmente. La pressione di serraggio esercitata dagli anelli SMA è stata valutata per diversi valori del gioco iniziale tra l’elemento a memoria di forma e i tubi a vuoto. Sono state analizzate differenti configurazioni geometriche dell’interfaccia anello SMA/tubi a vuoto. I carichi radiali dovuti all’azione delle SMA sulle camere da vuoto sono stati stimati sia attraverso misure estensimetriche (Strain Gage - SG) che con tecniche di correlazione digitale di immagine (Digital Image Correlation - DIC), utilizzando una procedura numerica sviluppata *ad hoc*. È stato inoltre proposto un metodo di progettazione basato su un nuovo parametro di prestazione della tenuta a vuoto. Quest’ultimo è stato definito sulla base dei risultati numerici ottenuti attraverso simulazioni agli elementi finiti (Finite Element - FE) e un modello di conduttanza di letteratura. Sono state condotte diverse prove sperimentali di tenuta a vuoto su prototipi di camere connesse attraverso manicotti SMA. Tali prove sono state effettuate anche dopo invecchiamento a temperatura ambiente e cicli termici ripetuti. Alcuni prototipi sono stati esposti a intense radiazioni ionizzanti (dose assorbita> 100 kGy) presso la facility CHARM (Cern High Energy AcceleRator Mixed Field) del CERN e il comportamento funzionale degli accoppiamenti, in termini di tenuta a vuoto e smontabilità, è stato successivamente verificato.

I principali risultati delle analisi effettuate hanno rivelato che la pressione di contatto non è significativamente influenzata dal gioco iniziale tra il manicotto SMA e le camere da vuoto a causa del plateau nella risposta tensione-deformazione del materiale. Lo smontaggio termico e il successivo ri-clampaggio sono stati ottenuti sfruttando la memoria di forma a due vie delle leghe. Le prove di tenuta a vuoto hanno mostrato che il vincolo per applicazioni UHV risulta soddisfatto (leak rate<10^{-10} mbar l s^{-1}) anche dopo diversi cicli termici.

In conclusione, è stato dimostrato che i connettori SMA proposti possono essere installati senza l’utilizzo di flange di collegamento; sono compatti e più leggeri dei dispositivi CF e QCF attualmente utilizzati nei sistemi UHV al CERN. Inoltre, non prevedendo l’utilizzo di bulloni di serraggio, riducono sensibilmente i tempi di installazione e smontaggio. Possono essere sfruttati per la realizzazione di giunzioni bi-materiale e, soprattutto, permettono l’attivazione ed il controllo da remoto, ottenibile, ad esempio, attraverso collari di riscaldamento/raffreddamento rimovibili.

Sulla base di questi risultati sono già state identificate possibili applicazioni negli acceleratori del CERN. È infatti stato proposto un primo utilizzo per ISOLDE (Isotope Separator On Line DEvice). Una seconda applicazione è il sistema a vuoto del Large Hadron Collider (LHC) tra i due esperimenti ad alta luminosità (ATLAS e CMS) ed i magneti quadrupoli utilizzati per la focalizzazione/de-focalizzazione del fascio. Le particelle ad alta energia inducono alti livelli di radioattività in prossimità dei collimatori e conseguentemente l'accesso al personale è fortemente limitato; l'utilizzo di anelli SMA con funzionalità di installazione e disaccoppiamento a distanza potrebbe essere utile per evitare la contaminazione e l'irradiazione del personale tecnico in queste aree. Infine, l’utilizzo dei connettori SMA è già previsto nella CLEAR test facility al CERN. Quest’ultima fornisce il fascio elettronico per gli studi relativi al Compact Linear Collider (CLIC). Il vantaggio principale dei manicotti SMA, in questa particolare applicazione, sarebbe relativo ai loro limitati ingombri.

ACKNOWLEDGMENTS

Being part of both Dr. Chiggiato's group at CERN and Prof. Furgiuele's group at UNICAL has been a real privilege as well as a vibrant and exciting experience.

I am heartily grateful to Paolo and Cedric who have given me the chance to deepen my knowledge and skills in the creative and cosmopolite environment of one of the most prestigious research center in the world. Their guidance has been immensely valuable and encouraging; their competence and professionalism have been excellent examples for me. Thank you very much for all your suggestions and support!

I am enormously thankful to Prof. Furgiuele for his constant availability as well as his unique frankness. Thanks a lot, Prof., for having given me the possibility to work in your outstanding research group!

Very special thanks go to Prof. Carmine Maletta, I had the privilege of being guided by. He is an excellent professor and a marvelous person. The enthusiasm he shows for his work is contagious and motivational. The words needed to show the extent of my gratitude and esteem toward him would not fit this page so I have to summarize my recognition by means of the following word: Grazie!

Finding friends among your colleagues/officemates is usually not that easy: Emanuele, Giulia, Caterina, Piergiorgio at UNICAL and Marco (Caro Marco!) at CERN have demonstrated to me how lucky I have been (for Emanuele and Giulia: I will never forget our lovely summertime in the lab. Thanks a lot! Mpuuuu!)

Warm thanks go to Renato, Diego and Ernesto for having endured me in the lab. Their support has been great as well as their entertaining company.
Similarly, I want to thank Erik along with Pawel, two colleagues I had the pleasure to collaborate with, at CERN; their kindness and professionality have been outstanding.

I am greatly thankful to the whole "UNICAL family" composed by Prof. Pagnotta, Luigi, Marco, Giovanna, Piergiorgio, Pietro, Chiara; having fun while working is such a gift! Many thanks guys for the amusing time we have had!
All the people I have met at CERN during the last three years have greatly contributed to my professional and personal growth. I have encountered amazing scientists and I have found good friends and colleagues like Alessandro, Fabrizio, Luca, Marco, Giorgio, Max, Gabi, Miriam, Stefano, Luis, Alexis, Javier, Ida, Roberto, Julien, Rafa and many more: working at CERN and living in Geneva have been great mainly thanks to the lovely moments spent together.

I want to heartily thank my "old but gold" precious friends from Cosenza. I do not want to list them because they perfectly know who they are. Thank you, guys, for the quality of the time we continue to spend together!

Lastly, I would like to thank my family for all their sacrifices, their love and constant support in all my pursuits. Mamma, Papà, Fede: Grazie di tutto!

CONTENTS

LIST OF FIGURES

LIST OF TABLES

1. INTRODUCTION

1.1 High energy physics at CERN.

The modern high energy physics needs extremely sophisticated systems to explore world of elementary particles constituting the matter. Complex scientific instruments, namely accelerators and colliders, aim to produce, accelerate and collide beams of particles in order to investigate new elementary events, announcing potential discoveries, and providing more statistics for the already known reactions. The European Organization for Nuclear Research, known as CERN, operates the largest particle physics laboratory in the world. CERN's accelerator complex includes particle accelerators and colliders. It can handle beams of different types of particles (electrons, positrons, protons, antiprotons and "heavy ions"). Each type of particles is produced differently, but then passes through a similar succession of acceleration stages, moving from one machine to another. The first steps are usually provided by linear accelerators, followed by larger circular machines: Proton Synchrotron Booster (PSB), Proton Synchrotron (PS), Super Proton Synchrotron (SPS), and Large Hadron Collider (LHC) (Fig. 1.1)

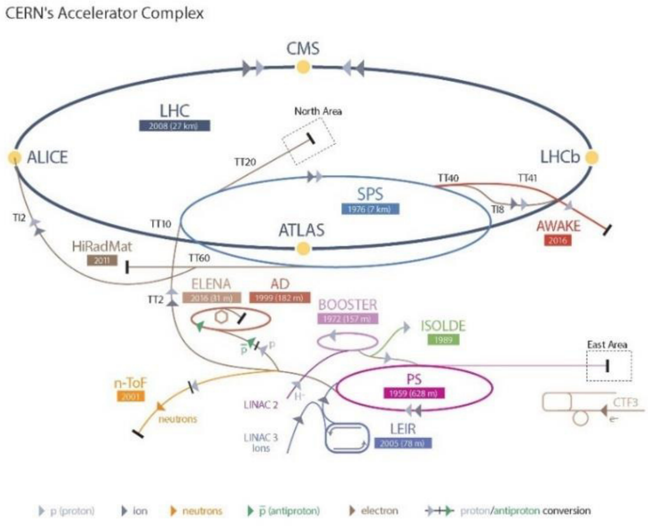

Figure 1.1: CERN accelerator complex

The structure of a circular accelerator comprises usually accelerating cavities, bending dipoles to keep the beam on its circular orbit and focusing/defocusing quadrupole magnets. The LHC magnets operate at cryogenic temperature of 1.9 K in order to exploit the superconductivity and produce high magnetic bending or focusing/defocusing field. The LHC structure is unique and the superconducting magnets are cooled by means of the super-fluid helium (He-II) down to 1.9 K. Two magnetic channels housed in the same yoke and cryostat guide two parallel beams, which save space in the tunnel and reduce by about 25% the cost of two separate lines (see Fig.1.2). The beam in one pipe circulates clockwise while in the other one circulates anticlockwise. Beams collide in correspondence of the detectors. The latter are four in LHC and they are integrated in the main ring: the ALICE for ion physics study, the LHCb for matter/antimatter investigations, the ATLAS as well as the CMS for general physics experiments, but mainly connected to the Higgs' model study. LHC was deigned to reach up to 7 TeV energy per beam. The luminosity is another important indicator of the performance of an accelerator: it is proportional to the number of collisions that occur in a given amount of time. The design luminosity of the LHC is 10^{34} $cm^{-2}s^{-1}$ (Brüning *et al.*, 2004), which was first reached in June 2016.

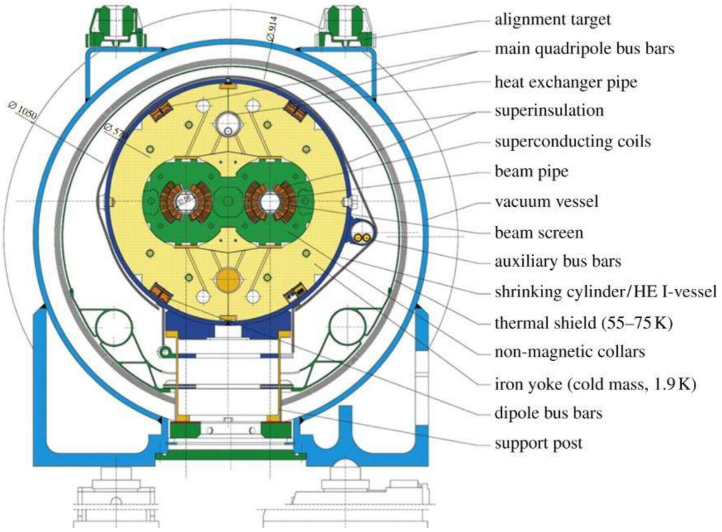

Figure 1.2: Cross section of a LHC dipole

The accelerator complex includes the Antiproton Decelerator and the Online Isotope Mass Separator -ISOLDE- facility (Koster, 2001), and feeds several experimental areas like the Compact Linear Collider (CLIC) test area and the neutron time-of-flight facility (nTOF). Protons are not the only particles accelerated in the LHC. Lead ions for the LHC start from a source of vaporized lead and enter a linear accelerator before being collected and accelerated in the Low Energy Ion Ring (LEIR). They then follow the same route to maximum energy as the protons. Furthermore, there are a number of experiments exploiting the CERN facilities such as the Advanced Proton Driven Plasma Wakefield Acceleration Experiment (AWAKE) and the Extra Low ENergy Antiproton ring (ELENA). AWAKE experiment aims at studying plasma wakefield generation and electron acceleration driven by proton bunches. It is a proof-of-principle R&D experiment at CERN and the world's first proton driven plasma wakefield acceleration experiment. ELENA is a compact ring for cooling and further deceleration of 5.3 MeV antiprotons delivered by the CERN Antiproton Decelerator (AD). The AD physics program is focused on trapping antiprotons; the ultimate physics goal is to perform spectroscopy on antihydrogen atoms at rest and to investigate the effect of the gravitational force on matter and antimatter.

1.2 Vacuum systems at CERN.

To avoid colliding with gas molecules inside the accelerator, the beams of particles in the LHC travel in a vacuum, called beam vacuum, as empty as interstellar space. In the cryomagnets and the helium distribution line, the vacuum acts as a thermal insulator, to reduce the amount of heat coming from the surrounding room-temperature environment into the cryogenic parts which are kept at 1.9 K (-271.3°C).

The vacuum system of the LHC is among the largest in the world; a total of 104 kilometers of piping is under vacuum. The insulating vacuum, equivalent to some 10^{-6} mbar, is made up of about 50 km vacuum vessels. This vacuum system requires more than 250,000 welded joints and 18,000 demountable vacuum seals. The remaining 54 km of pipes under vacuum are the beam pipes, through which the LHC's two beams travel. They work in a Ultra High Vacuum (UHV) regime: the pressure in these pipes is in the order of 10^{-10} to 10^{-11} mbar, a vacuum almost as rarefied as that found on the Moon. Beam pipes include 48 km of arc sections, kept at 1.9 K, and 6 km of straight sections, kept at room temperature, where beam-control systems and the insertion regions for the experiments are located (Brüning *et al.*, 2004).

In the arcs, the ultra-high vacuum is maintained by cryogenic pumping of 9000 cubic meters of gas. As the beam pipes are cooled to extremely low temperatures (1.9 K), the gases condense and adhere to the walls of the beam pipe by adsorption (Chiggiato, 2016).

Two important design features guarantee UHV conditions in the room-temperature sections. One is the presence of Non Evaporable Getter (NEG) coatings (Benvenuti, 1998), that absorb residual molecules when heated acting as a distributed pumping system; the other important characteristic is that the room-temperature sections allow "bakeout" of all components at temperature higher than 200°C. Bakeout is a heating stage of the vacuum chambers aimed to improve the quality of the vacuum (reducing the final pressure of the system) by accelerating the degassing phenomena from the pipe walls (Chiggiato, 2016). The heating stage (for NEG activation and bakeaout) need to be performed according to CERN accelerator operations, to keep the vacuum at the desired low pressure.

1.3 The need of remote operations at CERN.

The majority of CERN’s accelerator beam lines are installed in approximately 50 km of underground tunnels; the earth above and around the tunnels provides radiation shielding. When particle beams are circulating in the machines, personnel access is not allowed for radiation safety reasons. Collisions between the particles present in the circulating beams and residual gases or beam losses in the accelerator devices result in an induced radioactivity of the irradiated components which can be less or more significant depending on their position within the accelerator complex.

The High-Luminosity Large Hadron Collider (HL-LHC) project (Brüning and Rossi, 2015) aims to improve the performance of the LHC in order to increase the potential for discoveries after 2025. The objective is to increase luminosity by a factor of 10 beyond the LHC's design value. The higher the luminosity, the more data the experiments can gather to allow them to observe rare processes. High-Luminosity LHC will produce up to 15 million Higgs bosons per year, compared to the 1.2 million produced in 2011 and 2012. This means that even when the beams are no longer circulating, personnel access to certain areas is not possible until sufficient time (cooling time) has passed for reducing the radiation levels (decay). Radioactivity levels in some critical areas such as sectors close to beam collimators (Redaelli, 2013) and the final focusing inner triplet quadrupole magnets, will intensify by a factor of 16 in the next 20 years of operation. These significant increases have direct implications on the maintenance of these facilities, which often need personnel interventions for routine operations and technical problem troubleshooting.

The CERN Radiation Protection Group defines these access restrictions. In fact, CERN has safety procedures in place to control and limit the radiation exposure of personnel; safety-critical and safety-involved systems are regulated by means of the As Low As Reasonably Achievable (ALARA) approach (Forkel-Wirth *et al.*, 2013). Figure 1.3 provides an example of the life-cycle of operations in CERN's beam facilities that necessitate the implementation of the ALARA regulations.

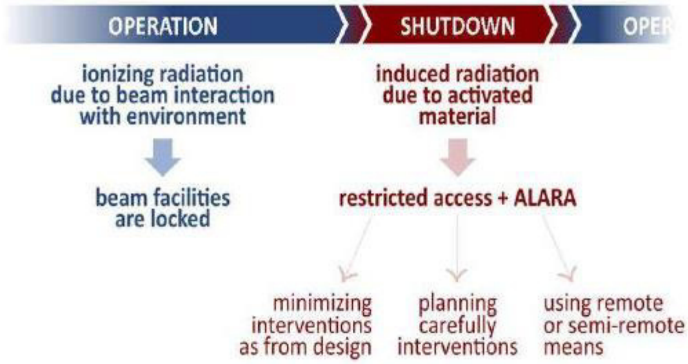

Figure 1.3: Application of ALARA and intervention operation restrictions in CERN facilities.

CERN's Occupational Health and Safety and Environmental Protection (HSE) Unit monitors ambient dose equivalent rates inside and outside CERN's perimeter and releases of radioactivity in air and water. The results of the measurements allow the preventive assessment of radiological risks and the minimization of individual and collective ionizing radiation doses. The dose limit for a person conducting maintenance operations at CERN is 6 mSv per year and for normal employees at CERN is 2 mSv per year. In some areas in ATLAS and CMS, particle debris generated by the 14 TeV proton-proton collisions induce radioactivity doses higher than 5 mSv h^{-1} so that stringent access regulations are applied. For these reasons, remote techniques are being considering at CERN and the exposure time of the technicians for inspections, measurements and handling are continuously decreasing.

In fact, remote handling development activities at CERN were initiated in the 1960s. Successful projects were run throughout the 1970s and 1980s (Kershaw *et al*., 2013) and included the design of remote mobile inspection devices, a remote mobile multi-purpose remote handling vehicle equipped with servo manipulators (Mantis) and a remotely operated custom-designed mobile crane. In addition, modular drive units were investigated for custom geometry manipulator arms, along with tooling devices for specific tasks. Several remotely controlled devices were proposed since the LHC installation was completed in 2007. Some of the in-service system upgrades are the LHC remote inspection train, the ISOLDE robots and the Remotely Operated Vehicle (ROV)(Kershaw *et al.*, 2013). Further efforts on this direction are mandatory in view of the future HL-LHC upgraded accelerators (Brüning and Rossi, 2015).

1.4 Needs of quick and compact connection systems for beam-pipe couplings

The design of leak tight connections for Ultra High Vacuum (UHV) systems is a key subject of vacuum technology. Design requirements become even more stringent when dealing with UHV beam-pipe coupling in high-energy particle accelerators, where reliability and safety are core issues. For this specific application, additional needs often arise: strict geometrical and/or space limitations, connection of dissimilar materials and installation in restricted access areas where the duration of the maintenance operations is strictly controlled and minimized.

Beam-pipe coupling in particle accelerators is nowadays provided by metallic flanges that are tightly connected by several bolts or heavy and large collars. Their installation or dismounting in radioactive area contributes to the radioactivity dose received by the operators. Remote interventions are being considered at CERN in the framework of the High-Luminosity LHC project (Brüning and Rossi, 2015) and robot interventions are under study for a few selected areas. In this framework, Shape Memory Alloys (SMAs) offer a unique possibility to generate tight connections and fast clamping/unclamping by remotely changing the temperature of the SMA junction unit, exploiting a solid-state transformation between an austenitic and a martensitic phase (Duerig *et al.*, 1989; Otsuka and Wayman, 1998). Because of their shape recovery capabilities and actuation principles, SMAs can be used to develop a new generation of vacuum tightening systems for accelerator beam-pipe coupling. Such SMA-based connectors can provide significant benefits in terms of space occupancy, bi-material joining and, above all, possible remote thermal activation. Specifically, ring-shaped SMA couplers can be used for beam-pipe joining in room temperature sections of CERN accelerators, without the necessity of a connection flange and bolts; in addition, they are smaller and lighter than the systems currently adopted and can be quickly mounted and dismounted by heating/cooling collars.

1.5 Research objectives

The research activities focused on the design of SMA-based, dismountable and thermally activated connection systems for UHV chambers that could be used in restricted access areas (highly radioactive environment), *e.g.* as beam-pipe couplers to be installed in room temperature sections of CERN accelerators. The concept is based on a SMA sleeve; it can have two sizes: a smaller, contracted version after heating, and a larger one after cooling. The SMA sleeve could easily be installed at room temperature around the extremities of the vacuum chambers when it is slightly larger in martensitic state, and then heated up (exploiting possible bakeout processes) to get the contracted austenitic shape and clamp the vacuum pipes; the vacuum leak tightness of the joint would be guaranteed even after subsequent cooling to the operating temperature (room temperature). The dismounting would be obtained re-inducing the martensitic structure by cooling the sleeve below the room temperature in order to activate the two-way shape memory mechanism (Duerig *et al.*, 1989; Otsuka and Ren, 2005) associated with a re-expansion of the SMA element. The research objectives of this work are summarized as follows:

- SMA material definition and procurement: selection of SMAs showing suitable shape memory behavior within specific thermal ranges in order to ensure easy mounting and unclamping by well-defined temperature variations.
- Thermo-mechanical characterization of SMA material and rings.
- Developments of *ad-hoc* design tools for SMA-based couplers.
- Experimental/numerical assessment of the SMA sleeve/pipe clamping pressure and its variation during thermal cycling *i.e.* heating (installation during bakeout process) and cooling (dismounting).
- Optimization of the SMA sleeve/pipe interface aimed to get reliable leak tight joints for UHV systems even after multiple thermal cycles and room temperature ageing.
- Realization and experimental validation (by means of mechanical and leak tightness tests) of SMA-based prototype vacuum chambers.
- Experimental assessment of the SMA-connectors’ functional behavior after exposure in highly radioactive environment.

1.6 Thesis outline and contributions

The organization of the thesis and its research contributions are here briefly described:

- *Chapter 1:* this introduction chapter gives an idea about the objectives of the thesis.

- *Chapter 2*: the branches of vacuum technology for particle accelerators are highly interdisciplinary ranging from the applied physics and material science to the mechanical engineering. In this chapter, some fundamentals of vacuum technology are examined.

- *Chapter 3*: demountable joints between various vacuum components are essential and widely used in UHV systems because they can be removed/resealed to facilitate dismounting for possible system upgrades or maintenance. In this chapter, a description of the most common UHV joining techniques is proposed with a particular focus on those used at CERN for beam-pipe couplings.

- *Chapter 4*: in this chapter, SMA general features are presented as well as their applications with a particular focus on generic SMA-based fastening and connection systems commercially available as well as those of recent scientific interest.

- *Chapter 5*: a SMA-based detachable system for beam-pipe couplings is presented herein and investigated by finite element (FE) simulations and experimentally, by means of mechanical, leak tightness and irradiation tests. A novel vacuum performance parameter, used for coupling optimization, is here defined based on a sealing model and the FE results. SMAs selection criteria and characterization, as well as the design and experimental assessment methods for the proposed beam-pipe SMA connectors are described herein. Some novel contributions from this chapter are published in literature (Niccoli *et al*., 2017a; Niccoli *et al*., 2017b).

- *Chapter 6:* the results of the numerical and experimental analyses of commercial NiTiNb rings and NiTiNb-based couplings are reported and discussed in this chapter. The best coupling configurations were identified by using the sealing performance parameter proposed in *Chapter 5*. The mechanical and functional performance of the NiTiNb-based couplers are described. Some novel results about these investigations are published in literature (Niccoli *et al*., 2017a; Niccoli *et al*., 2017b).

- *Chapter 7:* the results of experimental analyses of non-commercial NiTi rings and NiTi-based UHV couplings are reported; in particular, mechanical, leak tightness, and irradiation test results are discussed herein.

- *Chapter 8*: this chapter concludes the thesis along with its impact and the contributions and presents some avenues for future studies on the proposed SMA beam-pipe connectors; their future applications at CERN are described as well.

2. BASICS OF VACUUM TECHNOLOGY FOR PARTICLE ACCELERATORS

2.1 Introduction

The branches of vacuum technology for particle accelerators are highly interdisciplinary ranging from the applied physics and material science to the mechanical engineering in the phase of design and production. In this chapter, some fundamentals of vacuum technology are examined.

2.2 Basic notions on vacuum technology

A rarefied gas in equilibrium is always described by the ideal gas equation of state (Lafferty, 1998):

$$p\,V = Nk_BT \tag{2.1}$$

or

$$p\,V = nk_BT \tag{2.2}$$

Where *p*, *V* and *T* are gas pressure, volume and temperature respectively; k_B is the Boltzmann constant (1.38 10^{23} J/K); *N* is the total number of molecules in the gas and *n* is the gas density. The most common pressure units are mbar and Torr (1mbar = 10^2 Pa = 0.75 Torr). The number of molecules of gas can be expressed as pressure-volume (*pV*) values at a given temperature. Pressure-volume quantities are converted to number of molecules dividing them by k_bT as given in the equation of state. In vacuum systems, pressures span several orders of magnitude (see Table 2.1).

Table 2.1: Degrees of vacuum and their pressure boundaries (Lafferty, 1998).

Definition	Pressure Boundaries [mbar]
Low Vacuum	10^3-1
Medium Vacuum	1-10^{-3}
High Vacuum HV	10^{-3} - 10^{-9}

Ultra High Vacuum UHV	10^{-9}- 10^{-12}
Extreme Vacuum XHV	$<10^{-12}$

Degrees of vacuum are defined by upper and lower pressure boundaries. Different degrees of vacuum are characterized by different pumping technologies, pressure gauges, materials and surface treatments. For example, ion sources operate in the degrees of vacuum that are usually called medium and high vacuum, while in the LHC experimental beam pipes the Ultra High Vacuum range (UHV) is attained.

In any physically limited vacuum system, molecules collide between each other and with the walls of the vacuum envelope. In the first case, a characteristic parameter is defined as the average length of the molecular path between two points of consecutive collisions, i.e. the mean free path λ. It is inversely proportional to the gas density *n* and the collision cross section σ_c (Lafferty, 1998). For elastic collisions between hard spheres, λ can be written in terms of the molecular diameter δ.

$$\bar{\lambda} = \frac{1}{\sqrt{2}\,\pi n \delta^2} = \frac{k_B T}{\sqrt{2}\,\pi p \sigma_c} \tag{2.3}$$

The ratio of $\bar{\lambda}$ and the characteristic dimension of a vacuum system (*D*) is called Knudsen number and is a key parameter for the gas dynamic regime definition (Lafferty, 1998):

$$K_n = \frac{\bar{\lambda}}{D} \tag{2.4}$$

In fact, when the mean free path is very small, like at atmospheric pressure, the collisions between particles have a significant influence on the gas flow. When the path is in the range of the dimensions of the vacuum vessel, molecular collisions with the wall become preponderant. For even longer $\bar{\lambda}$ the gas dynamic is dominated by molecule-wall collisions: intermolecular interactions lose any effect on the gas flow (see Tab. 2.2).

Table 2.2: Gas dynamic regimes defined by Knudsen number.

K_n range	**Regime**	**Description**
$K_n > 0.5$	Free molecularflow	Gas dynamics dominated by molecule-wall collisions
$K_n < 0.01$	Continuous (viscous) flow	Gas dynamics dominated by intermolecular collisions

$0.01 < K_n < 0.5$	Transitional flow	Transition between molecular and viscous flow

Typical beam pipe diameters are of the order of 10 cm. Therefore, free molecular regime is obtained for pressures in the low 10^{-3} mbar range or lower. Except for ion sources, vacuum systems for accelerators operate in free molecular regime (Chiggiato, 2016)

2.3 Gas kinetics

The kinetics of ideal-gas molecules are described by Maxwell-Boltzmann distribution (Lafferty, 1998). For an isotropic gas, the model provides the distribution of the molecular speed magnitudes. The average speed of molecules $\bar{v}$ in a Maxwell-Boltzmann distribution is given by:

$$\bar{v} = \sqrt{\frac{8k_BT}{\pi m}} = \sqrt{\frac{8RT}{\pi M}}\ [m/s] \tag{2.5}$$

where m is the mass of the molecule, M is the molar mass, R is the ideal gas constant. Another relevant result of Maxwell-Boltzmann theory is the calculation of the molecular impingement rate ν on a surface, i.e. the rate at which gas molecules collide with a unit surface area exposed to the gas. Assuming that the density of molecules all over the volume is uniform, it can be shown (Lafferty, 1998) that:

$$\nu = \frac{1}{4} n\, \bar{v} \tag{2.6}$$

Usually ν is expressed in mbar l cm^{-2} s^{-1}. Numerical values as a function of pressure, at room temperature are shown in Table 2.3.

Table 2.3: Impingement rate for common gases at room temperature at some selected pressures.

Gas	**Pressure [mbar]**	$\boldsymbol{\nu}[\frac{\textbf{molecules}}{\textbf{s cm}^2}]$
N_2	10^{-3}	2.9×10^{17}
	10^{-8}	2.9×10^{12}
H_2	10^{-3}	1.1×10^{18}
	10^{-8}	1.1×10^{13}
	10^{-8}	1.1×10^{7}
H_2O	10^{-3}	3.6×10^{17}

10^{-8}	3.6×10^{12}

2.4 Conductance in free molecular flow

In free molecular regime, the net gas flow between two points of a vacuum system, Q, is proportional to the pressure difference (p_1 - p_2) between the same points:

$$Q = C(p_1 - p_2) \tag{2.7}$$

C is gas conductance of the vacuum system between the two points. In free molecular regime, the conductance does not depend on the pressure. It depends only on the mean molecular speed and vacuum system geometry. If the gas flow units are expressed in terms of pressure-volume (for example mbar l/ s), the conductance is reported as volume per unit time, i.e. l/s.
It follows from this definition that when two conductances C1 and C2 are connected together, the total conductance C is given by

$$C_{tot} = C_1 + C_2 \text{for parallel connection} \tag{2.8}$$

$$\frac{1}{C_{tot}} = \frac{1}{C_{tot}} + \frac{1}{C_{tot}} \text{ for series connection} \tag{2.9}$$

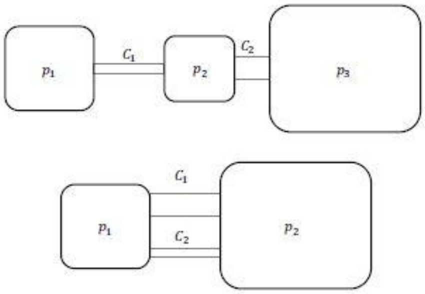

Figure 2.1: Schematic drawings of components installed in series (top) and parallel (bottom).

2.4.1 Conductance of an orifice

The conductance is easily calculated for the simplest geometry, i.e. a small orifice of surface A and infinitesimal thickness dividing two volumes of the same vacuum system (see Fig. 2.2) in isothermal condition.

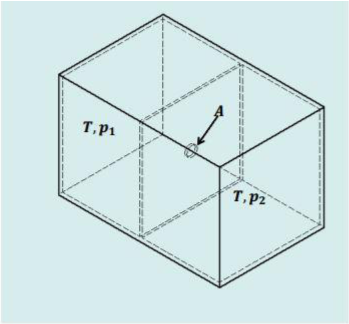

Figure 2.2: Schematic drawing of two volumes at different pressures p_1 and p_2 divided by a small orifice of surface A

The net molecular flow from one volume to the other may be calculated by the molecular impingement rate given by Eq. 2.6. The number of molecules of volume 1 that goes into volume 2 ($\varphi_{1\to 2}$) is:

$$\varphi_{1\to 2} = \frac{1}{4} A n_1 \bar{v} \tag{2.10}$$

while from volume 2 to volume 1 is:

$$\varphi_{2\to 1} = \frac{1}{4} A n_2 \bar{v} \tag{2.11}$$

The net molecular flow is given by the difference of the two contributions:

$$\varphi_{1\to 2} - \varphi_{2\to 1} = \frac{1}{4} A(n_1 - n_2)\bar{v} = \frac{1}{4}\frac{\bar{v}}{Tk_b} A(p_1 - p_2)\ \left[\frac{\text{molecules}}{\text{unit time}}\right] \tag{2.12}$$

Expressing the flux in pressure-volume units we finally obtain:

$$Q = \frac{1}{4}\bar{v}A(p1 - p2) \tag{2.13}$$

Comparing Eq. 2.13 and 2.7, it is clear that the conductance of the orifice is proportional to the surface area of the orifice and the mean speed of the molecules:

$$C = \frac{1}{4}\bar{v}A \propto \sqrt{T/m} \tag{2.14}$$

In particular, the conductance of the orifice is inversely proportional to the square root of the molecular mass:

$$\frac{C_1}{C_2} = \sqrt{m_2/m_1} \tag{2.15}$$

2.4.2 Conductance in a complex geometry

For geometries more complex than orifices, the transmission probability τ is introduced. If two vessels, at the same temperature, are connected by a duct (see Fig. 2.3), the gas flow from V_1 to V_2 is calculated multiplying the number of molecules impinging on the entrance section of the duct by the probability for a molecule to be transmitted into vessel 2 without coming back to vessel 1, $\tau_{1\rightarrow 2}$:

$$\varphi_{1\rightarrow 2} = \frac{1}{4} A_1 n_1 \bar{v}\, \tau_{1\rightarrow 2} \tag{2.16}$$

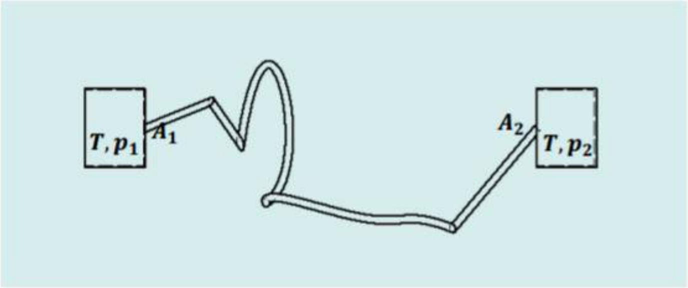

Figure 2.3: Schematic drawing of two vessels connected by a complex duct.

After few mathematical operations it can be found that, for complex geometries:

$$C = C' A_1\, \tau_{1\rightarrow 2} \left(p_1 - p_2\right) \tag{2.17}$$

Where *C′* is the conductance per unit area of an orifice. These results show that the conductance depends only on the speed of molecules and on the transmission probability, which depends on the geometry of the connecting duct. One of the main goals of vacuum computation is to find the value of $\tau_{1\rightarrow 2}$.

It may be calculated analytically for simple geometries by means of relatively complex integral equations (Clausing, 1971). For the very common case of long tubes of uniform circular cross section of length *L* and radius *R* ($L/R >> 1$) the Santeler equation (Santeler, 1986) gives transmission probability with less than 0.7 % error.

$$\tau = \tau_{1\rightarrow 2} = \tau_{2\rightarrow 1} = 8R/3L \tag{2.18}$$

Conductances of more complicated components are calculated by Test-Particle Monte Carlo methods (TPMC). The system is first modelled in three dimensions, then TPMC codes generate molecules at the entrance of the component, pointing in “random” directions according to the cosine distribution. When molecules impinge on the internal wall of the component, they are reemitted again randomly. The program follows the molecular traces until they reach the exit of the component. The transmission probability is given by the ratio of number of “escaped” particles and “injected” molecules (Davis, 1970). Many simulated molecular trajectories are needed to reduce the statistical scattering. The reference TPMC software at CERN is Molflow+ (Kersevan and Pons, 2009). This powerful tool imports 3D drawing of vacuum components and generates “random” molecules on any surface of interest. Fig. 2.4 shows an example of a kicker magnet simulated by Molflow+

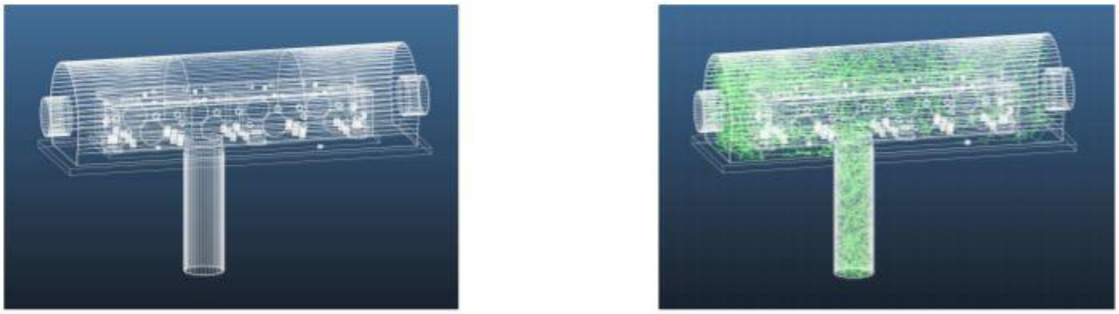

Figure 2.4: Meshes used for Monte Carlo simulation of the MKQVL kicker of SPS. The second picture shows molecular tracks (in green) generated by Molflow+ code.

2.5 Pumping speed

In vacuum technology, a pump is any component that removes molecules from the gas phase. A vacuum pump is characterized by its pumping speed *S*, which is defined as the ratio between the pumped gas flow Q_p (pump throughput) and the pump inlet pressure p.

$$S = \frac{\mathrm{Q}_p}{\mathrm{p}} \quad [l/s] \tag{2.19}$$

The pumping speed unit is volume over time, thus the same unit as conductance. In a more general way, *S* can be defined as the derivative of the pump throughput with respect to the pump inlet pressure:

$$S = \frac{\partial \mathrm{Q}_p}{\partial \mathrm{p}} \tag{2.20}$$

The pump throughput can be written as the gas flow φ through the cross section of the pump inlet (surface area A_p) multiplied by the capture probability σ, i.e. the probability for a molecule that enters the pump to be definitely removed and never reappears in the gas phase of the vacuum system.

$$\mathrm{Q}_p = \varphi A_p \, \sigma = \frac{1}{4} A_p \, n\bar{v} \, \sigma \tag{2.21}$$

Considering Eq. 2.14 and 2.2,:

$$\mathrm{Q}_p = A_p \, C'n \, \sigma = A_p \, C'\sigma \frac{p}{k_b T} \tag{2.22}$$

From the definition of pumping speed and converting in pressure volume units:

$$S = A_p \, C'\sigma \tag{2.23}$$

Therefore, the pumping speed is equal to the conductance of the pump inlet cross section multiplied by the capture probability. The maximum theoretical pumping speed of any pump is obtained with $\sigma = 1$ and it is equal to the conductance of the pump inlet cross section.

The pumping speed given by the suppliers is called nominal pumping speed; it refers to the pump inlet. The effective pumping speed S_{eff} is the one acting directly in the vacuum vessel of interest. The effective pumping speed is lower than the nominal due to gas flow restrictions interposed between the pump and the vessel.

The effective pumping speed is calculated considering the gas flow from the vessel to the pump. Taking into account Eq. 2.14 and Eq. 2.20:

$$Q = C_1(p1 - p2) = Sp_2 = S_{eff}p_1 \tag{2.24}$$

$$\frac{1}{S_{eff}} = \frac{1}{S} + \frac{1}{C} \tag{2.25}$$

As a result, for $C \ll S$, $S_{eff} \approx C$. In other words, the effective pumping speed does not depend on the installed pump if the conductance of the interposed connection is very low.

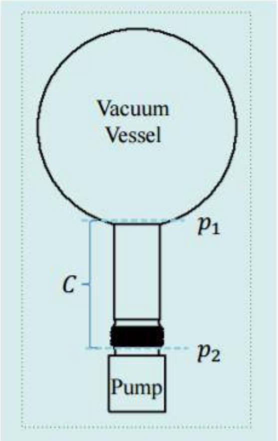

Figure 2.5: Schematic drawings of component of a gas flow restriction of conductance *C* interposed between a pump of pumping speed *S* and a vacuum vessel.

2.6 Pressure profile calculation

The calculation of the pressure profile is an essential task for vacuum system design. In general, the contributions to the total pressure of localized and distributed gas sources are considered separately and finally added. This is possible because in most of the cases the equations that describe pressure profiles are linear (Chiggiato, 2016). This may not be true if the pumping speed is pressure dependent.

The pressure in a vacuum vessel is obtained by taking into account Eq. 2.19 and the intrinsic limitation p_0 of the installed pumping system:

$$p = \frac{Q}{S} + p_0 \tag{2.26}$$

The base pressure p_0 can be expressed as the pressure attained by the system without any gas load (Chiggiato, 2016). When many vessels are interconnected, the flow balance is written (node analysis (Chiggiato, 2016).). This analysis leads to a system of linear equations from which the pressure values in each vessel are calculated. In case of uniformly distributed outgassing and lump pumps, the pressure profiles are calculated analytically for simple geometries (Chiggiato, 2016; Lafferty, 1998)

For more complex systems numerical solutions are needed. For example, long beam pipes are subdivided into small units to calculate the axial pressure distribution; the small units are considered as single vacuum chambers (volume and conductance) in series. The conductance of a single small unit is equal to the conductance of the entire vacuum chamber times the number of units (Chiggiato, 2016).

2.7 Pumps description

The vacuum pumps can be classified according to the physical principle they use to empty the vessels. A simplified overview on existing vacuum pumping technologies is shown on Fig. 2.6. In particular, a distinction is made between gas-displacement vacuum pumps and gas-binding (capture) vacuum pumps. In capture vacuum pumps the molecules remain inside the pump itself by chemical bonds (Getter Pump, Ion Pump) or cryopumping. The Gas Transfer Pumps instead displace gas from the vacuum side to an exhaust side, thanks to a mechanical action on gas molecules.

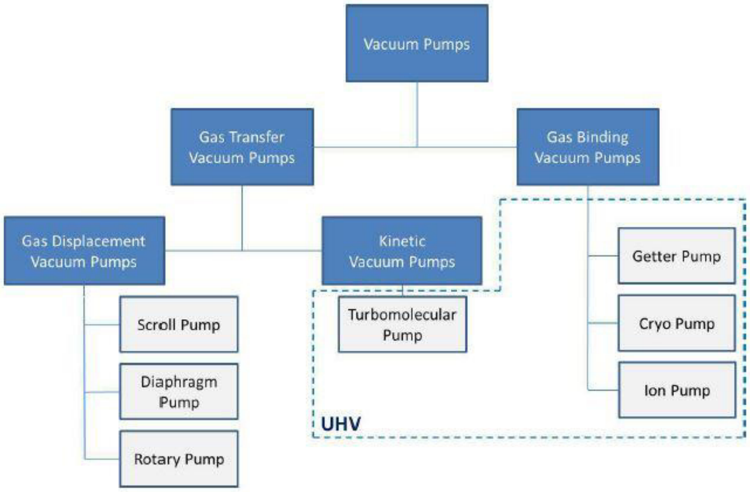

Figure 2.6: Scheme of the main types of vacuum pumps.

2.8 Sources of gas within the vacuum system

The ultimate pressure which can be reached in a vacuum system depends both on the effective pumping performance and the gas influx coming from the vacuum envelope and from any components contained within it. Thus, when the best possible pump is used, the main difference between a vacuum vessel which achieves only low vacuum and one that achieves ultrahigh vacuum, is that in the latter case the total rate of influx of gas is twelve orders of magnitude less than in the former case (Weston, 1985)

2.8.1 Thermal outgassing

The release of gas molecules from the vacuum material itself (vacuum pipes and related devices) represents, in most of the cases, the dominant source of gas in UHV systems. This gas release can be defined as (Chiggiato, 2016):

- thermal outgassing: when the gas removal is spontaneous, i.e. provoked by thermal vibration at standard temperature of the apparatus;
- degassing: when gas molecules are freed by deliberate action, for example heating at high temperatures or bombarding the surface with particles (photons, electrons, ions) (see section 2.8.2);

Different phenomena can explain outgassing, like gas dissolution and diffusion (see Fig. 2.7). Outgassing properties depends on the nature of materials and on the applied surface and thermal treatments. Any material may contain gas which was trapped during the manufacturing and treatment of the bulk or has diffused into it during exposure to atmospheric conditions. The reduction of the outgassing rate is the prime objective in attaining UHV conditions and sets the main criterion to the choice of materials for ultrahigh vacuum use.

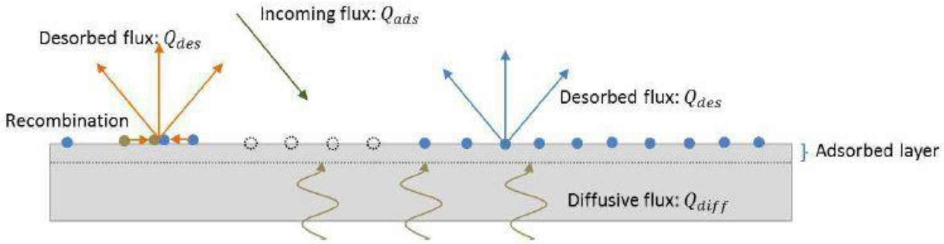

Figure 2.7. Fluxes for a general surface

Water outgassing in metals

Widely recognized experimental results (Dylla 1993; Kanazawa, 1989) show that water vapor dominates the outgassing process of metals in vacuum. For smooth metals, the outgassing rate is inversely proportional to the pumping time, *t* (see Fig.2.8). The water outgassing rate for stainless steel at room temperature can be empirically described by the following equation (Chiggiato, 2016).

$$Q_{H_20} = \frac{3\text{x}10^{-9}}{\text{t[h]}} \frac{mbar\ l}{cm^2 s} \tag{2.28}$$

Such behavior determines the pressure-time evolution of unbaked metallic vacuum systems. The average time that a molecule spends on the surface before being desorbed is defined as mean sojourn time τ. This term is dependent on the surface temperature *T* and on the molecule binding energy *E* (Lafferty, 1998):

$$\tau = \tau_0\, e^{E/RT} \tag{2.29}$$

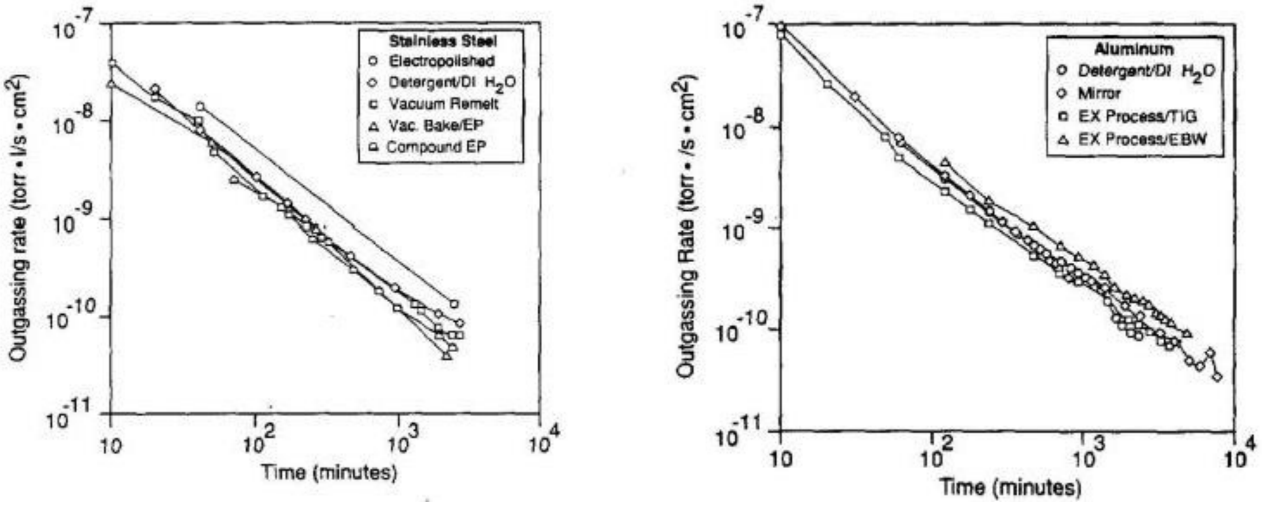

Figure 2.8: Water vapour outgassing rate of stainless steel and aluminum after four different surface (H. F. Dylla 1993).

with τ_0 the nominal period of vibration of an adsorbed molecule, of the order of 10^{-13} s (Lafferty, 1998) and *R* the gas constant. At room temperature, water binding energies during a pump-down varies in a window between 15 kcal/mole and 25 kcal/mole (Redhead, 1995a; Redhead, 1995b). Water vapor outgassing rate may be reduced by acting either on molecules binding energies (changing the surface nature) or on the system temperature. The latter may be divided in two alternative solutions (Chiggiato, 2016):

1. Heating in situ during part of the pump-down time (bakeout). The bakeout is very effective for metals if it is carried out of at least 12h at temperatures higher than 120°C. Water molecules are removed (since τ decreases at higher *T*) and are pumped out faster during the heating time. A much lower pressure is obtained when the system is cooled down again to room temperature, (see Fig. 2.9). Bakeout is performed in the room temperature section of the LHC beam-pipes as well as in other room temperature beam-pipes within the CERN facilities.

2. Permanently cooling the vacuum system to cryogenic temperature during operation: water molecules have a longer sojourn time and lower pressures are quickly achieved. Note that the molecules are still on the surface, but the temperature is too low for them to be desorbed. The arc section of the LHC beam-pipes are kept at 1.9K to exploit this cryopumping effect.

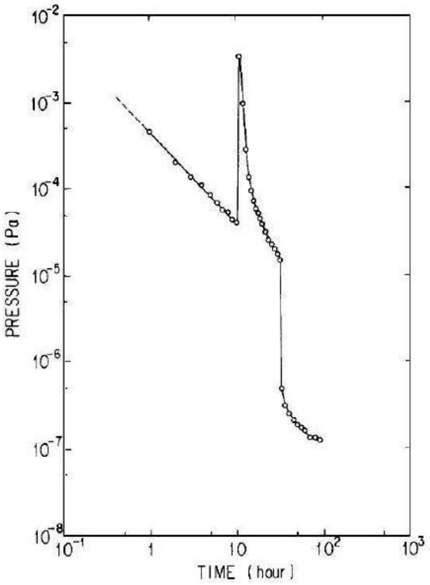

Figure 2.9: Pressure evolution in an aluminum chamber (Kanazawa, 1989). The pressure increase represents the beginning of the bakeout. The pressure drop follows the system cooling down to room temperature.

Hydrogen outgassing

When water vapour desorption is strongly reduced, the outgassing process is led by H_2. This gas is dissolved in metals as single H atoms. Its diffusion is relatively fast and, after recombination on the surface, it can be released as molecular hydrogen (Chiggiato,2016). As for water vapor, hydrogen-outgassing rate is reduced by heating the vacuum components. Higher temperatures increase the H atoms mobility and, as a result, accelerate the depletion of the residual hydrogen content. However, there is a crucial difference between water vapor and hydrogen. Each time the vacuum system is exposed to air, water molecules re-adsorb on the surface, while hydrogen is not recharged in the bulk of the metal (Dylla, 1993; Chiggiato, 2016).
As for an activated process Q_{H2} depends exponentially on temperature (Chiggiato, 2016).:

$$Q_{H_20} \propto e^{-E/k_bT} \tag{2.30}$$

where E is the activation energy for the diffusion process (about 0.52 eV for austenitic stainless steel).

Hydrogen outgassing measurements: throughput and accumulation methods

The intrinsic outgassing rate of a solid or liquid is the quantity of gas leaving per unit time per unit of exposed geometric surface, or per unit mass of the sample, at a specified time after the start of evacuation. The geometric surface area is the visible surface area without correction for surface roughness, waviness or open surface porosity. The measured (or net) outgassing rate is the difference between the intrinsic outgassing rate and the rate of readsorption on the surfaces in the test chamber. The readsorption rate depends on the measurement method being used, and the surface area and surface properties of the test chamber.

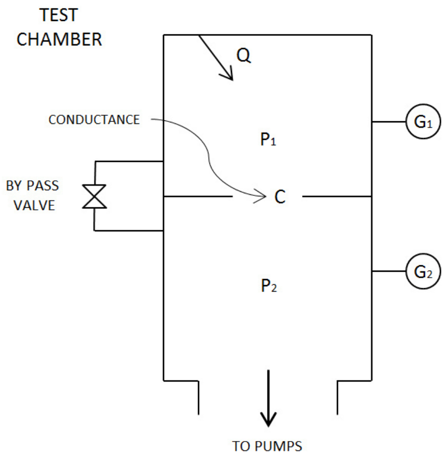

Figure 2.10: Schematic diagram of the system used to measure outgassing rates q by the throughput method. The two vacuum gauges (or RGAs) G_1 and G_2 are used to measure the pressure drop (P_1-P_2) across the conductance C.

The measured outgassing rate is nearly equal to the intrinsic rate for some methods under certain conditions (i.e., the readsorption rate is zero). For most materials the outgassing rate is proportional to the exposed surface area, but for some materials the outgassing rate may also depend on the thickness. A schematic diagram of the system for measurements by the throughput method is shown in Fig. 2.10; see (Elsey, 1975). While the net pumping speed is different for the various components in a gas mixture under molecular flow conditions, the throughput of each gas species leaving the chamber at any instant can be determined by measuring the partial pressure of the gas in the chamber and multiplying by the net pumping speed for that gas. The net pumping speed may be computed from conductance formulas. A quantity called the nitrogen equivalent throughput can be monitored by measuring the pressure with a gauge using the calibration factor for nitrogen. If the net pumping speed is sufficiently large, the gas originally filling the free space in the chamber can be quickly removed and the throughput will become a function only of the outgassing rate of the chamber and sample therein (provided that leaks, and outgassing or pumping in the gauges, are insignificant). The outgassing rate of the chamber can then be measured as a function of time until the pressure begins to approach the ultimate pressure of the pumping system. For the throughput method the outgassing rate per unit area is given by

$$q_a = (P_1 - P_2)C/A \tag{2.31}$$

When the pressure on the pump side of the orifice P_2 is very small compared with chamber pressure P_1 then Eq. 2.31 becomes

$$q_a = P_1 C/A \tag{2.32}$$

Another method similar to the throughput one is based on gas accumulation over different times. In this case, after pumping down and baking, the chamber in which the gas is accumulated is isolated from the rest of the system by a variable leak valve. At time t_a the leak valve is opened. Pressure evolves as shown below in Fig. 2.11

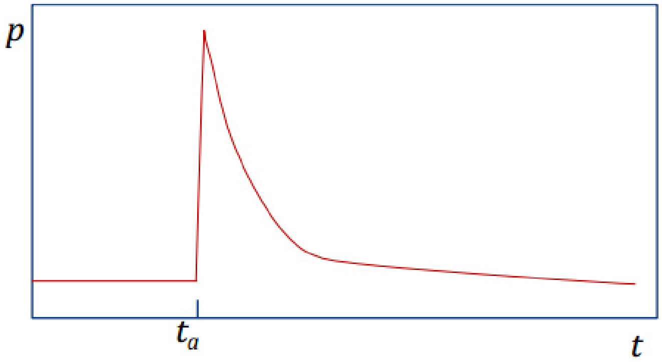

Figure 2.11: Release of the gas accumulated long over a certain amount of time.

The accumulation method extends the limits of the throughput method to lowest outgassing rates. In fact, it limits the effect of the gauge and of system's outgassing. The total evolved gas quantity can be measured by integrating the area under the desorption curve, upon aperture of the valve, as:

$$Q(t_a) = Q_s + Q_b = S_{eff} \int_{t_a}^{t_a+\Delta t} p(t)\, dt \tag{2.33}$$

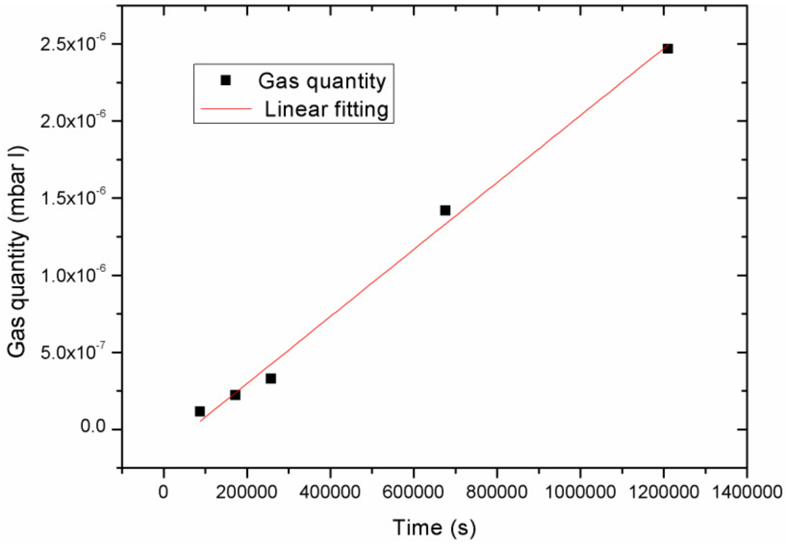

Figure 2.12: Interpolation of gas quantities accumulated over different times.

By plotting gas quantities accumulated over different ta it is possible to know the outgassing rate of the chamber. In fact, as shown in Fig. 2.12, it is represented by the slope of the line connecting the points of these quantities. Along the experimental campaign this particular method has been chosen to conduct all the outgassing measurements. Fig 2.13 depicts the technical scheme of the system used in the laboratories of CERN.

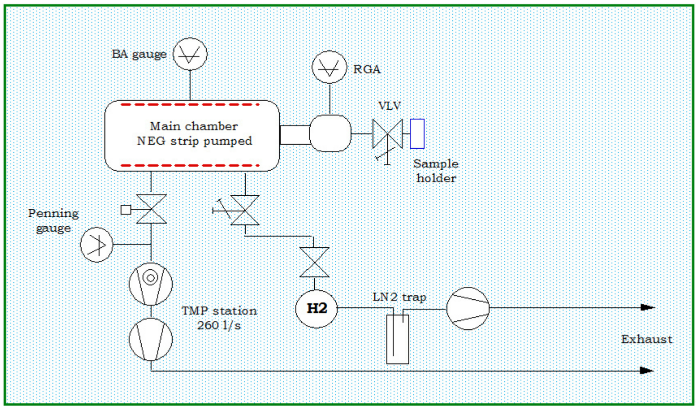

Figure 2.13: Technical scheme of the system used in the laboratory of CERN

2.8.2 Dynamic outgassing

Outgassing stimulated by photons, ions and electrons created by high energy and high-intensity particle beams in accelerators and storage rings represents a serious limitation for the design of vacuum systems. In high-energy, high-intensity accelerators and storage rings for electrons and positrons, the particle beams emit intense synchrotron radiation in a forward-directed narrow cone. This energetic photon flux produces strong outgassing from the vacuum system and thus a large dynamic pressure increase which limits the beam lifetime in the machine and may cause increased background in the colliding beam experiments. In storage rings with intense, positively-charged beams of protons and positrons the pressure can increase due to ion-induced desorption from the walls of the beam pipe. Ions created from the residual gas are repelled by the positive space-charge potential and are accelerated towards the wall. Ions may gain energies of several hundred eV per ampere of circulating current and are thus very effective for desorbing strongly-bound gas molecules. Gas desorption-induced by beam generated ions was a serious limitation to the performance of the Intersecting Proton Storage Rings (ISR) at CERN in the past and is a major concern for the vacuum system design of the Large Hadron Collider (Grobner, 1999).

2.8.3 Permeation

In the previous section the flow of gas from the interior of the bulk substance by diffusion was discussed. When the material forms the envelope of the vacuum vessel, a second cause for a concentration gradient is present, due to the difference between the gas pressures on the opposite sides of the envelope material. Generally, for most combinations of gas and solid used for vacuum envelopes, it is of no great importance at room temperatures, with the exception of the passage of helium through some glasses. It is worth pointing out that the temperature increase of the vacuum envelope, normally obtained during bakeout process (which is advantageous in terms of post-treatment outgassing loads) promotes the permeating the gas flow from the outside into the vacuum system. The permeation is mainly function of the temperature. Detailed data about permeation and outgassing for a wide spectrum of vacuum materials (polymers, metals and ceramics) can be found in literature (Perkins, 1973).

2.8.4 Vaporization

If atoms or molecules bound together in solid or liquid phase have a sufficient kinetic energy to overcome the binding forces, they can escape into the gas phase. If the bulk medium, i.e. the solid or liquid, is in a vessel (closed system) then all the vaporized gas will be trapped within the vessel. Their density and pressure, will rise up to an equilibrium value, the vapor pressure. At that point the rate of vaporization per unit area, is equal to the rate of their condensation. The rate of evaporation of a certain substance in vacuum depend only on its temperature and its intrinsic nature. When the product of the vaporization flow and the exposed surface area of the evaporating substance provides a gas load equal to the effective pumping rate, the vacuum system will be limited by the process of evaporation. Any material used with or within a vacuum system have an intrinsic vapor pressure. High vapor pressure materials have to be limited as much as possible in order to reduce their evaporative gas load to an acceptable minimum. Greases and lubricants but also metallic materials that have high vapor pressures (zinc or cadmium) have to be avoided in vacuum systems.

2.8.5 Gas leaks in vacuum systems

If any small hole exists in vacuum vessels, pipes or components gas can flow from the outside atmosphere into the vacuum. It is therefore necessary to reduce the number and size of these leaks so that the total rate of gas influx is less than the product of available pumping speed and the pressure. Most solid materials, when free from imperfections, are perfectly leak tight. Usually leaks occur in correspondence of joint of the vacuum envelope. Permanent joining methods such as soldering, brazing and welding are all capable of providing leak-free joins. For materials which are not joinable by such methods, it is often possible to obtain leak-tight joins using elastomer or soft metal gasket seals, or even various adhesives with suitably low vapor pressures. The technology of demountable seals is described in section 3.4.2. The use of a helium leak detector for testing vacuum vessels provides a very sensitive test for leaks; the minimum detectable influx of helium using a leak detector is of the order of 10^{-11} mbar l s^{-1}.

Pressure differences, vibrations thermal loads or even particle radiation and other causes can lead to failure or modifications in the stress/strain field occurring in the joints; therefore, it is of vital importance to design and create joints which will remain leak tight under these conditions.

In practice, it is impossible to build a completely leak-tight vacuum system. And this is not even necessary. On the other hand, the leak rate must be small enough to allow the required pressure level to be reached. Therefore, it is important to specify an acceptable leak rate for each vacuum system. After manufacturing of a vacuum vessel it must be proven that the tightness specifications are fulfilled. Further checks are necessary during as well as after assembly and installation to locate possible leaks created during the previous steps. Thus, leak detection is an important step in the production of vacuum to guarantee that the required pressure and gas composition conditions of a vacuum system can be reached. Adequate methods and leak detection equipment have been developed over the past decades following the ever-increasing demands by industry (Zapfe, 2007).

The leak rate is defined as the *pV* throughput of a gas through a leak. It is a function of the type of gas,

pressure difference, and temperature. In a system of volume *V* the leak rate Q_l is given by

$$Q_l = V\,\frac{(\Delta \mathrm{p})}{\Delta \mathrm{t}} \tag{2.27}$$

Where *Δp* is the pressure rise during the time interval *Δt*

As an example, for a high vacuum (HV) system indicative value of helium leak rates are here reported (Zapfe, 2007)

– $Q_l < 10^{-6}$ mbar l/s: very tight HV system
– $Q_l < 10^{-5}$ mbar l/s: tight HV system
– $Q_l < 10^{-4}$ mbar l/s: leaky HV system.

The UHV constraint, instead, are satisfied if:
– $Q_l < 10^{-10}$ mbar l/s: tight UHV system.

2.8.6 Virtual leaks

Virtual leaks refer to mistakenly trapped gas volumes in the vacuum. They originate, for example, while mounting a screw in a blind tapped hole under atmospheric pressure. In fact, virtual leaks do not limit the ultimate pressure of the system, but increase the time required to obtain it. Virtual leaks can usually be avoided by proper design of components.

2.9 Pump down curve and pressure limits of vacuum systems

In a properly designed, leak free vacuum system, the outgassing (and not the volume gas removal) determines the final pressure in the high vacuum region. Water vapor, permeation, and stimulated desorption are obviously very important. The relative roles of surface desorption, diffusion, and permeation are a function of the materials used for construction (steel, aluminum, ceramic, or glass), the seals (metal gaskets, or single- or differentially-pumped elastomer gaskets), and the system history (newly fabricated, unbaked, chemically cleaned, or baked). The mathematical description of a pumping problem can be solved easily with certain approximations starting from mass balance equations (Chiggiato, 2016). The pressure over time curve for a vacuum chamber going from atmospheric pressure P_0 to any degree of vacuum is called the pump-down curve. During this descent, after the evacuation of atmospheric gases, the pressure level is determined by the wall outgassing (desorption of adsorbed layers or diffusing molecules) and the pumping surfaces (pumps, wall itself). The solution is:

$$P(t) = P_0 e^{-\frac{St}{V}} + \frac{Q_{H_20}}{S} + \frac{Q_{H_2}}{S} \tag{2.34}$$

Where P_0 is the initial pressure, V the system volume and S the pumping speed. From this equation, a composite pump-down curve is obtained and it is represented in Fig. 2.14. Equation 2.34 illustrates the relative roles of the main phenomena involved in UHV systems. The first term in the solution represents the pressure drop over time that is due to the gas in the chamber volume (red curve). In this initial stage, the pressure is reduced exponentially with time as the volume gas is removed. The remaining two terms represent the contribution of other gas sources, water vapor Q_{H_20} , and hydrogen Q_{H_2} . They are slowly varying functions over time and become dominant after the initial pumping period has passed. After some time the first term on the right-hand side is zero and the pressure is determined by water vapor (blue curve) and, in the end, by hydrogen (yellow curve). In this phase, surface desorption controls the rate of pressure decrease. In a typical unbaked system, most of the gas load is water vapor, however nitrogen, oxygen, carbon oxides, and hydrocarbons are also present. The material and its thermomechanical history determine the total quantity of gas released. Q_{H_20} term decays slowly, often as t^{-1}. Then hydrogen term Q_{H_2}represents the H_2 outgassing rate which does not change significantly with time. In fact, it is an intrinsic value for materials once the thermal history is known.

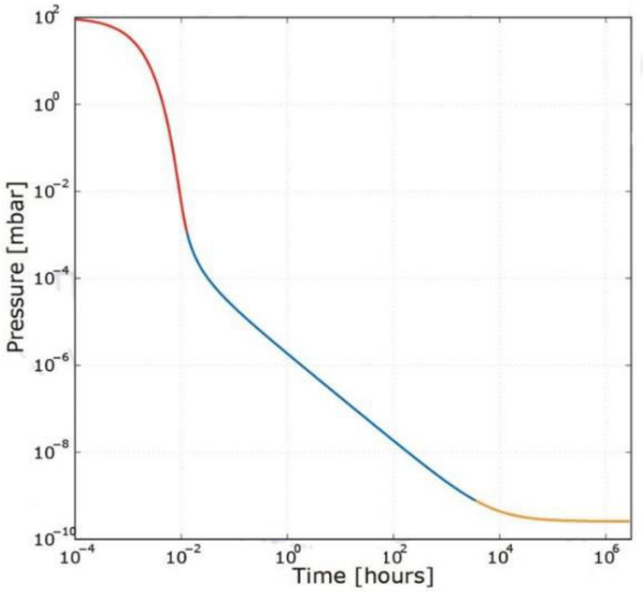

Figure 2.14: Rate limiting step during the pumping of a vacuum chamber.

The order of importance of the processes is not always as shown in Fig. 2.14. Elastomer gaskets have a high permeability for atmospheric gases and if the system contains a significant amount of these materials, it would be the dominant permeation source. The level of outgassing resulting from electron, photon, and ion-stimulated desorption processes is not shown in Fig. 2.14. These processes play a dominant role in determining the ultimate pressure of many particle accelerators. The desorption yield from energetic electrons and ions is a function of incident particle's energy, the material and its cleaning treatment, and the time under vacuum

3. JOINING TECHNIQUES IN VACUUM TECHNOLOGY FOR PARTICLE ACCELERATORS

3.1 Introduction

It is clear that the ultimate pressure of a vacuum system depends on the effective pumping speed of the pumping system as well as on the influx of gas from the vacuum envelope and any components contained within it. The reduction of the gas load is therefore the prime objective in attaining UHV conditions and the primary constraint for choosing materials for UHV applications.

UHV materials must have very low vapor pressure and, in order to accelerate water desorption phenomena from the interior walls of the system, they must be bakeable to temperatures which are usually of the order of 300°C, without losing their mechanical strength or being chemically or physically damaged. If they are part of the vacuum envelope, the permeation of gas through them must be negligible. Furthermore, they have to be corrosion resistant when exposed to air baking (heating).

Outgassing rate and mechanical/physical stability are not the only criteria for vacuum materials. The ease of manufacturing, the ability to be welded, brazed or generally seamed with leak-tight joins is also essential. Moreover, very high radiation level is usually detected in some areas of the high-energy physics equipment, such as the LHC. High intensity radiation can modify the physical and mechanical properties of metals (Schuchman, 1965; Byun and Farrell, 2004) and polymers (Peacock, 1980). Lastly, the materials have to be cost effective. The use of polymers is strongly limited in UHV vacuum systems of particle accelerators mainly due to their very high outgassing rate, low particle radiation resistance and thermal degradation.

Beam-pipe couplings at CERN is guaranteed by means of detachable connections systems. Austenitic stainless steels are widely used for vacuum chambers and coupling flanges because they fulfil most of the stringent requirements for UHV and are fairly easily obtainable at a reasonable cost.

Dismountable seals and valves are mainly made of stainless steels used in conjunction with softer metal gaskets (i.e. aluminum or copper) which allow high baking temperatures (above 300°C) and create leak-free metal joints. The gasket seals are defined as deformable and resilient parts placed between two rigid surfaces, the flanges, to obtain a leak-free seal. The seals form leak-tight joints loaded by compressing a gasket between the sealing parts.

Demountable seals between various vacuum components (pipes, pumps, sensors etc.) are essential and widely used in UHV systems because they can be removed/resealed to facilitate dismounting for possible system upgrades or maintenance.
In this chapter, a description of the most common UHV joining techniques is proposed with a particular focus on those used at CERN for beam-pipe couplings.

3.2 Materials for vacuum chambers and flanges

In modern particle accelerators there are several parameters to be taken into account for the construction of vacuum chambers. Machinability, weldability and good mechanical and physical factors are crucial aspects to consider. In addition, proper magnetic at low and room temperatures are important properties for vacuum systems working at cryogenic temperatures, such as the Large Hadron Collider (LHC). Nevertheless, baking at high temperatures imposes specific choices of material grades of suitable tensile and creep properties in a large temperature range. The materials that better own these characteristics are stainless steels. For this reason they are widely used in vacuum applications. Austenite is non-magnetic, does not undergo any ductile-to-brittle transition below room temperature and is less subject to grain growth at high temperatures. For these reasons, the austenitic grades are a first choice for vacuum applications. Austenitic grades, because of their high Cr and Ni content, are the most corrosion resistant of the stainless steel group. The three grades of stainless steels 304L, 316L, 316LN are of main interest for vacuum applications and covered by CERN specifications (CERN technical specification No. 525, 1002, 1004). AISI 304L is a general-purpose grade. For vacuum applications, the grade should be purchased through a careful specification, aimed to achieve a substantially austenitic microstructure and a controlled maximum level of inclusions. AISI 316L is a Mo-containing grade. Molybdenum enhances corrosion resistance and austenitic stability versus martensitic transformation. The ferrite-promoting characteristics of Mo have to be compensated by adjustments in Cr and Ni to achieve an almost fully austenitic microstructure. Owing to its formability, ductility and increased austenitic stability compared to 304L, this grade is covered by a special CERN specification for application in LHC interconnections. AISI 316LN is a nitrogen containing stainless steel. Nitrogen increases austenite stability as well as yielding and tensile stress, while allowing ductility to be maintained down to cryogenic temperatures.

3.3 Materials for gaskets

Gaskets must be easily deformable so that the material can flow and fill the surface irregularities of the flanges. On the other hand, the gasket should be resilient enough to maintain a proper leak free contact with the flanges over a wide range of compression forces and temperatures due to the thermal deformation of the gasket/flange assembly. Chemical, thermal and particle radiation resistance have to be as high as possible. Low permeation and outgassing rates are required. Materials used for gaskets can be classified in the following material-based categories: rubber, plastic and metal. To have a wide overview of all kind of materials, their main properties are collected and shortly described in Table 3.1 (Roth, 1994). The main advantage of rubber (natural, Nitrite rubber, Neoprene and Silicone), which determines its extensive use, is the fully elastic behavior even at high deformation levels. Unfortunately, some other features decrease the range of applications in which the rubber seals can be used. Intrinsic limitations are laying in the low mechanical resistance at extreme temperatures and the high permeability and chemical instability (especially for natural rubber).

Table 3.1 Gasket materials

Feature	Rubber gasket	Plastic gasket	Metal gasket
Compressibility	-	++	+
Elasticity	++	-	-
Plasticity (re-using capabilities)	++	+	-
Hardness	-	+	++
Outgassing	-	+	++
Permeability	-	+	++
High temperature behavior	+	-	++
Low temperature behavior	-	+	++
Chemical stability	+	++	++

Vacuum system with operative pressure range of 10^{-5} to 10^{-7} mbar are almost entirely sealed with elastomer gaskets, of which Viton is the most commonly used material. Viton ® (A and B) has a lower permeability than any other rubber. Viton, can be used to about 150°C (Peacock, 1980). Unfortunately, the atmospheric water vapor permeates seals at high rates as well as oxygen (Yoshimura ,1989). In fact, the high rate of gas permeation is the main reason not to use such seals in vacuum conditions lower than 10^{-7} mbar.

If UHV condition are required (pressures lower than 10^{-9} mbar), it is necessary to bake the components of the system to accelerate desorption of gas and vapour (see section 2.8.1). The minimum baking temperature required is 200°C. This temperature is sufficient to promote thermal degradation of elastomers resulting in rapid gas evolution. The polyimide polymers can withstand baking at this temperature without degradation. On the other hand, they have high rates of water desorption, greater than Viton (Edwards *et al*., 1977; Edwards *et a*l., 1979).

Fluocarbons as material for gaskets is known as Teflon, but the other trade names as PTFE, Fluon, Kel-F, Hodtaflon are also used in vacuum technique. Teflon gaskets need higher sealing pressure then the rubber ones. The temperature range in which the fluocarbon gaskets may be used is quite wide. The maximum temperature for vacuum systems containing Teflon is specified to 425°C. At this temperature material changes from being relatively dense to porous and its volume grows by a large factor (Roth, 1994). The Teflon is chemically stable, never hardens, never adheres and is completely inert but Its use it limited in particle accelerator due to the low radiation resistance.

The last group of gasket materials are metals. They show the lowest outgassing rates and the best thermal and particle radiation resistance. In fact, most of them are extensively used in bakable UHV seals. This group contains mainly gold, aluminum, copper, as well as indium, lead and rarely nickel, silver, iron and others. They can be employed in different applications according to the peculiar physical and thermal - mechanical constraint of each seal. For example, if the joint is subjected to elevated temperatures in bake out processes, it is important to design for enough elastic springback to maintain adequate sealing force inspite of the stress relief and plastic deformation induced by high temperature creep phenomena. Gold has a low yield point and shows no oxidation while heating. It also has similar coefficient of thermal expansion as stainless steel and this can be an advantage in demountable seals. On the other side, gold gaskets need high compressive forces (deformation hardening in gold is significant) and they are quite expensive especially for large geometries (Holden *et al.*, 1959). Gold gasket are not widely exploited due to the high price and their use is limited in niche applications.

Indium as a gasket material is used generally in wire form for room temperature applications. It shows high ductility at these temperatures and no high sealing pressure is required. The gasket is usually just an indium wire with overlapped end, instead of proper O-ring shape, which is sealed in the joint by indium cold welding during compression between flanges. Traditional O-ring seals exist but they are not very common. Indium is also used to flanges and gaskets plating (Schuchman, 1965). Indium does not degrade at temperatures lower than 150°C and can be used for ultimate pressure not lower than 10^{-9} mbar. It melts at 155°C and is therefore not suitable for UHV bakeable systems.

On the contrary, copper-based gasket are extensively employed in UHV systems. The advantage of this material is the possibility to use it up to temperature 800°C even if at 300-400°C creep induced stress relaxations already occur. A disadvantage of copper gasket is tendency to oxidize when heated in air. The copper oxide evaporates and condenses on the faces of the flanges (near the seal) which periodically have to be cleaned. During bakeout of UHV systems, hard oxide layers will form on the surface of the copper gaskets that are exposed to air, unless the gaskets are provided with some protection. At CERN, several surface layer protections (silver, gold, indium, nickel coatings) have been tried on the copper gaskets (Wikberg, 1968). Only silver and gold plated gaskets gave good UHV performance. The oxidation of the copper has been overcome by silver plating the gaskets at minimum 5 μm, even if it is not a solution commonly employed perhaps due to the higher cost with respect to pure copper gaskets.

Aluminum is one of the most common materials for gaskets. It is one of the cheapest materials for seals and is mostly used in the shape of wires or thin foils. It can be used up to about 300°C showing limited creep relaxation phenomena. Some disadvantages are with high sealing force required and the diffusion of the aluminum into the flange through cracks in the oxide surface layer.

The other metals like lead, silver or stainless steel are rarely used for gaskets.

3.4 Joining technologies

Vacuum systems very often consist in evacuable and hermetically sealed components (vessels, pipelines, measuring devices, etc.). In addition to the selection of suitable materials and their surface and thermal treatments, the joining technologies applied are crucial for the quality of the generated vacuum.

The connections between vacuum components can be classified as static and dynamic according to their function, which can be fixed or moveable in different degrees of freedom. According to manufacturing aspects, a distinction is made between detachable and permanent connections. Restrictions for the possible joining processes arise from peculiar design constraints (Jousten, 2016).

3.4.1 Permanent connections

A permanent connection is a connection made by joining that can only be removed under acceptance of a damage or destruction of the joined parts. In vacuum technology, the permanent connections are realized mainly through welding, brazing, or bonding.

Welding

In vacuum technology, common welding techniques are tungsten inert gas welding, microplasma welding, electron beam welding, laser beam welding, friction welding, explosion welding, and diffusion bonding. The tightness of the connection is reached through the absence of pores, bonding defects, and other irregularities. It is worth pointing out that oxidations and microstructural modifications in heat affected zones can directly or indirectly negatively influence the outgassing behavior of the connection. The use of welding fillers in vacuum technology is critically examined because of the extremely high cleanliness requirements that are necessary for weld seams.

Brazing

By means of the brazing the materials are connected with the aid of the liquefaction of an additional component that is called solder. The melting temperature of the base material is not reached during the process. The permanent connection originates from wetting the solid base material with the liquid solder and from diffusion of the molten solder into the base material. Solder components form no intermetallic phases with base materials. Thanks to this features, materials with different melting ranges can be connected with each other (e.g., steel with copper, ceramics/glass with stainless steel). Brazing is preferentially used in case of formed components with low wall thicknesses or narrow tolerances or hardly accessible joints. In vacuum technology, brazing is widely used to realize metal to ceramic connections, steel copper connections, or for components made of nonferrous metals (e.g., titanium and aluminum).

Adhesive bonding

Adhesive bonding is a nonthermal material-bonded joining process in which an additional component (adhesive) wets the surfaces of the base material. In particular, adhesive bonding finds application when the material to be joined are not easily weldable (e.g., titanium, tantalum with stainless steel), or brazable (aluminum or plastics) and if a low-distortion and low strength joining is requested. Bondings are always subject to aging and their durability is determined by mechanical (static and dynamic forces), chemical (humidity, solvents), and physical (heat, UV, and particle radiation) influences. Owing to the abovementioned limitations adhesive bonding is not widely employed in vacuum systems of particle accelerators.

The joining technologies such as brazing, welding, and bonding have application preferences depending on the materials of the joining partners that should be considered in their selection (see Table 3.2).

Table 3.2 Joining technologies for different material pairings (K. Jousten, 2016).

Material pairing	Brazing	Welding	Bonding
Ferrous metals/Fe metals	0	+	0
Non-Ferrous metals/Non-Ferrous metals	+	0	0
Non-Ferrous metals/ Ferrous metals	+	0	+
Metal/Glass	+	-	+
Metal/Ceramic	+	-	+
Glass/Ceramic	-	-	+
Plastic/Metal	-	-	+

(+) frequently applied; (0) possible/uncommon; (-) unsuitable/impossible or possible with high technological effort

3.4.2 Detachable connections

For reason related to flexibility and maintenance most of the individual components of a vacuum facility are detachably connected with each other. These connections need to comply with different process-related requirements:

- Operative pressure range
- Sealing capabilities (leak tightness)
- Outgassing behavior
- Temperature resistance
- Chemical resistance
- Radiation resistance
- Magnetizability
- Particle radiation resistance
- Availability and cost

In table 3.3 some dismountable connections commonly used in vacuum systems of particle accelerators (Jousten, 2016; Garton , 2011) are reported. All demountable connection systems in vacuum technology need a sealing medium to ensure the necessary leak tightness. Connections can be classified as elastomer sealed and metal sealed:

Table 3.3: Some common types of vacuum flanges and seals used in the accelerator area

Area of application	**Connecting system**	**Seal Partner**	**Seal**	**Temperature Range**	**Typical helium leak rate (mbar l s^{-1})**
High Vacuum	ISO/KF flanges	Flat sealing surface	Elastomer/Aluminum ring	-200°C /+150°C	<10^{-8}
Ultra High Vacuum	Helicoflex®	Flat sealing surface	Covered metal spiral ring	-270°C/+700°C	<10^{-10}
	VATSEAL	Flat sealing surface	Copper ring	-200°C / +300°C	<10^{-11}
	Conflat® CF	Knife edge	Copper ring	-200°C/ +450°C	<10^{-11}
	Quick Conflat® QCF flanges	Knife edge	Copper ring	-200°C/ +350°C	<10^{-11}

Elastomer sealed connections

Elastomer sealed connections are based on compressed seal materials and are applicable from overpressures down to vacuum ranges.

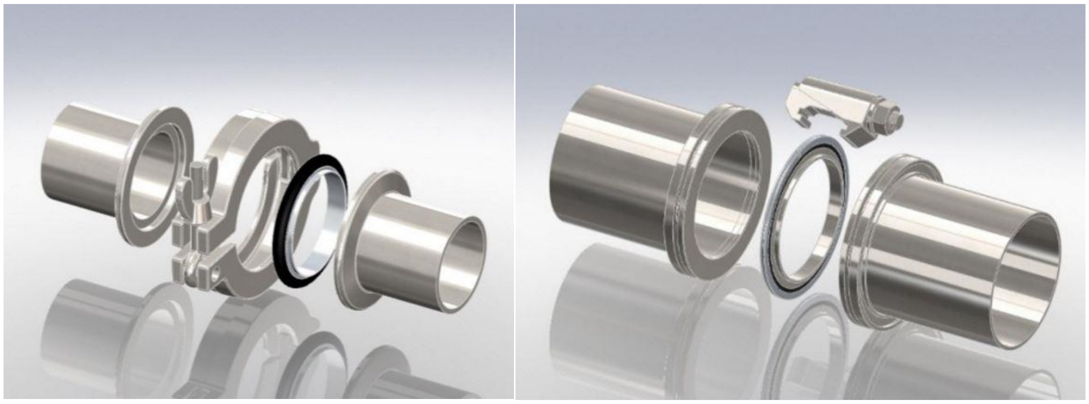

Figure 3.1. Klein Flange – KF (left) and ISO-K flange (right) (www.hositrad.com)

In KF and ISO flanges (see Fig.3.1), which are widely employed in vacuum systems, the elastomer O-ring seal is usually held by an internal centering ring and it is compressed of about 25% by the axial force which is generated by the two sealing plates serrated by the bolts. The hermetic sealing is guaranteed by the elastic recovery forces occurring at the seal/plate interface. By evacuating the inner volume, the originating pressure difference generate an additional clamping force increasing the sealing effect. The material composition as well as its geometry determine the lower pressure limiting the reachable vacuum level. With suitable selection and design, it is possible to use elastomer seals for an ultimate pressure of 10^{-10} mbar. Their use is anyway limited in UHV systems due to the high outgassing rates and low radiation and temperature resistance. KF joint consists of two identical and infinitely rotatable flanges, a centering ring with seal, and a clamp. The centering ring centers and spaces the flanges, retains the 0-ring seal, and limits the 0-ring compression. The clamp holds the joint together and provides the sealing force. Some clamps are closed with a wingnut, others with a toggle lever. Lever-closed clamps are convenient when the joints are frequently disassembled. There are two types of flange assemblies, claw clamp (ISO-K) and bolt flange (ISO-F). Both use an O-ring hold in place by a centering ring. The bolt type flanges are assembled by using a set of bolts to fix the position of the flanges. The claw clamp flanges use double claw clamps to hold two flanges together. The use of the claw clamps means that mating flanges can be connected together in any orientation.

Metal sealed connections

In most of UHV applications metallic gasket are used as sealing elements. They are preferred due to the low outgassing rate and the high physical stability in case of particle radiations and thermal loads. Plastic flow induced in the seal during the mounting phase close any possible leak path at the flange/gasket interface. The history of metal seals is closely related to that of UHV. The first UHV compatible metal-sealed valves were designed by Alpert (Hoffman *et al*., 1998) at the Westinghouse

Research Laboratories. Shear seal flanges using flat copper gaskets were first described by Lange and Alpert (Hoffman *et al*., 1998), and were made commercially until about 1962. The shear seal principle, as illustrated in Figure 3.2, performed well, but the flanges were inconvenient because they were sexed and a high axial force (high bolt tensioning) was required to obtain an effective sealing.

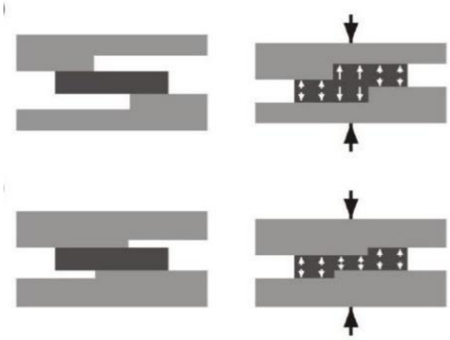

Figure. 3.2 Shear seals principles (flanges in light grey, gasket in dark grey)

A bakeable joint which has been designed to provide sufficient elastic deflection as well a high seal force is the Batzer flange (Milleron and Wolgas, 1980), schematically shown in Fig. 3.3. When the joint is bolted up, the flanges deflect elastically to a slightly conical shape. The potential creep deformation of the gasket is much less than the elastic flange deflection so most of the initial sealing force remains after bakeout. However, with long accumulated high temperatures holding times the internal stresses in the gasket can completely relax with a significant decrease of the contact pressures. The joint can remain leak tight as long as differential thermal expansion is limited.

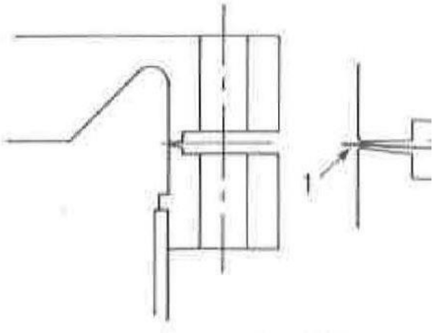

Figure 3.3 Schematic depiction of a Balzer flange (the element “1” in the zoomed area is the 0.08 mm aluminum gasket) (Milleron and Wolgas, 1980)

The conical flat (CF) type joint has been presented by Varian in 1962. The solution consists of flat copper gasket compressed by two flanges with knife edges (Fig.3.4). The original geometry of the sealing surface was conical, normal to the gasket surface on one side and ridge inclined at an angle of 70° on the second side of the knife edge. Nowadays, there are several variants of CF geometry. They are different from the point of view of both angles of the knife and the tip radius (Kurokouchi *at al.*, 2003), the gasket thickness (1.6 - 2.0mm) and the knife imprint depth (0.3 - 0.4mm). Most manufacturers have opted for a Varian marketed under the trade name of ConFlat® and this has become the accepted standard.

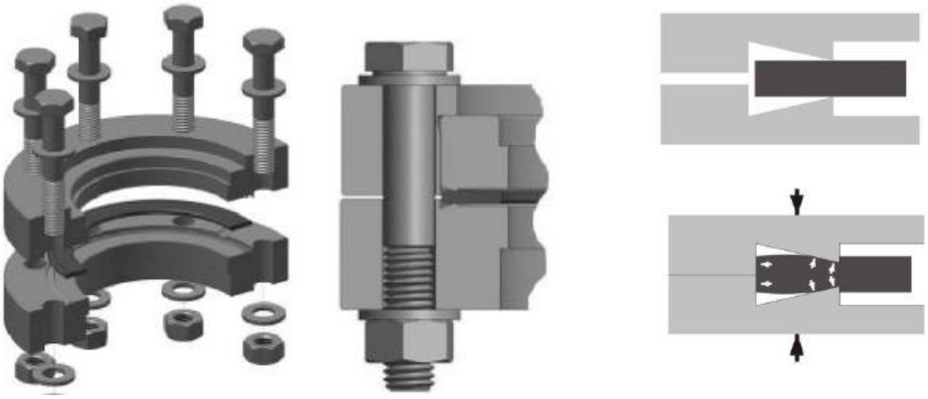

Figure 3.4 Schematic drawings of the CF flange system (left) and cross section of the knife edge (right) (www.vacom.de).

The CF seals seem to be one of the most reliable and common solution for UHV systems and it is widely used in vacuum systems of particle accelerators. Due to the metal gasket, it can withstand high temperatures (needed for bakeout treatment) and ionizing radiation background. A typical CF joint compresses a 1.6-2mm thick pure copper gasket between 20° angled sealing edges machined on the faces of opposing flanges.

The seal edges sink into the gasket to a normal depth of 0.36-0.40 mm per edge, produce interface pressure several times exceeding the gasket yield strength. CF flanges range from 10 to 300 mm diameter. The cost of larger gaskets has discouraged applications for larger sizes.

Advantages described by Wheeler (1977) include good resealing if the flanges are not closed, bakeout ability to 450°C, and very good tolerance for flange and gasket damages (scratches). Other features are the identical flange seals (no male and female halves) and no special techniques required for sealing (Yoshimura, 1989). Disadvantages are the high sealing force and the time consuming installation and removal due to the high number of bolts to be screwed (see section 3.6).

If a coupling consisting of a flange pair and seal it is able to remain leak tight when subjected to the differential motions caused by the unavoidable temperature gradients induced by the heating, inevitably some of its elements store energy elastically. In the case of elastomer sealed connections, the elastomer itself has this function. In CF flanges the elastic deformation of the flange pair helps to maintain the seal (Wikberg, 1990; Kitamura, 1994). The problem of seal integrity is more difficult as CF flanges grow larger. Sixteen-inch CF flanges may not remain leak free after baking. (Hoffman *et al*., 1998). Taking into account these issues, the Helicoflex® seal, developed by CEFILAC (France), has been designed to provide a very high elastic reset. It is a metallic 0-ring consisting of a helical garter spring made endless by welding, a layer of hard metal to distribute the force from the discrete turns of the spring, and an outer layer of a softer seal metal such as aluminum, copper, or silver (see Fig. 3.5). This solution provides a better distribution of the reset sealing forces in a wide thermal range.

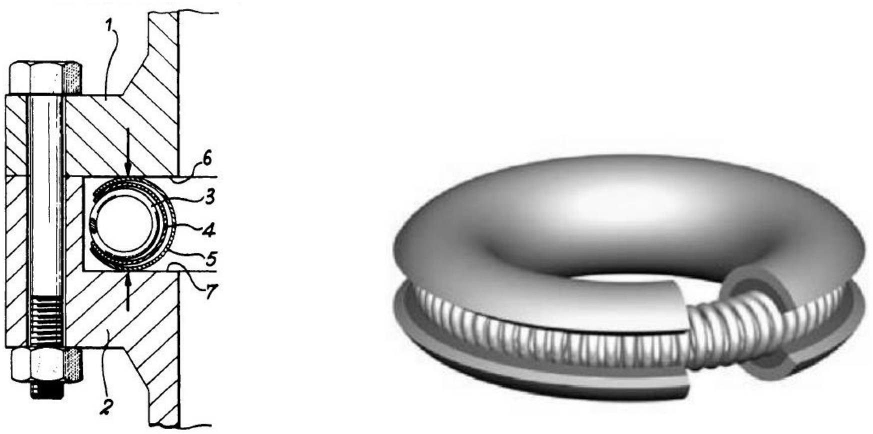

Figure 3.5: The Helicoflex seal (Hoffman *et al.*, 1998)

Many other metal seals are available commercially. Aluminum seals of diamond cross section for installation between flat-faced flanges as shown in Fig.3.6 are available commercially. Unterlerchner (1990) reported the results of a study at CERN on this type of seals proving their reliability. When CF flange knife-edges are damaged by careless handling, they may not seal with the standard gaskets; Fend (1996) proposed a solution describing a seal for use with CF flanges as sketched in Figure 3.6. These corner-crush gaskets are available in aluminum, copper, and nickel, and require only about 50% of the sealing force of a standard CF gasket of the same material

Figure 3.6: Seal detail of a diamond cross section aluminum seal between flat flanges (left) and of standard CF flanges using corner-crush gasket(right)

The Swagelok® tube fitting is used mostly in power generation industry to create UHV joint (Fig.3.7). It is placed over the pipe and tightened, forcing a pair of internal ferrules to interface with the pipe surface creating a strong grip and seal. Pipe ends with Swagelok® fitting attached can be bolted together to form a vacuum tolerant joint. Swagelok fittings are single use and new pipe length must be used for each new joint.

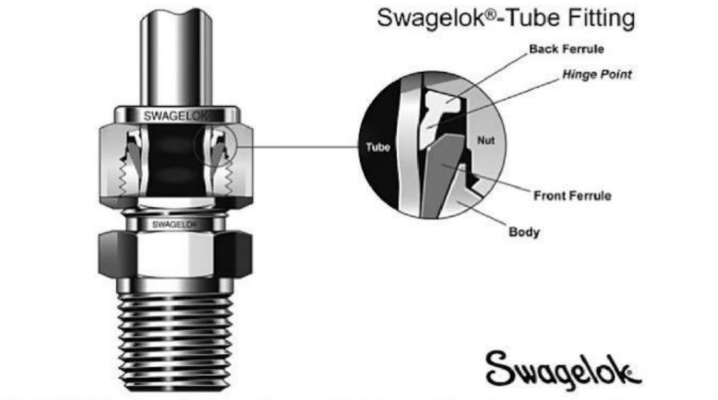

Figure 3.7: Sealing principle of a Swagelok ® tube fitting (www. Swagelok.com)

The quick disconnect vacuum flanges represent an upgrade of the classical CF systems (see Fig.3.8). The quick connect system proposed by Vacom® is widely used at CERN and combines the assembly principle of the KF connections with the sealing principle of the CF flanges. The sealing force is applied though a clamp chain on the conically shaped flanges. This clamp can either have a latch mechanism or have one or two bolts which replace the latch mechanism.

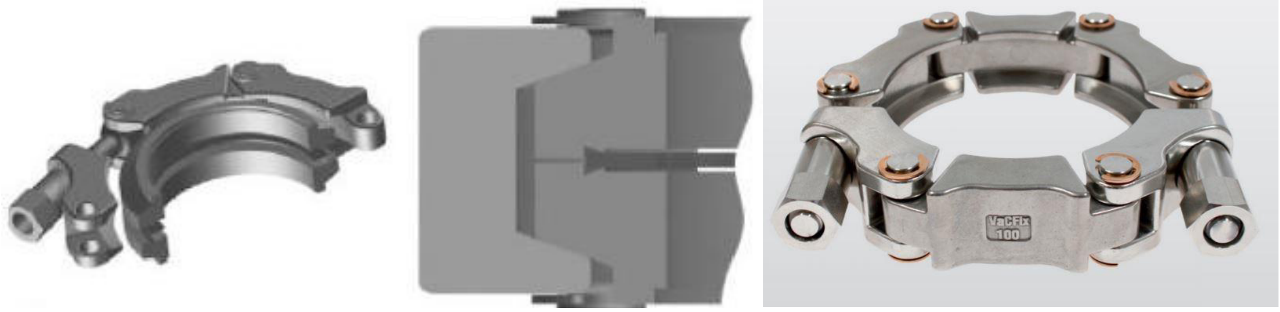

Figure 3.8 Schematic drawings of the QCF® flange system proposed by Vacom® (left) and photography of a VacFix ® chain clamp (right).

The use of the chain clamp (normally made of stainless steel) ensure the same tightness and operational safety than the conventional CF enabling a substantially easier and quicker assembly of the flanged joint due to the limited number of screws (one or two). The cons are manly related to the space occupancy and the weight (see section 3.6). In addition to flat gasket rings, concave rings with an open (C-ring) or round cross section as well as diamond-shaped (rhombic) cross sections are used as sealing elements (see Fig.3.8).

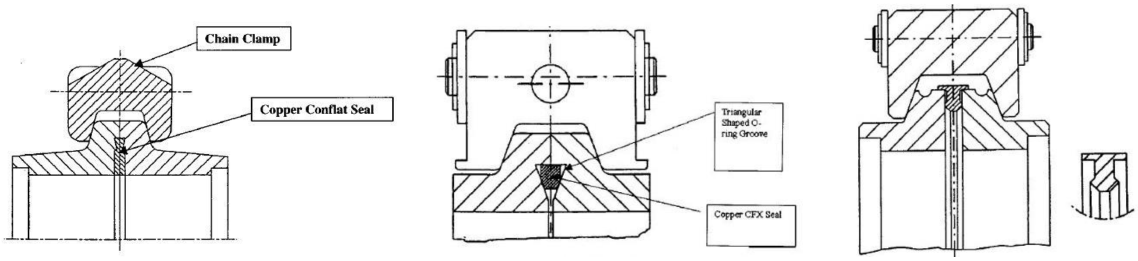

Figure 3.9 Schematic drawings of 3 quick disconnect flanges (Mapes, 2001).: EVAC CF flange assembly (left), EVAC CFX flange assembly (center) and EVAC ISO flange assembly (right).

Quick connect flanges can use either a seal retainer ring or an O-ring groove to capture the seal. In Fig.3.9 are illustrates some other quick disconnect flanges widely used in UHV system at Brookhaven National Laboratory (Mapes, 2001). These EVAC flanges use a two-bolt chain clamp to apply the force to the flanges necessary to compress the seals and form a leak tight vacuum joint. The three types of EVAC flanges depicted in Fig.3.8 are CF, CFX, and ISO. All three types are fabricated from stainless steel and have a 20° taper. The CF and CFX EVAC flanges use chain clamps made of stainless steel. The ISO flange uses an aluminum chain clamp which limits its use to temperatures up to 150°C. The CF and CFX flanges use copper seals while the ISO flange uses an aluminum diamond seal. The ISO chain clamp is the lightest of all the chains. CFX type flanges do not have a knife edge. To make a seal, the gasket used with these flanges is deformed into a triangular shape O-ring groove.
A very extensive and useful compendium of vacuum seals and connections has been made by Roth (1994). " New" seal designs are proposed in the literature but it is quite hard to acquire reliability data. There are a considerable number of commercial metal seal design but generally they do not provide both the high sealing force and the amount of elastic springback required for reliable bakeable vacuum seals to be used in UHV systems of particle accelerators. In fact, at CERN mainly CF and Quick connect systems are used for beam pipe couplings (Fig.3.4 and 3.8).

3.5 The sealing mechanism

The sealing mechanism of metal gasket seals has been extensively investigated in literature (Roth, 1972; Roth, 1983; Buchter, 1979). Although the mechanism is reasonably understood there is not a real scientific foundation for seal design analysis and most of the numerous designs of UHV metal seals that have been reported are based on empirical or phenomenological evaluations.

Only the flanges joined together, even with very good finished surfaces, are not sufficient to make proper connection in sense of the leak tightness (Roth, 1972; Roth, 1983; Buchter, 1979). Even the smallest air channel due to the rugosity and waviness of the material are not allowed in Ultra High Vacuum (UHV) systems because they constitute considerable leaks.

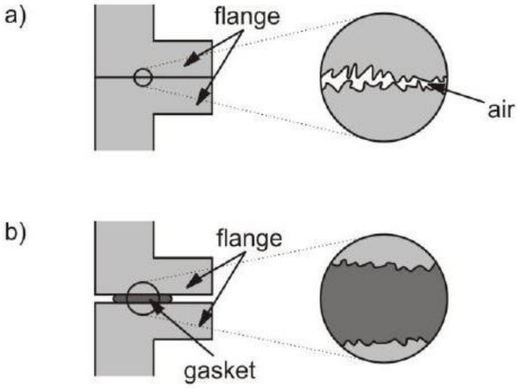

Figure.3.10: Seal cross-section: (a) without gasket- not leak tight; (b) with inserted gasket- leak tight

A soft gasket between the sealing parts is needed, which fills up irregularities and micro channels even for rough surfaces (see Fig.3.10), up to at least 6μm (Moore, 1965).

Gasket seals requires a perfect alignment with respect to flange surfaces and usually high compressive forces in order to be effective. The ideal gasket behavior should be elastic-plastic. Plastic behaviour is desired at a micro scale, in correspondence of the contact area with the flange surfaces in order to easily fill the flange gap and irregularities. On the contrary, elastic properties are needed at a macroscopic level in order to obtain a proper contact pressure over the whole clamping process and thermal stages (bakeout).

Unfortunately, it is quite hard to find materials with perfectly plastic behaviour in correspondence of the contact surface maintaining elastic characteristics within the bulk. The most commonly used rubber and elastomers show a hyper elastic behavior but their use is limited in UHV due to the low thermal and radiation resistance and the high outgassing. Soft metals (for example copper, gold, silver, aluminium) have good plastic properties and can be used in the bakeable UHV systems. Normally the yielding stress of the gasket metal is significantly lower than that of the flange. The deformation hardening of the gasket material induces higher contact pressures and consequently higher sealing forces. In order to reduce the required force acting on the flanges (often by means of a number of bolts) the contact area in some designs is reduced as much as possible (for example in knife-edge seals, ridge seals). Because of the severe plastic deformations induced and the related hardening effect and residual stresses, hardened gaskets cannot be re-used for subsequent sealing processes.

3.5.1 The surface roughness influence in leaking

There are two possible leaking mechanisms. The first is connected with the porosity, where leaking appears due to gas flow through the gasket material (permeation). This type of leaking is crucial for elastomer seals and it is significant in the range of 10^{-9}Torr (see section 2.8). The second possibility is connected with the surface roughness of sealing parts and takes place in the space between the surfaces of the gasket and the flange (see section 2.8). This leaking process is sensitive to the sealing pressure acting between contact surfaces of gasket and flanges. If the pressure is not high enough to force the gasket material into the irregularities of the surface (and fill them), the leak produced may be significant.

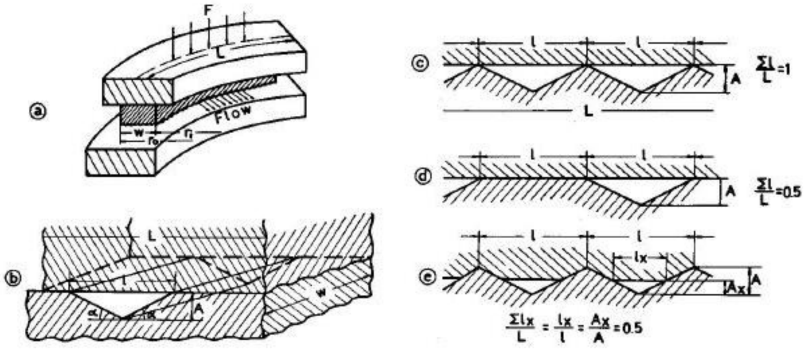

Figure.3.11: Dimension of the seal: (a) The interface contact annulus; (b)a typical leak path ; (c) the surface contact (machined surface); (d) single paths on the surface; (e) loaded interface contact (Roth, 1972)

The leak paths are determined by the profiles of the surfaces in contact. These surfaces are characterized by randomly distributed peaks and valleys and the leak path cross-section can be modeled as triangular. In fact, Roth (1972) noticed that on the machined surfaces more than 90% of the peaks has slopes of 1°-4° with α~4° (see. Fig 3.10). With reference to Fig.3.11, the generic length of the leak path is equal to the width *w*.

3.5.2 Conductance of the Leak Path

The conductance (in case of molecular flow, see chapter 2) for simplified triangular cross-section leaking path was presented by Roth (1972) in the following form:

$$C = 19.3\frac{\left(\frac{T}{M}\right)^{\frac{1}{2}}A^3}{2\left(1+\frac{1}{cos\alpha}\right)tg\alpha}\frac{K}{w}\ 10^4 \tag{3.1}$$

where C denotes the molecular flow [l/s], T is the temperature [K] of the gas, M is the molecular weight of the gas [u], A is the height [m] of the triangular leak path cross-section (roughness), α is the slope (mainly α=4°), w is the length [m] of the leak path, usually considered equal to the gasket width (Roth A., 1972), and K is a correction factor depending on the value of the ratio A/l. Because most of the leak tests are made by using helium leak detectors at room temperature (T=25°C) eq.3.1 can be transformed to the simplified form:

$$C = C_{01}\frac{A^3}{w} \tag{3.2}$$

where

$$C_{01} = 19.3\frac{\left(\frac{T}{M}\right)^{\frac{1}{2}}K}{2\left(1+\frac{1}{cos\alpha}\right)tan(\alpha)}\ 10^4 \tag{3.3}$$

The number of leak path per unit length of the seal *n* is described as follows:

$$n = \frac{tan(\alpha)}{2A}\left(\frac{\sum l}{L}\right) \tag{3.4}$$

where *l* is the top line length of triangular cross-section [m] and *L* is the gasket circumference length [m] and Σ*l/L is* density of the leak paths. Using the previous equations, the total conductance per unit length for a seal can be written as:

$$C/L = C_{01}\frac{A^2}{2w}\ tg\alpha\left(\frac{\sum l}{L}\right)10^2 \tag{3.5}$$

$$C/L = C_{02}\frac{A^2}{w}\ \frac{\sum l}{L} \tag{3.6}$$

When helium is considered as a flow medium (standard leak test), and the temperature is set to 25°C, C_{02} is equal to 34. If the flow medium is air, C_{02} decreases to 18.7. The C_{02} coefficient depends on the working condition (temperature *T*), the flow medium properties (*M*) and geometry parameters (Σ*l/L, K, α)* as shown below.

$$C_{02} = 19.3\frac{\left(\frac{T}{M}\right)^{\frac{1}{2}}K}{4\left(1+\frac{1}{cos\alpha}\right)tg\alpha}\ 10^6 \tag{3.7}$$

Those equations are valid for the cases, when no load is applied to the flanges. To reduce the cross-section of leaking path the compression of the gasket is required. This way, the height *A* (roughness) is decreased to A_x (Figure 7). The Σ*l/L* = A_x/A relation leads to the following formula.

$$\frac{C}{L} = C_{02}\frac{{A_x}^2}{w}\ \frac{\sum l}{L} = \ C_{02}\left(\frac{A_x}{A}\right)^3\ \frac{A^2}{w} \tag{3.8}$$

The deformation factor A_x/A can be expressed as a function of the sealing pressure *P* and parameter *R* (Roth, 1972). This pressure acts due to the tightening force *F* and appears on the contact area. The sealing factor *R* expresses the sealing ability of the gasket material.

$$\frac{A_x}{A} = e^{-P/R} \tag{3.9}$$

$$P = F/Lw \tag{3.10}$$

$$\frac{C}{L} = C_{02}\frac{A^2}{w}\ 10^2 e^{-F/(LwR)} \tag{3.11}$$

The sealing process can be expressed as dependent on the force applied to the flanges, geometry and gasket material properties *R*. The experimentally obtained date can be expressed in the form of leak rate (*Q*) versus axial force (*F*) curves. From *Q*-*F* curves it is possible to derive the conductance-contact pressure (*C*-*P*) curves for different materials (with different *R*). The *R* factor can be expressed as *P* value needed to decrease the conductance by about e^{-3}=0.05 and it needs to be experimentally identified (Roth, 1972). The final formulation can be modified accordingly:

$$\frac{C}{L} = C_{02}\frac{A^2}{w}\ 10^2 e^{-3F/(LwR)} \tag{3.12}$$

The sealing factor to be used in equation (3.12) for different gasket materials are presented in Table 3.4.

Table 3.4. Sealing factor of different gasket materials (Roth, 1972)

Material	Hardness	Sealing factor R [MPa]
Copper	Very Hard	323.6
	Hard	88.3
	Soft	49.0
Nickel	-	117.7
Aluminum	Hard	58.8
	Soft	29.4
Stainless Steel	Hard	88.3
	Soft	58.8
Lead	Soft	6.7

3.5.3 The sealing curve and the effect of the bakeout

The tightening curve in terms of *C-P* relationship (see Fig. 3.12) may contain three different sealing stages: accommodation, normal and local sealing. The *accommodation* phase corresponds to the beginning of the process (P/R =0) and usually goes up to *P/R=5-6* value [MPa/m]. In this stage the flange surface is pushed into the softer sealing surface overcoming its waviness. The interface contact is gradually established along the real surface profile of the flange and the real contact area increases. After a further increase of the force acting on the flanges (*P/R* is rising), the *normal sealing* is reached. In this stage the leak paths existing at the interface contact are gradually throttled by interpenetration or flattened.

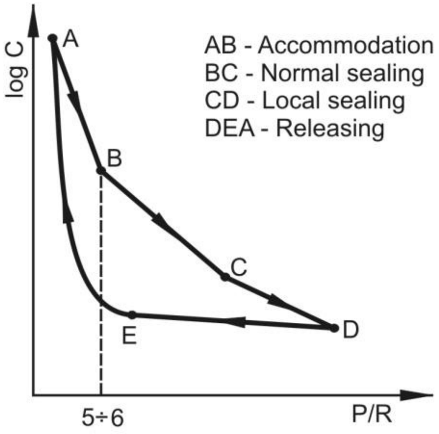

Figure.3.12: a typical sealing curve

Upon further increase of the force applied to the flanges, the effect of *local sealing* (Figure 3.12) may appear. This stage is due to the conductance of local grooves, deeper than other leak paths. Normally local groves are made by scratches, machining marks or other damage acting through the sealing surfaces. The sealing process for those groves proceeds less effectively than for normal leaking path. This is the reason why the slope for this stage (line C-D in Fig.3.12) is lower than that for *normal sealing* (line BC).

The unloading curve varies according to the mechanical behavior of the gasket. If the deformations occurred in the gasket (and flanges) during the loading phase (A-D in Fig.3.12) is entirely elastic, the releasing curve coincides exactly with the tightening curve. If the deformation during tightening is entirely plastic, then during the release the conductance remains constant, *i.e.* the releasing curve correspond to a horizontal line. For elastic-plastic deformation the releasing curve is located between those of the two overmentioned cases. It was verified that even when the releasing curve is horizontal, it extends approximately to force corresponding to the limit between the accommodation and the normal sealing stage (point B), then the conductance begins to rise (point E). This phenomenon was explained by the fact that in this region the elastic recovery deformation of the waved surface in contact begins to separate the sealing elements (Roth, 1994). In case of baking (see section 2.8.1), the heating stage modifies the stress/strain field in the assembly at high and low temperatures (operating condition at room temperature). The modification is due to a combination of an effect of material softening (mainly occurring in the gasket) and a differential expansion of the parts. In most cases the overall result is a loss of load; if this loss is too large, leaks appear. If the thermal expansion coefficients of gasket, flange, bolts, are not exactly the same, any thermal variation produces a difference in the relative dimensions of the parts. The overall effect of these dimensional differences results either as an additional tightening or a releasing of the seal. If, upon heating, the gasket expands less than the flange, the result is similar a contraction of the gasket. And leak can appear upon heating. The contact pressure at the flange-gasket interface is a function of the seal geometry, the gasket yield stress as well as its young modulus (Roth, 1983). Interface pressure decreases by decreasing both of them. As a result of the softening of the materials the value of yielding stress may decrease slowly or drop quickly within the temperature range. Figure 3.13 shows the variation of the aluminum and copper yield stress, σ_t, as a function of the temperature (σ_t is normalized to the yield stress value measured at 0°C, σ_0). The aluminum shows a sudden drop of σ_t/σ_0 at about 150 °C down to values of about 0.2 and below, while the copper shows a drop at about 250 °C but only to $\sigma_t/\sigma_0 \approx 0.6$.

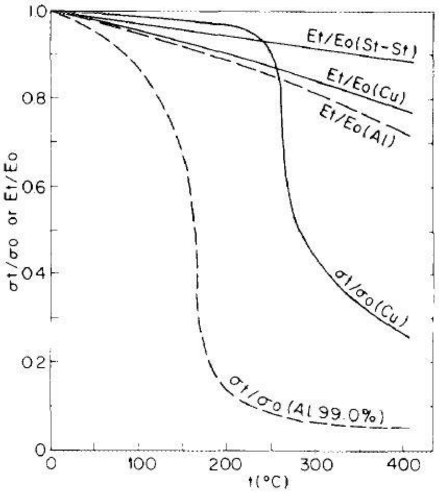

Figure.3.13: Yield stress and Young's modulus variation with temperature for copper and Stainless steel (Espe, 1966)

This strong variation of the mechanical performance of the gasket materials represent one the main reason why the copper gaskets are preferred to the aluminum ones for high temperature backing applications. The effect of softening and relative expansion of the sealing parts have to be carefully taken into account in the design of bakeable vacuum systems.

3.6 Beam pipe couplings: reliability aspects and limitations

The vacuum systems employed at CERN are confronted with tight design constraints. The wide operative thermal range as well as the high radiation loads represent the most stringent ones. The UHV joints need to be extremely reliable, from bake-out temperatures, about 300°C, down to about -270°C reached in some of the accelerator sections.
Among the detachable seals, CF joints and their upgrade, the quick disconnect flanges (see Fig.3.14), are the most used for beam-pipe couplings in room temperature sections of CERN accelerators because they can withstand significant radiation and thermal loads (up to temperatures above 350°C), they do not have male and female halves and can ensure reasonably easy gasket handling. Other advantages are represented by the high resistance of the flange seals against surface damages and scratches (Varian, 1967). The main drawbacks are the high sealing forces required and the price, which can be significantly high especially for large couplers. However, it is worth pointing out, that although they have been using at CERN for more than 40 years their use has not been totally free of problems or complications.

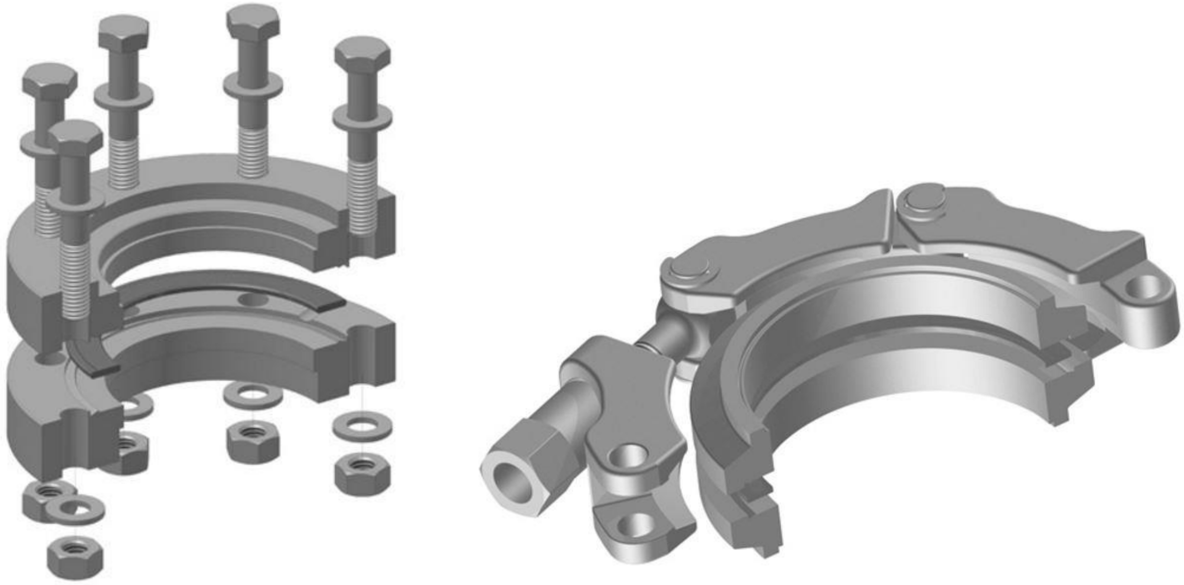

Figure.3.14: An example of (a) Conflat ® (CF) and (b) Quick disconnect Conflat® (QCF) connection systems (www.vacom.de)

About reliability aspects of CF joints, it is worth noting that Unterlechner (1977, 1987) presented extensive reports on the CF failures in UHV systems. Different mechanisms were identified as responsible of leaking joints: the first was related with the temperature dependence of the copper yielding stress which drops from about 200 MPa to 50 MPa in the annealed state during bake out (300°C) inducing a relaxation of the knife/seal contact pressure (see section 3.3). To overtake this issue the OFS copper with higher recrystallization threshold was proposed. OFS copper has a low silver content (0.1% Ag) and can withstand heating stages up to 350°C for several hundreds of hours.

In addition, the oxidation of the copper gasket surface was mentioned by Wikberg (1968) as a leak source; the most fitting solution for this problem was a 5μm Ag-coating; numerous coated gaskets have shown excellent performance and no leaks were recorded even after 800h at 350°C (200 cycles each of 4h).

Another reason of the unsuccessful sealing capabilities of CF joints is represented by the temperature mismatch between the flanges and gaskets occurring during bake-out heating. Metal sealed flanges stay leak tight as long as the deformed gasket is able to follow their relative displacements. Inhomogeneous temperature distributions during bakeouts, however, can cause considerable temperature differences and consequently significant diameter variations in a pair of flanges. Leaks appear as soon as the difference in terms of displacements of steel/copper mating sealing surfaces is too high and the contact pressure drops. The stainless steel has a very high coefficient of thermal expansion which is almost identical to that of copper, but it has a thermal conductivity which is 26 times lower than copper one. During the heating, obtained by means of bakeout jackets (metallic resistive collars heated by Joule effect), up to 30°C average temperature difference can occur in a pair of flanges with dissimilar mass distribution (Unterlerchner, 1977); even higher differences, of up to 60°C, were measured between an open flange (215 mm outer diameter) and a blank flange (Unterlerchner, 1987). The replacement of the massive central part of a blank flange by a welded-in thin walled domed end effectively solved this problem. However, seal integrity-related issues are particularly serious for large CF flanges; 16-inches (nominal outer diameter) CF flanges may not remain leak free after baking. (Hoffman *et al*., 1998).

The CF flange connection is guaranteed by a certain number of bolts that varies according to the assembly dimension. The bolts are subjected to high tensile stresses during the installation due to the mechanical deformation of the gasket as well as during the operative condition of the joint; bolts ensure a proper mechanical stability of the gasket/flange assembly in a wide thermal range. The bolt tensile load may change during the bakeout as a consequence of the aforementioned temperature differences within the assembly. Plastic deformations are unavoidable if the bolts are already pre-stressed up to their yield point (Unterlerchner, 1977). In fact, both tensile and shear stresses act in bolts transversal section. Tensile loads occur due to the flange axial clamping while shear stresses depend on the tolerances and friction at the bolt-nut interface. This stress field can reach considerable values especially on reused material and the loss of axial bolt force that can be reached, at a given tightening torque, is more than 50%. For this reason, high strength bolts with yield point of about 900 MPa are necessary. Material with lower yield stresses may impair considerably the reliability of the joint. Furthermore, it is essential that the flange faces are parallel during the tightening. The alignment of the copper gasket is fundamental as well. Most CF flanges have two small grooves, about a millimeter wide, machined into the bolt face; these are for locating special clips that hold the gasket in place while the flanges are brought in the operative position. Just prior to tightening the clips are removed. A torque wrench is used to facilitate uniform tightening. Moreover, it is highly recommended that a molybdenum grease or graphite loaded grease is used on the threads. When CF flange bolts have been used more than once the threads in the flange and the screws may have stretched. In this case, it is recommended that the same screws are reused in the stretched threads (with a little molybdenum grease) as they have a similar profile. Sometimes the use of new screws in stretched threads causes binding and difficult bolt mounting (Garton, 2011).

All the above considerations clarify that the use of CF flanges it is not free of complications and that their proper installation is crucial in terms of reliability of the joints.

In accelerator environments, especially proton machines, high background radiations impose the use of fast and reliable joining devices such as the quick disconnect vacuum flanges (see Fig.3.14b). The use of bolt-free flanges significantly reduces the radiation dose absorbed by the operators when installing or removing vacuum chambers in restricted-access accelerator areas. A number of different solutions for quick chain-type coupling have been using at CERN as well as in other laboratories. The time for disassembling and reassembling a chain-based flange is about 10 times lower than a bolted one (CF) of the same dimensions. The dismounting and mounting time (in case of trained operators) of a 32 bolts -12 inch outer diameter CF flange can reach 45 minutes; in case of a quick flange, it is just about 5 min (Mapes, 2001). The advantages in terms of radiation exposure time is considerable. The main drawbacks of the chained flanges are related to the weight which can be considerable as well as the large dimensions that can cause problems or limitations in terms of space occupancy and positioning. A stainless steel chain suitable for a 100 mm (nominal diameter) flange has an outer diameter of about 180 mm and a weight of more than 2.5 Kg. Furthermore, the lubrication of the chain clamp (as well as that of the bolts in traditional CF flanges) is essential to guarantee proper operational conditions of the joints. Similarly to the bolts in CF flanges, chain clamp segments are lubricated with molybdenum disulfide whose quantity and distribution has to be carefully controlled and limited due to the high outgassing rate of the lubricants as well as dangerous contamination problems in radiation environments (Stepina and Vesely, 1992).

It therefore is evident that, in view of the new High Luminosity (HL-LHC) accelerators (Brüning *et al.*, 2004), the use of both standard ConFlat® Flanges (CF) and quick disconnect flanges could results in critical operational issues and significant design limitations. Radiation doses will increase by a factor of 16 in some areas of CERN facilities. The mounting and dismounting of bolted CFs need to be carefully performed and are strongly time-consuming, leading to dangerous radiation doses to operators. Quick disconnect flanges, instead, are safer because they can be installed more quickly, but they are very expensive (from 1000 to 2500 € depending on the dimensions), large and unwieldly components (due to the heavy chain clamps) that can cause remarkable issues in terms of volume occupancy, positioning and handling. Furthermore, possible lubricant contaminations in radiation environments could occur in case of the use of these traditional joining devices.

Within this scenario, new, fast and compact UHV coupling systems were developed in this work (see following chapters), such as by exploiting the unique functional and mechanical properties of Shape Memory Alloys (SMAs).

4. ADVANCED MATERIALS FOR NON-CONVENTIONAL COUPLING TECHNOLOGIES: SHAPE MEMORY ALLOYS

4.1 Introduction

The use of standard ConFlat® Flanges or quick disconnect flanges for beam-pipe coupling could result in significant design and operational/maintenance limitations (see section 3.6). It is clear that innovative remote-controlled systems need to be developed to reduce the exposure time of the operators especially in view of the HL-LHC upgrade (Bruning and Rossi, 2015).

Within this scenario, new UHV coupling systems need to be designed, such as by exploiting the unique functional and mechanical properties of Shape Memory Alloys (SMAs) (Duerig *et al.*, 1990). SMAs are able to recover large deformation (up to 10%) against very high opposing forces (up to 700 N/mm2), due to Pseudoleastic Effect (PE) and Shape Memory Effect (SME) (Duerig *et al.*, 1990; Otuska and Ren, 2005). These properties are due to a reversible solid state phase transition between the body-centered cubic austenitic structure (B2) and the monoclinic martensitic one (B19’) (Otuska and Ren, 2005). The phase transition is activated either by temperature variation (TIM, Thermally-Induced Martensite) or by applied stress (SIM, Stress-Induced Martensite). SMA-based couplers can be activated remotely, i.e. mounting and dismounting operations can be performed by temperature variations between the Transformation Temperatures (TTs) of the alloy. It represents a relevant advantage for applications in radioactive areas of particle accelerators. In this chapter, SMA general features are presented as well as their applications with a particular focus on generic SMA-based fastening and connection systems commercially available as well as those of recent scientific interest.

4.2 SMA general feature

4.2.1 Brief Overview and History

In 1932 a Swedish physicist, Arne Ölander discovered a rubber-like mechanical behavior in Au-47.5Cd alloy which was later explained by Chang and Read (1951) as due to a solid phase transformation between two crystallographic structures, austenite and martensite. In fact, Chang and Read (1951) observed a unique phenomenon while performing researches on the bending behavior of Gold-Cadmium bars. Upon loading, the AuCd bar deformed in a way consistent with expectation. However, after load removal and subsequent heating, the bar returned to its original undeformed shape. At the time of this bending experiment, the unique thermo-mechanical behavior of AuCd was not completely understood. A similar behavior was observed in 1938 in a CuZn (brass) alloy at the Massachusetts Institute of Technology, but the official recognition of SMAs took place only in 1962, when Buehler (1963) and his collaborators at the laboratories of the NOL (U.S. Naval Ordnance Laboratory) accidentally discovered the shape memory capabilities of the equiatomic Nichel-Titanium (NiTi) system while they were working on a project about materials resistant to corrosion and high temperatures. Since then, the ability of a material that apparently "remember" its original, undeformed shape upon heating is called shape memory effect (SME), and metallic materials which manifest this effect are classified as shape memory alloys (SMAs). After Buehler (1963), many researchers focused their research interests on this class of alloys and, in particular, on Nitinol, acronym of nickel, titanium and NOL (Wang and Buehler, 1963).

Apart from the SME, SMAs are characterized by another unique property related to the martensitic transformation known as pseudoelasticity (PE) or superelasticity (SE). It consists in the capability to mechanically recover large imposed deformations (up to 10%) isothermally, at high temperatures. Thanks to the peculiar feature of remembering their original shape, by temperature (SME) or stress (PE) variations, in the following decades, SMAs became the subject of considerable interest, both scientific and commercial. Many SMA-based products started to be developed in different application fields like industrial engineering, aerospace, and medicine. The first commercial success for a SMA application was the Raychem Corporation’s CryoFit™ ‘‘shrink-to-fit’’ pipe coupler in 1969 for the F-14 jet fighter built by the Grumman Aerospace Corporation. It was followed subsequently by the orthodontic bridge wires by George B. Andreasen in 1971 (Kauffman and Mayo, 1997). A shift towards minimally invasive medical procedures necessitated the availability of novel medical instruments (with unconventional properties) and Nitinol was well suited for this task. By the early 1980s new orthodontic and orthopedic applications were realized (Cragg *et al*., 1983; Dotter *et al*. 1983, Duerig, 1995); however, it was only in the 1990’s that NiTi applications proliferated with the commercial breakthrough of stents that revolutionized the medical industry (Duerig *et al.*, 1999; Duerig, 1995). Availability of microtubing and precision laser cutting of tubing also aided in the promulgation of the Nitinol superelastic technology (Duerig *et al*., 1999).

In the 1990’s, the term shape memory technology (SMT) was introduced (Abrahamsson and Bjiimemo, 1994). SMA device design has changed in many ways ever since and SMAs have found commercial application in a broad range of industries including aerospace, robotics and biomedical (Van Humbeeck, 1999; Sun *et al.*, 2012). Many devices for space missions, like satellites, were realized by exploiting the peculiar properties of SMAs. For example, the Russian space program has developed devices that take advantage from the SME for the antennas opening and solar panels adopted in space station Mir (Razov and Cherniavsky, 2003). Nowadays, NASA uses SMA actuators successfully, which have replaced old traditional mechanisms (Hartl and Lagoudas, 2007; Duerig *et al.*, 1990). Since SMAs have both the intrinsic function of an actuator and a sensor thanks to the SME, they are promising candidates for micro-actuators, to be used in micromachines and other miniaturized systems.

Furthermore, SMA actuators have been successfully applied in low frequency vibration control systems (Baz *et al.*, 1990) and automotive (Strittmatter, 2011; Butera, 2008; Kumar and Lagoudas, 2008).

Systematic and intensive research work is still needed to enhance the performance of SMAs (Hirose, 2012; Duerig *et al*., 1990) especially to increase their bandwidth, fatigue life and stability (Karhu and Lindroos, 2010). Experimental approaches are necessary to enhance the attributes of SMAs, by tailoring the material compositions and thermomechanical treatments in order to achieve a proper operating temperature range and better functional stability, as well as to improve their mechanical response. In the last years, many SMAs have been introduced. Although iron-based and copper-based SMAs, such as Fe–Mn–Si, Cu–Zn–Al and Cu–Al–Ni, are low-cost and commercially available, owing to their poor thermo-mechanical performance (Huang, 2002), they are not as diffused as the NiTi-based ones. The latter show the best functional response: they manifest a significantly high recovery deformation due SME and PE (up to 10% compared to 5% of the Cu-based alloy) and they are thermally stable showing excellent corrosion resistance. Furthermore, due to their high mechanical strength, NiTi-based devices are used as structural elements and fully exploited in the biomedical field (stents, pins, ecc.) showing excellent bio-compatibility (Petrini and Migliavacca, 2011). For all of these reasons, nowadays, NiTi-based alloys are the most studied and applied SMAs.

4.2.2 Crystallographic Structure: martensitic transformation.

SMAs are characterized by two main peculiar properties: the shape memory effect (SME) and the pseudo-elasticity (PE). They represent respectively the ability of an SMA to "remember" thermally (SME) or mechanically (PE) its original shape after significant applied deformations; they are related to the possibility of such materials to manifest, in certain thermo-mechanical conditions, particular microscopic crystallographic configurations known as the martensitic (also known as "*product*") and austenitic (also known as beta or "*parent*") phase. The presence of either phase depends mainly on the temperature and/or on the applied stress. The austenite (*γ phase*) is stable at high temperature and low applied stress and is characterized by a body centered cubic cell (BCC), *B2*, while the martensite (*α′* phase), is stable at low temperature and high applied stress and has a distorted monoclinic cell (see Figure 4.1), B19′.

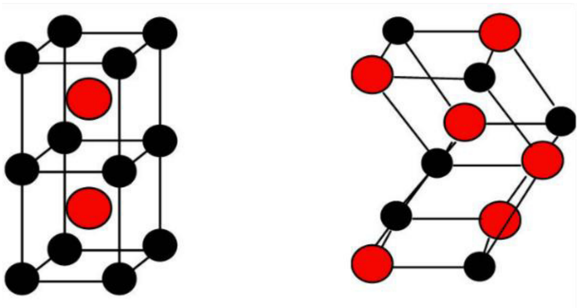
(a) (b)

Figure 4.1: (a) Austenite and (b) Martensite lattice structures

The phase transformation mechanism can be activated in two different ways:

- Thermally induced (TIM, Thermally Induced Martensite);
- Stress induced (SIM, Stress Induced Martensite);

SMAs exhibits thermoelastic martensitic transformations, which are realized if the martensite nucleates and grows continuously in tandem with the lowering of the temperature and, per contra, shrinks and disappears as the temperature is raised (Funakubo, 1987; Delaey *et al.*, 1974; Krishnan *et al.*, 1974; Warlimont *et al.*, 1974). There are no sudden appearances or disappearances of large groups of plates ("burst"); the transformation essentially proceeds in equilibrium between the 'chemical driving energy' (the difference between the free energies of austenite and martensite phases) and the 'resistive elastic energy' (due to the transformation) and often exhibits small local discontinuities or jumps during the growth of a martensite plate, termed as 'degenerate elastic transformations' by Delaey (1974).

From an energetic point of view, the martensitic transformation is a first order solid phase transformation induced by the free energy (ΔG) difference associated to the martensitic and austenitic microstructure.

Figure 4.2 shows the free energy trends, for the austenitic (γ) and martensitic (α') structure, as a function of the applied temperature. In particular, it is possible to observe that, for a specific value of temperature, T_0, the free energy difference of the system is zero. T_0 represents the thermodynamic equilibrium temperature between the two phases. For values of temperature lower than T_0 the martensite is the stable structure while for temperatures higher than T_0 the austenite is the stable structure. In figure 4.2 the characteristic transformation temperatures of the alloy are also reported, in particular M_S and M_F are, respectively, the initial and final martensitic transformation temperatures while A_S and A_F are, respectively, the initial and final austenitic transformation temperatures; details about them will be given in section 4.2.3. An applied stress can support the martensitic transformation but the operating temperature has to be lower than a specific value called martensite desist temperature M_D, which is usually higher than A_f in SMA properly processed (thermal-mechanically) to improve pseudoelasticity.

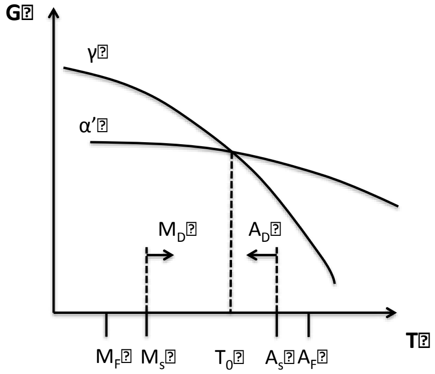

Figure 4.2: Free energy trends, as a function of the temperature, for the austenitic (γ) and martensitic (α') structure

The reason why there is a value of temperature M_D above which the martensitic transformation due to deformation does not occur is clearly justified in figure 4.3, where the transformation (τ_{sit}) and plastic (τ_{NP}) shear stresses are plotted, as a function of the temperature. The transformation shear stress (τ_{sit}) increases with the temperature because the higher the temperature the higher the energy (opposing to ΔG) needed for the process, that means a higher required shear stress to allow the martensitic transformation.

In this way, it is possible to define M_D as the temperature above which an applied stress induces plastic deformation; below M_D, transformation mechanisms can occur.

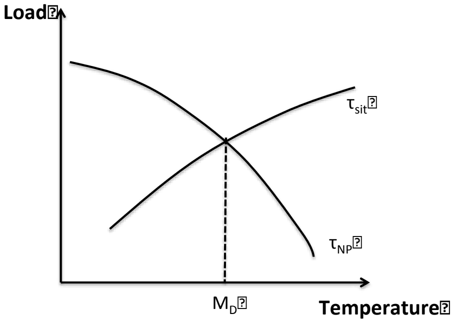

Figure 4.3: transformation (τ_{sit}) and plastic (τ_{NP}) shear stress as a function of the temperature.

From a crystallographic point of view, it is possible to define two kinds of solid state phase transformations: *diffusive* and *displasive* transformations. In diffusive transformations, the new phase is generated by means of large atomistic movements, with a consequent rupture of the crystal lattice. This phenomenon implies the generation of a new phase with a chemical composition different from the parent one. This kind of transformation depends on the time and temperature.

In displasive transformations, the atoms rearrange in a new crystal lattice, without changing the chemical composition of the parent phase. Since there is no atomic migration, the displasive transformations are time independent and, since the fraction of the new generated phase depends only on the reached values of temperature, they are also called athermal transformation (Meng *et al*., 2011).

In SMAs, transformation does not occur by diffusion of atoms, but rather by shear lattice distortion. Such a transformation is known as martensitic transformation. Each martensitic crystal formed can have a different orientation direction and is known as *variant*.

The assembly of martensitic variants can exist in two forms: twinned martensite, which is formed by a combination of "self-accommodated" martensitic variants, and detwinned or reoriented martensite in which a specific variant is dominant. The reversible phase transformation from austenite (parent phase) to martensite (product phase) and vice versa forms the basis for the unique behavior of SMAs.

Martensitic phase transformation is a consequence of two different contributes: *Bain Strain* and *Lattice Invariant Shear*.

Bain Strain is the crystal lattice deformation characterized by a series of atomic movements by which the new structure is generated. The complete transformation process is shown in Figure 4.4. Starting from the austenitic structure (a), a very small movement is required for each atomic plane (b-c) in order to reach the final configuration of the martensitic structure (d). All these small movements are called Bain Strains.

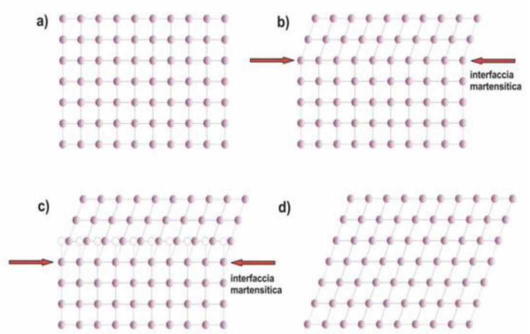

Figure 4.4: Bidimensional scheme of the phase transformation from a) austenite to d) martensite. As shown in the figure, the atomistic movement is short enough to avoid chemical bonds rupture

The last part of the transformation, the lattice invariant shear, is an accommodation of the new generated structure (martensite), whose shape and volume are usually different from the surrounding parent phase (austenite).

Typically, there are two different mechanisms by which the accommodation phenomena can occur: slip or twinning, Figure 4.5. In both cases, the material is able to keep the same microstructure with the same lattice constants, but the twinning is a reversible process, while the atomic slip modifies irreversibly the microstructure of the material, due to the rupture of the atomic bonds.

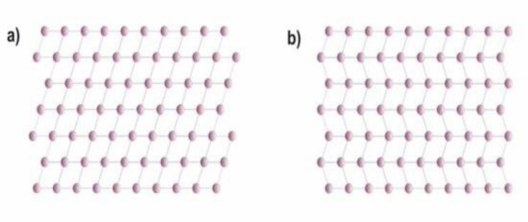

Figure 4.5: (a) atomistic slip e (b) twinnning.

In shape memory alloys, twinning is the dominant accommodation mechanism. Twinning typically occurs along a specific plane called twin boundary, Figure 4.6, that is a plane of symmetry where the resistance energy is very low and the atoms are free to move.

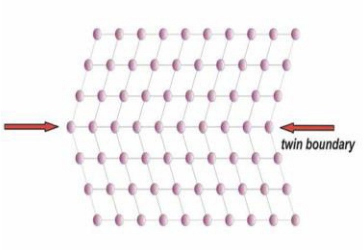

Figure 4.6: representation of a twin boundary.

Due to the peculiar properties of the twin boundary, Figure 4.7, under the effect of an applied shear stress, the microstructure is arranged according to a preferential variant, the one whose orientation is more favorable to the applied load. This phenomenon is called detwinning and the final result is a macroscopic shape variation.

The phase transition from austenite to martensite is called *forward transformation*. The transformation results in the generation of several martensitic variants, up to 24 for NiTi. The arrangement of variants occurs such that the average macroscopic shape change is negligible, resulting in twinned martensite. When the material is heated from the martensitic phase, the crystal structure transforms back to austenite, and this transition is called *reverse transformation*, during which there is no associated shape change (under the hypothesis of absence of SME induced by martensitic pre-deformation).

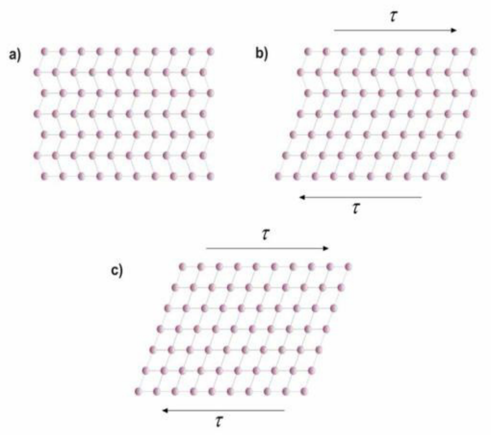

Figure 4.7: an applied stress generates a movement of the martensitic twin boundaries. The result is a macroscopic geometric shape variation.

A schematic of the crystal structures of twinned martensite and austenite for a SMA and the transformation between them is shown in Figure 4.8. During the forward transformation, austenite, under zero load, starts to transform to twinned martensite at the martensitic start temperature (M_s) and completes transformation to martensite at the martensitic finish temperature (M_f). At this stage, the transformation is complete and the material is fully in the twinned martensitic phase. Similarly, during heating, the reverse transformation initiates at the austenitic start temperature (A_s) and the transformation is completed at the austenitic finish temperature (A_f).

If a sufficiently high mechanical load is applied to the material in the twinned martensitic phase (at low temperature), it is possible to detwin the martensite by reorienting a certain number of variants (see Figure 4.9). The detwinning process results in a macroscopic shape change, where the deformed configuration is retained when the load is released (Lagoudas, 2008). A subsequent heating of the SMA to a temperature above A_f will result in a reverse phase transformation (from detwinned martensite to austenite) and will lead to complete shape recovery (see Figure 4.10). Cooling back to a temperature below M_f (forward transformation) leads to the formation of twinned martensite again with no associated shape change observed. The process described above is referred to as the One Way Shape Memory Effect (OW-SME) (see section 4.2.4). In addition to thermally induced phase transformation, transformation can also be induced by applying a sufficiently high mechanical load to the material in the austenitic phase. The applied stress, if sufficiently high, induces a fully detwinned martensitic structure. If the temperature of the material is above A_f, after the initial loading stage, a complete shape recovery is observed upon unloading to austenite. This material behavior is called the pseudoelastic effect (see section 4.2.5.

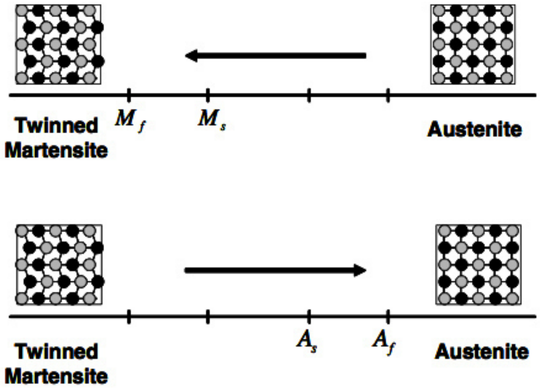

Figure 4.8: Temperature-induced phase transformation of an SMA without mechanical loading (Lagoudas, 2008).

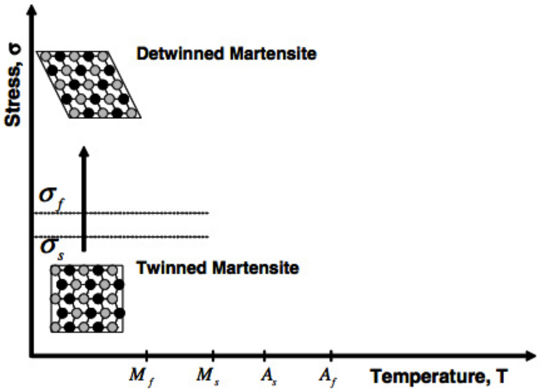

Figure 4.9: Schematic of the SMA detwinning under an applied stress (Lagoudas, 2008).

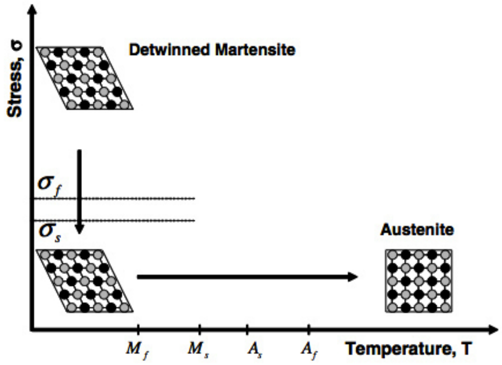

Figure 4.10: Schematic of the shape memory effect (SME) of an SMA showing the unloading of a detwinned structure and the subsequent shape recovery by heating (transforming to austenite) under no loading condition (Lagoudas, 2008).

4.2.3 Characteristic Temperatures and Phase Transformations

The phase transformation mechanisms in SMAs occur with a thermal hysteresis. In Figure 4.11 the different phases of the material and the characteristic temperatures, that determine the beginning and the end of phase transformations, can be recognized.

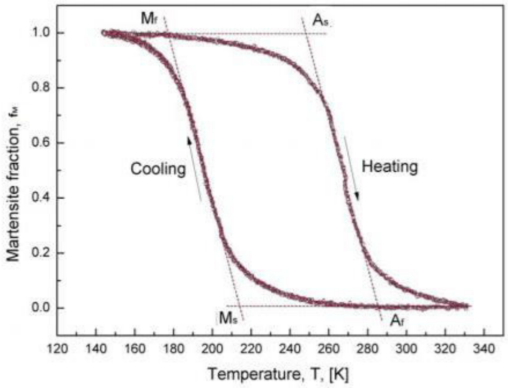

Figure 4.11: Hysteretic behavior obtained, under a constant applied stress, by heating and cooling a sample. The tangent lines allow to get the characteristic transformation temperatures.

In particular:

- **A_s**, or *Austenite Start*: during the heating phase, is the temperature at which the transformation from martensite to austenite starts.
- **A_f**, or *Austenite Finish:* during the heating phase, is the temperature at which the transformation from martensite to austenite ends.
- **M_s**, or *Martensite Start*: during the cooling phase, is the temperature at which the transformation from austenite to martensite starts.
- **M_f**, or *Martensite Finish:* during the cooling phase, is the temperature at which the transformation from austenite to martensite ends.

These temperatures are a function of the alloy composition, manufacturing processes, thermo-mechanical treatment conditions and applied stress, and their interval can be more or less wide. Looking at a SMA sample with a microscope, it is possible to observe that by decreasing the temperature, martensitic plates start to generate gradually and with continuity. The same type of process occurs during the inverse transformation. The first plate of martensite that is generated at the M_S temperature is the last one to be transformed into austenite at the A_f temperature, and, vice versa, the last plate of martensite that is generated at the M_f temperature is the first one to return austenite at the A_s temperature (Otsuka and Ren, 2005).

The thermal hysteresis, defined as the difference between A_f and M_S , depends on the alloy analyzed and its specific properties. In fact, even with very small variations in percentages of the different components, drastic effects on the transition temperatures of the alloy can be recorded. This is one of the most important engineering property of these materials, namely the possibility to tailor different phase transition temperatures according to specific requirements of each application. Transformation temperatures depends also on the applied stress. The relationship between applied stress and the transformation temperatures (TT) is described by the Clausius-Clapeyron relationship. The relation for a uniaxial stress is written as follows (Otzuka and Waiman, 1998):

$$\frac{d\sigma}{dT} = \frac{\Delta S}{\varepsilon_{tr}} = const. \tag{4.1}$$

where σ is a uniaxial stress, ε_{tr} the transformation strain, ΔS the entropy of transformation per unit volume. Under the hypothesis of constant ε_{tr} , the right-hand part of eq. 4.1 is constant. Hence, Eq. 4.1 expresses a linear relationship between the transformation temperature T and the external stress σ. Strictly speaking, however, Eq. (4.1) is valid only on the microlevel of the oriented crystal lattice or in a single variant transforming SMA single crystal. $\frac{d\sigma}{dT}$ is basically a material parameter related to the type of structural transition involved. $\frac{d\sigma}{dT}$ value for polycrystals is influenced by several factors, including the heat treatment and the thermomechanical history of the alloy (Otzuka and Waiman, 1998). Typical values for this very important property (in MPa/°C) are between 4 and 20 for the martensitic transformation in NiTi.

Furthermore, according to the operating temperature, the alloy manifests different mechanical behaviors, as showed in Figure 4.12, where the SMA stress-strain response, in different thermal conditions, is reported.

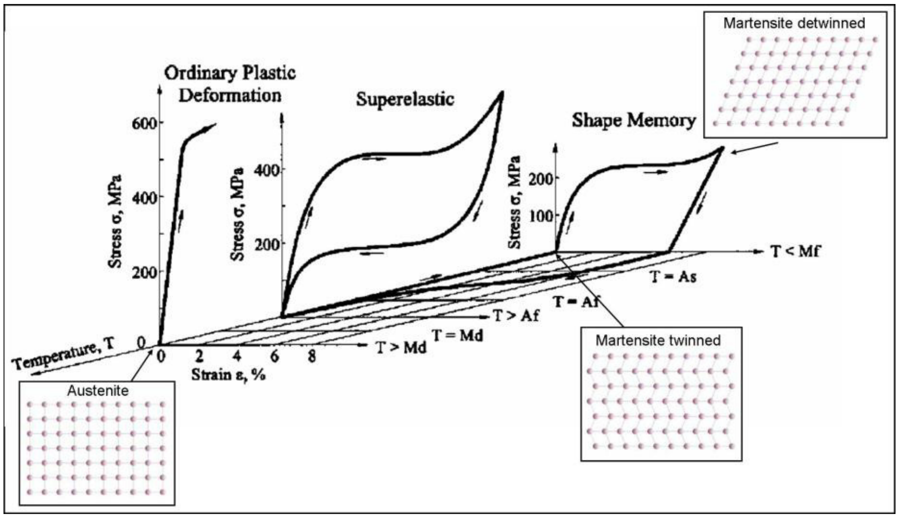

Figure 4.12: SMA stress-strain response obtained at different operating temperatures: (a) T > M_D, no martensitic phase transformation is recorded, the material is characterized by a stable austenitic structure and exhibits the typical behavior of a common engineering metal. (b) A_f< T < M_D the material shows the pseudo-elastic behavior. (c) T < M_f the material exhibits a stable martensitic structure (detwinning process) (Duerig *et al.,* 1990)

For values of temperature below A_s, the material in martensitic state can be easily deformed with low stresses, and after unloading, the residual strain can be completely recovered by heating above A_f: in the final configuration, the material is fully transformed in austenite recovering, from a macroscopic point of view, its original shape, as represented in the strain-temperature plane of Figure 4.12.

If the applied temperature is in a range between A_f and M_D (as described before M_D is the temperature above which an applied stress induces plastic deformation, while, below this value transformation mechanism can occur) the material exhibits a pseudoelastic behavior: this means that the material after an applied load is able to completely recover severe deformations (up to 10%)

No shape recovery is recorded if the operating temperature $T > M_D$. In these conditions, in fact, the material exhibits a pure austenitic behavior, i.e. common plastic slip mechanisms in the crystals occur, with no transformation phenomena.

4.2.4 One Way Shape Memory Effect

A SMA exhibits the shape memory effect (SME) also known as One Way- Shape Memory effect (OW-SME) when it is deformed in the twinned martensitic phase, then unloaded and subsequently heated above A_f. Owing to the OW-SME the SMA regains its original shape by transforming back into the parent austenitic phase. The nature of the SME can be better understood by following the thermo-mechanical loading path in a combined stress-strain-temperature space as shown in Figure 4.13. Figure 4.13 shows experimental data for a typical NiTi specimen tested under uniaxial thermo-mechanical loading. σ, ε and T represent respectively the stress, the strain and the temperature. Starting from the parent phase (point A in Figure 1.13), the stress-free cooling of austenite below the forward transformation temperatures (M_s and M_f) results in the formation of twinned martensite (point *B*). When the twinned martensite is subjected to an applied stress that exceeds the start stress level (σ_S), the reorientation process is initiated, resulting in the growth of certain favorably oriented martensitic variants. The stress level for reorientation of the variants is far lower than the permanent plastic yield stress of martensite. The detwinning process is completed at a stress level, σ_f, that is slightly beyond the end of the plateau (Liu and Xie, 2007) in the σ-ε diagram in figure 4.13. The material is then elastically unloaded from C to D and the detwinned martensitic state is retained. Upon heating in the absence of stress, the reverse transformation initiates as the temperature reaches A_s, (at point *E*) and is completed at temperature A_f (point F), above which only the parent austenitic phase exists. In the absence of permanent plastic strain generated during detwinning (Liu and Xie, 2007; Otsuka and Ren, 2005) the original shape of the SMA is regained completely (indicated by A). The strain recovered due to the phase transformation from detwinned martensite to austenite is termed as the transformation strain (ε_t). Subsequent cooling to martensite will again result in the formation of self-accommodated twinned martensitic variants with no associated shape change, and the whole cycle of the SME can be repeated. The above described phenomenon is called OW-SME, or simply SME, because the shape recovery is achieved only during heating after the material has been detwinned by an applied mechanical load.

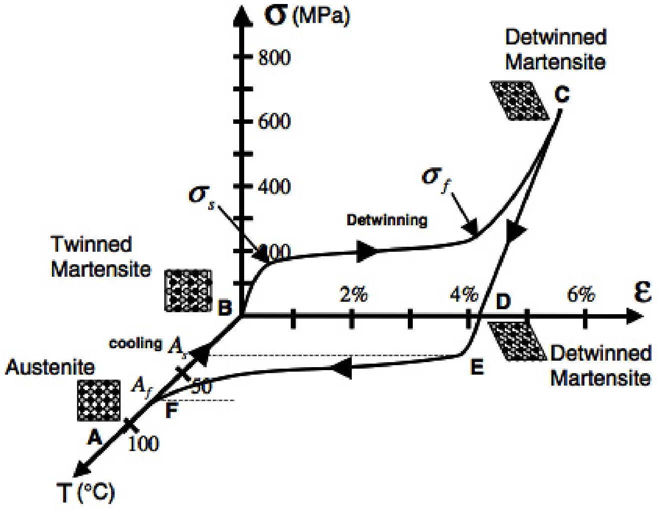

Figure 4.13: stress-strain-temperature data exhibiting the OW-SME for a typical NiTi SMA (Lagoudas, 2008).

4.2.5 Two Way Shape Memory Effect

SMAs can exhibit repeatable shape changes under no applied mechanical load when subjected to a cyclic thermal load. They can remember a cold shape in addition to their hot shape (OW-SME). This behavior is termed two-way shape memory effect (TW-SME) and it can be observed in a SMA material which has undergone a certain thermo-mechanical cycling along a specific loading path (training).

In comparison with one-way shape memory alloy (OW-SMA), where an additional element such as a spring is needed for providing an external force to reset the cold shape upon cooling, a TW-SMA has an intrinsic memory of its cold shape and can lead to a more compact and simplified configuration of smart actuators and structures. This may be of benefit to industrial and surgical applications where a limited working space is often encountered.

TW-SME is not a natural feature of the alloy, but rather is a ‘learned’ or ‘trained’ behaviour. Repetition along a loading path for a certain number of cycles can induce changes in the microstructure, which causes macroscopically observable permanent changes in the material behavior.

Training an SMA refers to a process of repeatedly loading the material following a cyclic thermo-mechanical loading path until the hysteretic response of the material stabilizes and the inelastic strain saturates. The TW-SME behavior can be achieved by adopting different training sequences (Contardo and Guenin, 1990; Miller and Lagoudas, 2000; Ren and Otsuka,2000). Several training methods have been proposed in literature. These methods are can be classified as one-time martensite deformation and thermomechanical cycling treatment. The one-time martensite deformation method is easily obtained by deforming the alloy in the martensite phase. However, only a small two-way memory effect can be produced (Luo and Abel, 2007; Otuska and Wayman, 1998). Liu *et al*. (1998) envisaged that the two-way recoverable strain could be increased by imposing a severe martensitic deformation. The maximum strain of 4.1% was achieved in a near-equiatomic NiTi alloy wire sample at a deformation strain of 13.3% beyond the recoverable limit of NiTi OW-SMA (about 8%), which is comparable to the best two-way shape memory effect achieved by other training methods. However, the large amount of plastic strain introduced by such a high level of deformation inevitably reduces the memory strains associated with the hot shape. In fact, the level of deformation strain in martensite is a trade-off between the induced two-way and one way strains, when developing TW-SMA by martensite deformation.

Thermomechanical cycling treatment is based on the repetition of a cycle that include the transformation from austenite to preferentially oriented martensite or from deformed martensite to austenite. This method seems to be more effective than one-time martensite deformation and is widely applied. There are four basic thermomechanical cycling training methods, known as shape memory cycling, constrained cycling of deformed martensite, pseudoelastic cycling and combined shape memory and pseudoelastic cycling (Duerig *et al*. 1990). Other thermomechanical cycling training methods are also documented in the literature (Sun and Wu, 1994), but they are actually variants or combinations of the above four methods with fewer new aspects.

Let us consider the case of cyclic thermal loading of an SMA specimen under a constant applied stress initially applied on the material in martensitic condition (Figure 4.14). During the first thermal cycle, only a partial recovery of the strain generated during cooling is observed upon heating with some permanent (irrecoverable or plastic) strain generated during the cycle. A small, permanent strain remains after each thermal cycle is completed. The additional permanent strain associated with each consecutive cycle begins to gradually decrease until it practically ceases to further accumulate (figure 1.14). A similar behavior can be noticed in the case of mechanically cycling an SMA repeatedly in its pseudoelastic regime, until saturation takes place (figure 4.15).

TWSME is a result of the dislocation array introduced during training. These permanent defects create a residual internal stress state, thereby facilitating the formation of preferentially – oriented martensitic variants when the SMA is cooled in the absence of external loads. If the internal stress state is modified for any reason (e.g., aging at high temperature or mechanical overload), the TWSME is perturbed (Rodriguez and Guenin, 1990)

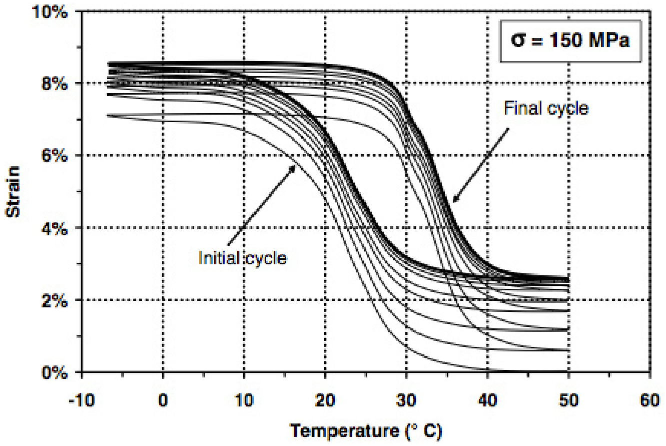

Figure 4.14: Thermal cyclic loading of a NiTi shape memory alloy under constant load of 150 MPa, example of constrained cycling of deformed martensite training (Lagoudas, 2008).

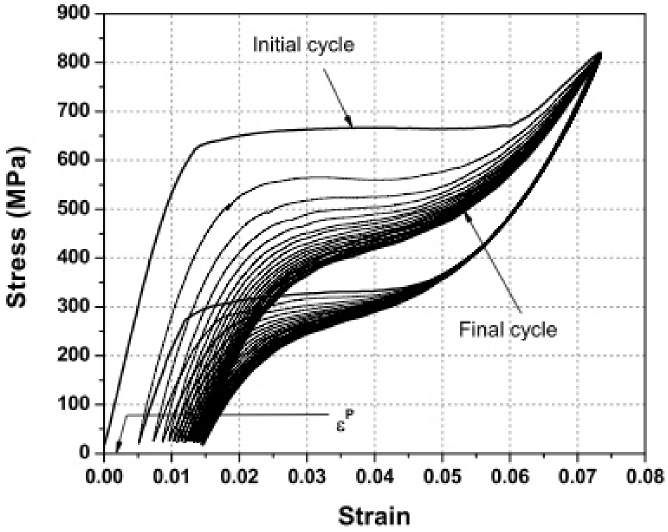

Figure 4.15: Pseudoelastic response of an as-received NiTi wire with Af = 65 ◦C, tested at a temperature of 70 ◦C. Also shown is the stabilized pseudoelastic hysteresis loop after 20 cycles. Example of pseudoelastic cycling training (Lagoudas, 2008).

4.2.6 Pseudoelasticity

The pseudoelastic behavior of SMAs is associated with stress-induced transformation, which leads to strain generation during loading and subsequent strain recovery upon unloading at temperatures above A_f. A pseudoelastic thermomechanical loading path generally starts at a sufficiently high temperature where stable austenite exists, then develops under an applied load to a state at which detwinned martensite is stable, and finally returns to the austenitic phase when returned to zero stress state.

To illustrate the pseudoelastic behavior in greater detail, let us consider the thermomechanical loading path (A → B → C → D → E → F → A) in Figure 4.16, which starts at zero stress at a temperature above A_f. When a mechanical load is applied, the parent phase (austenite) undergoes elastic loading (A → B). At a specific load level, σ^{Ms}, martensitic transformation occurs. Note that the stress-induced transformation from austenite to martensite is accompanied by the generation of large inelastic strains; in fact, the transformation proceeds (B → C), to the stress level (σ^{Mf}) indicating the end of the transformation.

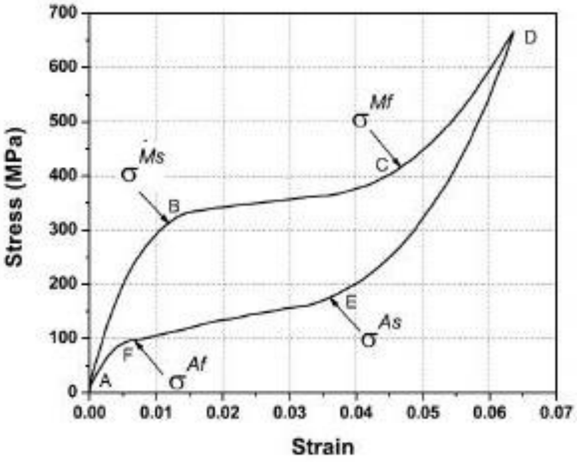

Figure 4.16: a typical the stress–strain curve of a pseudoelastic SMA (Lagoudas, 2008)

The completion of martensitic transformation is indicated by a distinct change in slope on the σ-ε curve, which is associated with the elastic loading of the martensitic phase. A subsequent increase in the stress causes limited transformation phenomena and mainly the elastic deformation of detwinned martensite occurs (C → D). When the stress is released gradually by unloading, the martensite elastically unloads along the path (D → E). At point E, at a stress level σ^{As} the detwinned martensite begin to revert to austenite. The process is accompanied by the recovery of the strain due to phase transformation at the end of unloading. The end of the transformation back into austenite is denoted by the point at which the σ-ε unloading curve rejoins the elastic region of austenite (point F corresponding to stress σ^{Af}). In absence of inelastic or plastic deformations (previously induced during loading), the material then elastically unloads to A. The forward and reverse phase transformation during a complete pseudoelastic cycle results in a hysteresis, which, in the σ-ε space, represents the energy dissipated in the transformation cycle. The transformation stress levels and the size of the hysteresis vary depending on the SMA material and testing conditions. It is important to point out that the characteristic stresses σ^{Ms}, σ^{Mf}, σ^{As},σ^{Af} increases linearly with temperature according to eq. 4.1, very often with two different Clausius-Clapeyron constants describing the martensitic characteristic stresses and the austenitic ones, respectively C_M and C_A.

The detwinned martensite that forms from austenite as a result of the applied stress is stress-induced martensite (SIM). Many thermomechanical loading paths that can result in the formation of SIM.

Generally, the term pseudoelasticity describes both superelastic behavior and so-called rubber-like behavior (Otsuka and Wayman, 1998). The reversible phase transformation (described in this section) caused by a thermomechanical loading path is strictly called the superelastic behavior. The rubber-like effect is an exclusive behavior of the martensite phase only and occurs due to the reversible reorientation of martensite. The resulting σ-ε curve is similar to the superelastic curve, and this phenomenon is called the rubber-like effect to emphasize the similarities with the nonlinear elastic behavior of rubber. In SMAs exhibiting the rubber-like effect, the stress required to detwin martensite is generally lower (Liu and Xie, 2007) if compared σ^{Ms}. In this work the term pseudoelasticity is referred to the superelastic behavior of SMAs only.

4.2.7 A More General Overview of Shape Memory Behavior

So far SME and superelasticity have been considered as two separate effects. If stress is applied at intermediate temperature, however, between A_f, and A_s, this may result in a combination of the two effects. To illustrate this idea, it is useful to consider a stress-temperature plot (see Figure 4.17). In this plot, the line representing the critical stress to induce martensite, σ_{Ms} has a positive gradient, since this stress increases linearly with temperature, from the Clausius-Clapeyron relationship (eq. 4.1). The line representing the stress required to induce slip, σ_S, decreases with temperature, since dislocation motion becomes easier at higher temperatures, due to reduced energy barriers. σ_S depends strongly on the microstructure of the alloy and its thermo-mechanical history (Otsuka and Ren, 2005).

The SME is obtainable in a wide range of of temperature: stable detwinned martensitic variants can be induced by loading below M_s. They would revert in austenite on heating above A_s. Superelastic loading path is represented by any vertical line cutting through the superelastic region, in which the initial stress is insufficient to induce the martensitic transformation but, once the critical stress value (σ_{Ms}) is reached, unstable variants are formed that revert to the parent phase upon unloading.

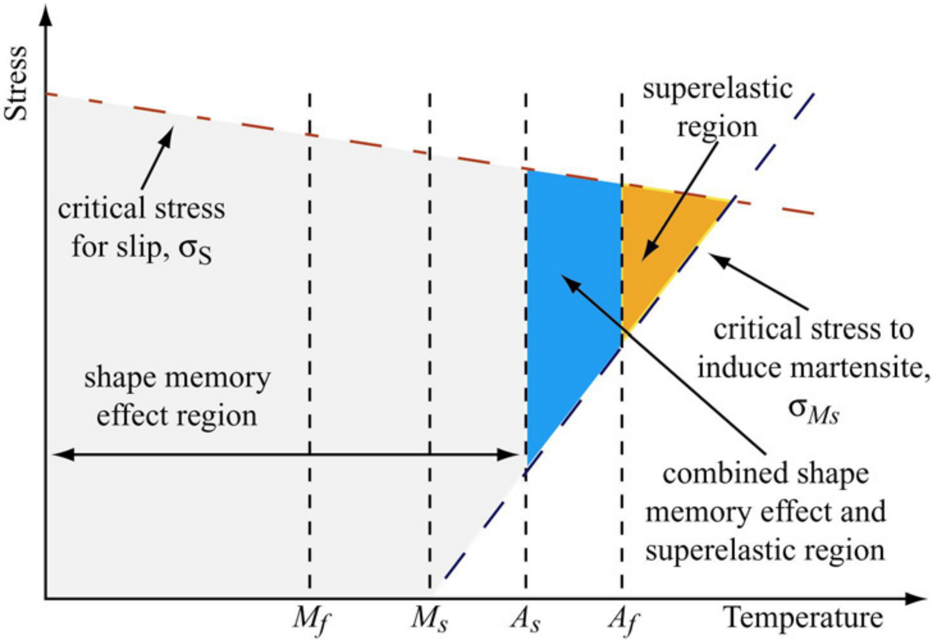

Figure 4.17: Stress-temperature plot for a typical shape memory system (Otsuka and Ren, 2005)

Figure 4.17 also demonstrates the potential for a shape memory material to exhibit the SME and superelasticity simultaneously. Increasing the applied stress above σ^{Ms} between A_s and A_f, will induce some stable and some unstable martensitic variants: only the unstable variants will revert to the parent phase, on removal of the applied stress, leaving some temporarily stable variants and some temporary deformation: these temporary variants will revert on increasing the temperature above A_f.

Figure 4.18 illustrates the key to superelasticity: σ^{Ms} must be lower than σ_S at temperatures above A_s. Thus, if, in Figure 4.18, σ_S were equal to σ^{Ms} at a temperature below A_s, the material would exhibit no superelasticity, but could still exhibit the SME.

Clearly Figure 4.18 only represents the behavior of one specific SMA. The temperature A_s may in practice be below M_s and, from the discussion above, σ^{Ms} may equal σ_S below A_S.

4.2.8 NiTi-based Shape Memory Alloy

Despite the discovery of the shape memory goes back to the '50s, the interest for SMAs, from an engineering point of view, was only recognized when the NiTi based alloy called Nitinol (Nickel Titanium Naval Ordnance Laboratory), from the name of the laboratory where it was discovered (Buehler, 1963). Over the past four decades, the NiTi binary alloys have been thoroughly investigated and today, from the commercial point of view, they are the most important, thanks to their flexibility, the excellent performances in terms of shape recovery and good mechanical properties.

Moreover, these alloys have excellent corrosion resistance and biocompatibility, which make them widely used in various biomedical applications. Their realization, however, is rather expensive for several factors: the thermomechanical response is strongly dependent on the Ni-Ti relative composition and thermomechanical history of the alloy: this requires a very high accuracy in composition selection and material processing. Moreover, due to the reactivity of titanium at high temperatures, their casting has to be performed in vacuum or inert atmosphere. The nickel-titanium system has a high solubility for a number of other elements. Generally, the ternary element is added to provide stability of some characteristic of the material e.g. a change to the transformation temperatures, a variation in the hysteresis width or extra mechanical stability of the material.

Due to the significant costs and the difficulties in processing, in the early seventies researches on alternative shape memory materials, starting from ternary NiTi based alloys, have been carried out. Some ternary nickel-titanium-based alloys also exhibit shape memory characteristics.

4.2.9 Near-equiatomic nickel-titanium system

NiTi is an intermetallic compound existing in the Ti-Ni phase system and melting at 1310 °C (Fig 4.18) . At 1090C NiTi exhibits an order-disorder transformation, with the ordered body centered cubic, B2 phase occurring below 1090 °C and the disordered body centered cubic phase occurring above. The TiNi phase field is surrounded by two phase regions. On the Ti-rich side there is TiNi + Ti_2Ni , while on the Ni-rich there is of TiNi + Ni_3Ti (Otsuka and Ren, 2005). A marked decrease in solubility for nickel at temperatures lower than 1090 °C occur in Ni-rich NiTi phase field, thereby enabling the creation of a Ni-rich supersaturated solid solution by means of rapid quench from high temperatures. Subsequent reheating to temperatures below the single phase region induces the formation of Ni-rich precipitates.

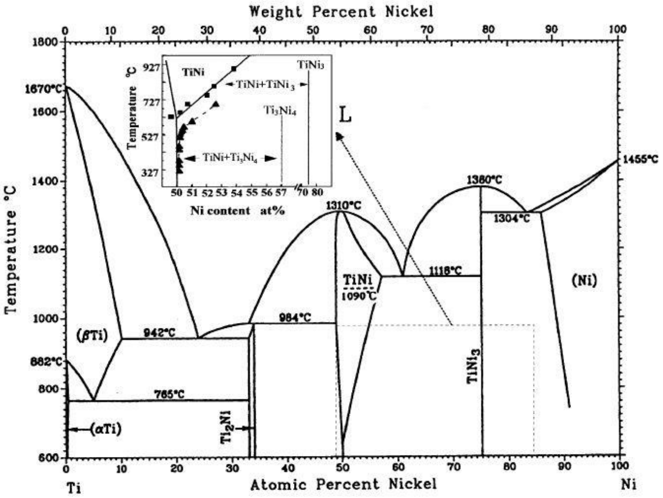

Figure 4.18: Nickel-titanium phase diagram (Otsuka and Ren, 2005): the region around 50 at% Ni is expanded in Figure 4.19.

The transformation phenomena in SMAs and particularly in NITi are strictly dependent on the microstructure of the alloy. Factors such as Ni content, aging, thermo-mechanical treatment and addition of alloying elements, which affect the structure, are strongly related to the mechanical and functional properties of SMAs.

The metastable phase equilibrium between TiNi phase and Ti_3Ni_4 (see Fig. 4.19) phase is very useful in adjusting transformation temperatures and in designing heat-treatments for improving shape memory characteristics. Ti_3Ni_4 is quite stable at temperature below 600 °C and under normal aging condition only Ti_3Ni_4 is observed. Observing the diagram is clear that when precipitation reaction occurs, formation of Ti_3Ni_4 precipitates is accompanied by a decrease in Ni content of the TiNi matrix. Transformation temperatures increases accordingly as explained in the following paragraphs.

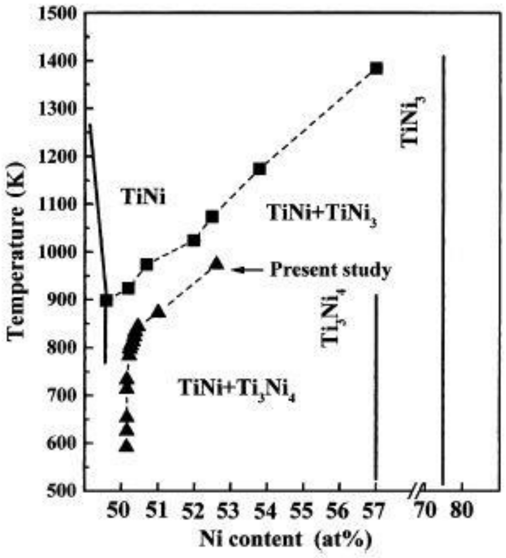

Figure 4.19: Phase diagram between TiNi (B2) phase and metastable Ti3Ni4 precipitates. Phase equilibrium between TiNi and TiNi3 is also shown (Otsuka and Ren, 2005).

Transformation Paths of NiTi

While fully annealed near-equiatomic Ti-Ni alloys transform from the B2 parent phase directly to the monoclinic B19' phase, thermally cycled or thermo-mechanically treated near-equiatomic Ti-Ni alloys transform in two steps, i.e., from the B2 parent to the R-phase and then to the B19'. The R-phase is essentially a trigonal distortion of the cubic austenite phase and occur introducing precipitates and/or strain/stress-field inhomogeneities in the material structure (Otsuka and Ren, 2005). The R-phase presence can be clearly demonstrated through the appearance of a second transformation peak, often only in the cooling curve obtained using differential scanning calorimetry (see Figure 4.20).

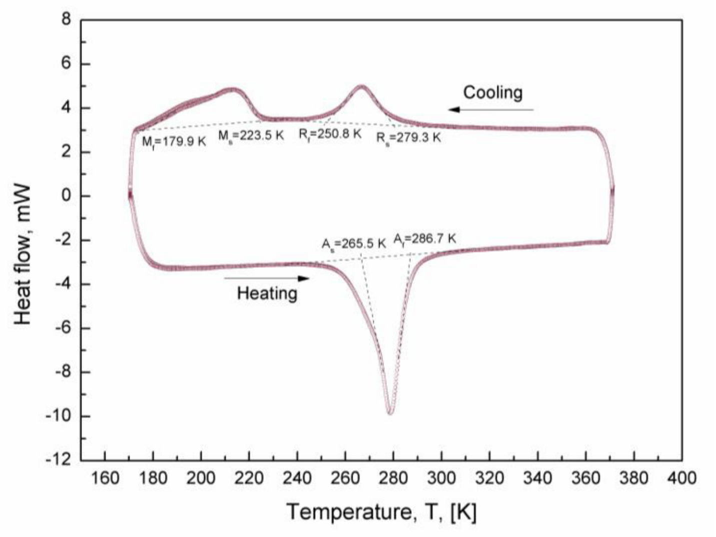

Figure 4.20: Differential scanning calorimetry plot demonstrating two-phase transformation on cooling via the R-phase.

Processes which promote the R-phase formation include precipitation hardening and cold working (Carroll *et al.,* 2004; Peltonen *et al.,* 2008; Stroz, 2002; Khalil-Allafi *et al.,* 2006). On further cooling, the R-phase typically converts to the B19’ phase unless the B19’ phase is completely suppressed. Previous studies have also shown that the B19’ phase may convert to the B2 phase on heating without passing through the R-phase (Peltonen *et al.,* 2008) (see Fig.4.20). R-phase has a reduced thermal hysteresis associated with its transformation back to and from the B2 phase if compared with the B19’ phase. Furthermore, the amount of transformation strain associated with the R and B19’ phase is significantly different. The Shape memory deformation associated with the B2-B19’ phase transformation can reach values up to 10%. Shape memory phenomena involving the R-phase transition only exhibits a maximum strain of 2% (Dlouhy *et al.,* 2004; Peltonen *et al.,* 2008).

Influences of the Martensitic Phase Transformations in NiTi

The factors that can influence the NiTi transformation temperatures are numerous. Among them, the most important ones are: the Ni composition, the precipitation in Ni-rich NiTi alloys, the aging heat-treatments, ternary alloying elements and point defects and dislocations. It has been shown that a change in Ni content by a 0.1at% causes a shift of M_s of about 10 °C (see Fig.4.21).

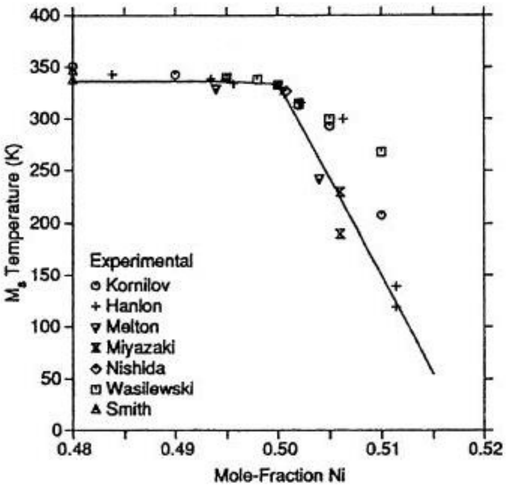

Figure 4.21: Ms temperature as a function of Ni content for binary NiTi alloys. Different symbols represent data from different authors. The solid line is given by thermodynamic calculations (Otsuka and Ren, 2005).

M_S temperature varies owing to the dramatic increase in strength of TiNi matrix with increased Ni content; the Ni-richer material it is less capable of accommodating the strains associated with the martensitic transformation (austenitic stabilization) and thus requires an undercooling to transform (Khalil-Allafi, 2002; Dlouhy *et al.,* 2004). Residual strains and dislocations also impact the martensitic transformation (Wu, 1999; Peltonen *et al.,* 2008; Frick *et al.,* 2004). Grain refinement has the potential to influence the martensitic transformation mechanisms, but as the majority of the studies have utilized severe plastic deformation to refine the grain size, it is difficult to separate the effects due to the high dislocation density and those due to grain size (Valiev *et al.,* 2006, Frick *et al.*, 2005). Studies conducted on the M_S temperature of various grain sizes of TiNi resulting from growth at temperatures exceeding 900C have shown the M_S temperature to decrease with increasing grain perimeter. Classical theories relating to martensitic nucleation suggest that nucleation of martensitic occurs heterogeneously at grain boundaries, suggesting that reductions in grain size should serve to promote the martensitic transformation by increasing the relative volume of grain boundaries in a material these acting as nucleation sites. (Ghosh and Olson, 1994a; Ghosh and Olson, 1994b). Moreover, it has been suggested that the accommodation of strains associated with the martensitic phase formation is far easier at smaller grain sizes, thus the transformation temperature increases (Valiev *et al*., 2008). Precipitation hardening has strong effects on the yelding stress of the material as well as on its shape memory an pseudoelastic performance (Otsuka and Ren, 2005). It causes the shift of the transformation temperatures as well, however it not widely acknowledged as to whether this result is due to a change in the matrix composition resulting from precipitate formation or if it is due to strain effects associated with the precipitate or some combination of the two (Gall *et al.,* 1999; Carroll *et al.,* 2004; Frick, 2004; Frick, 2005; Otsuka and Ren, 2005). Aging a fully annealed Ni-rich NiTi at temperatures between 400 °C and 500°C results in an increase of the transformation temperatures (Funakubo, 1897; Pelton, 2000; Otsuka and Ren, 2005). This may be explained by the formation of Ti_3Ni_4 precipitates reducing the overall Ni content of the matrix. Despite the intensive recent interest and the publication of a number of highly credible studies on the possible mechanisms for ageing-induced multiple stage transformation behavior, comprehensive on the transformation and mechanical properties is lacking, largely owing to the complexity of the issue itself. In fact, ageing involves three independent parameters, i.e. temperature, time and alloy composition (Zheng *et al.,* 2008). The effects of thermal cycling and deformation cycling has a significant influence on the transformation temperatures as well (Otsuka and Ren, 2005; Otsuka and Wayman, 1998).

Another method to vary the Ni-content (and the transformation temperatures consequently) is through tertiary alloying elements. Among the elements that increase the transformation temperature, Pt, Zr, Hf, Pd and Au are the prominent ones. In fact, Ti-Ni-(Hf, Zr, Pd) are considered as probable candidates for high-temperature shape memory applications (Van Humbeeck, 2001; Otsuka and Ren, 2005; Bozzolo *et al.,* 2005; Bozzolo *et al.,* 2007; Noebe *et al*., 2006).

The instability of near-equiatomic nickel-titanium alloys is therefore clear. The transformation temperatures of the material are governed closely by the Ni content in the NiTi matrix, the dislocation density and the precipitates and this could easily be altered if the material is subjected to cyclic loading, or large temperature fluctuations. Despite these problems, or perhaps because of them, near-equiatomic nickel-titanium has extremely useful shape memory properties, which can be controlled by careful manipulation of processing conditions.

4.2.10 Alloys with Narrow Hysteresis

The partial replacement of copper atoms in nickel lattice location has interesting effects on the material properties, resulting in obvious advantages. Ternary Ti-Ni-Cu alloys exhibit a lower sensitivity to the temperature, an evident reduction of the hysteresis related to the transformation, from 30 °C to less than 10 °C, an increase of the damping capability, and finally a significant difference in stiffness between the martensitic and austenitic phase. These properties make them particularly advisable for the realization of actuators for intelligent systems (Otuska and Wayman, 1998).

4.2.11 Alloys with Wide Hysteresis: the NiTiNb system.

Some ternary NiTi-X systems provide a better functional performance (Singh, 2016; Bozzolo, 2005) because they ensure higher TTs and larger thermal hysteresis with respect to NiTi alloys. For example, the addition of niobium to the binary Ni-Ti alloys allows to decrease the start temperature of the martensitic phase transformation, M_s and also to increase the thermal hysteresis of the alloy. Such a type of alloys are particularly suitable for the realization of coupling and fastening devices (Zhang *et al.,* 1990; Duerig *et al*., 1990)**.** In general, the microstructure of cast NiTiNb alloys consists of a NiTi matrix, β Nb-particles in a eutectic mixture with the matrix and Nb-rich nano-precipitates

(Shi *et al*., 2012; Shi *et al*. ,2013; Shi *et a*l., 2014; Zheng *et al.,* 1998). The matrix contains mostly Ni and Ti with some dispersed Nb (Duerig and Melton, 1989b; Piao *et al*., 1992; Shi *et al*.,2012) and has a *B2* type structure. Only the matrix undergoes the martensitic transformation. The microstructure of NiTiNb SMAs is dependent on both the Nb content and the ratio of Ni to Ti (Shi *et al*., 2013; Zheng *et al*., 1998; Piao *et al*., 1992a; Wang *et al.*, 2012; Uchida *et al*.,2007). Fig. 4.22 shows the SEM micrographs of some typical NiTiNb alloys with different compositions, $Ni_{50}Ti_{49}Nb_1$, $Ni_{50}Ti_{47}Nb_3$, $Ni_{49.6}Ti_{45.9}Nb_{4.5}$ and $Ni_{47}Ti_{44}Nb_9$. Experimental results indicated that for $Ni_{50}Ti_{50-x}Nb_x$ series alloys, only when the Nb content is greater than 2 at% a few of the isolated β-Nb particles can dissolves in NiTi(Nb) matrix (where NiTi(Nb) represents the NiTi metallic compound with dissolution of Nb atoms). Furthermore, higher Ni/Ti ratio favors the suppression of precipitation of β-Nb phase. For example, $Ni_{49.6}Ti_{45.9}Nb_{4.5}$ alloy is characterized by a single NiTi phase, even though the percentage of Nb reaches 4.5 at%. One of the most studied SMA with wide hysteresis is $Ni_{47}Ti_{44}Nb_9$ (Duerig and Melton, 1989b; Piao *et al*., 1992a; Zhang *et al*. 1990); its microstructure is shown in Fig. 4.22(d) consisting primary NiTi(Nb) phase (dark grey) and eutectics of NiTi(Nb) and β-Nb (light gray).

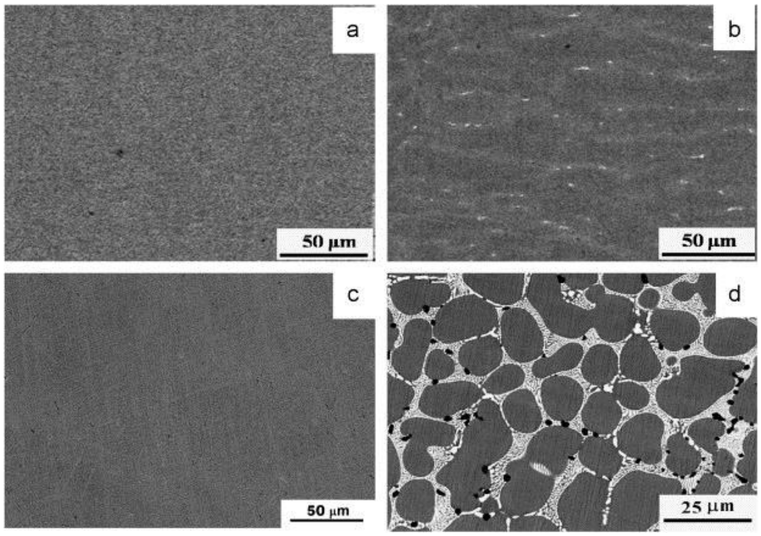

Figure 4.22: The microstructures of (a) Ni50Ti49Nb1, (b) Ni50Ti47Nb3, (c) Ni49.6Ti45.9Nb4.5 and (d) Ni47Ti44Nb9 alloys (Wang *et al*.,2012)

Heat treatments are commonly carried out for altering the microstructure and consequently for relieving internal stresses, improving ductility/hardening and toughness and modifying the shape memory behavior of NiTiNb SMAs (Siegert *et al*., 2002, Shi *et al*.,2013; Zheng *et al*. 1997, Zheng *et al.*, 1998). High temperature aging can promote the formation of Ni-rich precipitates thus varying the Ni/Ti ratio in the matrix so that the Ti content increases (Zheng *et al*., 1998). This ratio influences significantly the transformation temperatures of the alloy (Zheng *et al*., 1998, Uchida *et al*.,2007). Generally NiTiNb alloy with high Nb content have wider thermal hysteresis (Af-Ms higher than 50°C) if compared with NiTi alloy (hysteresis of about 30-40 °C). It is reasonable to believe that the wider intrinsic hysteresis might be associated with its composite microstructure, especially with the presence of a large amount of β-Nb phase (Wang *et al*, 2012; Piao *et al*., 1992b) that enhances the frictional stresses resisting the crystallographic transformation.

The wider hysteresis of NiTiNb SMAs is associated with a significant increase of the reverse transformation temperatures A_s and A_f during shape memory (SME) recovery after a severe deformation in martensitic state. The soft β-Nb particles during isothermal pre-straining deform plastically. In fact, their flow stress matches or slightly exceeds that of pure Nb, estimated between 150-200 MPa (Otuska and Wayman, 1998; Duerig and Melton, 1989b). Plastic deformations occurring at the level of the micro-constituents are correlated to an increased thermal driving force for the reverse transformation that results in higher A_s and A_f temperatures (and wider hysteresis) only for the first heating cycle after pre-deformation (Duerig and Melton, 1989b; Shi *et al*., 2014; Piao *et al.,* 1992b; Zhang *et al.,* 1990; Liu and. Galvin 1997; Liu and Favier, 2000; Otuska and Wayman, 1998). The M_s and M_f temperatures are almost unaffected (Otuska and Wayman, 1998) or show a slight decrease (Okita *et al*.,2006). The reason for the increased driving force for the reverse transformation has been explained differently (Duerig and Melton, 1989b; Piao *et al*. 1993; Liu and Favier, 2000; Piao *et al*., 1992b; He and Rong, 2004). One possible explanation is that the plastic deformation of Nb-rich particles results in frictional stresses resisting the shape recovery process of the detwinned martensitic variants (Duerig and Melton, 1989). Piao (1993), instead, suggested that the dislocation arrays, induced by plastically deforming Nb-rich particles, is associated with a release of stored elastic energy in the NiTi(Nb) matrix; as this energy, after martensitic prestrain, becomes not available to assist the reverse transformation anymore, A_s is driven to higher temperatures as well as A_f. Few studies have explored by deeper analysis these phenomenological understandings (Piao *et al.,* 1993; Shi *et al*., 2012; Zheng *et al*., 1998). In any case, it is clear that the interaction of the β Nb-rich particles with the transforming NiTi(Nb) matrix determine the effective transformation temperatures and the functional behavior of NiTiNb alloys. Moreover, hot and cold working processing provides a mean to alter the microstructure in order to control the transformation temperatures and mechanical properties (Siegert *et al*., 2002). It is evident that the martensitic pre-strain results in a certain amount of residual inelastic deformations, after unloading. Depending on the level of the imposed pre-strain, plastic deformation can take place, and thus only a fraction of residual inelastic deformation is recovered by SME (Duerig and Melton, 1989b; Otuska and Wayman, 1998; Zhang *et al.,* 1990). Several studies primarily investigate the influence pre-strain in certain thermal ranges (Duerig and Melton, 1989b; Zhao *et al*., 2006; Zhang *et al.,* 1990; He and Rong, 2004; Kusagawa *et a*l.,2001; Piao *et al.,*1992), where the deformed martensite is stable after unloading. Duerig and Melton (1989) reported that the A_s temperature during SME recovery increases with increasing applied pre-strain and the recovered strain is maximum for an applied pre-strain of about 12%. Zhang *et al.* (1990) found that pre-straining martensite to 16% results in recovery ratios (the ratio of the recovered memory strain to the residual inelastic strain after pre-strain) greater than 75%. Furthermore, stress-induced martensite

(SIM) obtained by loading NiTiNb samples between M_s and A_s seems to be effective in increasing the A_s temperature, while retaining sufficiently large recovery ratios (Zhang *et al*., 1990; Zhao *et al.,* 2006)

The internal plastic deformation is a necessary mechanism to compensate for the orientation mismatch among the preferentially oriented martensite variants in neighboring grains (Zhang *et al.* 1990, Zhao *et al*. 2006); considering that this internal plastic deformation is introduced by a directional external stress, it is likely that the internal stress created by this internal plastic deformation is directional too, thus having the potential to induce a two-way memory effect (see section 4.2.5). In fact, a two-way strain higher than 2% has been measured in NiTiNb samples in free recovery condition after a martensitic prestrain higher than 12% (Meng *et al*., 2006; Okita *et al*., 2006; Otsuka and Wayman, 1998).

4.2.12 Copper and Iron Based Alloys

Although NiTi SMAs offer excellent pseudoelastic and shape memory properties and biocompatibility, they are relatively expensive compared to Cu-based SMAs. Good electrical and thermal conductivity along with their good formability makes Cu-based SMAs an attractive alternative to NiTi. Copper-based alloys generally exhibit a lower thermal hysteresis than NiTi, with transformation temperatures highly dependent on the composition. A precise change from 10^{-3} to 10^{-4} at.% is sometimes necessary to achieve reproducible transformation temperatures within a 5°C range. The main Cu-based alloys are the Cu-Zn and Cu-Al systems. CuZnAl - The CuZn binary alloys are very ductile and have resistance to intergranular fracture as compared to other Cu-based alloys (Otuska and Wayman, 1998). Their mechanical behavior is limited to stress levels of approximately 200 MPa due to the low critical stress for slip. Within the operational range of stress, the alloy exhibits perfect SME and pseudoelasticity, but the transformation strain is limited to about 3-4% (Otuska and Wayman, 1998). These materials also exhibit very poor cyclic behavior (Funakubo, 1987). Recently, several other Cu-based SMAs are in development, such as CuAlMn which has good ductility and CuAlNb which is suitable for high temperature applications.

FeNiCoTi and FeMnSi are the main ferrous SMAs. $FeNi_{31}Co_{10}Ti_3$ after specific thermomechanical treatment, exhibits SME with transformation strains of about 3%. The alloy exhibits a thermal hysteresis of approximately 130°C and higher strength if compared with NiTi (Sehitoglu *et al*., 2006). Another ferrous alloy with good commercial prospects is FeMnSi. Si is primarily added to improve the shape memory effect and raise the critical stress for slip in austenite. When subject to training under a specific thermomechanical loading path, these SMAs exhibit complete SME. The transformation strains in these alloys are in the range of 2.5-4.5% (Otuska and Wayman, 1998).

4.2.13 Applications of SMAs

Although the NiTi alloy was discovered by William Buehler in 1959 (Kauffman *et al.*, 1997), the potential to commercialize SMA applications became available after the SME in NiTi alloy was revealed by William Buehler and Frederick Wang in 1962 (Kauffman *et al.*, 1997; Buehler *et al.*,1963). Nitinol alloys are cheaper to produce, easier and safer to handle, and have better mechanical properties compared to other existing SMAs at that time (Kauffman *et al.*, 1997). The first commercial success for a SMA application was the Raychem Corporation's CryoFit™ ''shrink-to-fit'' pipe coupler in 1969; SMA based coupling applications extensively analyzed in the section ##. Since the 1980's, the commercial application of NiTi alloys has developed in many areas due to the greater demands for lighter and more compact actuators, especially in the biomedical sector, exploiting the unique mechanical and functional performance of SMA (see Fig.4.23).

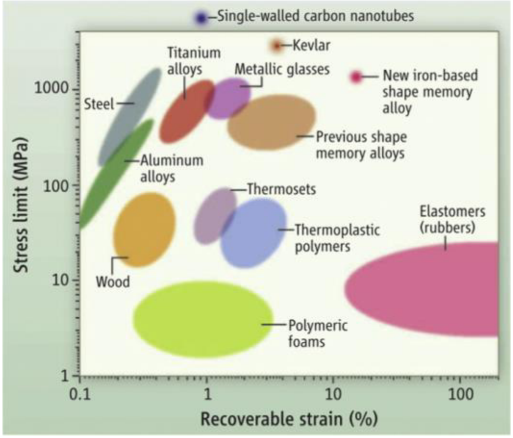

Fig. 4.23. Comparison of stress and strain limits between new developed SMA and other engineering materials (Jani et al., 2015).

SMA applications can generally be divided into four categories: free recovery, constrained recovery, work production and pseudoelasticity (Fig.4.24).

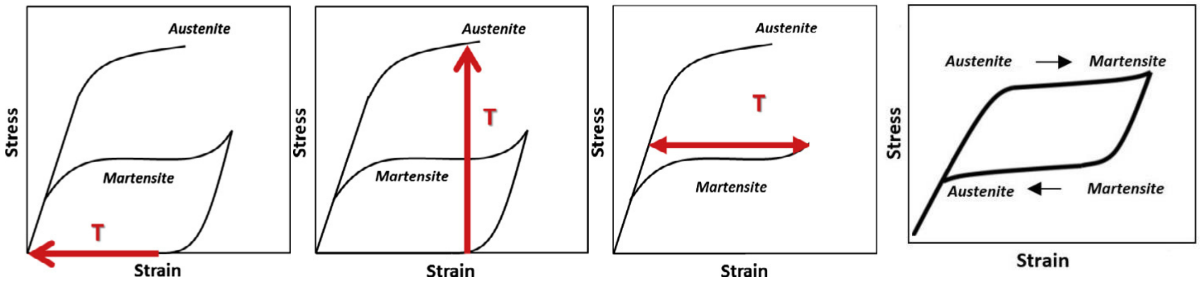

(a) (b) (c) (d)

Fig.4.24: SMA application categories: free recovery (a), constrained recovery (b), actuation/work production (c) and pseudoelasticity (d)

In free recovery applications Fig.4.24a, the function of the SMA element is to generate motion or strains. The memory element in martensitic state is deformed (detwinned) and then released (no load applied). It remains in stretched condition until heated above the transition temperature and shrink back to its original form. A commercial examples is the Simon Nitinol ® filter.

In constrained recovery applications Fig.4.24b, the shape change of the memory element is prevented and SMe generates a force on the mechanical obstacle when heated above its austenitic transition temperatures. Few commercial examples are the hydraulic couplings, fasteners and connectors CryoFit™, Cryocon®, UniLok®, CryOlive®, CryoFlare®, CryoTact®, Permacouple®, Tinel Lock® and BetaFlex™.

In work production (actuation) applications Fig.4.24c, there is motion against a stress and thus work is being done by the force generated by the SMA element. Very often a Two-way-effect is induced by an external reset load in SMA actuators: the memory element contracts upon heating (austenitic transformation) against opposing forces (very often a convectional spring) that stretch SMA element and reset the mechanism upon cooling when the SMA is in its martensitic state. Few examples are electrical actuators (VEASE™, SMArt Clamp™), thermal actuators (Memrysafe ®, circuit breaker, window or louvre opener, valves), and heat engines.

The pseudoelasticity applications Fig.4.24d are isothermal in nature and exploit the capability of SMAs to recover high deformations mechanically. Some commercial examples are the eyeglass frame (TiFlex™, TITANFlex®), orthodontic archwire, Mammelok® breast hook, guidewires, anchors and underwire brassiere are some existing examples.

The number of commercial applications is growing each year (see Fig. 4.25). The largest application segment of the market is actuators and motors, with sales of nearly USD10.8 billion (55% of the total market) in 2010 and forecasted to increase significantly (Fig.4.26).

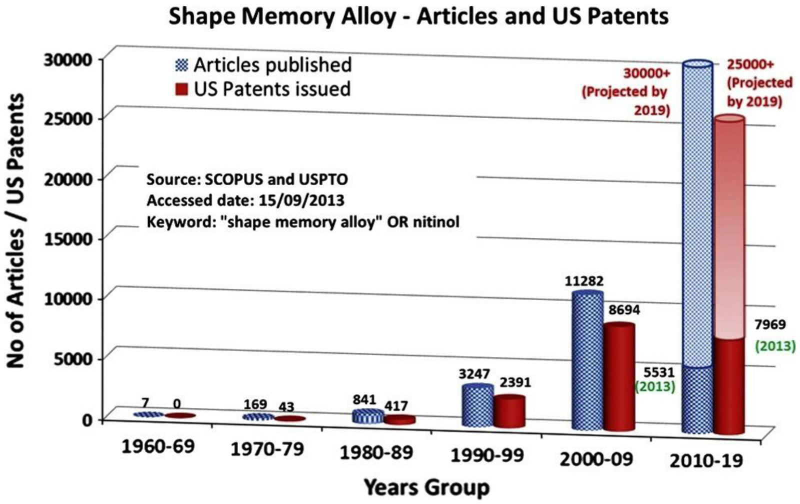

Fig.4.25 Number of ‘‘Shape Memory Alloy’’ articles and patents by years-group (Jani et al., 2015).

SMA are arousing lots of interests in many sectors: starting from biomedical field (orthodontic wires, dental implants, stents, orthopedic implants), to aerospace (smart wings for airplanes, couplings and fastening), from their use as actuators (for example in the automotive field), to the exploitation of their good damping capability (seismic dampers).

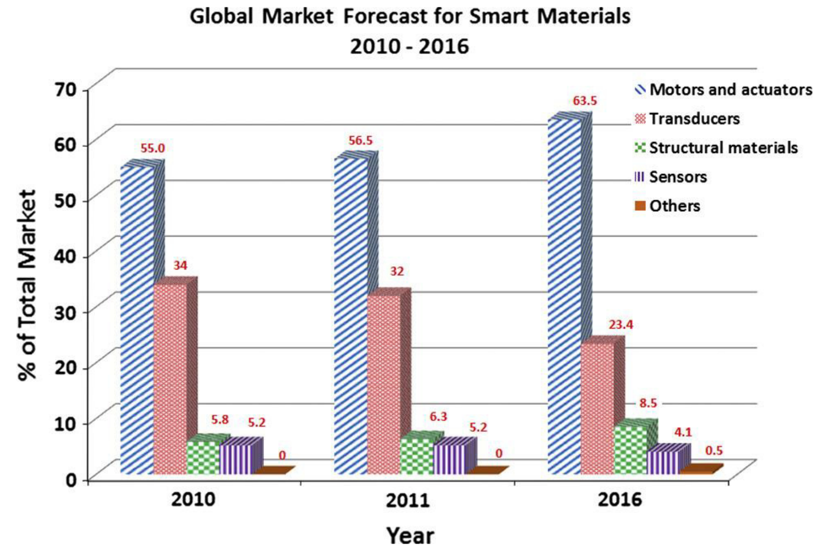

Fig 4.26: Global market forecast for smart materials for 2010–2016 (McWilliams, 2011).

In particular, the biomedical applications exploit the combination of biocompatibility (Mantovani *et al*., 2000), wear resistance, strength, capability to recover mechanically or thermally high deformations (up to 10%).Aerospace applications exploit the damping capability of SMA, in order to reduce the vibrations, obtaining a greater efficiency and a significant decrease of the noise in the surrounding environment. The ability of SMA to work in the absence of gravity makes them particularly advisable for space applications. In particular, these alloys are suitable for applications in the automotive field, thanks to their simplicity and lightness.

SMA actuators provide an excellent technological opportunity to replace conventional actuators such as electric motors, pneumatics and hydraulics due to their unique characteristics and ability to react directly to environmental stimuli; thus promoting the development of more advanced and cheaper actuators with a significant reduction in mechanical complexity and size. For instance, the NiTi SMA displays one of the highest work density at 10 J cm^3 which is a factor of 25 times greater than the work density of electric motors (Jani *et al*., 2015). Finally, especially in the civil field, several applications exploit the high inherent damping capability.

Aerospace Applications

SMA technology implementation in the aerospace industry has spanned the areas of fixed-wing aircraft, rotorcraft, spacecraft and work in all these areas is still progressing. Some of the more recent applications of SMAs and research on their potential uses in these areas are described in the following sections (Lagoudas, 2008).

There have been a number of other efforts to integrate SMA elements into aerostructures. One includes looking into the possibility of pairing SMAs and Micro-Electromechanical Systems (MEMS) to decrease the turbulent drag of an aerodynamic surface (Mani *et al*., 2003). The usefulness of active materials in tailoring propulsion systems was demonstrated through the SAMPSON program (Pitt *et al*., 2001). One of the uses of SMAs in this program was to change the geometry of an F-15 engine inlet. Engine noise levels during takeoff and landing have become more highly regulated worldwide. To reduce this noise, some designers are installing chevrons onto engines to mix the flow of exhaust gases and reduce engine noise. Research is being performed into methods by which SMA beam components can be embedded inside chevrons. The SMA beams bend the chevrons into the flow during low-altitude flight or low speed flight, thereby increasing mixing and reducing noise. During high-altitude, high speed flight, these SMA beam components cool into martensite, thereby straightening the chevrons and increasing engine performance (Mabe *et al*., 2005). The current Boeing design for these variable geometry chevrons can be seen in figure 4.27.

A different solution to the active chevron problem has been proposed by NASA. In this design, SMA strips are installed on each side of the chevron centroid during the fabrication process (Turner *et al*., 2006). Upon heating, the SMA strips contract alternately, leading to asymmetric stresses within the chevrons and therefore create a bending moment.

Figure 4.27: Boeing variable geometry chevron (J. Mabe, R., 2005)

One study proposed the use of SMA torque tubes to vary the twist of rotor blades, as found on tiltrotor aircraft (Jacot *et al*., 2006). Other rotorcraft applications include using SMA wire components for collective control (Loewy *et al*., 1997) and minimization of the blade vortex interaction noise.

SMAs have been used in space applications to address problems related to actuation and release in zero atmosphere environment as well as vibration damping during spacecraft launch. The scalability of SMA actuator designs also facilitates fabrication of smaller release devices for smaller satellites in need of compact release mechanisms (Willey *et al*., 2001) SMAs are also used in actuation of various components such as solar panels. An early design of this used SMA torsional elements to actuate solar collectors (Birman, 1997). The Lightweight Flexible Solar Array (LFSA) (Carpenter, 2001) used thin SMA strips as hinges, which deploy the folded solar panels upon heating in approximately 30 seconds.

In addition to actuation, another attractive application for SMAs is vibration isolators and dampeners (Godard *et al*., 2003). The mechanical hysteresis in the pseudoelastic behavior is representative of the energy that an SMA can dissipate during a cycle. Further, the change in the stiffness from the initial elastic region to that in the transformation region makes it an effective tool to isolate vibrations.

Medical Applications

The shape memory and pseudoelastic characteristics coupled with the biocompatibility of NiTi make them an attractive candidate for medical applications (see Figure 4.28). The combination of these unique characteristics has led to the development of various applications such as stents, filters, orthodontic wires as well as devices for minimally invasive surgery (Petrini and Migliavacca, 2011).

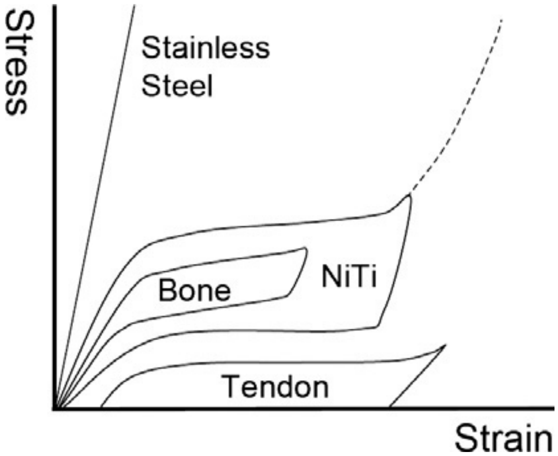

Fig. 4.28. The stress versus strain relationship for superelastic nitinol, stainless steel, bone and tendon tissues (Morgan, 2004)

Several investigations have been performed to study the biocompatibility and biofunctionality of NiTi alloys (Shabalovskaya, 1995; Ryhanen, 1999). Excessive intake of nickel can be poisonous to the human body but nickel, titanium and its compounds are intrinsically biocompatible and are commonly used in orthopedic and orthodontic implants (Mantovani, 2000). The oxidation of titanium results in a coating of TiO2, which provides a corrosion-resistant layer, making such a device stable within the human body. The properties of SMAs have been successfully implemented in a variety of dental applications. Nitinol orthodontic archwires have been used since the 1970s (Andreasen and Hilleman, 1971) and are more effective than other alter- native materials. In a linear elastic material like stainless steel, there is a large increment in stress, for a small increment in strain which results in a large amount of force on the tooth for a small amount of corrective motion. The advantage of pseudoelastic arch wires is the ability to operate in the pseudoelastic plateau, during which the material has a near-zero stress change over a large strain increment. As a result, they provide a nearly constant, moderate force to actively move the teeth over a longer period of time compared with stainless steel. Further, the material composition and processing can be engineered to produce different levels of optimal force. An example of Nitinol orthodontic braces is shown in figure 4.29a

Another key dental application for SMAs involves the use of Nitinol drills used in root canal surgery, which involves careful drilling within the tooth (figure 4.29b). The advantage of these Nitinol drills is that they can bend to rather large angles, which induce large strains, yet still withstand the high cyclic (Thompson, 2000)


(a) (b)

Figure 4.29: Orthodontic application of SMAs: (a) Nitinol braces used for alignment purposes in dental applications. (b) A schematic showing a NiTi drill used for root canal surgery (Lagoudas D., 2008).

An early cardiovascular SMA device was the Simon Filter®. The device acts as a filter that traps clots traveling in the blood stream. The release from the constraint and the active properties of the SMA filter cause the filter to expand and it assumes its original shape as shown in figure 4.30a (Duerig *et al*., 1997). A more common cardiovascular application is the "self-expanding" NiTi stent. After being constrained, the NiTi stent is introduced into the body where the temperature exceeds *Af* of the stent material. It is then released in the artery where it expands to its original larger diameter (due to pseudoleasticity) and gently pushes outward on the walls. Furthermore, the device can adapt to any oblong passage as compared to the balloon inflated steel stents that are biased towards a circular shape. Figure 4.30b shows an illustration of a Nitinol stent in the constrained and deployed configuration.

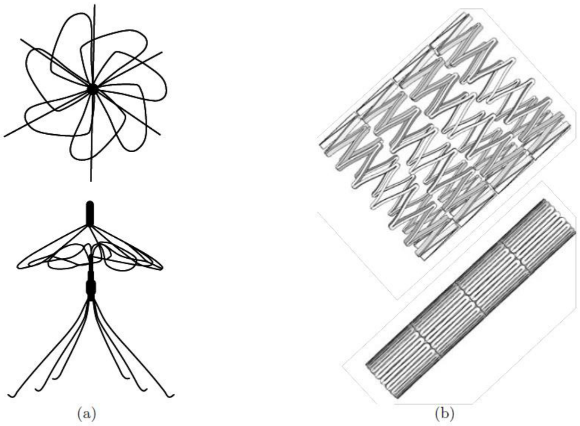

Figure 4.30: Cardiovascular devices that utilize the engineering properties of SMAs: (a) Top view (above) and side view (below) of the Simon filter in the deployed configuration (T. Duerig *et al*., 1997). (b) A self-expanding Nitinol stent shown in the deployed configuration (above) and constrained state (below) (Lagoudas D., 2008).

The devices developed for orthopedic applications are used to support injured, weakened or fractured bones. One such device is the spinal vertebra spacer, used to provide local reinforcement to the vertebrae and prevent motion during the healing process. The device applies a constant force on the joint while providing flexibility (Machado and Savi, 2003). Porous SMAs represent a different kind of material form and can be used as artificial bone implants (Lagoudas and Vandygriff, 2002). The porous nature of the material enables the existing bone tissue to migrate inward, increasing bonding strength.

Other instruments using the shape memory effect behavior include surgical tools with grippers, scissors and tongs used in laparoscopy procedures. Pseudoelastic guide wires are widely used in surgery due to their kink resistance and superior flexibility (Duerig *et al*., 1997).

Automotive Applications

Shape memory alloys have been used in automobiles for applications ranging from impact absorption to sensing and actuation. The pseudoelastic behavior hysteresis provides an effective system to dissipate vibrations and impact. This property has been used for impact absorption on armor vehicles in military (Paine and Rogers, 1994) and commercial applications (Barnes *et al.*, 2006). One design for an impact absorption application required the deployment of a protective panel within 5-7 ms. The limited response time of commercially available actuation devices (10 ms) is overcome by the use of an SMA element. The device can be released in 3 ms and then reset for another actuation. SMAs can also be used for sensor and actuation purposes simultaneously. An application that exploits this behavior is the SMA spring for the continuous variable transmission in the Mercedes A class. The spring acts as a sensor that monitors the temperature and actuates a valve at a specific temperature, which changes the direction of oil flow. SMA binary actuators are proposed for automotive tumble flaps (Bellini *et al.*, 2009).

General Motors (GM) has been working on SMA applications since the mid-1990s; so far GM has earned 247 patents and recently the seventh-generation of the Chevrolet Corvette was the first vehicle with a SMA actuator to actuate the hatch vent that releases air from the trunk for easier closing of the trunk lid (General Motors News, 2013).

Other applications developed for trains include the thermally actuated switch for the radiator fan in diesel engines and steam traps for the steam heating system in passenger trains. Both of these applications utilize the SME.

Other Applications

In addition to the aerospace, transportation and medical industries, there are many other fields and applications that incorporate SMAs. The oil industry has shown extensive interest to use the SMA actuation capabilities in release devices and protection systems for downhole drilling equipment. The high operating conditions have also opened the avenue for the use of HTSMAs in these devices (Anderson and Sangesland, 1999). Some commercial solutions in which SMA are exploited as sensor and actuator are Memrysafe® and Firechek® (Fig4.31) from Memry® which are respectively domestic device to control the hot water flow and an industrial safety solution to prevent flammable and dangerous gasses from flowing (Stoeckel and Waram, 1992). The pseudoelastic behavior has also been used in a wide range of applications. Developers of vibration control devices in civil structures have shown interest in pseudoelastic behavior of NiTi due to its capability to dissipate energy through a large mechanical hysteresis (Saadat *et al*., 2002). Other applications that employ the pseudoelastic behavior are flexible metallic eyeglasses and headphones, that can be bent without breaking (Otsuka and Wayman, 1998). SMAs have also been used in sporting goods like golf clubs where the SMA embedded in the club absorbs the impact of the strike. In a recent study, an innovative approach of knitting SMA wires into different patterns has shown to produce complex shape changes such as rolling, spiraling, arching and folding (Evans *et al*., 2003). The ability to generate such unique configurations using SMAs can open prospects for other novel design applications (Spinella *et al.*, 2009; Bellini *et al.*, 2009). Recently, a novel approach was proposed for using SMAs as actuators at higher stress level and temperatures than those conventionally used (Tuissi *et al*., 2015).

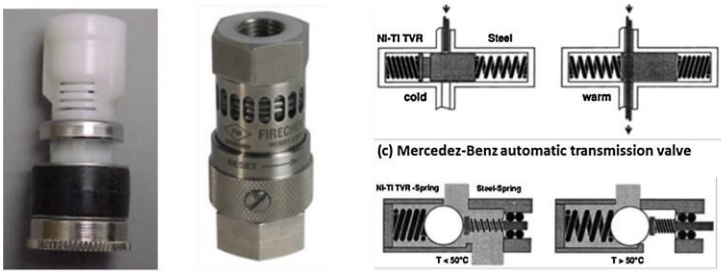

(c) Mercedez-Benz automatic transmission valve

(a) Memrysafe® antiscald valve

(b) Firechek® industrial safety valve

(d) Anti scald valve

Figure 4.31: NiTi thermovariable rate springs applications (Jani JM, 2015).

4.3 Constrained recovery mechanism in SMA: principle and applications

4.3.1 The generation of recovery stress

If the recovery of the austenitic (hot) shape of a material showing SME is prevented during heating above A_s, recovery stresses are generated. A uniaxial case is analyzed in Fig.4.32: the generation of recovery stresses starts from a macroscopic deformation, up to a maximum value ε_t, at a temperature T_d aimed to induce stable detwinned martensitic variants (Fig. 4.32a). ε_{unl} represents the residual inelastic deformation after unloading. During subsequent heating, free recovery occurs due to SME up to a temperature T_c (Fig. 4.32b). The material partially transform back to austenite recovering a deformation equal to the difference between ε_{unl} and ε_c. The recovery of the remaining deformation, the contact strain ε_c, is impeded by an external mechanical obstacle (modeled as infinitely rigid in Fig. 4.32). Therefore, increasing the temperature above T_c, recovery stress is generated (Fig. 4.32c). The latter increases up to a maximum value σ_r occurring in correspondence of the martensite desist temperature M_D.

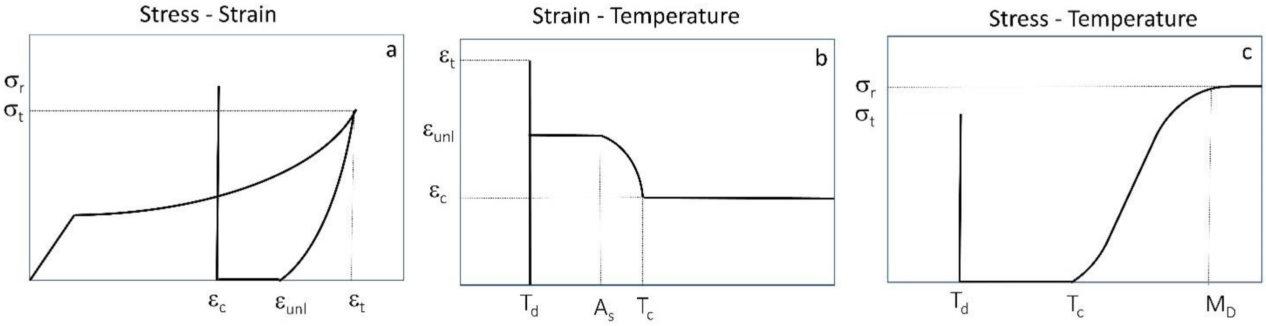

Fig.4.32: Schematic depiction of the uniaxial constrained shape recovery mechanism: the stress-strain relationship (a), strain-temperature relationship (b) and stress-temperature relationship (c).

This shape memory property is the basis of some very successful shape memory applications, e.g. the pipe couplings (Duerig and K.Melton, 1989; Duerig *et al.*, 1990). Nevertheless, the number of studies on this shape memory effect is rather limited (Jackson *et al.*, 1972; Perkins, 1975; Friend, 1986; Duerig *et al.*, 1990; R. Stalmans *et al.*, 1995; Sittner *et al*. 2000). In fact, the scientific understanding of this property is still strictly limited, which can be partly explained by the shortage of reliable experimental results. Furthermore, there are few mathematical models which allows to predict quantitatively the recovery stress generation by means of a limited number of input parameters, (Kosel and Videnic, 2007; Piotrowski *et al.*, 2012; Sittner *et al*. 2000). The recovery stresses typically increase almost linearly with increasing temperature (Stalmans *et al.*, 1995). The average slope of the measured σ-T curve between T_c and M_d (Fig.4.31c) was on specific conditions found close to the well-known Clausius–Clapeyron coefficient (see Eq. 4.1), and some authors even considered the recovery stress measurements as an additional experimental method to determine the characteristic slopes (dσ/dT) for SMA materials (Duerig *et al*., 1990). However, experimentally measured σ-T curve is non-linear in the case of polycrystalline SMAs (Sittner *et al*. 2000). In fact, based on a systematic thermomechanical investigation of Cu–Zn–Al polycrystals, Stalmans (1995) concluded that the dσ/dT slope recorded in recovery stress tests on polycrystalline SMAs is not really a material constant and found that it depends to some extent on the prestrain ε_t, the thermomechanical history, training, etc.

In a very general case, the total strain of a material exhibiting SME, ε_T, can always be subdivided into a transformation component ε_{tr} an elastic component ε_e, a plastic component ε_{pl} and a thermal component ε_{th}.

During constrained recovery, the total strain ε_T is equal to the contact strain ε_c, so:

$$\varepsilon_T = \varepsilon_c = \varepsilon_{tr} + \varepsilon_e + \varepsilon_{th} + \varepsilon_{pl} \tag{4.2}$$

Under the hypothesis of a mechanical obstacle infinitely rigid and with identical thermal expansion coefficient to the shape memory element the quantity $\varepsilon_{ct} = \varepsilon_c - \varepsilon_{th}$ is independent of both temperature and stress, i.e. ε_{ct} is constant during the generation of recovery stresses:

$$\varepsilon_{ct} = \varepsilon_c - \varepsilon_{th} = \varepsilon_{tr} + \varepsilon_e + \varepsilon_{pl} = const. \tag{4.3}$$

From Eq. (4.3) it follows that, during the constrained shape recovery mechanism, a certain amount of detwinned martensite variants transform to austenite (if they are not anymore thermally stable) and therefore the quantity ε_{tr} decreases while $\varepsilon_e + \varepsilon_{pl}$ increases of the same extent.

Consequently, if ε_{ct} is sufficiently high, plastic deformation occurs and ε_{pl} increases during constrained heating. The yield stress of the material, σ_y, is, in that case, an upper limit to σ_r. In general, M_D corresponds to the temperature where the stress to induce martensite (increasing with increasing temperature above M_s due to Clausius-Clapeyron) equals σ_y which decreases with increasing temperature (see section 4.2.7). In fact, recovery stress shows a maximum value, σ_r, at $T = M_D$ (Fig. 4.32c).

Conversely, if ε_{ct} is sufficiently small so that it is within the elastic deformation range of the SMA sample, the latter can retransform completely during constrained heating. The recovery stress obtainable in this case is $E_A * \varepsilon_{ct}$ where E_A is the Young modulus of the austenite. This represents a lower bound limit for σ_r.

In fact, maximum recovery stress, σ_r, in NiTi-based alloys, ranges from about 300 to 900 MPa depending on the alloy and its microstructure (Cross *et al*., 1969; Jackson *et al*., 1972; Such, 1974; Perkins, 1975; Duerig *et al*.,1990; Friend, 1986; Abramov, 2005). Apart from SMA composition and thermo-mechanical history, σ_r depends on ε_c as well as ε_{unl} (which is intrinsically related to ε_t as evident from Fig.4.32). Generally, σ_r, is a non-monotonic function of ε_{unl} (see Fig. 4.33)

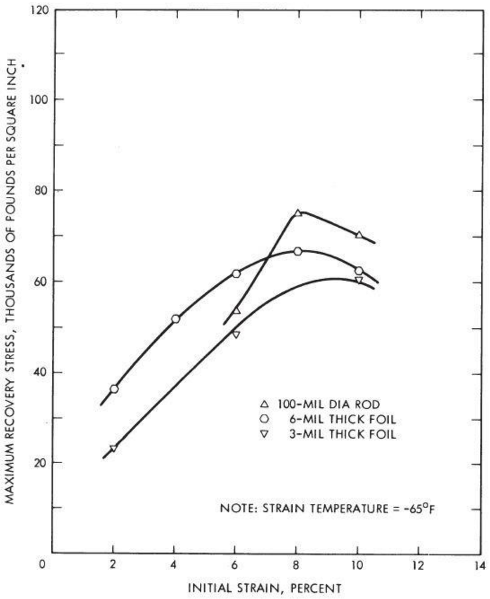

Figure 4.33: maximum recovery stress σ_r for NiTi as a function of ε_{unl} (initial strain) (Cross *et al.*, 1969)

Figure 4.34a shows that recovery stress generally increases with contact strain, $\varepsilon_{C,}$ implying that low contact strains are to be avoided. In fact, the stresses developed during recovery typically fall 10-15% below the isothermally measured austenitic tensile curve (Duerig *et al.*, 1990; Perkins, 1975).

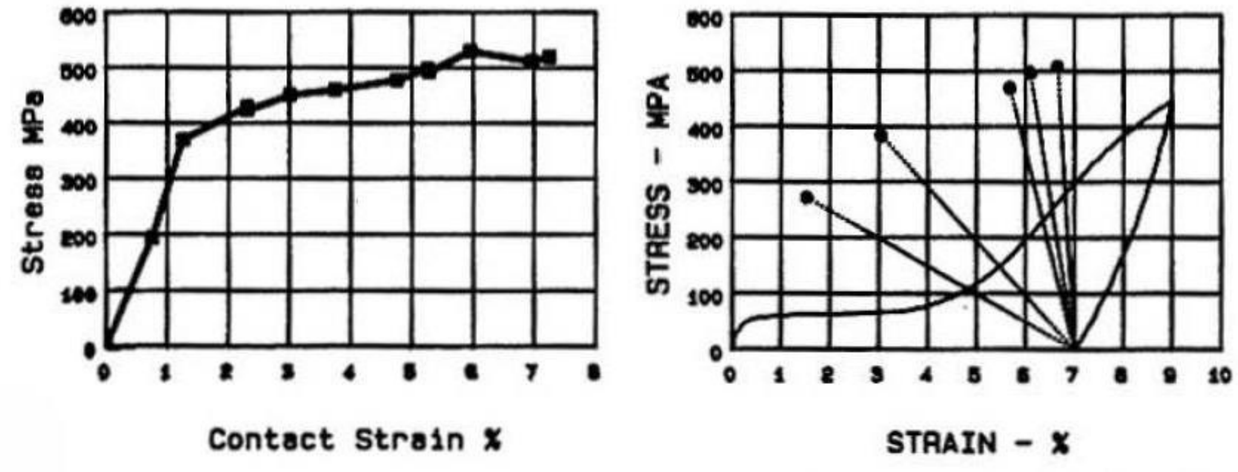

Figure 4.34: (a) maximum recovery stress σ_r for NiTiFe as a function of ε_c (ε_{unl} =7.3%) and (b) maximum recovery stress σ_r for NiTiFe obtained for different substrate compliance (Duerig and Melton, 1989)

All the above considerations relate to SMAs whose recovery is constrained by an absolutely rigid substrate with the same coefficient of thermal expansion as the memory material. In reality, the substrate is subjected to elastic or elastic-plastic deformations. During the constrained recovery process, after heating above $T_{c,}$ the SMA thermomechanical path is controlled by the substrate compliance and by the mismatch between the SMA and the substrate thermal expansion coefficients. As an example, Figure 4.34b shows the recovery stress developed during recovery against different elastic substrates with thermal strains identical to the SMA. The higher the substrate compliance the lower the recovery stress but, comparing Figure 4.34b with Figure 4.34a it is clear that the curve obtained by fitting the recovery stress values for each substrate (Figure 4.34b) has lower values than that obtained for rigid constraint (Figure 4.34a). It is then clear that recovery stress is a path dependent property, not immediately predictable.

4.3.2 Main features of SMA-based constrained recovery applications

Apart from the high recovery stress, one advantage of the SMA are related to their low unloading modulus after recovery which about 1/3 of the steel moduli (Duerig *et al*, 1990). This results in a low susceptibility of the SMA joint to stress decay over a wide range of temperatures and conditions. However, stress relaxation can occur in SMA constrained recovery applications due to overheating (yielding stress decrease with temperature and creep-like mechanisms), or overcooling which may induce martensitic variants (TIM). Regarding the overheating issues, it is important to point out that NiTiFe alloys do not show any creep phenomena at temperatures below 350°C (Duerig *et al*, 1990) and no creep phenomena are observed in austenitic NiTi subjected to 220 MPa stress at 200°C for 1500h (Raj and Noebe, 2013). Once the full recovery stress is reached at M_D (see Fig. 4.32), stress decay during cooling, may occur for several reasons:

- the thermal expansion coefficient mismatch between SMA and substrate alters the final recovery stress by an amount equal to $\Delta\sigma$, which is proportional to $\Delta\varepsilon = -\Delta\alpha\Delta T$ and to the material stiffness, where $\Delta\alpha$ is the SMA/substrate thermal expansion coefficient mismatch and ΔT the temperature decrease equal to the difference between M_D and T, with T indicating the actual temperature.
- When the SMA temperature is lower than the martensite desist temperature ($T< M_D$), SIM can occur by inducing a stress variation according to Clusius Clapeyron $\Delta\sigma = \Delta T\ (d\sigma/dT)$
- The SMA austenitic Young's modulus (unloading) is a function of the total pre-imposed deformation ε_t and the temperature T. A stress decrease $\Delta\sigma$ proportional to ΔE_A may occur by cooling (ΔE_A is the Young's modulus variation with the temperature ΔT).
- The thermally induced R-Phase transition often proceed the martensitic transformation (see section 4.2.9). Although transformational strains not higher than 2% can be achieved, (Dlouhy *et al*., 2004; Peltonen *et al*., 2008) the recovery stress reduction associated with A→R transformation can be significant.
- A strong relaxation occurs by cooling below the martensite start temperature of the alloy, due to the formation of TIM (see section 4.2.2). If a full recovery force is needed in the SMA application, as the SMA is under stress (σ_r), the minimum required operational temperature T_{op} has to be higher than $M_s^{\sigma} = M_s + \sigma_r\ (d\sigma/dT)^{-1}$ due to Clusius Clapeyron relationship (Otzuka and

Waiman, 1998) as well as higher than the R-phase start temperature $R_{S,}$ according with the point listed above.

It is crucial to take into account all these effects when dealing with SMA-based constrained recovery applications. The SMA selection (composition), manufacturing and and thermo-mechanical processes have to be accurately tailored, taking into account the design constraint of each application in order to guarantee proper recovery stress values within the chosen operative thermal range of the SMA-based device.

4.3.3 Classification of SMA constrained recovery applications

SMA constrained recovery applications can be classified as follows:

- **Tube and pipe couplings**: expanded martensitic sleeves are fit around tube or pipe and shrunk by heating to make fast and reliable joints

- **Fasteners**: SMA components which fasten or join together objects or devices different from signal carrying electrical connectors or pipes.

- **Electrical connectors**: devices with very low insertion forces and high extraction forces, compact and suitable for to high pin density connections

In most of constrained recovery applications SMA is used for pipe couplings or generic fasteners. In these two categories SMA is heated above M_D during recovery and is used once. After installation SMA is a structural member of the system and permanent joint are guaranteed in a certain thermal range as discussed in section 4.3.2
In the electrical connection group, multiple applications are required and in fact, SMA is usually not heated above M_D to avoid any degradation in terms of shape memory capabilities of the alloy.

Tube and pipe couplings

The first commercially successful application of SMA was as hydraulic couplings for the Grumman F-14 (Figures 4.35 and 4.36). After more than 1.5 million installations without in-service failures, nearly all new military aircraft have specified NiTi couplings as the only permissible system for joining hydraulic lines. These couplings certainly have been the most successful application of shape memory in the world today. They are a good example of biaxial constrained recovery. The couplings are made by machining a cylinder, usually with circumferential sealing lands on the inner diameter (ID), while the alloy is in the austenitic condition. They are cooled to form martensite, and expanded by means of a tapered mandrel. If the outer diameter (OD) of the inserted tube is intermediate between the as-machined and as-expanded ID of the SMA coupling, then when the coupling is heated above A_s, it recovers, compress the tube and create an excellent joint. Teeth machined on the coupling lD form a metal-Io-metal seal, and a tapered tail coaled with a polymeric compound provides strain relief and the necessary fatigue performance. NiTiFe couplings (Cryofit ®) are expanded in liquid nitrogen and start to contract -100°C, with complete shape recovery at temperatures lower than room temperature, so no heating tools are required. CryoFit's performance were tested successfully in accordance with aerospace industry standards (Van Humbeek, 1999).

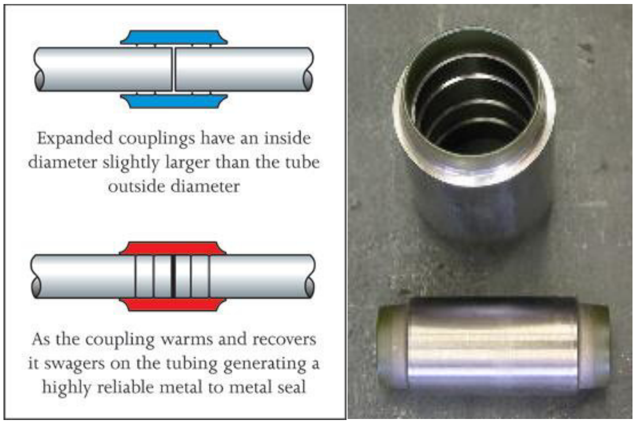

Fig 4.35. Principle of operation of a SMA pipe coupler (http://www.aerofit.com)

Although liquid nitrogen storage and shipping is not an issue for most large aircraft manufacturers, there are applications for which cryogenics are impractical. The NiTiNb wide hysteresis alloy was the result of a focused research effort aimed to obtain a SMA based coupling to be shipped at ambient temperatures in the expanded condition by means of a martensitic stabilization (see section 4.2.11). Liquid nitrogen dewars were no longer required. Unlike NiTiFe alloys, for NiTiNb a heating system is necessary.

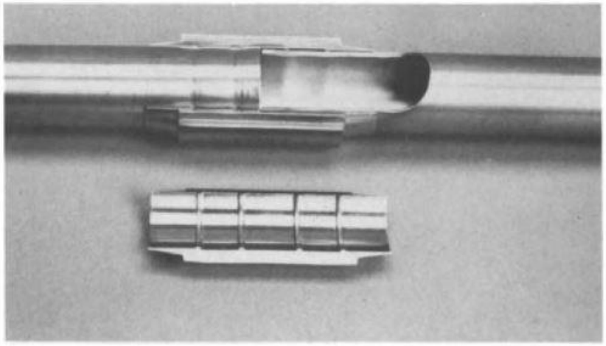

Fig 4.36. A cut away of an installed SMA coupling (Duerig *et al*., 1990)

One of the advantages of NiTi aircraft hydraulic couplings is that they can be installed in difficult to access areas, and the tubing can be placed close together or close to a bulkhead, etc. The use of a heater takes away this advantage and in fact, so far, NiTiNb couplings have only used as repair couplings.

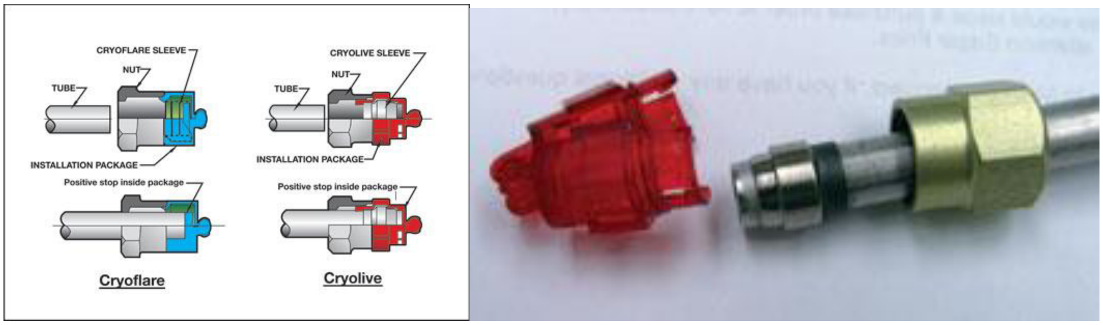

Fig 4.37. Cryoflare ® and Cryolive® couplings (http://www.aerofit.com).

A second development during the last decades was the coupling system named Cryolive® and Cryoflare® fittings. Here the SME is used to install a flareless end fitting, Fig 4.37. The assembly as-shipped includes a plastic cap which acts as an end stop during installation and helps to thermally insulate the SMA allowing comfortable installation time. The tube is inserted into the assembly, the SMA sleeve start to contract by exposing it at ambient temperature, then the plastic cap is removed and the nut screwed onto the connection piece.

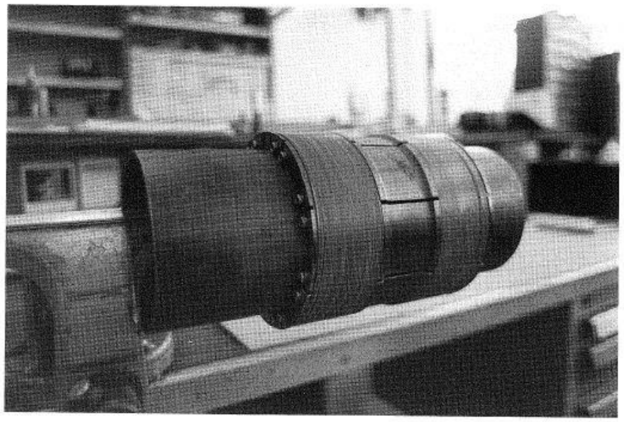

Fig 4.38: Strenght reinforcement of a pipe weld using SMA wire wraps (Otuska and Wayman, 1998)

The sealing arrangement is shown in Fig 4.37. This sleeve is shrunk onto the tube to form a metal to metal seal, and a nut then compresses and seals the external part of the sleeve for creating a joint. Cryolive® (flareless) and CryoFlare ®(flared) end fittings shrink and crimp down on the tube with high radial force, producing a leak proof metal to metal seal between the tube and sleeve.

An interesting recent development is the use of SMA as a reinforcement for of a pipe weld. Prestrained wires of NiTiNb are wrapped around a fitting installed over a pipe weld, Fig 4.38. On heating, the wire contracts and compresses the fixture. This technique can be used either to reinforce the pipe weld, creating compressive stresses to prevent cracking in the welding region.

Fasteners

The term 'fastener' indicates a SMA component which is used to fasten or join together things different from electrical connections or tubes. An example is represented by SMA rings used to join screening braid to adapters, see Fig 4.39a. Originally these rings were machined but the advent of welded rings from NiTiNb alloys has changed their commercial diffusion considerably, although for some applications the weld-bead is unacceptable and machined rings are still used (applications needing very high recovery stress). Fasteners can be installed to precisely locate components with a controlled pre-load, e.g. bearings on a shaft (Fig 4.39) or can provide hermetic seals as represented in Fig 4.40.

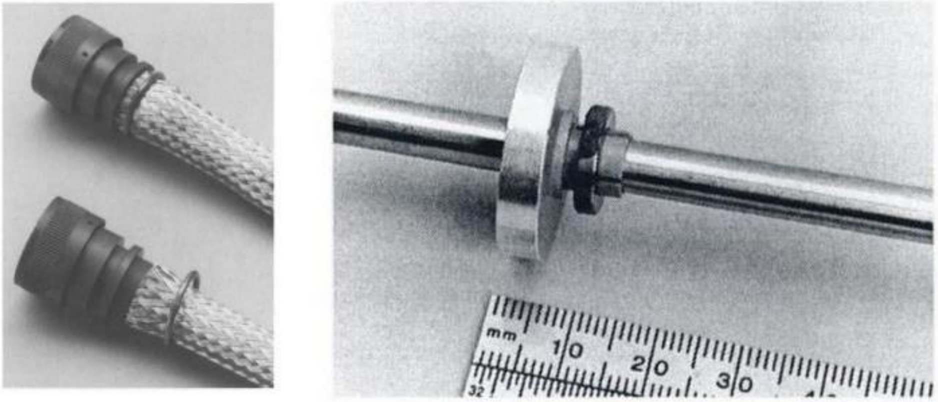

Fig 4.39: (a) A shape memory ring using for fastening the braid against a controlled surface on the adapter and (b) prototype of a gear blank assembled on a shaft using a NiTiNb ring (Otuska and Wayman, 1998).

Sealing thin walled metal cylinders to metal, caeramic or plastic substrates it is quite complex. O rings, sealants, adhesive are often not effective and traditional joining tecqniques such as soldering, welding or brazing are used just for metal to metal seals and often risck of overheating make them impracticable. SMAs offers an alternative sealing technology. In fact, the vacuum leak rates for 3.6 cm diameter aluminium-aluminium couplings, obtained by means of NiTi rings (Fig 4.40) is below 10^{-8} mbar l s^{-1}.

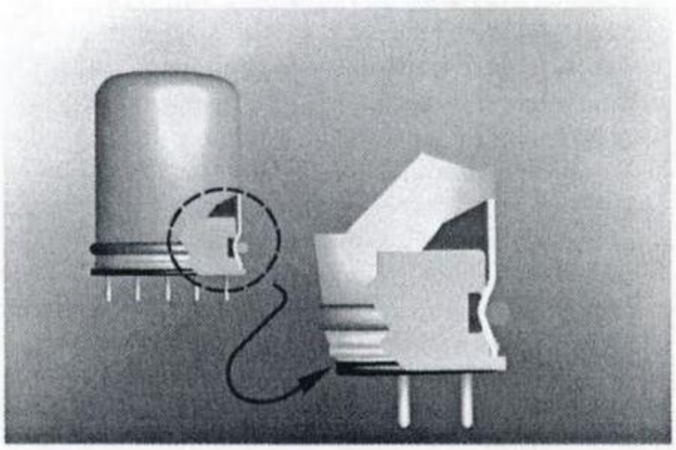

Fig 4.40: Schematic cut-away of a hermetic seal made using a NiTi ring (Otuska and Wayman, 1998).

Electrical connections

Unlike most tube or pipe couplings, electrical connectors have to guarantee several connect/disconnect cycles. This is obtained by exploiting the different mechanical response between the austenitic and martensitic phases, usually in combination with a resetting compliance such as a mechanical spring. In the original Cryocon® connector, Fig 4.41, the slit ends of a Cu-Be tube are open in order to act as a bias spring. An expanded martensitic SMA ring is installed and is ready to recover the contracted austenitic hot shape and bend the extremities (contraction of the mechanical spring). This is illustrated schematically in Fig 4.41a, where mechanical equilibrium is reached at point A (minimum displacement between the extremities) in the austenitic condition and point B (maximum displacement between the extremities) in the martensitic state. On thermal cycling, the stroke B-A is then obtained. This represents the principle of operation of most actuators. If in the open condition B a connector pin is inserted, then on heating the connector will close. In fact, once contact is made with the pin in point C in Fig. Fig 4.41 (b), then further recovery of the SMA ring will elastically compress the pin and the force will increase more rapidly (path C-A). The reverse loading path (A-C-B) will be obtained by cooling the SMA below M_S. For the Cryocon connector, the SMA ring typically has an M_S (under stress) below the lowest operating temperature of the connectors, opening is done by cooling the connector with liquid nitrogen. The Cryocon guarantees very high connection forces; they are shock and vibration resistant. In fact, it can withstand the high inertial forces and dynamic loads acting on missile control systems. The maximum stress in SMA, during operation, has to be lower than the SMA austenitic yield stress otherwise poor cyclic performance are induced.

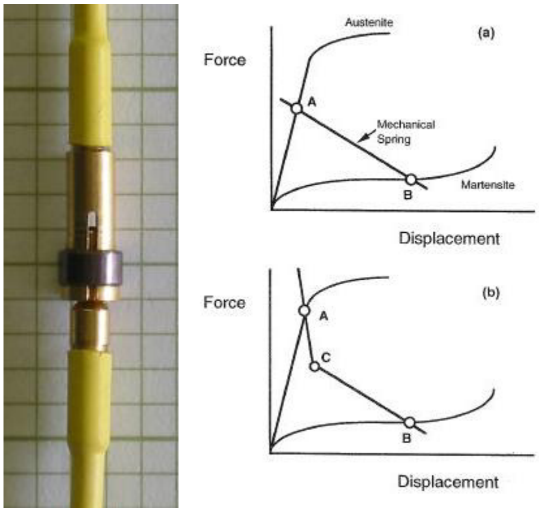

Fig 4.41: Photography of the Cryocon ® connector (www.intrinsicdevices.com) and schematic illustration of the force-displacement relation between an SMA element and a mechanical spring. In (a) the system displaces between points A and B on thermal cycling. In (b) on heating, contact is made with the pin at point C, the line CA represent the stiffer compliance of the pin (Otuska and Wayman, 1998).

In Cryocon® connectors SMA rings contracts the austenitic condition. This configuration generally results in the highest contact force, using the higher strength of the austenite. However, it is also possible to use the SMA/spring combination in reverse, such that on heating, the SMA displaces against the spring storing energy in it. On subsequent cooling, this stored energy is used both to make the electrical contact and to re-deform the SMA component. In this case the SMA has an M_s temperature

typically above room temperature, and installation can be done for example by electrically heating the SMA. An example of this kind of connector is shown in Fig. Fig.4.42.

High M_s type connector offers the convenience of ease of installation but a significantly of lower contact

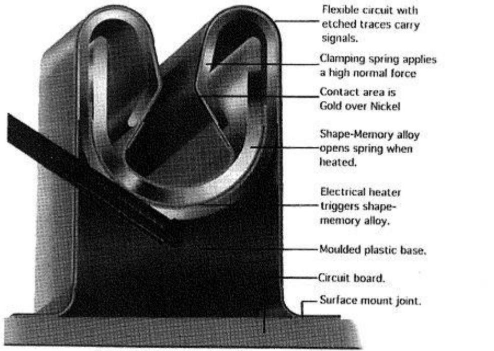

Fig. 10.5. The Betaflex™ electrical connector. (Photograph courtesy of Beta Phase Inc., Menlo Park, CA)

Fig.4.42: The Betaflex™electrical connector (Photography courtesy of Beta Phase Inc., Menlo Park, CA)

forces. Several SMA connectors are used in parallel in the DIP connector, which consist of multiple line of Cryotact® contact (Fig.4.43a). It was designed for interconnect Dual-in-line packages to circuits boards. The SMA drivers are now stamped reducing the cost per line (Fig.4.43b). The Cryotact design limits the SMA overstress and high pin tolerances are allowed so that industrial pin can be used. Nevertheless, the cost-performance ratio of this new connector did not allow a widespread commercial use.

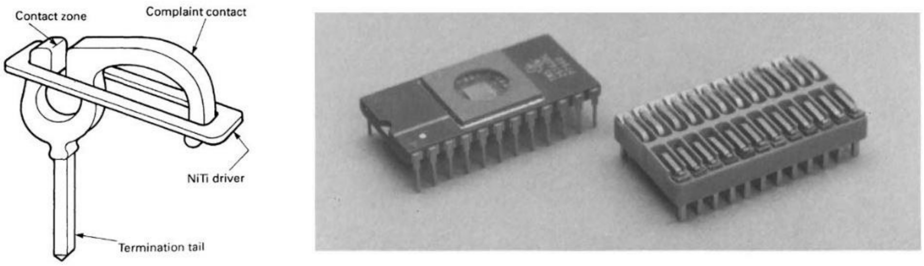

Figure.4.43: The Cryotact contact assembly (a) and the DIP connector assembly (b) (Duerig *et al*., 1990)

4.3.4 Advantages of SMA couplers and fasteners

SMAs have unique properties that give several advantages over conventional fastening techniques (Duerig *et al*., 1990; Van Humbeek, 1999). A brief list of the advantages and disadvantages is here reported:

Main advantages:

- *Large tolerances in joining parts*: large recovery strains are exploited in SMA fasteners and they can accommodate large tolerances on mating parts. Shape memory strains are at least one order of magnitude larger than the elastic or thermal strains exploited in conventional joining technologies. The looser tolerances lead to cheaper and more reproducible part to be assembled.
- *Uniform radial pressure*: if compared with multipoint crimping, split clamps, hose clamps the stress applied by a SMA ring is much more uniform because the SME occur throughout the material and the clamping pressure is homogenously distributed along the contact area
- *High elastic interference*: thanks to the low elastic modulus and the high recovery stress, installed SMA rings have significant elastic interference with their substrates and therefore they are particularly resistant to thermal variations (within the operative thermal range) and vibrations. A 0.05% decrease in the effective diameter of the substrate would decrease the stress in a conventional steel ring by 40% while just 7% in NiTi-based couplings
- *Low installation temperatures*: most of the SMA fasteners can be installed from cryogenic temperature (exploiting the natural heating for the shape recovery) to 150°C-200°C. This

represents a significant advantage if compared with traditional permanent joining techniques such as brazing or welding.

- *Operation insensitive installation*: the fasteners have to be just positioned and then heated up to the installation temperature to get full recovery stress.
- *Lightweight and compactness*: the use of alloys with high *recovery* stress results in thin-walled SMA structures that helps to achieve very compact design. In addition, the lower density of titanium and of the intrinsic sensor/actuator function of the SMAs results in further weight reduction.
- *Reliability*: NiTi-SMA fastener provide a highly reliable joint for demanding applications. In fact, over 300000 couplings are put in service. Shape memory alloys have been used to produce fasteners and seals for over 40 years without any operational losses, SMA couplings have an excellent track record.

Main disadvantages:

- *Limited operating thermal range*: The operating temperatures in SMA fasteners range from about -90°C to over 300°C. The lower bound is represented by the martensitic transformation and subsequent relaxation. The upper bound is represented conventional creep-like phenomena and ageing influence on the functional properties of SMAs.
- *Cost*: NiTi-SMA couplings provide a highly reliable joint for demanding applications such as aerospace and defense, but their relatively high cost has been a barrier to more widespread commercial use. Cu-based and more recently Fe-based couplings are cheaper, but because of the lower recovery force of these alloys, they result in a lower performance system. To date, all the fastener successes of SMA have been in higher performance niche markets.

4.3.5 Commercial SMA couplers and fasteners

Nowadays there are some commercial fasteners available in the market even if there is a very limited number of companies in the field. Intrinsic Devices, Inc. (www.intrinsicdevices.com) specializes in the manufacture of NiTi-based shape memory alloy products used for fastening, sealing and electrical interconnection. They produce a family of standard heat shrinkable metal rings under the name UniLok®. Other products include tensioning rods, expanding rings, and expanding plugs and pins. Intrinsic's fasteners are ready to contract (or expand) due to SME. The positioning of the part and its heating above the specified temperature is enough for their installation. UniLok is a family of nickel-titanium shape memory alloy rings used for permanent (OW-SME) and semi-permanent (TW-SME or OW-SME with resetting force) fastening, sealing, and electrical interconnection. The rings shrink in diameter when heated, producing a uniform radial clamping pressure. The maximal recovery stress value of the SMA material is provided by the manufacturer (Intrinsic Devices Inc.) is around 200 MPa. A well-known expression (www.intrinsicdevices.com; Popov, 1998; Duerig *et al*., 1990) used for axisymmetric solids having perfectly plastic behavior, can be applied for estimating the clamping pressure that the SMA ring can generate after the constrained recovery process: Pa = 200 ln(D/d) where Pa is the contact pressure between the SMA ring and the substrate while *d* and *D* are the inner and outer diameter of the SMA ring, respectively. Of course, the formula gives very rough values. The actual SMA recovery stress (and clamping pressure) in a certain assembly, as already discussed, strongly depend on the thermomechanical history of the coupling and the physical and mechanical properties of the substrate (see section 4.3.1 and 4.3.2); therefore, is extremely complex to be predicted. The price for the SMA rings provided by Intrinsic varies considerably with their dimension and functional capabilities (and quantity). It ranges from about 70 $ for small and thin rings (internal diameter of about 20mm, 1mm thick and 3mm of axial length) and up to more than 1000$ for rings of about 45mm of internal diameter and 8 mm of wall thickness. Commercial permanent couplers and fittings are provided by Aerofit as well (http://www.aerofit.com). Saes Group major industrial applications are in the automotive and aerospace sectors. SAES develops sealing plugs, locking rings, actuators and connectors for electronic and safety devices (http://www.memry.com/). Airdrome is another company (http://www.airdrome.com/) specialized in SMA tube fitting devices.

4.3.6 Recent developments in SMA couplings

NiTi-based coupling devices attracted noticeable interest for applications in the field of nuclear engineering. The shape memory couplings were thought to be convenient for remote-control operation in replacing structural components of reactors. First proposals for the use of SMAs to simplify maintenance operations for fusion reactor components have been made few decades ago (Nishikawa *et al*., 1986; Nishikawa *et al*., 1989; Besseghini *et al.*, 1996; Tuissi *et al*., 1998). SMA-based seals were studied to connect the Cassette Compact Toroid Reactor (CCTR) plasma container to a divertor (Nishikawa, 1986). It has been proved that the stress generated by the constrained recovery of a shape memory sleeve can be used to deform soft metal seals in order to obtain vacuum tight (leak rate < 10^{-9} mbar l s^{-1}) connections (Nishikawa *et al*., 1989; Besseghini *et al.*, 1996; Tuissi *et al*., 1998) even after subsequent thermal cycles (Besseghini *et al.*, 1996; Tuissi *et al*., 1998). These development activities were followed by investigations of the effects of neutron irradiation on the mechanical properties of SMAs. Preliminary tests showed that the transformation temperatures of NiTi alloy shifts to lower temperatures (Matsukawa *et al.*, 1999) and a 30% reduction in reversible strain was found in NiTi alloys after being irradiated with a fast neutron fluence (E > 1 MeV) of about 10^{25} m^{-2} (Hoshiya *et al.,* 1998) while TiPdCr alloys showed higher radiation resistance if compared with NiTi (Hoshiya *et al.*, 1996). However, annealing temperatures above 523 K after the irradiation seems to restore the original conditions (Hoshiya *et al.,*1998). The changes in the transformation behavior and in the mechanical properties were thought to be due to the modifications in local lattice structure. SMAs have been used as part of a retrofit joint restraint, used to strengthen suspect welded pipe joints in fission power plants (Kornfeldt *et al.*, 1997).

SMA couplings are being developing in aerospace, in particular in satellite instrumentations and devices. In particular, the Tropospheric Emission Spectrometer (TES) is an instrument payload that will fly on the Aura spacecraft as part of the Earth Orbiting Satellite (EOS) program to study and measure global ozone distribution. Shape Memory Alloys (SMAs) are employed to relieve stresses in the 100 kg TES optical bench after launch. The SMA passively releases the non-kinematically-mounted optical bench when cooled to its operating temperature of 180K and automatically reclamps the bench to regain full bolt preload when warm. This allows the bench to be unstressed during operation, safely survive launch loads and negates the need for manual intervention at the joint interface after every thermal test cycles (Rosing *et al*., 2005). Most NASA missions require the use of a launch lock for securing moving components during the launch or securing the payload before release. NASA is exploring the development of a novel launch lock mechanism that is activated by a SMA ring, a rigid element and an SMA ring holding flexure (Badescu *et al*., 2014). The traditional collet-chuck mechanism for tool clamping is a significant source of errors in spindles due to stack-up tolerances. This, in turn, adversely affects the tool's error motions particularly in demanding micro-cutting operations performed with ultra-high-speed miniaturized spindles. Hence, novel thought for miniature tool clamping is needed to minimize tool run-out and error motions in order to meet the necessary cutting speeds and accuracy requirements. Shape Memory Alloy (SMA) based solutions for the clamping of miniature tools are being explored (Malukhin *et al*., 2011). About the medical applications, it is worth mentioning that a novel annuloplasty ring with a shape memory alloy core has been developed to facilitate minimally invasive mitral valve repair (Purser *et al*. ,2011).

Furthermore, wide hysteresis NiTiNb alloys (section 4.2.11) are becoming more and more attractive for fastener and clamping systems (Duerig and Melton, 1989b, Borden, 1991, Li *et al*., 2015, Choi *et al*. 2013, Ozbulut *et al*., 2015; Uchida *et al*. 2007; Yamamoto *et al*. ,2008; Ying *et al*. 2015; Tabesh *et al*. 2012; Videnic *et al*. 2008; Piotrowski *et al*. 2012; Malukhin *et al*. 2012). Despite their importance for industry, NiTiNb SMA has attracted very little attention in research works. Different studies have been carried out to assess the possible use of NiTiNb rings as pipe couplers (Yamamoto *et al*., 2008; Ying *et al*., 2005); Tabesh *et al*. 2012; Videnic *et al*. 2008; Piotrowski *et al*., 2012) and few numerical (Tabesh *et al*. 2012; Piotrowski *et al*., 2012) and analytical (Videnic *et al*. 2008) models of the constrained recovery of SMA rings have been proposed recently.

5. SMA-based beam-pipe connectors: SMA characterization, design and experimental methods

5.1 Introduction.

The concept of the SMA-based beam pipe connector is based on a Two-Way memory alloy ring. The commercial and non-commercial SMA rings which were selected and investigated are already pre-strained and they are ready to contract due to the SME. The SMA sleeve would be installed at room temperature in martensitic state around the chamber extremities and then heated up to induce its contracted austenitic shape and shrink it onto the steel chambers (OW-SME), assuring the leak tightness of the connection (leak rate $<10^{-10}$ mbar l s^{-1}), by means of a soft sealing element (coating or gasket). The thermal hysteresis is exploited in order to have a full clamping force (and a leak tight joint) at room temperature. The dismounting would be obtained re-inducing the martensitic structures by cooling the sleeve in order to activate the TW-SME mechanism associated with a re-expansion of the ring.

Even though SMA ready-to-use connectors are available (see. Section 4.3.5), no design and selection criteria have been developed yet. As a consequence, *ad-hoc* experimental and numerical methods are needed, especially when dealing with reliability and safety issues in radioactive environment. Furthermore, so far, the functional performance of SMA-based couplers in UHV systems of particle accelerators has not yet been investigated and proper design tool and experimental assessments criteria need to be developed to comply with very strict CERN requirements (see section 5.2).

Within this framework, the use of SMA rings as beam-pipe coupling elements for future applications in high-energy particle accelerators was investigated. Two SMA compositions, NiTiNb and NiTi alloys, were properly selected. The tightening performance of SMA rings was assessed by extensometer tests, strain gauge measurements and Digital Image Correlation (DIC), as well as by Finite Element (FE) simulations. Following these studies, a UHV beam-pipe detachable connection was proposed and experimentally validated.

The proposed prototype coupling system consists of a SMA ring, two steel chambers to be joined, and a sealing element to be placed at the SMA-steel interface i.e. a copper coating or a thin cylindrical aluminum/copper gasket to be mounted onto the chamber extremities. A novel vacuum performance parameter was defined based on the sealing model described in section 3.5.2 and the

FE results, and different coupling configurations were studied for the optimization of the contact interface. Experiments on selected coupling configurations were carried out to evaluate the leak tightness of the connections.

Furthermore, as the SMA based beam pipe couplers are planned to be used mostly in restricted access area of particle accelerators, the material response in a radioactive environment needed to be verified. As a consequence, numerical and experimental studies were carried out to analyze the structural and functional damage induced by proton/neutron irradiation using the CHARM (Cern High energy AcceleRator Mixed field) facility at CERN.

The SMAs selection and characterization as well as all the design and experimental assessment methods for the proposed beam-pipe SMA connectors are described in this chapter.

5.2 Material selection

In view of the HL-LHC upgrade (Bruning and Rossi, 2015) the mounting and dismounting time of the SMA connectors need to be reduced as much as possible in order to limit the radiation exposure of the operators and to simplify the maintenance activities (see chapter 1). Baking collars can be used for the SMA coupler installation which, in fact, is extremely easy and fast, consisting just in the positioning of the gasket, SMA and the heating collar onto the vacuum chamber extremities. The dismounting, instead, is a more critical operation and need to be performed by means of liquid nitrogen or, generally, by cooling elements which have to be put in contact with the SMA connector (e.g. cooling collars). The higher the dismounting temperature (and the martensitic TT) of the SMA coupler, the lower the dismounting time and the radiation load absorbed by the operators in the surroundings.

However, some temperature constraints need to be addressed in SMA coupling technology. In fact, thermo-mechanical stability under a wide temperature range is usually required (see sections 4.3.2 and 4.3.3) in some critical applications, such those in particle accelerators; In these applications, TIM should be avoided during service and OW-SME and TW-SME should be exploited for a limited number of activation cycles, *i.e.* for occasional mounting/dismounting operations. For these reasons, different studies have been carried out to assess the possible use of NiTiNb rings as pipe couplers (see section 4.3.6). The wide thermal hysteresis of NiTiNb alloys (more than 100°C) enhances the reliability of the SMA coupler and simplify the SMA selection process. In fact, NiTiNb-based couplers can guarantee a full clamping force over a wide thermal range. The only limitation of such couplings is related to the low dismounting temperature (≈-120°C) which is intrinsically related to the martensitic TT of NiTiNb alloys.

On the contrary, binary NiTi alloys have higher martensitic TT and lower thermal hysteresis (A_s-M_f) than ternary NiTiNb ones; unfortunately, this implies a lower thermal range with full clamping force but also a faster disconnection owing to higher dismounting temperatures. It is therefore clear that, the material selection, in case of NiTi alloys, becomes a critical task.

Figure 5.1 illustrates a depiction of the temperature constraints for UHV beam-pipe coupling in particle accelerators. The figure also shows a schematic comparison between the thermal-induced transformations of wide and narrow hysteresis alloys, such as the ternary NiTiNb (see section 4.2.11) and the binary NiTi systems, respectively. A temperature range is identified, between the T_{op} and T_M ($T_{op}<T<T_M$), where the alloy must exhibit a stable microstructural response, *i.e.* it does not undergo phase transition phenomena. In particular, T_{op}, namely operative temperature, is the service temperature (about room temperature) of the coupling in the particle accelerator while T_M, namely mounting temperature, represents the maximum temperature achievable for the mounting operations. In fact, the austenite start temperature of the alloy (A_{s1}), at which ring contraction starts during heating, must be sufficiently higher than the mounting temperature T_M to prevent any possible accidental activation and, consequently, to simplify the stocking and mounting operations.

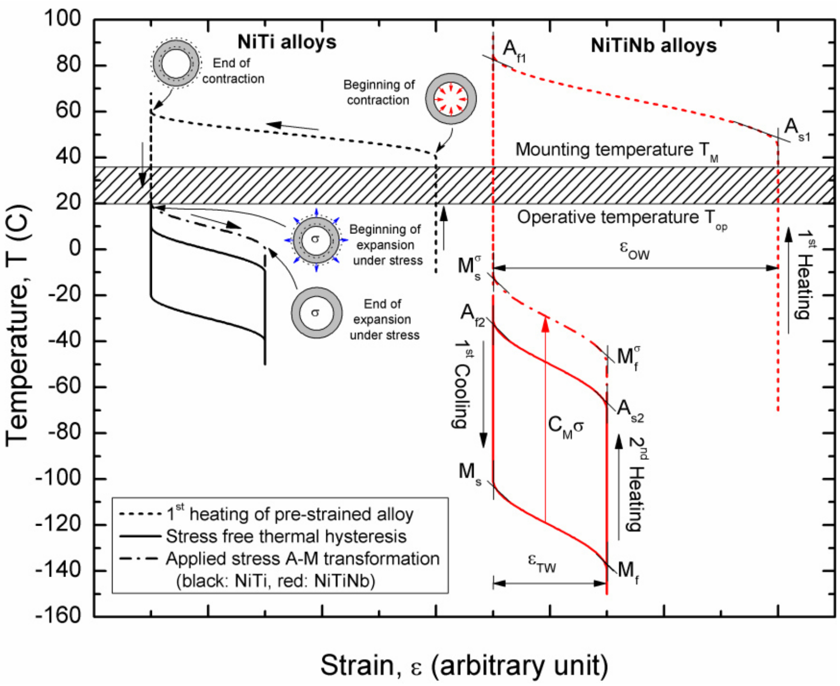

Figure 5.1: Temperature constraints for beam-pipe coupling in particle accelerators and schematic comparison of the thermal hysteresis between NiTi and NiTiNb alloys.

For this reason, T_M is around the human body temperature (T_M>37 °C). On the other hand, the operative temperature T_{op}, *i.e.* the temperature at which the connection works in particle accelerators (around 20 °C), must be higher than the martensite start temperature (under stress), M_s^{σ},, at which ring enlargement/dismounting starts during cooling (see section 4.3.2). This is to prevent possible contact pressure decrease, which could affect the leak tightness of the coupling.

As well know (see section 4.3.2) martensite start temperature M_s^{σ},, is higher than that of the base material in stress free conditions ($M^{\sigma}_s > M_s$), due to the Clausius-Clapeyron relation (eq. 4.1). This temperature shift is schematically shown in Fig. 5.1 by the dash-dot curves. The conditions $M_s^{\sigma} < T_{op}$ and $T_M < A_{s1}$ suggest the transformation temperatures required, which are the main functional parameter of the selected alloys. However, it is worth pointing out the actual recovery stress, and consequently M_s^{σ}, is very difficult to predict and strongly dependent on the alloy thermo-mechanical history and loading conditions as well as the SMA geometry and the properties of the mechanical obstacle preventing the recovery (see section 4.3). Furthermore, the clamping pressure which is related to the recovery capabilities of the SMA ring and affected by the sealing material and geometry, is not the only parameter having an influence on the leak tightness performance of the joint; in fact, the surface roughness of the mating parts and both the gasket geometry and material play a crucial role on the sealing capabilities of the connection (see chapter 3). However, it is evident that SMA relaxations need to be limited in correspondence of T_{op}, therefore the temperature range (T_{op}-T_M) must be within the thermal hysteresis of the material. As a consequence, the wider the thermal hysteresis, the better the mechanical stability of the SMA connection. This is the main reason why wide hysteresis SMAs are commonly used for connection devices, such as the ternary NiTiNb system (see section 4.2.11). However, as schematically shown in Fig. 5.1, thermal hysteresis width of SMAs can be increased by proper thermomechanical training procedures which raise the austenite transformation temperatures, namely A_{s1} and A_{f1}, for the first thermally induced transformation (http://intrinsicdevices.com/)

Owing to the shift of the austenite TTs, both ternary NiTiNb and binary NiTi alloys could be used, as schematically shown in Fig. 5.1. It is worth pointing out that thermal hysteresis of NiTi is much narrow than that of NiTiNb and, consequently, the material selection and thermo-mechanical processing represent very critical tasks of the design process. In fact, accurate tuning of several parameter must be carried out to obtain a stable response of the alloy in the T_{op}-T_M range, including alloy composition and thermo-mechanical treatments. On the other hand, NiTi alloys provide significant advantages with respect to NiTiNb ones. In fact, binary NiTi SMAs allow dismounting at higher temperatures (around -50 °C for NiTi and -150 °C for NiTiNb), thanks to the higher martensite TTs. This leads to significant simplifications of the maintenance operations and increase in personnel safety. Moreover, NiTi alloys have higher commercial availability and, generally, lower cost.

Based on the constraints described above, the studies and the design of the SMA-based UHV connectors started with the Ni48Ti38Nb14 (wt.%) (Type H, Intrinsic Devices Inc., USA) alloys and finally focused on non-commercial Ni55Ti45 (wt.%) rings. The investigated rings are properly trained to exhibit two-way behavior (see section 4.2.5) as illustrated in Fig.5.1. NiTi rings were *ad-hoc* developed by Intrinsic Devices Inc., based on CERN technical constraints, and allow to get benefits from the higher martensitic TTs of NiTi alloys with respect to NiTiNb ones, as discussed above.

5.3 SMA ring-Steel pipe coupling process

Figure 5.2 shows the main mechanisms associated with the coupling process between a SMA ring and vacuum pipes. The generic process consists of the following steps:

1. **Mechanical pre-strain and training**: as-manufactured SMA ring is properly pre-strained to give OW-SME and TW-SME capabilities.
2. **Coupling assembly**: at a temperature $T \leq T_M$ (see Fig.5.1) the ring-pipe system is assembled with an initial assembly clearance ΔD. The clearance is the gap between the initial internal diameter of the SMA ring (ready to contract by heating) and the external diameter of the pipe;
3. **Thermal activation:** The SMA ring is heated above the austenite finish temperature of the pre-strained material ($T>A_f$) to activate OW-SME and then cooled down to the operative temperature (T_{op}). This occurs in four subsequent steps: 3.1) beginning of OW recovery at $T= A_s$; 3.2) ring-pipe contact at $T=T_c$, corresponding to the full recovery of the initial assembly clearance ΔD; 3.3) complete activation at T_{max}=200 °C (simulating a possible bakeout process) in order to induce a fully austenitic structure in the loaded ring ($T_{max}>A_f^{\sigma}$) as well as obtaining the maximum contact pressure (P_{max}); 3.4) cooling down to $T=T_{op}$, giving the final contact pressure of the assembly (P_{op}).

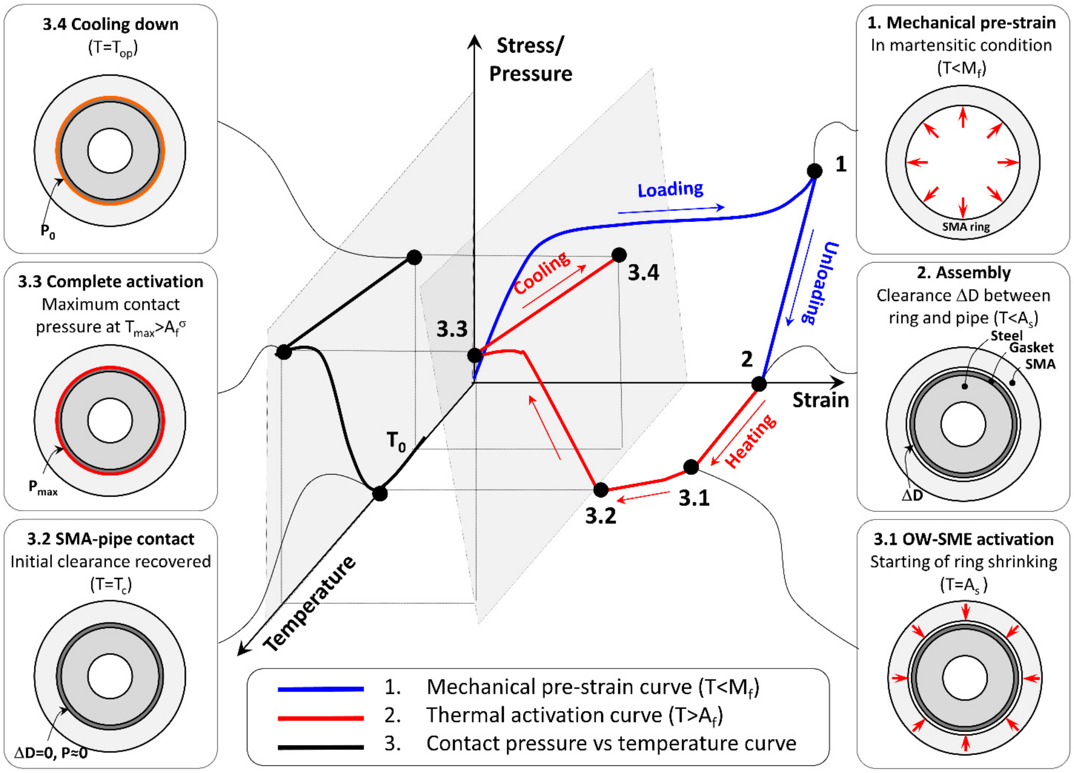

Figure 5.2: Schematic depiction of the SMA ring-pipe coupling mechanisms

Thermal dismounting was also analyzed by cooling down the assembly to $T<M_f$, thanks to the TW-SME, which causes a diameter expansion of the SMA ring.

5.4 SMA thermo-mechanical characterization methods

Semi-finished material, subjected to pre-strain in martensitic conditions, have been analyzed. The investigated rings and rods show both the OW and the TW Shape Memory Effects (see Fig 5.1). In particular, OW-SME represents the stress-free thermal recovery strain obtained from the first heating above the austenite finish temperature ($T>A_{f1}$). TW-SME represents the amount of reversible recovery deformation observed during subsequent thermal cycles between martensite and austenite finish temperatures.

The main thermo-mechanical properties of the alloy were measured by thermal cycles and tensile tests of SMA rods (3.2 mm diameter). The tests were carried out by using a universal testing machine (Instron E10000, USA), equipped with a climatic chamber (-170°C/+350°C). Strains were measured by an extensometer (accuracy class 0.5 ISO) with a gauge length of 10 mm and with wide operative temperature range (-265 °C/+200 °C). The same transducer was mounted on the internal diameter of the pre-strained SMA rings to measure the diameter variations under free thermal recovery (Fig 5.3). The free recovery capabilities of the pre-strained SMA rings were studied, in terms of both OW-SME and TW-SME, for subsequent thermal cycles. The thermal strains of the mounting elements were taken into account in the measurement of the ring diameter variation. The temperature was measured by a k-type thermocouple glued onto the specimen surface. The results of the free-recovery extensometer tests on SMA rings are reported in chapter 6 and 7.

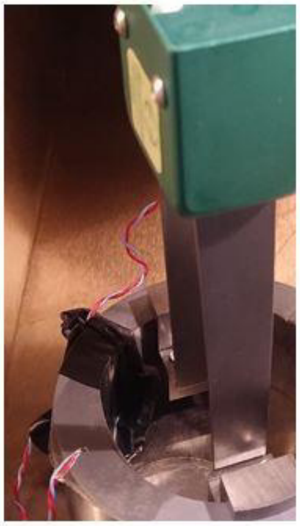

Figure 5.3: Instrumented SMA ring

Figure 5.4.a shows the curve true strain *vs* temperature (ε-T) obtained from the first stress-free heating stage ($\dot{T}$=3*10^{-2} °C*s^{-1}) above the austenite finish temperature of the pre-strained NiTiNb rods ($T>A_{f1}$), giving the OW-SME. Furthermore, TW-SME obtained from a subsequent thermal cycle between the TTs ($T<M_f$ and $T>A_{f2}$) is also shown. As expected (Duerig and Melton, 1989; Zhao *et al.*, 2006; Zhang *et al.*, 1990; Kusagawa *et al.*, 2001; Piao *et al.*, 1992) a marked reduction (more than 100 °C) of the austenite transformation temperatures (A_{s2} and A_{f2}) after the first thermal activation was observed.

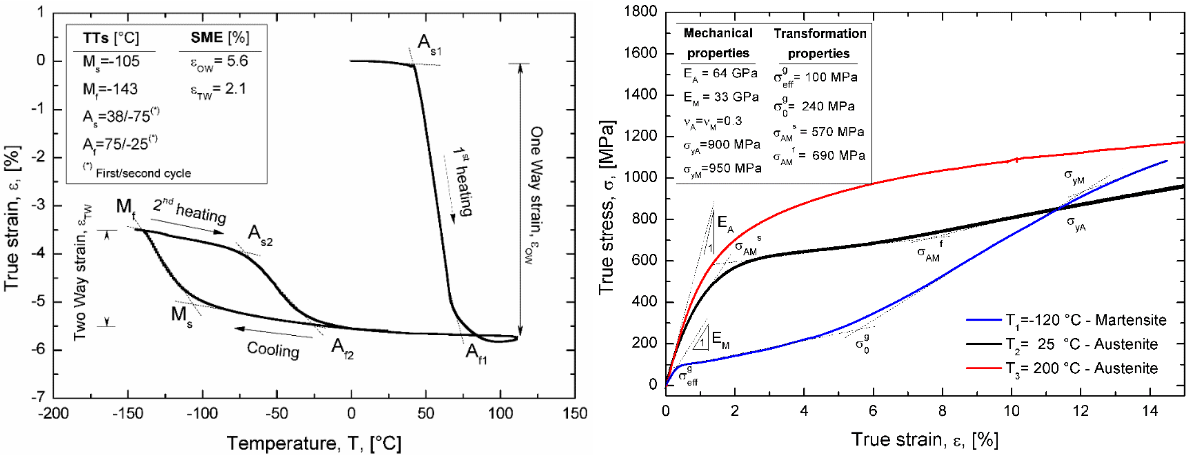

Figure 5.4: Thermo-mechanical properties of the investigated Ni48Ti38Nb14 (wt.%) alloy: a) true strain vs temperature (ε-T) obtained from a stress-free thermal cycle between the TTs and b) Isothermal uniaxial true stress *vs* true strain response (σ-ε) for three different values of the testing temperature.

Figure 5.4.b illustrates the isothermal true stress-true strain (σ–ε) response of the NiTiNb alloy ($\dot{\varepsilon}$=5*10^{-4} s^{-1}) at three different temperatures: T_1=-120 °C, T_2= 25 °C and T_3=200 °C. As shown in Fig.5.4a, the temperature T_1 corresponds to fully martensitic condition (the rod was previously cooled down to M_f) while T_2 and T_3 define fully austenitic conditions. However, the alloy exhibits a pseudoelastic response at $T=T_2$ and an elastic plastic behavior at $T=T_3$, *i.e.* with no evidence of stress-induced transformation (see Fig.5.4b). This denotes that T_3 is higher than the martensite desist temperature ($T_3>M_D$). The parameters identified in Fig.5.4 were used for calibrating the SMA constitutive model described in section 5.5.2

5.4.1 Strain gauge measurements

Figure 5.5 illustrates geometry and dimensions of the analyzed SMA rings (Fig. 5.5.a), together with a schematic depiction of the SMA-steel ring assembly (Fig. 5.5.b) used for strain measurements. The latter were aimed to the contact pressure estimation during the SMA clamping process (see section 5.3). The geometry of SMA rings was chosen among those commercially available based on CERN geometrical constraint (external pipe diameter of about 45 mm) and a qualitative estimation of the contact pressure after thermal activation (see section 4.3.5). Strains were measured by x-y electrical strain gauges (XC11, HBM), with wide operative temperature range (-200 °C/+250 °C). A photography of an instrumented steel ring is shown in Fig.5.6. Temperature was measured by a k-type thermocouple. Two strain gauges were glued (epoxy resin, EP310S, HBM) at the internal diameter of the steel ring with a relative angle of 120 °C (see Fig. 5.5.b).

A quarter-bridge configuration was adopted for strain measurements. As well known, this configuration gives an apparent strain during temperature change, namely thermal output. This apparent strain signal, was preliminary measured by stress-free thermal tests between -170°C and 200°C. The measured thermal output was subtracted from the strain signals obtained from the SMA-steel coupling.

The gauge factor variation with temperature was also taken into account. The average signal among the two SGs was considered, but differences between them were never greater than 5%. As shown in Fig. 5.5.b, steel rings with three different values of the outer diameters were manufactured in order to analyze the effects of the initial assembly clearance (*ΔD* in Fig. 5.5) on the contact pressure, as well as to assess the mounting/dismounting features. Furthermore, the wall thickness of the steel ring was chosen with the aim of maximizing the strain measurements sensitivity as well as to avoid yielding during thermal activation.

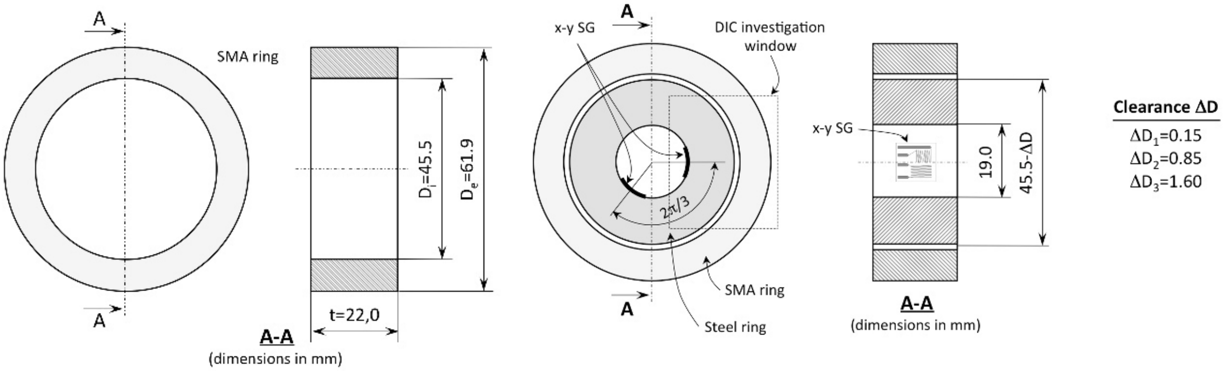

Figure 5.5: Schematic depiction of the coupling assembly: a) SMA Ring and b) SMA-Steel coupling with strain gauge location.

The contact pressure at the interface *P* was calculated, based on the theory of elasticity, by the measured circumferential and axial strain components (ε_θ and ε_z) at the inner diameter of the steel ring:

$$P = -\frac{E}{2(1+\nu)}\frac{D_e^2-D_i^2}{D_e^2}(\varepsilon_\theta - \varepsilon_z) \tag{5.1}$$

Where *E* and *ν* are the Young's modulus and the Poisson's ratio, while D_e and D_i are the external and internal diameters of the steel ring.

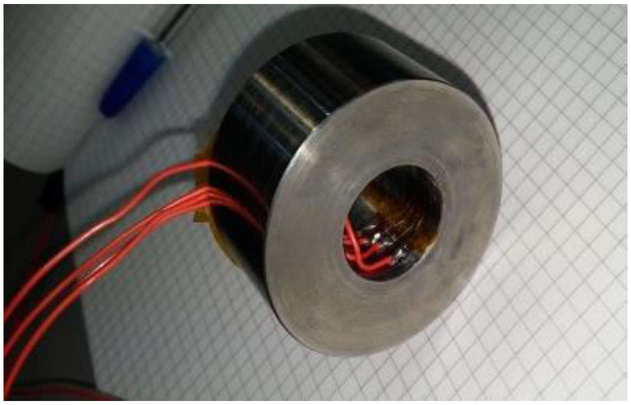

Figure 5.6: Instrumented steel ring

5.4.2 Digital Image Correlation measurements

Overview

The DIC method is a non-interferometric optical technique and has been widely accepted and commonly used as a powerful and flexible tool for the surface deformation measurement in the field of experimental solid mechanics. It directly provides full-field displacements and strains by comparing the digital images of the specimen surface in the un-deformed (or reference) and deformed states respectively. During the past few years, the DIC method has been extensively investigated and significantly improved to reduce computation complexity, achieving high accuracy deformation measurement and expanding application range. For example, the two-dimensional (2D) DIC method using a single fixed camera is limited to in-plane deformation measurement of the planar object surface. If the test object has a curved surface, or three-dimensional (3D) deformations need to be captured, the 2D DIC method is no longer applicable. To overcome this disadvantage of 2D DIC, 3D DIC based on the principle of binocular stereovision was developed.

Two-Dimensional DIC

In general, the implementation of the 2D DIC method comprises the following three consecutive steps, namely (1) specimen and experimental preparations; (2) recording images of the planar specimen surface before and after loading; (3) processing the acquired images using a computer program to obtain the desired displacement and strain information.

In fact, DIC compares a series of grey-scale images of a sample at different stages of deformation, tracking the movement of the pixel in the region of interest (ROI) (McCormick and Lord, 2012) and calculates displacement and strain by the use of correlation algorithms. 2D DIC setup consists of at least one digital camera, zoom objective and PC software. The specimen surface must have a random gray intensity distribution (i.e. the random speckle pattern), which deforms together with the specimen surface as a carrier of deformation information. The speckle pattern can be the natural texture of the specimen surface or artificially made by spraying black and/or white paints, or other techniques. The camera is placed with its optical axis normal to the specimen surface, imaging the planar specimen surface in different loading states onto its sensor plane. During the test, consecutive pictures are captured while samples are under deformation. The images are transferred to a PC and are analyzed through correlation algorithm by using software like Matlab ®, ARAMIS ™ or Vic2D™. In routine implementation of the 2D DIC method, the specified ROI is further divided into evenly spaced virtual grids, as shown in Fig.5.7. Each subset is characterized by a grey scale distribution denoted by a matrix of number, where each number represents a different grey scale for each pixel.

The basic principle of 2D DIC is the tracking (or matching) of the same points (or pixels) between the two images recorded before and after deformation as schematically illustrated in Fig.5.7. It is reasonable to assume that the shape of the reference square subset is changed in the deformed image. However, based on the assumption of deformation continuity of a deformed solid object, a set of neighboring points in a reference subset remains as neighboring points in the target subset.

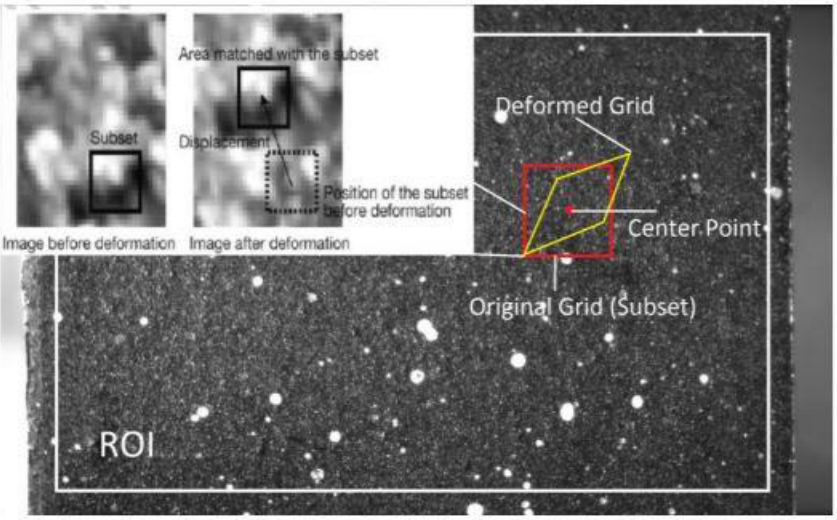

Figure.5.7: DIC image with illustration of a grid in the region of interest - ROI (Lin, 2015)

Thus, as schematically shown in Fig.5.8, the coordinates of point $Q(x, y)$ around the subset center $P(x_0, y_0)$ in the reference subset can be mapped to point $Q'(x', y')$ in the target subset according to the so-called shape function (Schreier and Sutton, 2002) or displacement mapping function (Lu and Cary, 2000). The first-order shape function that allows translation, rotation, shear, normal strains and their combinations of the subset is here considered as an example:

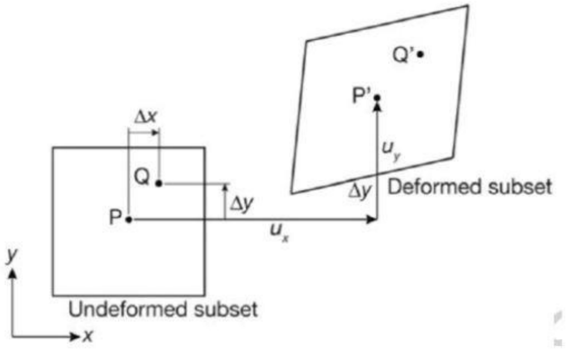

Figure. 5.8: Subset before and after the deformation

$$x' = x + u_x + \frac{du_x}{dx}\Delta x + \frac{du_y}{dy}\Delta y \tag{5.2}$$

$$y' = y + u_y + \frac{du_y}{dx}\Delta x + \frac{du_x}{dy}\Delta y \tag{5.3}$$

In the Eq. (5.2) and (5.3), *Δx* and *Δy* are horizontal and vertical distance from the center of the subset to the original point *Q*(x,y); the center point *P*(x_0, y_0) and a random point Q moved to *P'*($x_0 + u_x$, $y_0 + u_y$) and Q'(*x'*, *y'*) respectively. The displacement of *Q* is expressed by Eq. (5.2) and (5.3) and strains are obtained from the partial displacement derivatives. It is important to underline that constant strain (and/or rotation) are assumed in this particular investigated case (first-order shape function) and the subset remains a parallelogram.

Besides, the second-order shape functions proposed by Lu and Cary (2000), can be used to depict more complicated deformation states of the deformed subset. The latter form is the most commonly used; the strains vary throughout the subset that can become general quadrilaterals or have curved edges. As can be seen from equations (5.2) and (5.3), the coordinates of point (*x'*, *y'*) in the deformed subset may locate between the pixels (i.e. sub-pixel location). Before evaluating the similarity between reference and deformed subsets using the correlation criterion described previously, the intensity of these points with sub-pixel locations must be provided. Thus, a certain sub-pixel interpolation scheme should be utilized. In the literature, various sub-pixel interpolation schemes including bilinear interpolation, bicubic interpolation, bicubic B-spline interpolation, biquintic B-spline interpolation and bicubic spline interpolation have been studied. The detailed algorithms of these interpolation schemes can be found in numerical computing books (Press *et al.*, 2003).

From the perspective of function and economy, DIC has some outstanding advantages compare to conventional strain measurement. As a non-contact tool, DIC can investigate large visual areas and can be of a great value in special testing environments such as very high temperature conditions. DIC has the capability to track specular patterns in subsets over the whole ROI, which means a full field measurement able to capture local effects. Furthermore, if compared to other nondestructive and optical testing, DIC is quite economic.

DIC measurements

DIC method was used to analyze displacements and strain distribution during thermal activation of SMA rings. A CCD camera (Sony ICX 626 – Prosilica GT 2450), with a resolution of 2448x2050 pixels, equipped with a Rodagon objective (Rodagon f.80 mm - Rodenstock), was used (see Fig. 5.9). The SMA-steel coupling was observed through the optical glass window of the environmental chamber.

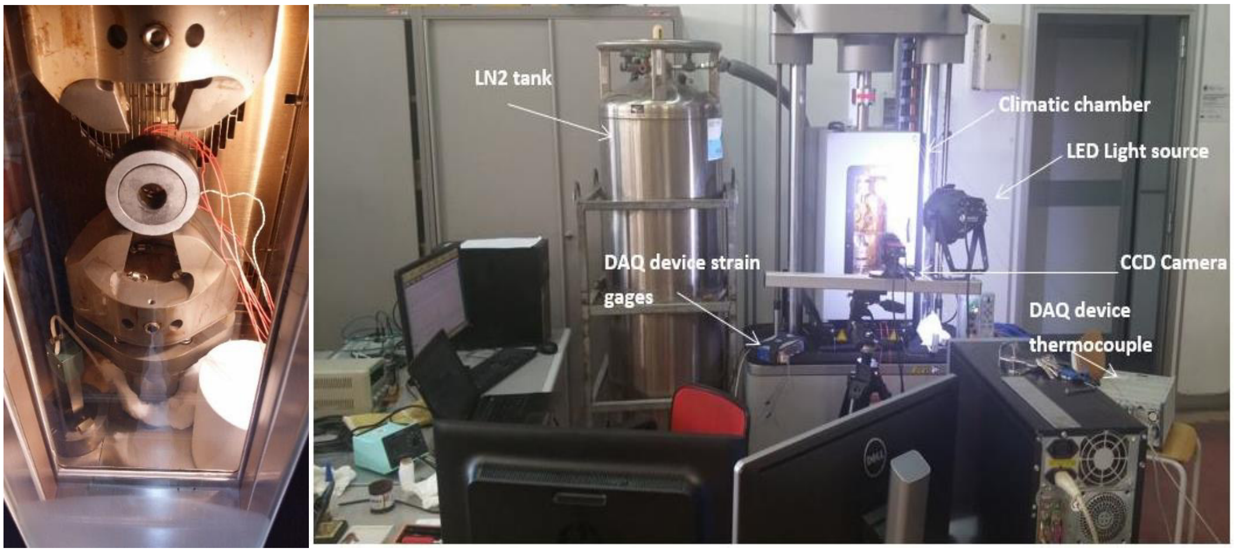

Figure 5.9: (a) Assembled SMA/steel rings for DIC and strain gauge measurements and (b) complete experimental setup for thermomechanical testing of SMA rings

Based on some preliminary studies, a proper magnification and a reduced observation window was selected (27.2 mm x22.8 mm), as schematically shown in Fig. 5.10, in order to obtain a satisfactory image resolution (90 pixels/mm).

The surfaces of the rings were speckled by air brush and high temperature resistant paints, as shown in Fig. 5.10. Correlation was performed by using a commercial software (VIC 2D, Correlated Solutions). As an example, the Fig. 5.10 illustrates the fringe contours of the total displacement of the SMA ring obtained upon heating up above A_{s1} (see Fig.5.4a)

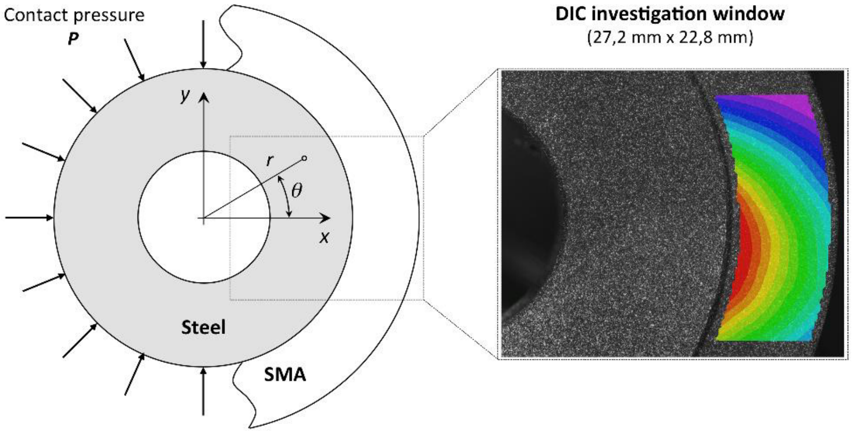

Figure. 5.10: DIC observation window of the SMA-steel rings coupling

An *ad-hoc* fitting procedure was developed, based on the theory of elasticity, to estimate the contact pressure at the SMA-steel interface. In particular, the method uses the experimentally measured displacement field of the steel ring and a least square regression method. If the steel ring is regarded as a thick walled cylindrical solid, subjected to an external pressure *P* at the outer diameter D_e, the radial displacement *u(r)*, as a function of the polar coordinate system (see Fig. 5.10), is given by:

$$u(r) = -P\left[K_1\, r + \frac{K_2}{r}\right] + \alpha\, \Delta T\, r \tag{5.4}$$

where α is the thermal expansion coefficient, ΔT is the temperature variation while K_1 and K_2 are given by:

$$K_1 = \frac{1-v}{E}\frac{D_e^2}{D_e^2 - D_i^2} \tag{5.5}$$

$$K_2 = \frac{1+v}{E}\frac{D_e^2 \cdot D_i^2}{D_e^2 - D_i^2} \tag{5.6}$$

The Cartesian components of the radial displacement *u(r)*, namely $u_x(r,\theta)$ and $u_y(r,\theta)$, can be expressed by:

$$\begin{bmatrix} u_x(r,\theta) \\ u_y(r,\theta) \end{bmatrix} = -P\left[K_1\, r + \frac{K_2}{r}\right]\begin{bmatrix} \cos(\theta) \\ \sin(\theta) \end{bmatrix} + \alpha\, \Delta T\, r \begin{bmatrix} \cos(\theta) \\ \sin(\theta) \end{bmatrix} \tag{5.7}$$

With $\theta = \tan^{-1}\left(\frac{y}{x}\right)$ and $r = \sqrt{x^2 + y^2}$.

Finally, equation 5.7 can be modified in order to account for the rigid displacements and rotations:

$$\begin{bmatrix} u_x(r,\theta) \\ u_y(r,\theta) \end{bmatrix} = -P\left[K_1\, r + \frac{K_2}{r}\right]\begin{bmatrix} \cos(\theta) \\ \sin(\theta) \end{bmatrix} + \alpha\, \Delta T\, r \begin{bmatrix} \cos(\theta) \\ \sin(\theta) \end{bmatrix} + A\, r \begin{bmatrix} -\sin(\theta) \\ \cos(\theta) \end{bmatrix} + \begin{bmatrix} B_{ux} \\ B_{uy} \end{bmatrix} \tag{5.8}$$

Where B_{ux} and B_{uy} represent the horizontal (x) and vertical (y) rigid body motions and A is the rigid body rotation parameter. Fitting DIC data with equation 5.8, by least square regression method, gives an estimation of the unknown parameters, *i.e.* the contact pressure P, the coefficient of thermal expansion α and the rigid body motion parameters (B_{ux}, B_{uy} and A). The procedure has been developed and implemented in Matlab®.

DIC procedure validation by FEM

In order to evaluate the accuracy of the procedure, previous numerical simulations, on an elastic ring subjected to an external applied pressure and a thermal load, were carried out. Figure 5.11 shows a schematic depiction of the investigated numerical case study, together with the applied boundary conditions, where r_e is the outer radius, 22.3 mm, r_i is the inner radius, 9.5 mm, and P_e is the applied external pressure.

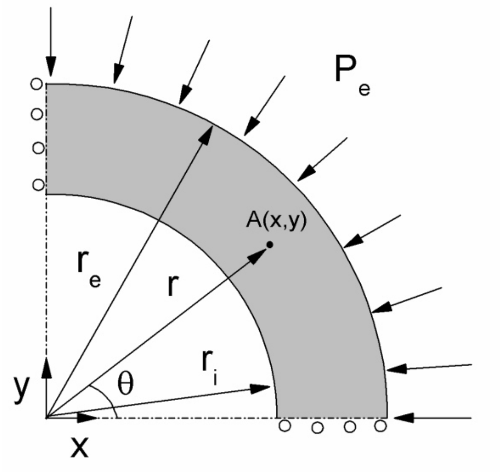

Figure 5.11: schematic depiction of the investigated case study.

Figure 5.12 shows the evolution of the mechanical and thermal loads imposed to the system. Both the pressure P_e and the ring temperature T, vary linearly with the simulating time that evolves from 0 to 1.

The modeled material is a steel with the thermo-mechanical properties reported in Table 5.1

Table 5.1: thermo-mechanical properties of the modeled material

Parameter	Value
Elastic modulus, E	210 GPa
Poisson's coefficient, ν	0.28
Thermal expansion coefficient, α	$1.3*10^{-5}$

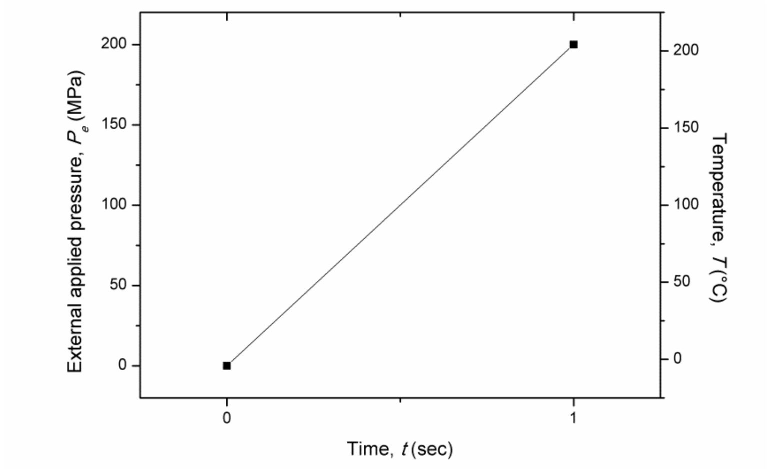

Figure 5.12: schematic depiction of the applied load evolution.

The horizontal, u_x, and vertical, u_y, displacement fields obtained from the numerical simulations are reported in figure 5.13.

Starting from the calculated numerical horizontal, u_x, and vertical, u_y, displacements, equation 5.8 allows to estimate the P_e, α, A, B_{ux} and B_{uy} by a linear regression analysis.

The five parameters were estimated for three different time of the simulation:

- t = 0.1 sec;
- t = 0.5 sec;
- t = 1 sec.

In all the cases results showed that the implemented procedure is able to evaluate the external applied pressure, the thermal expansion coefficient and the rigid body motion parameters (see Figure 5.14 and Table 5.2).

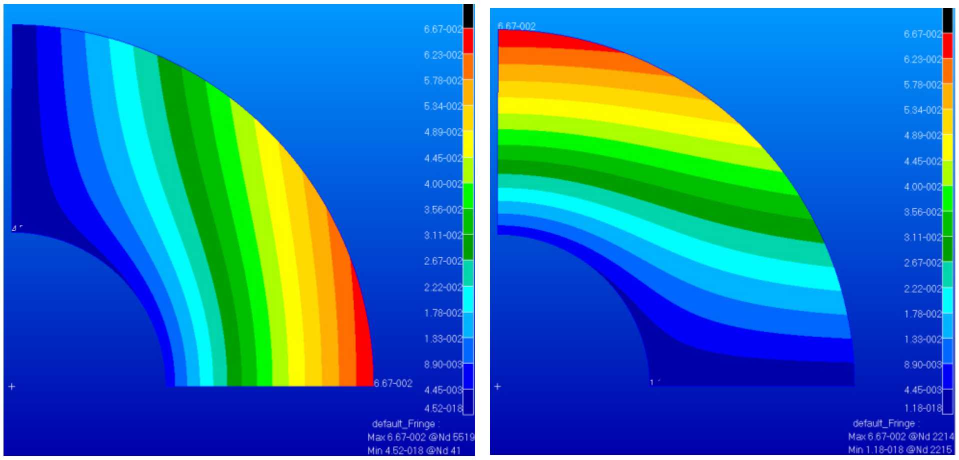

Figure 5.13: numerical displacement fields: horizontal displacements (left), vertical displacements (right).

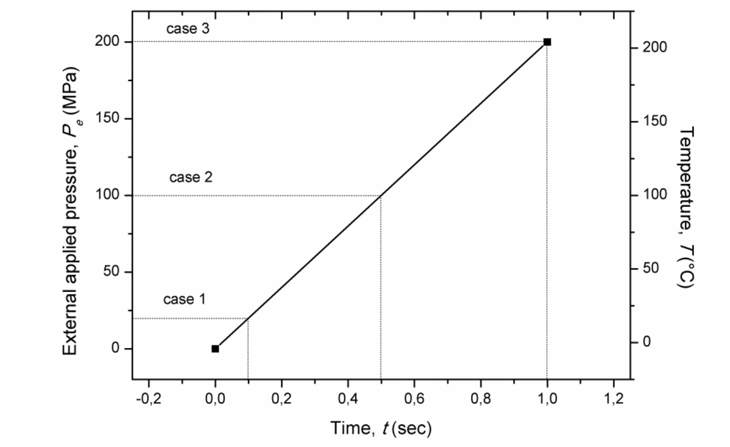

Figure 5.14: investigated cases for evaluating the accuracy of the procedure.

Results revealed a very good agreement between the imposed parameters and the regressed ones.

Table 5.2: Results obtained from the three investigated cases

Time **(sec)**	**P_e** **(MPa)**	**α** **$(10^{-5}/°C)$**	**A** **(rad)**	**B_{ux}** **(mm)**	**B_{uy}** **(mm)**
0.1	19.987	1.3*10-5	0	0	0
0.5	99.835	1.3*10-5	0	0	0
1	199.414	1.3*10-5	0	0	0

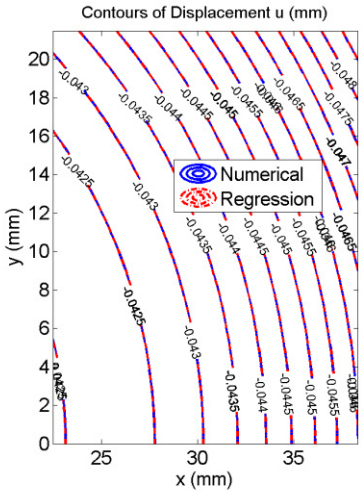

Figure 5.15: comparison between the numerical displacement field (*u*), blue contour lines, and the regressed one, red contour lines.

Figure 5.15 shows a comparison between the numerical displacement field (u), blue contour lines, and the regressed one (eq. 5.8), red contour lines providing a validation of the MATLAB® procedure.

5.5 SMA-based connector design methods

A SMA-based connection system for beam pipe couplings in particle accelerators was proposed and analyzed by both FE simulation and experimental measurements. Furthermore, a design method that involves FE results and a previously-reported sealing mode (see section 3.5.2) was developed and different coupling geometries were investigated.

5.5.1 SMA–pipe coupling geometry

Figure 5.16 illustrates a schematic depiction of the proposed SMA–pipe coupling assembly for UHV systems, together with the main characteristic dimensions. The assembly comprises the steel pipes (AISI 316LN), the SMA ring (Ni48Ti38Nb14 wt.% or Ni55Ti45 wt.%), and a sealing element, *i.e.* a copper coating to be applied onto the chamber extremities or a cylindrical gasket made of aluminum (EN AW-6082-O) or copper (C10100-O). A knife-free contact surface was designed to allow easy dismounting upon cooling to M_f. The proposed solution with cylindrical gaskets reduces at minimum the amount of possible leak paths and outgassing loads because the SMA would be outside the vacuum envelope and only the gasket/pipe interface needs to be properly sealed. Furthermore, the steel pipe has an increased external diameter (d_e) in the connection region to avoid yielding at the internal diameter of the pipe (d_i) because of the contact pressure generated during thermal activation of the SMA ring. In addition, the contact surface ratio (w/B) can be further adjusted to optimize the contact pressure at the pipe/gasket interface without causing any plasticization in the steel pipe (see section 5.5.4).

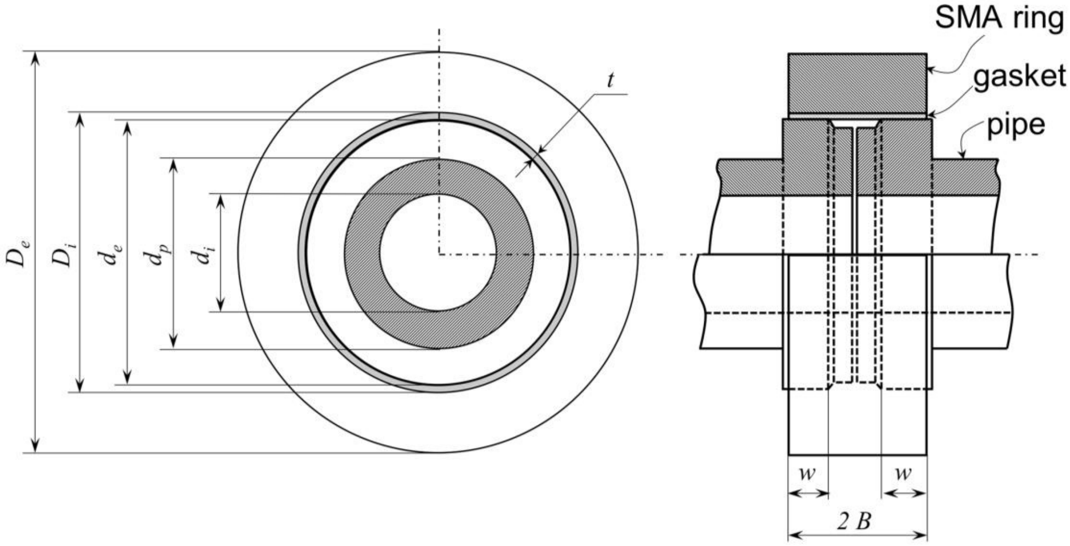

Fig. 5.16. Schematic depiction of the proposed SMA–pipe coupling assembly for UHV systems comprising steel pipes (AISI 316LN), SMA ring (Ni48Ti38Nb14 wt.% or Ni55Ti45 wt.%), and aluminum (EN AW-6082-O) or copper (C10100-O) gasket.

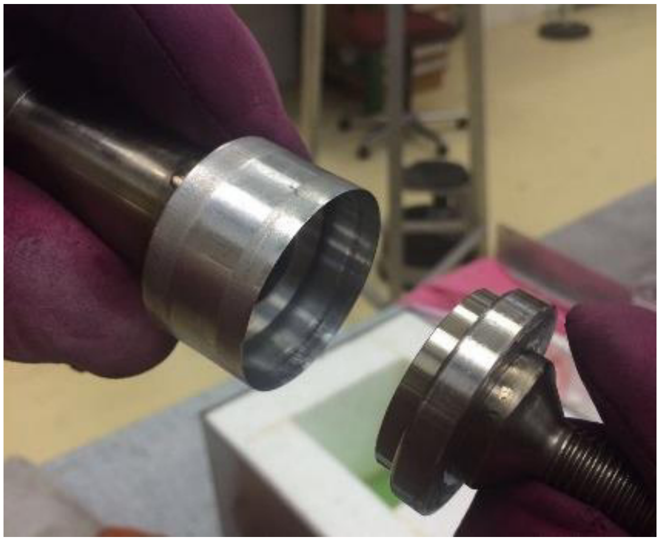

Fig. 5.17. Photography of proof-of-concept pipe–gasket coupling assembly for SMA-based connectors comprising a steel chamber (AISI 316LN) and an aluminum gasket (EN AW-6082-O).

The effects of different coupling configurations, obtained by varying the gasket thickness and the contact surface ratio (w/B), are analyzed and discussed in chapter 6. Figure 5.16 shows the clamped configuration of the system; *i.e.*, after thermal activation of the SMA ring obtained by heating to a maximum temperature $\underline{T_{max}}$=200°C than kept constant for 24 h (to simulate possible bake-out process) and a subsequent cooling to the operative temperature (T_{op}= 20°C).

The unclamped configuration is slightly different owing to an initial clearance, ΔD, between the SMA ring and the gasket/pipe, which is defined as the difference between the initial internal diameter of the SMA ring (D_{i0}) and the total external diameter of the pipe/gasket assembly (d_e+2t, where t is the gasket thickness). On the contrary, the internal diameter of the gasket and the external diameter of the pipe have the same nominal dimensions (d_e).

5.5.2 Thermo-mechanical constitutive model for SMAs

A summary description of the SMA thermo-mechanical model used herein is given in this section, for the sake of completeness as well as for a better understanding of the material parameters used in FE simulations. In particular, the adopted computational model by (Choudhry *et al.*, 2004), is based on a phenomenological approach. Among the various constitutive models available in literature, this model has been selected because of its ability to simulate the shape memory effect (OWSME) taking into account plastic deformations in SMA matrix. In fact, this is a very important feature of the investigated problem, because the non-homogeneous stress/strain distributions in SMA rings, occurring during the severe mechanical pre-strain, induce both martensite re-orientation and plastic deformations.

The model is based on additive decomposition of the total strains ($\boldsymbol{\varepsilon}$) in terms of elastic strain ($\boldsymbol{\varepsilon}^{El}$), conventional plastic strain ($\boldsymbol{\varepsilon}^{Pl}$), thermal strain ($\boldsymbol{\varepsilon}^{Th}$) and strain due to phase transformations ($\boldsymbol{\varepsilon}^{Ph}$). As a consequence, the total incremental small strain ($\boldsymbol{\Delta\varepsilon}$) is expressed as follows:

$$\boldsymbol{\Delta\varepsilon} = \boldsymbol{\Delta\varepsilon}^{El} + \boldsymbol{\Delta\varepsilon}^{Th} + \boldsymbol{\Delta\varepsilon}^{\mathbf{Ph}} + \boldsymbol{\Delta\varepsilon}^{Pl} \tag{5.9}$$

The phase transformation strain is further decomposed in trip strain ($\Delta\boldsymbol{\varepsilon}^{Trip}$) and twin strain ($\Delta\boldsymbol{\varepsilon}^{Twin}$):

$$\boldsymbol{\Delta\varepsilon}^{\mathbf{Ph}} = \boldsymbol{\Delta\varepsilon}^{\mathbf{Trip}} + \boldsymbol{\Delta\varepsilon}^{\mathbf{Twin}} \tag{5.10}$$

where $\boldsymbol{\Delta\varepsilon}^{Trip}$ is the deformation by the formation of oriented stress-induced martensite and $\boldsymbol{\Delta\varepsilon}^{Twin}$ is the deformation due to the reorientation of randomly oriented thermally induced martensite. The deformations $\boldsymbol{\Delta\varepsilon}^{Trip}$ and $\boldsymbol{\Delta\varepsilon}^{Twin}$ are given by eqs. (5.11) and (5.12)

$$\boldsymbol{\Delta\varepsilon}^{\mathbf{Trip}} = \Delta\mathrm{f}^{M}\mathrm{g}\big(\sigma_{\mathrm{eq}}\big)\,\varepsilon_{\mathrm{eq}}^{T}\,\frac{3}{2}\frac{\boldsymbol{\sigma\prime}}{\sigma_{eq}} + \Delta\mathrm{f}^{M}\varepsilon_{\mathrm{v}}^{T}\,\mathbf{I} + \Delta\mathrm{f}^{A}\boldsymbol{\varepsilon}^{\boldsymbol{Ph}} \tag{5.11}$$

$$\boldsymbol{\Delta\varepsilon}^{\mathbf{Twin}} = \mathrm{f}\,\Delta\mathrm{g}\big(\sigma_{\mathrm{eq}}\big)\,\varepsilon_{\mathrm{eq}}^{T}\,\frac{3}{2}\frac{\boldsymbol{\sigma\prime}}{\sigma_{eq}}\big\{\Delta\sigma_{\mathrm{eq}}\big\}\big\{\sigma_{\mathrm{eq}} - \sigma_{\mathrm{eff}}^{g}\big\} \tag{5.12}$$

In Eq. (5.11) and (5.12), *f* is the martesite volume fraction, $\Delta\mathrm{f}^{M}$ (≥0) and $\Delta\mathrm{f}^{A}$ (≤0) are the increment of formation of martensite and austenite, respectively; $\varepsilon_{\mathrm{eq}}^{T}$ and $\varepsilon_{\mathrm{V}}^{T}$ represent the deviatoric and volumetric part of the transformation strain, respectively, and they are obtained from uniaxial tension tests; $\boldsymbol{\sigma}'$ is the deviatoric stress tensor, σ_{eq} is the effective von Mises stress ($\sigma_{\mathrm{eq}} = \sqrt{(3/2)\,\boldsymbol{\sigma}':\boldsymbol{\sigma}'}$) and **I** is the identity tensor. In Eq. (5.12) the McCauley's bracket notation is used.

The function $g(\sigma_{eq})$ ($0 \leq g\big(\sigma_{eq}\big) \leq 1$) defines the evolution of the martensite transformation strain on the detwinning plateau. In fact, $\boldsymbol{\Delta\varepsilon}^{\mathbf{Twin}}$ is zero when σ_{eq} is below the twinning stress $\sigma_{\mathrm{eff}}^{g}$ (see Fig. 5.4b) and it is maximized when σ_{eq} approaches the stress corresponding to fully detwinned martensite σ_{0}^{g}.

As a consequence, g is equal to zero at the stress $\sigma_{\mathrm{eff}}^{g}$ ($g\big(\sigma_{\mathrm{eff}}^{g}\big) = 0$) and approaches unity at the stress σ_{0}^{g} ($g\big(\sigma_{0}^{g}\big) \approx 1$). The g function is in the following form:

$$g\big(\sigma_{eq}\big) = 1 - exp\left[g_a\left(\frac{\sigma_{eq}}{\sigma_0^g}\right)^{g_b} + g_c\left(\frac{\sigma_{eq}}{\sigma_0^g}\right)^{g_d} + g_e\left(\frac{\sigma_{eq}}{\sigma_0^g}\right)^{g_f}\right] \tag{5.13}$$

The coefficients g_a, g_b, g_c, g_d, g_e, and g_f are input of the model and represent calibration parameters. These latter can be obtained from a fitting of the uniaxial stress-strain curve of pure randomly oriented martensite within the detwinning region. Two additional parameters are used in the model to control the maximum value of g, namely cut off value g_{max}, at a given equivalent stress level, namely σ_{gmax}. More detailed information about the constitutive model can be found in (Choudhry *et al.*, 2004; Saeedvafa et Asaro, 1995)

5.5.3 Finite element model of the SMA/steel ring coupling process

The complete NiTiNb/steel rings coupling process illustrated in Fig. 5.3 was modeled, by using a commercial FE software code; the model was validated by means of the strain gauge and DIC experimental results described in sections 5.4.1 and 5.4.2. Results are reported in chapter 6. The following steps were modeled: (1) mechanical pre-strain, (2) coupling assembly and (3) thermal activation. Axisymmetric analyses were carried out by 2D four-noded quadrilateral elements (about 7700 elements), as shown in Fig. 5.18. A sensitivity test was done to determine the optimum number of elements to be used used. Only one half of the cross section was modeled due to symmetric geometry and loading conditions. In addition, a particular mesh refinement was adopted to model the SMA-steel interface. This allows to overcome computational issues related to the marked material and geometric non-linearity, due to both constitutive SMA model and contact analysis. In particular, both steel and SMA were modeled as deformable bodies and frictionless contact analysis were carried out. In fact, preliminary simulations showed that friction coefficient at the steel-ring interface does not play a significant role on the average pressure distribution.

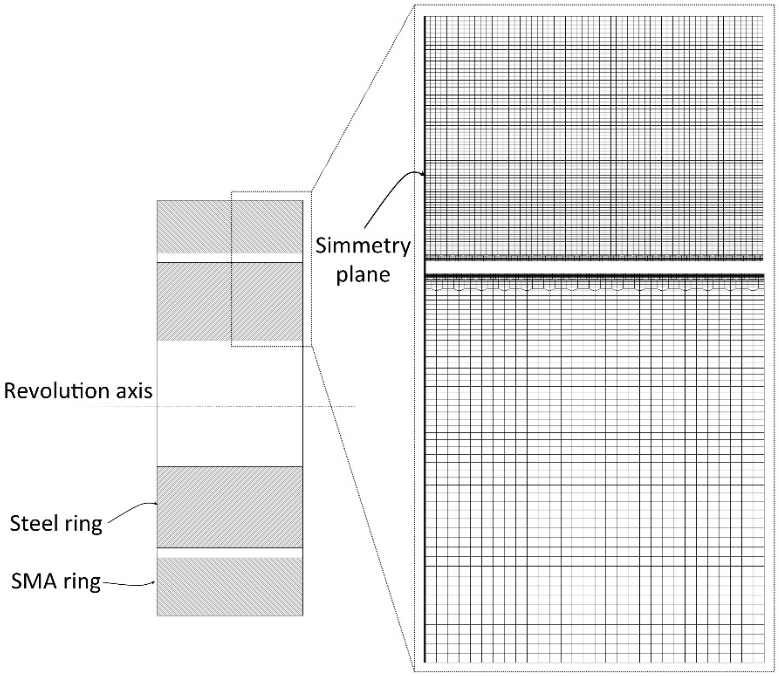

Figure 5.18: 2D axisymmetric FE model of the coupling assembly before thermal activation of the SMA ring.

The steel (ring was simulated as a linear elastic material (E=205 GPa, ν=0.3, α=1.3 * 10^{-5} °C^{-1}), while the NiTiNb ring was modeled by the special constitutive model for SMAs described in the previous section. The thermo-mechanical properties used for the SMA are summarized in Table. 5.3. Some of the material parameters were directly measured in this work, some others were found in literature (see notes in Table 5.3).

Concerning the transformation strain, the deviatoric part was considered equal to the measured uniaxial transformation strain (see Fig. 5.4.a), $\varepsilon_{\mathrm{eq}}^{T} = \varepsilon_{\mathrm{OW}}$, while the volumetric part was neglected $\varepsilon_{\mathrm{V}}^{T} = 0$. In fact, it is generally accepted that the martensitic transformations in the shape memory alloys (SMAs) are mainly characterized by the shear deformation of the crystal lattice and volumetric changes are at least one order of magnitude lower (Bhattacharya, 2003; Shimizu and Tadaki, 1984)**.**

Finally, calibration parameters of the function g were adjusted to fit the uniaxial stress-strain response of the material in martensitic condition ($T<M_f$).In particular, as shown in table 5.3 parameters g_c, g_d, g_e, g_f have been set to zero because, as described in literature (Choudhry *et al.*, 2004), they have a secondary effect on the detwinning stress- strain evolution.

Table 5.3. Thermo-mechanical and calibration parameters of the SMA constitutive model used for NiTINb

Symbol	Description	VALUE
E_A	Young's modulus of austenite, [GPa] (a)	64
ν_A	Poisson's ratio of austenite (b)	0.3
α_A	Coefficient of thermal expansion of austenite, [°C^{-1}] (c)	$11*10^{-6}$
S_{YA}	Yield strength of austenite, [MPa] (a)	900
A_s	Austenite start temperature, [°C] (a)	38
A_f	Austenite finish temperature, [°C] (a)	75
C_A	Austenite slope (Clausius-Clapeyron constant), [MPa °C^{-1}] (c)	5.5
E_M	Young's modulus of martensite, [GPa] (a)	33
ν_M	Poisson's ratio of martensite(b)	0.3
α_M	Coefficient of thermal expansion of martensite, [°C^{-1}] (c)	$11*10^{-6}$
S_{YM}	Yield strength of martensite, [MPa] (a)	950
M_s	Martensite start temperature, [°C] (a)	-105
M_f	Martensite finish temperature, [°C] (a)	-143
C_M	Martensite slope (Clausius-Clapeyron constant), [MPa °C^{-1}] (c)	5.5

f_0	Martensite initial volume fraction (d)	1
ε^T_{eq}	Deviatoric transformation strain (e)	0.056
ε^T_{v}	Volumetric transformation strain (f)	0
σ^g_{eff}	Twinning Stress (detwinning start stress), [MPa] (a)	100
σ^g_0	Non dimensional stress (detwinning finish stress), [MPa] (a)	240
g_{max},	Cutoff value of the *g* function (g)	1
σ_{gmax}	Stress value at g_{max}, [MPa] (g)	240
g_a	Calibration parameter of the *g* function (g)	-3.4
g_b	Calibration parameter of the *g* function (g)	10.5
g_c, g_d, g_e, g_f	Calibration parameters of the *g* function (g)	0

(a) Directly measured from thermomechanical testing of SMA rods (see Figs 5.4)

(b) Poisson's ratios taken from ref. (Piotrowski *et al.*,2012)

(c) Coefficients of thermal expansion and Clausius Clapeyron constants taken from ref. (Videnic *et al.*, 2008)

(d) Pre-strain is carried out in fully martensitic conditions ($T<M_f$)

(e) Deviatoric transformation strain assumed equal to one way strain, $\varepsilon^T_{eq} = \varepsilon_{OW}$ (see Fig. 5.4.a)

(f) Volumetric transformation strain neglected, $\varepsilon^T_{v} = 0$ (see Ref. (Bhattacharya , 2003; Shimizu and Tadaki, 1984)

(g) Parameters adjusted to fit the uniaxial stress-strain response in martensitic condition within the detwinning region.

Mechanical pre-strain of the SMA ring in fully martensitic conditions (T=-160°C) was simulated by an imposed radial displacement (u_0) at the internal diameter (D_{i0}), corresponding to a normal circumferential strain at the internal diameter ($\varepsilon_\theta=2u_0/D_{i0}$) equal to 13.5%. The latter value was chosen because it maximizes the OW and TW SME and induce a proper shift of the austenitic TT in NiTiNb alloys (see section 4.2.11). The initial internal diameter of the SMA ring before pre-strain (D_{i0}) was determined by preliminary simulations, with the aim to obtain a diameter, after pre-strain, equal to that of the commercial rings.

It is worth noting that martensitic stabilization due to such severe pre-strain, *i.e.* the marked increase of the austenitic TTs, is not simulated by the adopted constitutive FE model. In fact, the thermo-mechanical parameters in table 5.3 are relative to the pre-strained material, whose austenitic and martensitic TTs have been directly measured. In addition, pre-strain conditions are also affected by the ring dimensions, because strain distribution is not uniform along the ring thickness. For these reasons, great attention should be devoted in using the same material parameters to simulate different geometric configurations of SMA rings, unless specific measurements are made.

Figure 5.19 illustrates the stress and strain distribution within the SMA ring as a function of the normalized radius $((r-r_i)/((r_e-r_i))$ after the ring expansion. The normal circumferential and the equivalent von Mises stresses (σ_θ and σ^{VM}) are illustrated, together with the equivalent plastic and transformation (twinning) strain components (ε_{pl}^{VM} and ε_{tr}^{VM}). Results revealed significant residual stresses at the internal diameter, close to 200 MPa, as a consequence of marked plastic deformations, around 6%. Furthermore, as expected, compressive stresses were observed at the internal diameter and tensile stresses at the outer radius of the ring. In addition, the maximum allowable transformation strain (around 5.5 %) is reached in the whole cross section of the ring.

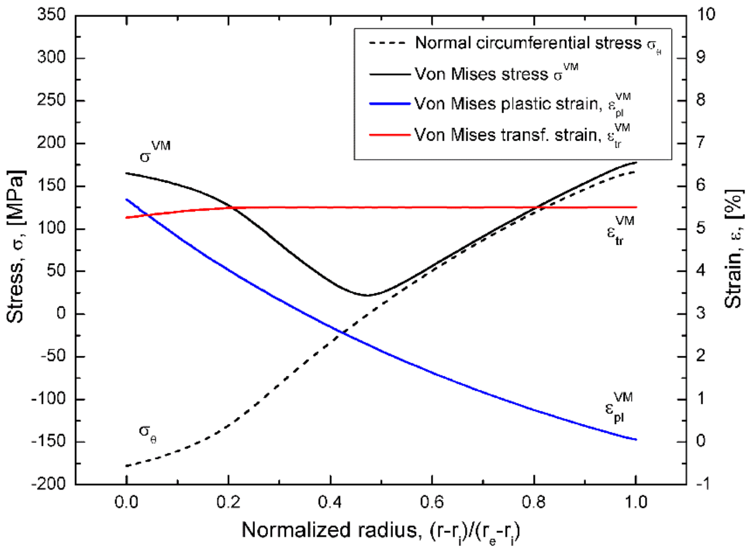

Figure 5.19: FE results on the effects of mechanical pre-strain in terms of stress and strain distribution within the SMA ring *versus* normalized radius $((r-r_i)/((r_e-r_i))$: normal circumferential stress (σ_θ), equivalent von Mises stress (σ^{VM}), equivalent plastic strain (ε_{pl}^{VM}) and equivalent transformation strain (ε_{tr}^{VM}).

After mechanical pre-strain the mesh of the steel ring is moved below that of the SMA ring (mounting). Finally, the thermal activation of the coupling is simulated by heating up to 200 °C and cooling down to 25 °C; the related results are reported in chapter 6.

5.5.4 SMA-steel pipe coupling optimization methods

The performance of the SMA–pipe coupling of Fig. 5.26 for different coupling configurations was analyzed in terms of contact pressure by a commercial FE software code and the constitutive model for SMAs (Choudhry *et al.*,2004) described in section 5.5.2. Table 5.4 reports the different analyzed configurations in terms of gasket thickness (t) and contact surface ratio (w/B). For comparative studies, the coupling type #1 was constructed without an aluminum gasket and with a 35 μm-thick electroplated copper coating on the outer surface of the steel chamber. The values of the other significant geometrical parameters of the couplings (*i.e.*, D_i, D_e, d_i and B) are illustrated in Fig.5.28.

Table 5.4. Main geometrical parameters of the investigated coupling configurations

Coupling type #	Gasket thickness, *t* (mm)	Coupling ratio, *w*/*B*
1(1)	None(1)	1.00
2	0.3	1.00
3	0.6	1.00
4	0.9	1.00
5	0.6	0.85
6	0.6	0.60
7	0.6	0.35

(1) 35 μm-thick electroplated copper coating

(2)

The three different stages of coupling, as illustrated in Fig. 5.4, were modeled: (1) mechanical pre-strain, (2) coupling assembly and (3) thermal activation. Axisymmetric analyses were carried out using two-dimensional four-noded quadrilateral elements. Only one half of the cross-section was modeled owing to both the symmetric geometry and loading conditions. Symmetric boundary conditions were applied on the symmetry plane for both the SMA ring and the aluminum gasket. The length of the pipe was selected to avoid the boundary effect in the contact region. As an example, Fig. 5.20 illustrates the mesh for the coupling type #6 (t=0.6 mm and w/B=0.6), which consists of about 30,000 elements. A sensitivity test was done to determine the optimum number of elements to be used. Fillet and corner radii (R) values equal to 1.5 mm were adopted to model the section variation. This value was chosen by preliminary simulations with the aim to avoid local plastic deformations in the steel pipe. The contact was simulated using a friction coefficient of μ=0.3. It is worth noting that the effects of the friction coefficient at the steel/ring interface were analyzed by preliminary simulations and it was found that it does not play a significant role in the average contact pressure. An accurate mesh refinement was made to model the contact interfaces, which overcame computational issues related to both material and geometric non-linearity (contact).

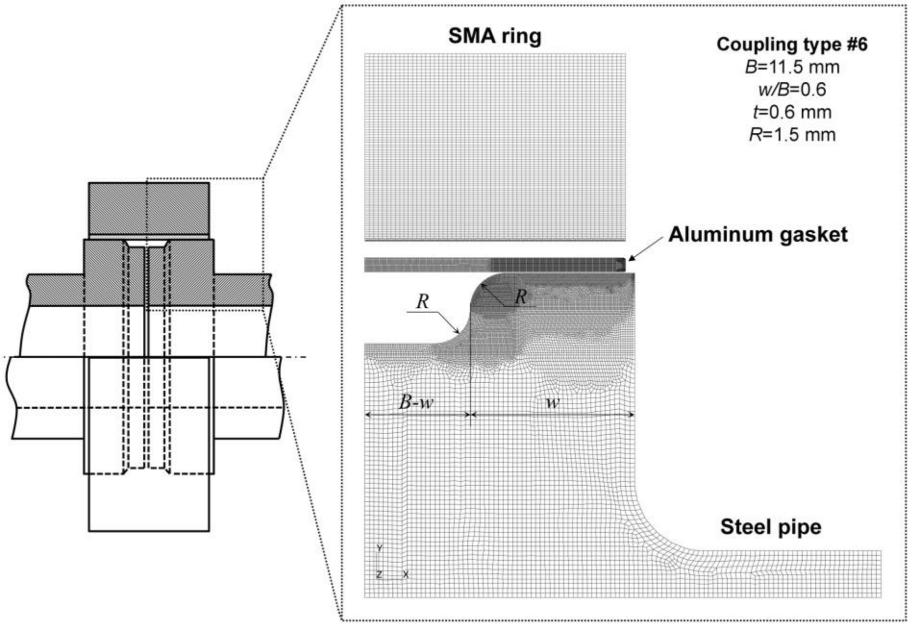

Fig. 5.20. Two-dimensional axisymmetric FE model of the coupling assembly before thermal activation of the SMA ring

Steel (AISI 316LN) and aluminum (EN AW-6082-O) alloys were modeled as temperature-dependent elastic–plastic materials with bilinear behavior to take into account the evolution of material properties during thermal activation and bake-out cycles (20°<T<220°C). The coefficients of thermal expansion (CTE) are kept constant owing to the very slight variation within the investigated temperature range. The thermo-mechanical properties used for the SMA (NiTiNb) are summarized in Table 5.3 while those of the steel and the aluminum are summarized in Table 5.5 and they come from the uniaxial tensile tests performed on steel and aluminum rods.

Table 5.5. Material properties used in FE simulations

Material	Material property	Value
Steel (AISI 316LN)	Young's modulus, E	210 GPa
	Poisson ratio, ν	0.3
	Coefficients of thermal expansion, α	1.65×10^{-5} °C^{-1}
	Yield strength, S_Y	T=20°C: 300 MPa
		T=100°C: 250 MPa
		T=200°C: 225 MPa
		T=300°C: 200 MPa

	Tangent modulus, E_T	T=20°C: 1360 MPa
		T=100°C: 1260 MPa
		T=200°C: 1230 MPa
		T=300°C: 1220 MPa
Aluminum (EN AW-6082-O)	Young's modulus, E	70 GPa
	Poisson ratio,	0.3
	Coefficients of thermal expansion, α	2.5×10^{-5} °C^{-1}
	Yield strength, S_Y	T=20°C: 54 MPa
		T=100°C: 45 MPa
		T=200°C: 41 MPa
		T=300°C: 32 MPa
	Tangent modulus, E_T	T=20°C: 660 MPa
		T=100°C: 550 MPa
		T=200°C: 290 MPa
		T=300°C: 50 MPa

Mechanical pre-strain of the SMA ring was simulated by applying a fixed radial displacement (u_0) at the internal diameter (D_{i0}), corresponding to a hoop strain ($\varepsilon_\theta=2u_0/D_{i0}$) equal to 13.5% (see section). After mechanical pre-strain, the mesh of the SMA ring was moved above that of the steel/gasket assembly (mounting). Finally, the thermal recovery was simulated by heating to 200°C and subsequent cooling to 20°C. The results of the FEM simulations are reported and discussed in chapter 6.

5.5.5 A novel sealing performance parameter

A novel model has been developed to analyze the leak tightness performance of the different coupling configurations (see Table 5.4). The model combines a reference conductance model (Roth ,1972), described in section 3.5.2, and the results obtained from FE simulations. In particular, this model takes into account both the contact pressure and the geometry of the contact surface. The conductance, C (free molecular flow), of a gas throughout a sealing surface (see Fig. 5.21) exhibits an exponential decrease with the contact pressure P:

$$C = K(L_e/w_e)\exp(-3P/R), \tag{5.14}$$

where K is a constant dependent on the temperature, the molecular weight of the gas, and the roughness of the contact surface. Following the reference model (see section 3.5.2), L_e is the effective length of the contact surface (orthogonal to the flow); w_e is the effective width (in the flow direction); and R is a factor expressing the sealing ability of the material, namely, the sealing factor.

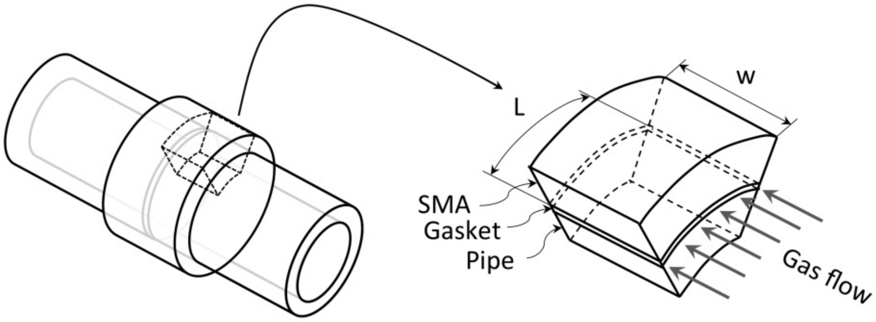

Fig. 5.21. Schematic depiction of the sealing geometry

Great attention should be devoted to the application of Eq. (5.14) to predict the conductance or the leak rate of a sealing coupling, as discussed in literature (Roth A.,1972). In fact, the model parameters must be calibrated (in terms of K, w_e, L_e and R) based on a number of experiments. However, the parameter $S=(C/K)^{-1}$ obtained from Eq. (5.14), which is the sealing parameter, can be used for comparative analysis between different configurations:

$$S = (C/K)^{-1} = (w_e/L_e)\exp(3\,P/R). \tag{5.15}$$

Therefore, a greater value for the parameter S signifies a lower leak rate of the coupling. In this investigation, the effective length L_e was considered identical to the physical value (L), and was equal to πd_e (see Fig. 5.21). On the contrary, the value of the effective contact width w_e is typically much less than the physical value of the coupling (w) and cannot be accurately determined (Roth A.,1972). Therefore, comparative analyses were made for different values of the ratio $\xi=w_e/w$, ranging from 0.1 to 1. The values of the sealing factor R for the aluminum gasket was taken in the range 30–60 MPa, as recommended in literature (Roth A.,1972)

5.6 Leak tightness tests

The vacuum performance of selected coupling geometries, was analyzed by leak tightness tests (see section 2.8.5). Fig. 5.22 illustrates the geometry and dimensions of a prototype vacuum pipe assembly with w/B =1 used for the leak tests. The chambers were made of AISI 316 LN steel, which is widely used in the vacuum systems of particle accelerators. Different pipes with different contact surface ratios w/B, were manufactured by turning/grinding processes. They possessed a mean surface roughness of R_a=0.45 μm. The aluminum gaskets were obtained by high precision turning, and possessed a mean roughness of R_a=0.63 μm. It is well-known that the surface roughness substantially affects the sealing performance of the assembly (Roth, 1972), and that large roughness values could result in intolerable air-leak rates through the gasket/pipe interface. However, the high local contact pressures obtained during thermal activation has a throttling effect on the leak paths. These phenomena are connected intimately with the local plastic deformation of the gasket.

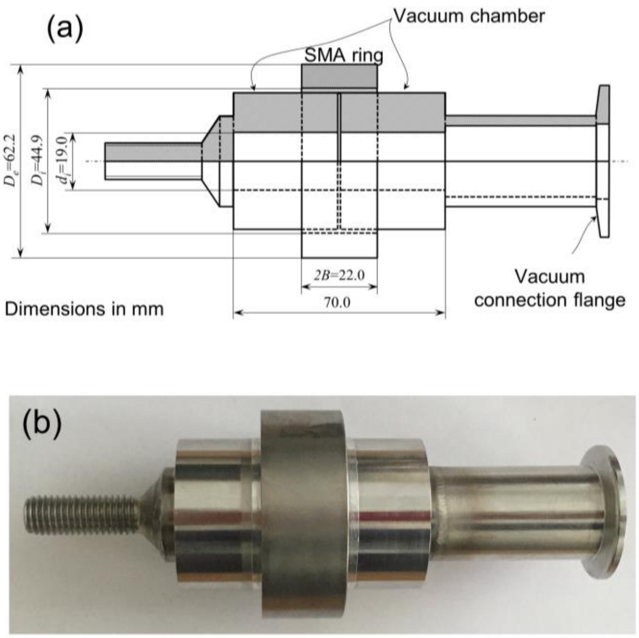

Fig. 5.22. Schematic drawing (a) and photograph (b) of a prototype vacuum chamber used for leak tightness and contact pressure tests (w/B=1).

Leak tests for NiTiNb- and NiTi-based assemblies (cfr. chapter 6 and 7) were carried out at room temperature after clamping and bake-out cycles using the helium leak detection method (Hilleret, 1999). The method uses a high-sensitivity (~10^{-11} mbar·l·s^{-1}) mass spectrometer tuned on the value of 4 amu (see Fig. 5.23).

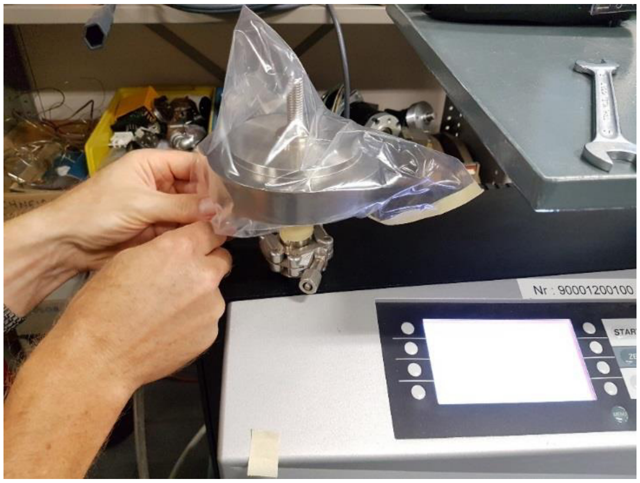

Fig. 5.23: operator performing a leak detection test

5.7 Irradiation tests on SMA prototype vacuum chambers

The proposed SMA-based device for UHV couplings are ideally suited for remote-control operations in restricted access areas of particle accelerators. A complete understanding of the effects of irradiation on the functional and mechanical behavior of SMA couplers is therefore a crucial part of the development program. The radiation load is strictly dependent on the installation areas of the couplers within the CERN facilities. The complex mixed field of stray particles present in CERN accelerators is composed by charged and neutral hadrons, photons, muons and electrons with energies ranging from GeVs down to thermal energies. This environment is not harsh only for the electronics but also for the materials (metals, polymers, etc.) used within the CERN facilities. Electronic equipment and materials need to be tested in a radiation field representative of the actual CERN accelerator areas; this allows studying their sensitivity to high-energy radiations in order to assure mid/long-term operation requirements. For this purpose, an irradiation facility called CHARM (Cern High energy AcceleRator Mixed field/facility was built at CERN (J. Mekki *et al.*, 2016). CHARM allows to test materials and devices in a variety of different representative radiation environments. Before the irradiation tests, it is essential to estimate the actual particle fields representative of the accelerator areas of interest. For this purpose, Monte Carlo simulations were performed and benchmarked with measurements carried out by special dosimeters in order to map properly the radiation fields occurring in peculiar areas of the CERN accelerator complex.

At CHARM, the proton extracted from the PS accelerator at 24 GeV/c, hits a cylindrical copper or aluminium target (see Fig.5.24). The resulting secondary mixed radiation field is used to test equipment at predefined test positions. Depending on the test position, the target material and the shielding configuration selected, the test samples are exposed to different particle spectra and fluxes. In addition, movable concrete or iron blocks with a thickness of 40 cm can be placed between the target and the test locations in different combinations. This enables the modulation of the particle spectra and the definition of the required radiation field (energy, composition and intensity).

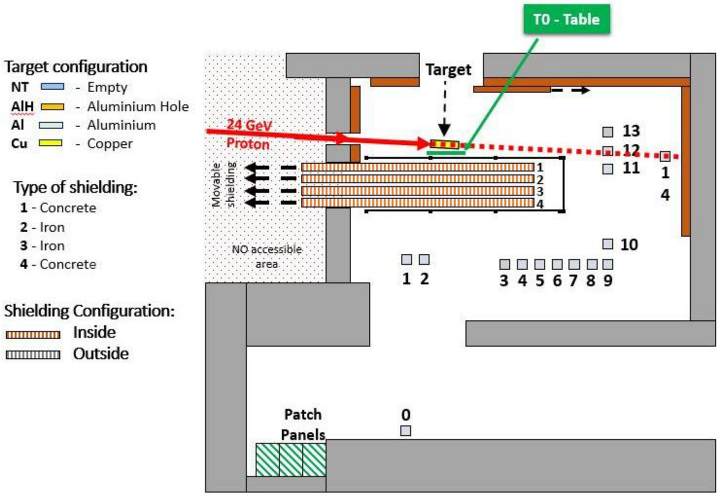

Figure 5.24. Sample placement at CHARM facility

5.7.1 Radiation damage

Ionizing radiations have an impact in both biological and non-biological elements. There are many sources of radiations abundant in nature such as the background cosmic radiation as well as others artificially created, like the particle beams in the accelerators.

Sources for ionizing radiations are mainly alpha particles (protons and neutrons), beta particles (electrons and positrons), and photons (gamma rays, X-rays). The ionizing radiation can affect humans with deterministic (high radiation exposure) and stochastic (low level of exposure) effects. Generally speaking, irradiation has four kind of effects on the materials: heating, impurity production, ionization and displacement damage. The irradiation results in a strong heat generation in the material lattice. The interaction of the particle flux with material lattice can be represented, from the thermodynamic point of view, via the heat generation rate. The impurity production effect appears mainly due to neutron and ion irradiation. Neutrons and ions, which lose energy during the interactions with the material, can become atomic impurities within the lattice. Target atoms colliding with irradiated high energy particles can be destroyed or produce secondary particles. Another radiation effect is the ionization process; ionization consists in adding or removing electrons from atoms or ions existing previously in the solid. It can also raise their energy level by moving the electrons to higher orbit layers. Ionizing radiation damages the chemical bonds. It has the highest influence on covalent bonds (mostly existing in organic matter), medium influence on ionic bonds and small influence on the metallic ones (mostly affected by the heat, instead). The irradiation exposure (flux of particles) implies the creation of clusters of defects in the material: this

is usually known as atomic displacement damage process. It correlates strongly with the onset and evolution of classical micro-damage (by treating clusters as micro-voids). The energy brought by the irradiated particles into the solid is dissipated mainly by elastic collisions with lattice atoms. The latter can be either ejected from their initial position transferring energy to the neighbors or simply moved to interstitial positions. These nuclear interactions lead to the production of a cascade of moving atoms and to the creation of defects within the lattice (interstitials and vacancies).
The ionizing radiation is measured and quantized using the following quantities:

- *Absorbed dose*: The absorbed dose, abbreviated as *D*, is the amount of energy locally deposited at a given location in matter. It is defined as the deposited energy (ΔE) per unit of mass of material (Δm). The absorbed dose not only depends on the incident radiation, but also on the absorbing material (depending on its mass). The energy deposited in a certain material due to ionizing radiation is measured in Gray (Gy = J Kg^{-1}).
- *Effective dose*: The effective dose, H_{eff}, is the tissue-weighted sum of the equivalent doses in all specified tissues and organs of the human body and represents the stochastic health risk to the whole body, which is the probability of cancer induction and genetic effects, of low levels of ionizing radiation. It takes into account the type of radiation and the nature of each organ or tissue being irradiated, and enables summation of organ doses due to varying levels and types of radiation, both internal and external, to produce an overall calculated effective dose. The SI unit for effective dose is the Sievert (Sv = J Kg^{-1}).
- *Dose rate*: The dose rate (Sv s^{-1}) is defined as the dose of ionizing radiation delivered per unit time

The dose limit for a person conducting maintenance operations at CERN is 6 mSv per year and for normal employees at CERN is 2 mSv per year. In some areas in ATLAS and CMS, particle debris generated by the 14 TeV proton-proton collisions induce radioactivity doses higher than 5 mSv h^{-1} so that stringent access regulations are applied.

5.7.2 Experimental and numerical methods

FLUKA (FLUktuierende KAskade) is a Monte Carlo code that very accurately simulates electromagnetic and nuclear interactions in matter (http://www.fluka.org/fluka.php). Over the years, it has become the standard tool to investigate beam-machine interactions, radiation damage and radioprotection issues in the CERN accelerator complex. The simulated dose map in a possible application area for SMA connectors during HL-LHC operations (Bruning and Rossi, 2015) is reported in Figure 5.25; it shows the dose map for one of the most radioactive area within the CERN accelerator complex: the inner triplet area of ATLAS experiment (ATLAS Collaboration, 1999) *i.e.* the area in correspondence of the beam focusing/defocusing quadrupole magnets. Results in Fig.

5.25 are representative of similar areas for the CMS experiment (LHC Experiments Committee, 1997) as well.

The FLUKA simulations predicted significant radiation doses in this area as they will increase by the factor of 16 in the next 20 years of operation

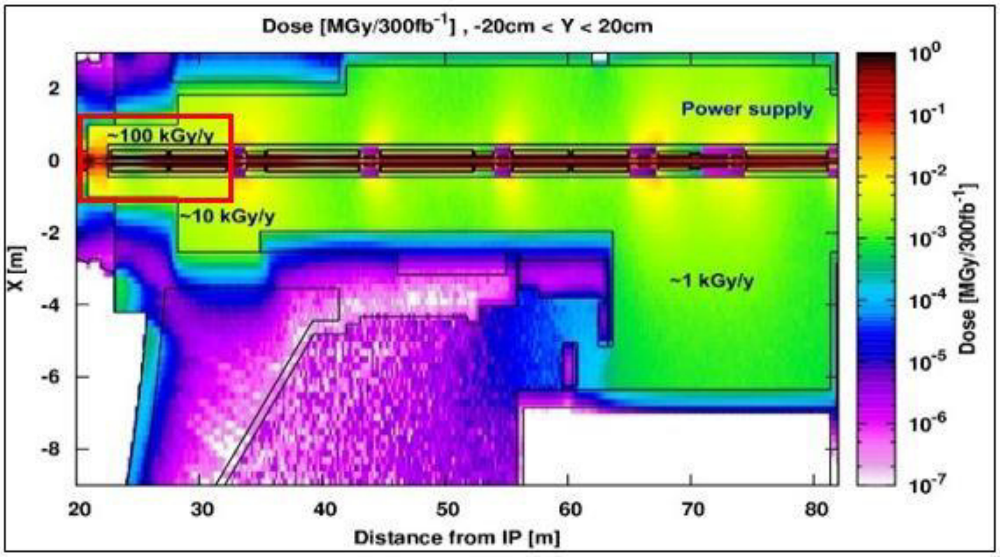

Figure 5.25. Dose map in the IT area right side of ATLAS for HL-LHC operation. (courtesy of F. Cerutti)

The predicted integrated dose for the HL-LHC inner triplets areas of ATLAS is about 100 kGy/y. The irradiation tests carried out at CHARM were designed in order to create a radiation field representative of the investigated area. Results on irradiation and post-irradiation tests of three different couplings are presented and discussed in section 7.6.

6. NiTiNb-BASED COUPLERS FOR ULTRA-HIGH VACUUM PIPES

6.1 Introduction.

Commercial NiTiNb rings showing TW behavior (Intrinsic Devices Inc., USA) were investigated. The functional performance of the NiTiNb/steel system (see chapter 5), in terms of contact pressure and mounting/dismounting features, was analyzed for repeated thermal cycles between TTs and for different values of the initial assembly clearance. The thermo-mechanical analyses of NiTiNb rings and NiTiNb/steel assemblies are reported and discussed.

Furthermore, the influence of gasket thickness and contact surface geometry in the proposed NiTiNb-based connectors were analyzed and the best configurations were identified by using the novel sealing model illustrated in section 5.5.5. The leak tightness of the connections (leak rate< 10^{-10} mbar l s^{-1}) was assessed experimentally. The results of the experimental and numerical analyses are reported in the following sections.

6.2 Stress free thermal recovery of SMA rings

The free recovery capabilities of the pre-strained NiTiNb rings were studied, in terms of both OW-SME and TW-SME, for subsequent thermal cycles. Figure 6.1 shows the normal circumferential strain (ε_θ) at the internal diameter of the SMA ring, together with the diameter variation ($\Delta D=\varepsilon_\theta D_i$), as a function of the temperature (T). A comparison between 5 subsequent thermal activations is also shown. In particular, OW-SME is activated by the first heating above A_{f1}, as also observed in NiTiNb rods (Fig. 5.4.a). A OW recovery strain (ε_{OW}) of about 6.1% was observed, corresponding to an internal diameter variation ΔD of about 2.8 mm. The ring was subsequently thermally cycled between TTs and the reversible TW-SME capabilities were recorded. A limited decrease of the TW strain (ε_{TW}) in the first three cycles was observed, with a stabilized value of about 2.0%, corresponding to ΔD=0.9 mm. Furthermore, a direct comparison between Figs. 5.4.a and 6.1 reveals a similar behavior between rods and rings although the residual stress distribution occurring in the latter after pre-straining. Very similar values of both TTs and OW/TW strains were found, as well as the same drop in the austenite transformation temperatures after the first thermal activation. This is a relevant result as material data obtained from NiTiNb rods were used to model the SMA ring in the FE analysis.

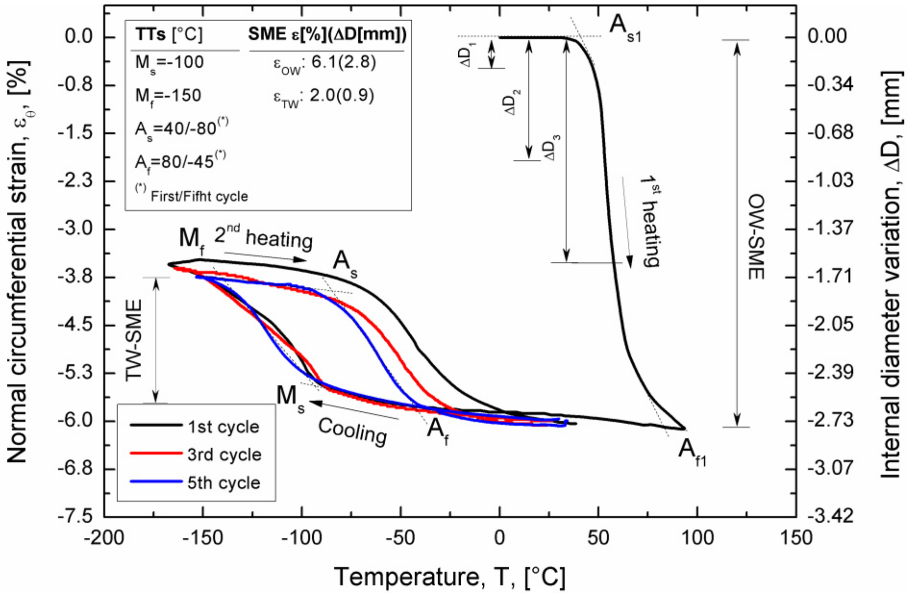

Figure 6.1: Stress free One Way and Two Way shape memory recovery capabilities of a NiTiNb ring after five subsequent thermal cycles, together with the values of the main functional parameters.

Finally, data obtained from stress-free thermal recovery tests were used to define the clearance values to be used in the subsequent SMA-steel coupling tests, as shown in Fig. 6.1.

6.3 Thermal activation of SMA-steel coupling

The evolution of the contact pressure at the SMA-steel interface as a function of the temperature, during thermal activation, was analyzed. The effects of the initial assembly clearance between SMA and steel (38NiCrMo3) rings were also investigated. Figure 6.2 illustrates the curves contact pressure *versus* temperature (*P vs T*), for the three values of the clearance (ΔD_1=0.15 mm, ΔD_2=0.85 mm, ΔD_3=1.60 mm) and for the 1st activation cycle (see section 5.4.1). In particular, strain gauge measurements (eq. 5.1) are compared with FE results in Fig. 6.2.a and with DIC results (eq. 5.8) in Fig. 6.2.b. Figure 6.2.a shows a good agreement between FE results and SG measurements for all investigated values of the clearance, with maximum pressure differences after thermal activation of about 2.5 %. FE values in Fig. 6.2a were taken at the symmetry plane of the ring; non-significant differences were observed along SMA/steel contact surface (around 5%). The figure shows the same trend for the three values of the clearance; the different steps of thermal activation (see Fig. 5.4) are also illustrated: ring-pipe contact at $T=T_{c1}$, complete activation at $T_{max}> A^{\sigma}_{f1}$, and cooling down to $T=T_{op}$. As a consequence of the thermally induced OW recovery mechanisms, a marked increase of the contact pressure between T_{c1} and A^{σ}_{f1}, was observed. It is worth pointing out that, A^{σ}_{f1} in Fig. 6.2a, corresponds to the temperature at which the SMA ring, under stress, becomes fully austenitic *i.e.* without thermally induced or stress induced martensitic variants. In fact, A_{f1}^{σ}, in Fig. 5.19a corresponds indicatively to M_D (see section 4.1). A slight increase above A_{f1}^{σ}, was also observed up to a maximum pressure P_{max}. This is mainly attributed to the mismatch of the thermal expansion coefficients (CTE) between the two materials (11*10^{-6} °C^{-1} for SMA and 13 *10^{-6} °C^{-1} for steel). Consequently, a decrease of the contact pressure was observed when cooling down to the operative temperature (T_{op}=25 °C) where a final operative pressure P_{op1} in the range 80-90 MPa was measured for the three investigated levels of the assembly clearance. More precisely, a slight decrease of P_{op1} from 91 MPa at the minimum clearance (ΔD_1=0.15 mm) to 78 MPa at the maximum clearance (ΔD_3=1.6 mm) was recorded.

The limited effect of the initial assembly clearance on the contact pressure represents a very interesting result. In fact, large assembly tolerances can be accepted for beam pipe coupling, without affecting significantly the tightening performance. Indeed, the larger the clearance the easier and faster the assembly operations, which is a relevant benefit especially in radioactive areas of particle accelerators.

Figure 6.2.a also illustrates a focus of curves near the contact temperature T_{c1}. Comparison between the FE curves shows a very small decrease of T_{c1} while decreasing the initial clearance. This is attributed to the high slope of the ε-T curve in the austenite transformation region (A_{s1} <T< A_{f1}). The larger differences between the three SG curves is also attributed to the experimental variability, *i.e.* to both material and measurements variability. Indeed, the investigated NiTiNb rings were provided with an error on the TTs of about +/- 3 °C. Finally, the figure shows that FE model does not accurately capture the different slopes of the curves in the heating stage (T_{c1} <T< A_{f1}^{σ}). The constitutive model does not take into account the whole complex non-linearity and non-homogeneous mechanisms occurring in the SMA ring during thermal activation. Figure 6.2.b shows a satisfactory agreement between SG and DIC results. Maximum differences (around 10%) were observed in the heating stage above A_{f1}^{σ} However, very small differences (never greater than 2%) were measured when cooling down to T_{op}. The differences observed at high temperatures are probably due to temperature gradients within the material, *i.e.* between the bulk and the ring surface where DIC is applied.

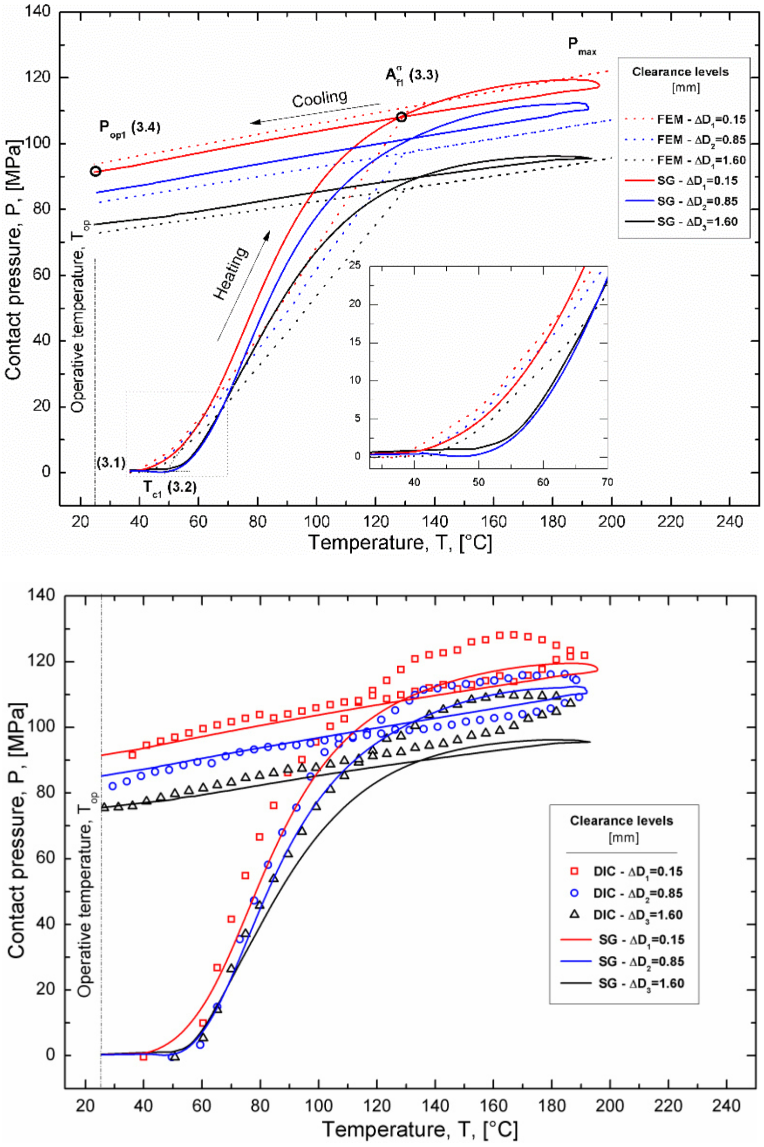

Figure 6.2: Evolution of contact pressure at the SMA-steel interface as a function of the temperature (P *vs* T) during thermal activation for the three values of the assembly clearance (ΔD$_1$=0.15 mm, ΔD$_2$=0.85 mm and ΔD$_3$=1.60 mm): a) comparison between strain gauge measurements and FE results an b) comparison between strain gauges and DIC results.

The main advantage in using the DIC method with respect to SGs consists in the fact that pressure can be estimated without any physical instrumentation of the coupling. In addition, SGs method provides local measurements while DIC can be used for full field analysis of the coupling process, *i.e.* it is able to capture possible local effects during thermal activation of the SMA rings.

6.4 Local analysis by DIC

As a representative example, the horizontal and vertical displacement fields, obtained from the DIC technique are reported in Figure 6.3. These results were obtained by correlating the first image of the assembly at T_{c1} and the last one, after thermal activation, at T_{op}

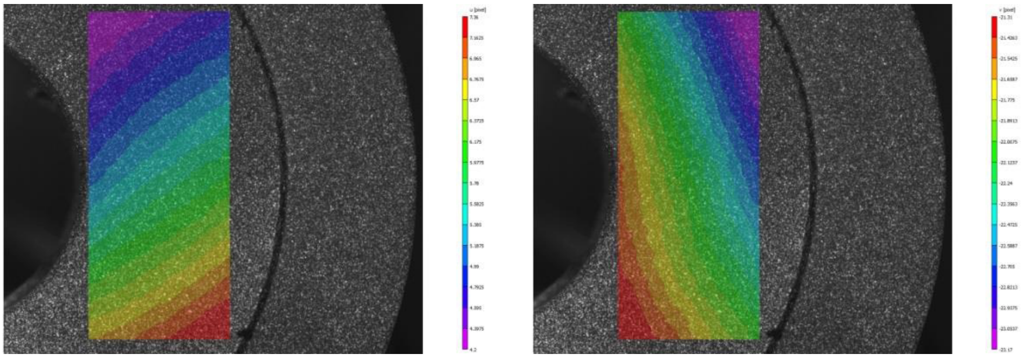

Figure 6.3: displacement fields obtained from the digital image correlation: horizontal displacements (left), u_x, vertical displacements (right), u_y.

Figure 6.4 shows a comparison between the experimental displacement field (u) after the elimination the rigid body motion components and the analytical elastic solution obtainable from the regressed parameters (eq. 5.8). Results revealed a very good agreement.

The experimental stress field was also analyzed (by means of the strain field) and the obtained results were compared with the analytical prediction (see figure 6.5). Results are referred to a specific stress profile obtained along a radius of the elastic ring. Even if some noise is observed in the DIC results, due to unavoidable measurement errors, they fit quite well the analytical solution.

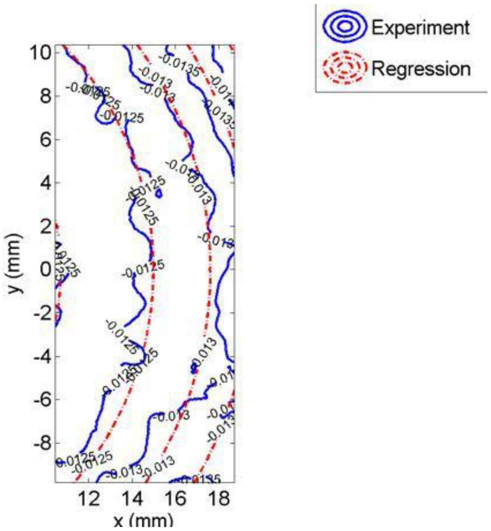

Figure 6.4: comparison between the experimental displacement field (u), blue contour lines, and the regressed one, red contour lines.

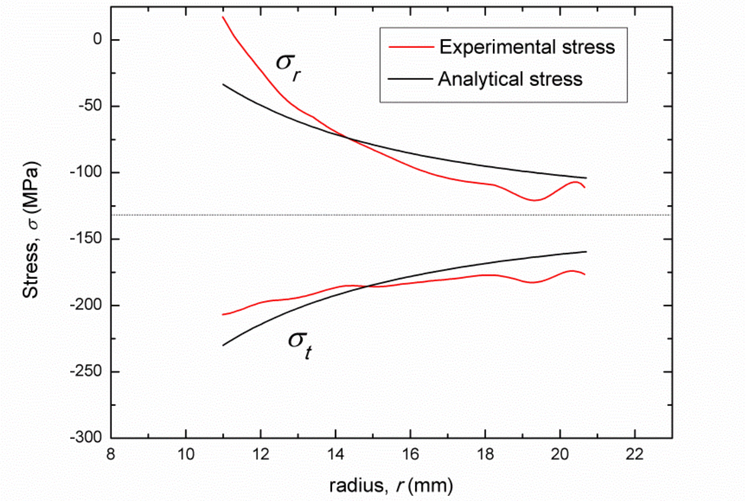

Figure 6.5: comparison between the experimental stresses, red lines, and the analytical ones, black lines.

The correlation technique was also employed to evaluate the presence of creep phenomena in the SMA ring when it is kept at 200 °C for 24 h in order to simulate the bake out procedure. Both strain fields in SMA and steel rings were analyzed by correlating the first image of the assembly at *T*=200°C and the last one after 24 h. As an example, Figure 6.6 shows the strain field recorded in an SMA ring. Results revealed that no significant deformations (strain values within the resolution of the measurements) occurred in both SMA and steel rings, confirming that creep phenomena are not significant in the investigated NiTiNb rings exposed at 200°C.

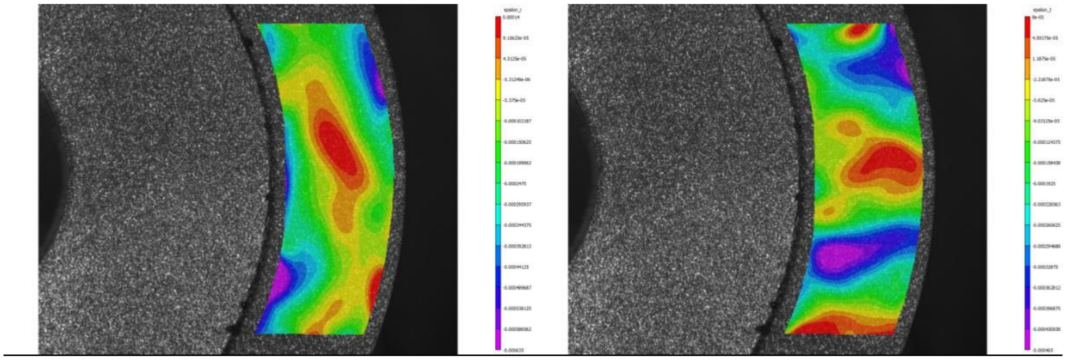

Figure 6.6: deformation field after creep test: a) horizontal deformations ε_{xx}, b) vertical deformations ε_{yy}.

6.5 Thermal dismounting of NiTiNb-steel ring couplings

The evolution of the contact pressure during cooling down to M_f was measured for the three investigated values of the assembly clearance, with the aim of analyzing possible thermal dismounting. Figure 6.7 illustrates the curves pressure *vs* temperature, for the three values of the clearance, obtained by SG measurements. These curves include the 1) first thermal activation (T_{op}-T_{max}-$\mathrm{T_{op}}$); 2) a subsequent cooling down to M_f (T_{op}-M_f); and 3) a second heating to the operative temperature (M_f-T_{op}). Similar trends between the three curves were measured. Starting from the end of the first thermal activation a slight pressure decrease is observed when cooling down to M_S^{σ} (martensite start under stress) mainly due to the mismatch of the CTE. A marked reduction occurs when further decreasing the temperature between M_S^{σ} and M_f, leading to zero contact pressure in the three assemblies at the unclamping temperature T_d. Figure 6.7 shows that the martensitic transformation (TIM) occurs in a wide temperature range during cooling, as demonstrated by the pressure gradient variations around M_S^{σ}. This is attributed to inhomogeneous transformation along the radius of the SMA ring, due to the Clausius-Clapeyron relation (Otsuka and Ren, 2005) and the non-uniform stress distribution along the SMA thickness. A sharper pressure variation is observed when approaching M_f, due to the SMA-steel separation which leads to zero contact pressure at T_d. The latter could be slightly higher than the actual M_f.

This result demonstrates that coupling can be always dismounted by cooling down to M_f (see Fig. 6.8), even if the selected clearance levels are not within the stress-free TW hysteresis range of the material (see Fig. 6.1). This is attributed to several stress-induced mechanism occurring during the first thermal activation, including slips, austenite to martensite transformations, martensite reorientations etc. All these mechanisms cause plastic and or/pseudoplastic deformation which increase the TW-SME of the material. In addition, the applied stress has a training effect on the SMA ring and it increases the volume fraction of favorably oriented martensite variants, resulting in an enhancement of the TW thermal recovery capabilities. In fact, the thermo-mechanical cycle (Fig. 6.7) can be considered as a constrained cycling of deformed martensite (Luo and Abel, 2007).

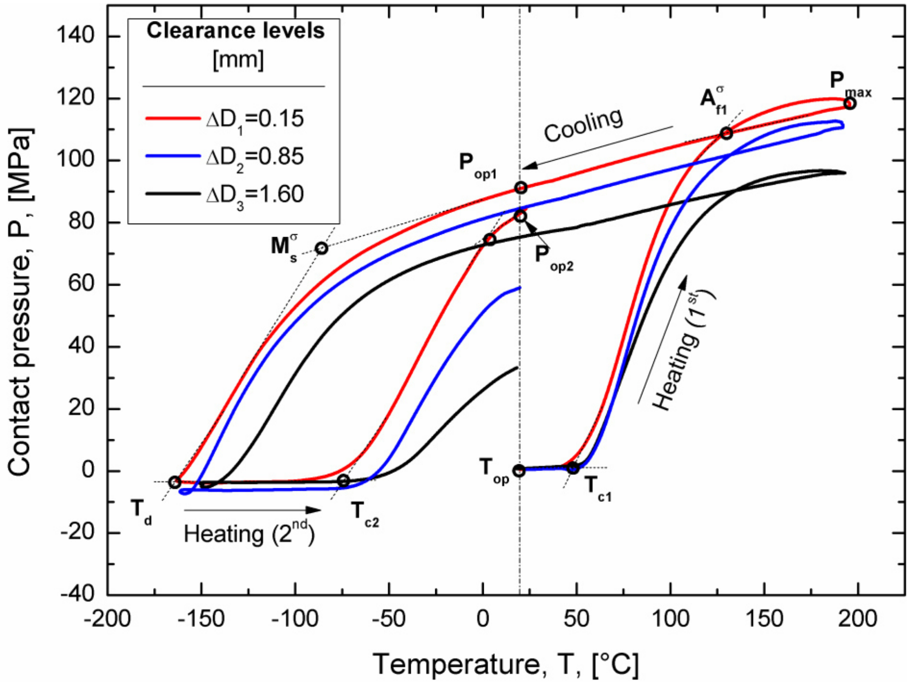

Figure 6.7: Evolution of the contact pressure at the SMA-steel interface as a function of the temperature (*P vs T*) for the three values of initial assembly clearance upon a complete thermal cycle including 1) first thermal activation; 2) cooling down to M_f and 3) re-heating to the operative temperature.

Thermal dismounting is an essential requirement for beam pipe coupling; it allows remote interventions by changing the temperature of the junction unit and reduce the presence of technical personnel close by radioactive equipment.

Finally, Fig. 6.7 shows the pressure evolution when re-heating the ring up to the operative temperature T_{op}. A noticeable increase of the pressure is observed, up to P_{op2}, starting from T_{c2} which represent the SMA/steel contact temperature in the 2nd heating cycle (T_{c2} is equal or slightly higher than the austenite start temperature A_{s2} of the activated material, see Fig. 5.4.a), which is attributed to the TW-SME of the rings. This is a remarkable result as it demonstrates that the coupling can be dismounted and re-mounted without pre-straining the ring thanks to TW-SME. However, it is worth noting that practical limitations exist and they should be taken into account in coupling designing: the temperature range for thermal activation is very low (lower than -70 °C) and the contact pressure at the second activation (P_{op2}) is lower than that resulting from the first one (P_{op1}). In particular, a lower reduction was observed for the minimum clearance (ΔD_1=0.15 mm), from 91 MPa to 82 MPa, while a marked drop was recorded for the maximum clearance (ΔD_3=1.60 mm), from 78 MPa to 34 MPa.

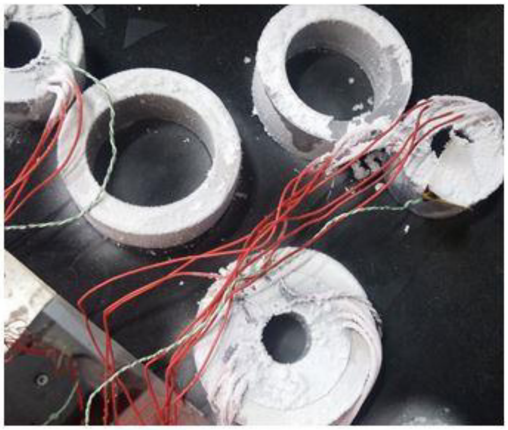

Figure 6.8: Dismounted SMA\steel couplings

In fact, a further increase of the pressure is expected if heating the ring to T_{max} and then cooling again to T_{op} (T_{op}-T_{max}-T_{op}) (see section 7.3). This is evident from the slope of the curve at the end of the second heating, which indicates that thermally induced austenite transformation is not complete. In this case, the aim of the measurements reported in Fig. 6.7 was to analyze the performance of the beam pipe coupling in particle accelerators after a possible cooling (dismounting) and a subsequent natural heating to operative temperature. Further information about the cycling behaviors of SMA couplings are reported in section 7.3.

6.6 Contact pressure analysis in NiTiNb-steel pipe couplings

The contact pressure in NiTiNb-based couplings was analyzed at the gasket/pipe interface. Table 6.1 reports the different analyzed configurations in terms of gasket thickness (*t*) and contact surface ratio (*w*/*B*).

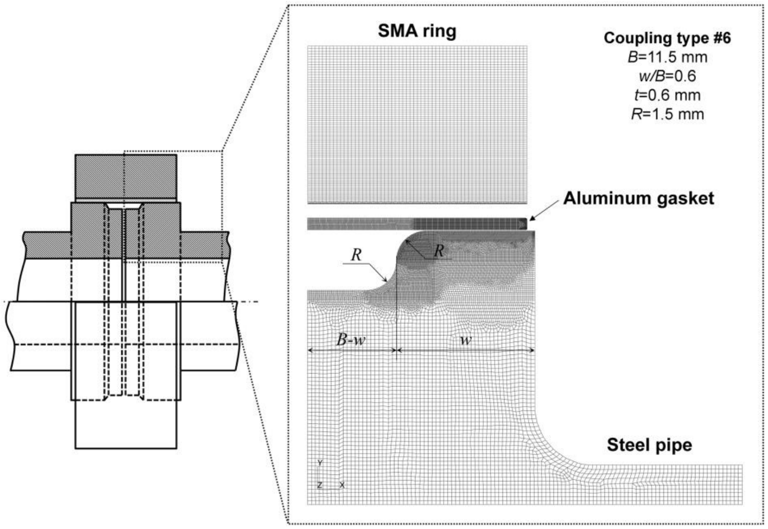

Fig. 6.9. Two-dimensional axisymmetric FE model of the coupling assembly before thermal activation of the SMA ring

Stainless steel rings (AISI 316LN) were used to simulate, as close as possible, the real operating condition in the accelerator as it is the same material normally used for the vacuum chambers. In fact, the CET of this material is different with respect to the 38NiCrMo3, and it could significantly affect the contact pressure evolution during thermal cycling.

The predictions of the FE models in terms of contact pressure during thermal activation (*P vs. T*) were preliminarily validated by comparisons with experimental measurements on NiTiNb/steel couplings (see section 5.4.1).

Table 6.1. Main geometrical parameters of the investigated coupling configurations

Coupling type #	**Gasket thickness, *t* (mm)**	**Coupling ratio, *w/B***
1(1)	None(1)	1.00
2	0.3	1.00
3	0.6	1.00
4	0.9	1.00
5	0.6	0.85
6	0.6	0.60
7	0.6	0.35

(1) 35 μm-thick electroplated copper coating

Figure 6.10 illustrates a comparison between the *P–T* curves for the NiTiNb/steel rings for coupling type #1 (Table 6.1) obtained from FE simulation and SG measurements (see section 5.4.1), where the FE values represent the average pressure along the contact surface. Good agreement between the FE and SG results were observed, with pressure differences after thermal activation (T=T_{op}) of about 5%., as discussed in section 6.3. A final pressure P_{op1} of about 85 MPa was recorded by the SGs. The trend of the curve in Fig. 6.10 is very similar to that obtained previously (see section 6.3) using NiTiNb and 38NiCrMo3 rings. A larger pressure decrease occurs in the NiTiNb/AISI 316LN system when cooling from 200 to 20°C owing to a larger mismatch of the CTE (NiTiNb: 11×10^{-6} °C^{-1}, AISI 316LN: 16.5×10^{-6} °C^{-1}). However, very similar values of the final pressure were obtained at the operative temperature T_{op} (~80 MPa). This represents an interesting result because it demonstrates that, at a certain temperature, the contact pressure is nearly constant because of the constant maximum recoverable stress in the SMAs owing to the transformation plateau in the stress–strain curve.

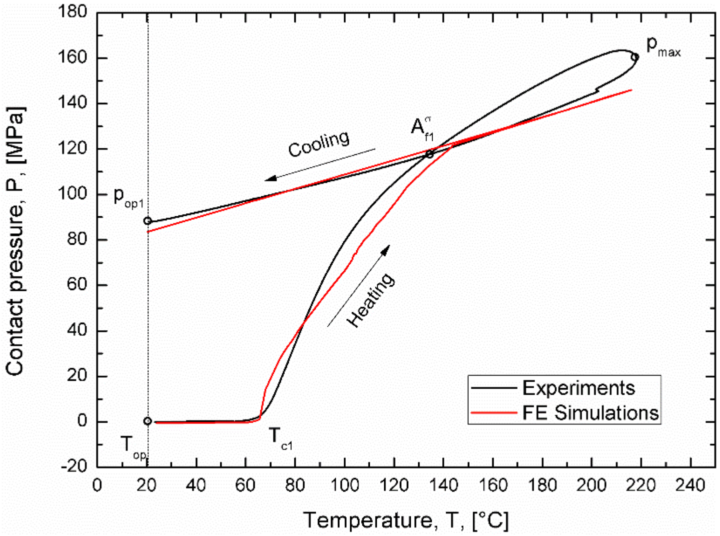

Fig. 6.10. Contact pressure at the ring/steel interface as a function of the temperature (*P vs. T*) for NiTiNb/steel ring coupling (ΔD=0.15) during thermal activation: comparison between strain gauge and finite element data

Figure 6.11 illustrates the pressure profiles along the contact line; *i.e.*, as a function of the normalized distance *s*/*B*, obtained from FE simulations for the coupling types #1, 2, 3 and 4 in Table 6.1.

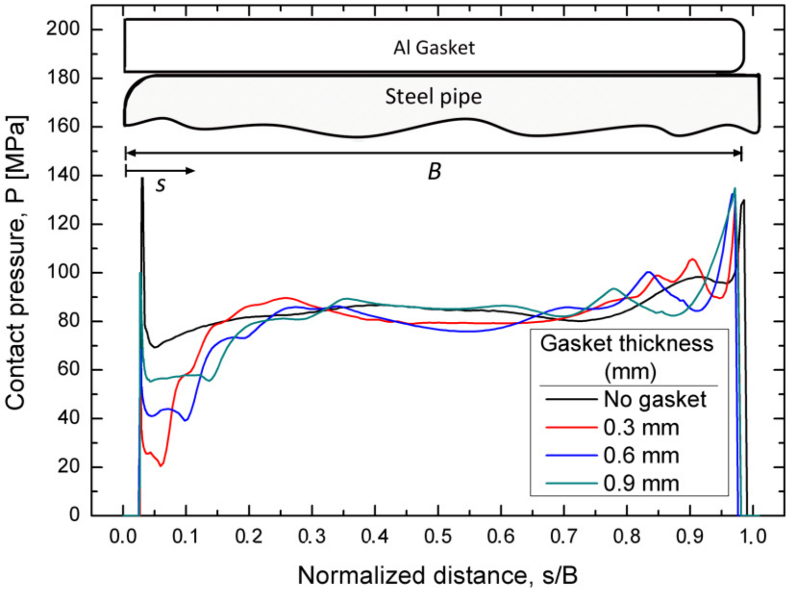

Fig. 6.11. Effects of the gasket thickness on the contact pressure (*P*) by FE simulations: *P vs*. normalized length (s/*B*), for the coupling types #1, 2, 3 and 4 (*w*/*B*=1)

In particular, four different configurations with a fixed contact surface ratio (*w*/*B*=1) and with different gasket thicknesses (None, 0.3, 0.6 and 0.9 mm) were compared. The curves show very similar trends with nearly constant pressures in the middle of the contact region (0.15<*s*/*B*<0.9), while local variations are observed at the symmetry plane (*s*/*B*=0) and at the end of the contact surface (*s*/*B*=1). The variations at the symmetry plane are attributed to the edge radius of the steel pipe, which generates local bending effects on the gasket. In particular, a local increase followed by a sharp decrease of the contact pressure is observed. Similar considerations can be extended to the local variations at the extremities of the contact region owing to the gasket edge radius.

Figure 6.12 illustrates the von Mises stress distribution in the steel pipe for the coupling type #3 (*w*/*B*=1 and *t*=0.6 mm) after the complete SMA thermal activation (T_{op}=20°C). As expected, maximum stresses are observed at the internal diameter of the pipe, but they never exceed the yielding limit of the steel. Very similar results are recorded for the other coupling configurations of Fig.6.11

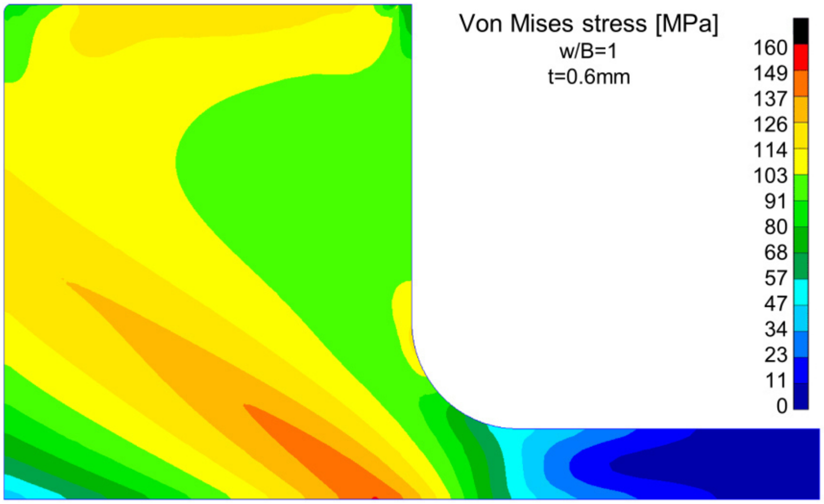

Fig. 6.12. von Mises stress distribution in the steel pipe for the coupling type #3 (*w*/*B*=1 and *t*=0.6 mm)

Finally, the results in Fig. 6.11 can be summarized as follows: the thickness of the gasket does not significantly affect the pressure distribution at the gasket/steel interface, and an average contact pressure value of 81 MPa was estimated with only small variations among the investigated configurations. This is a very interesting result because it demonstrates that gaskets with a customized thickness can be manufactured to fill the initial assembly gaps between the pipe and SMA ring. In fact, tolerances of the internal diameter of the SMA ring cannot be accurately controlled owing to the complex mechanisms occurring during mechanical pre-strain (*e.g.*, plastic deformations, phase transformations, re-orientations of martensite variants, elastic recovery, etc.). The dismounting of the SMA ring can be obtained by cooling (see section 6.5) owing to the two-way behavior of the alloy; however, it is worth noting that a large gasket thickness could affect the demountability of the chambers/gasket assembly at low temperatures owing to the thermal stresses occurring in the steel and the aluminum components because of the mismatch of the CTE.

On the contrary, easier dismounting is obtained with small thicknesses (0.3 mm), due to the lower stiffness and higher deformability of such gasket.

Figure 6.13 reports the effects of the contact surface ratio (*w*/*B*) on the contact pressure profiles. In particular, the curves *P vs. s*/*B* for four different coupling configurations with fixed gasket thickness (*t*=0.6 mm) and with *w*/*B*=1, 0.85, 0.6 and 0.35 are compared (Types #3, 5, 6 and 7, respectively).

The curves with *w*/*B*<1 show a similar behavior, where a pressure peak is initially observed at the beginning of the contact region followed by a pressure drop; this is attributed to bending effects of the gasket near the edge radius, as discussed previously.

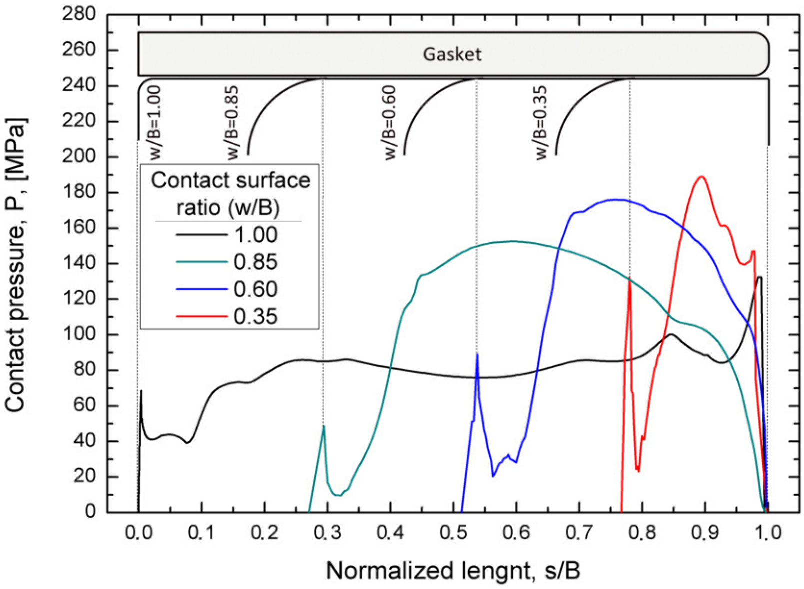

Fig. 6.13. Effects of the contact surface ratio (*w*/*B*) on the contact pressure (*P*) by FE simulations: *P vs.* normalized length (s/*B*), for the coupling types #3, 5, 6 and 7 (*t*=0.6 mm and *w*/*B*=1, 0.85, 0.60, 0.35)

A subsequent marked increase of the pressure is observed up to a maximum value around the middle of the contact line, where small pressure variations are observed around the maximum value followed by a final drop at the end of the contact line. These effects are qualitatively shown in the fringe plot of Fig. 6.14, which reports the von Mises stress for coupling type #6 (*t*=0.6 mm and *w*/*B*=0.6) after the SMA thermal activation (*T*=20°C). Both the peak at the beginning of the contact line and the maximum values at the middle are shown. In any case, the maximum von Mises stresses never exceed the yield strength of the material during the entire SMA clamping process.

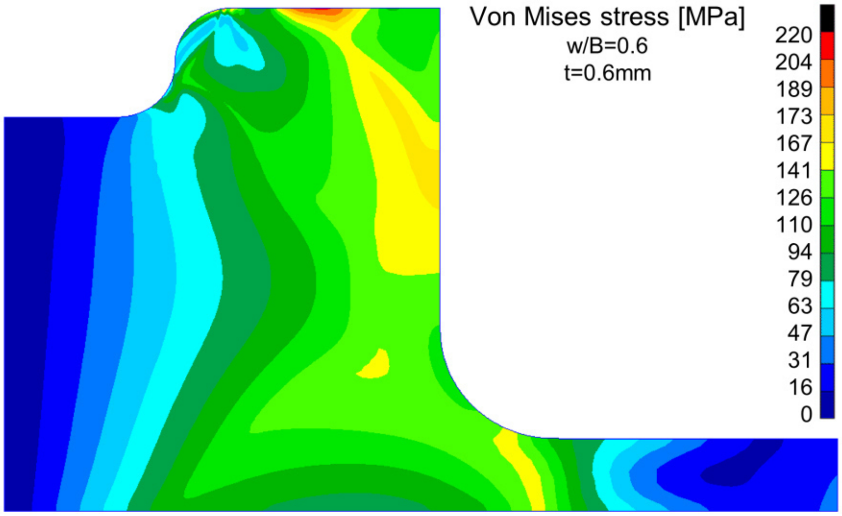

Fig. 6.14. von Mises stress distribution in the steel pipe for the coupling type #6 (*w*/*B*=0.60 and *t*=0.6 mm)

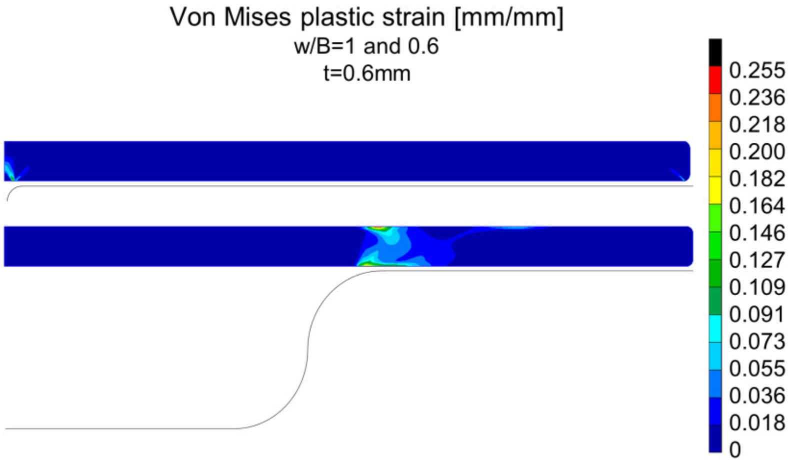

Fig. 6.15. von Mises plastic strain distribution in the gasket for the coupling types #3 (*w*/*B*=1 and *t*=0.6 mm) and #6 (*w*/*B*=0.60 and *t*=0.6 mm)

Figure 6.15 shows the von Mises plastic strain distribution in the aluminum gasket for the coupling types #3 (*w*/*B*=1 and *t*=0.6 mm) and #6 (*w*/*B*=0.60 and *t*=0.6 mm). In both cases, the highest strain values are reached near the edge radius of the steel pipe, mainly owing to local bending phenomena. In particular, maximum plastic strains of about 25% occur for the coupling type #6, while lower deformation values never higher than 17% take place locally in the coupling type #3. In both configurations, most of the gasket volume is not plastically deformed thanks to the high stress triaxiality occurring in the gasket during the SMA ring activation. However, it is worth noting that only bulk plastic phenomena are simulated by the FE analysis. In fact, localized plastic deformations owing to the real contact surface profile (peaks and valleys randomly distributed) are not taken into account.

Figure 6.16 reports the values of the maximum (P_{max}) and average pressures (P_{ave}) as well as of the total normal force acting on the contact surface (F_N), for the four coupling types of Fig. 6.13, as a function of the contact surface ratio (*w*/*B*). The total normal force was computed as the surface integral of the pressure distribution over the entire contact area. It was found that the normal force increases significantly with the ratio *w*/*B* (*i.e.*, with increasing the contact area) from about 50 kN for *w*/*B*=0.35 to about 120 kN for *w*/*B*=1. As a consequence, a pressure decrease is observed when *w*/*B* increases. In fact, P_{ave} ranges from about 80 MPa for *w*/*B*=1 to about 125 MPa for *w*/*B*=0.35.

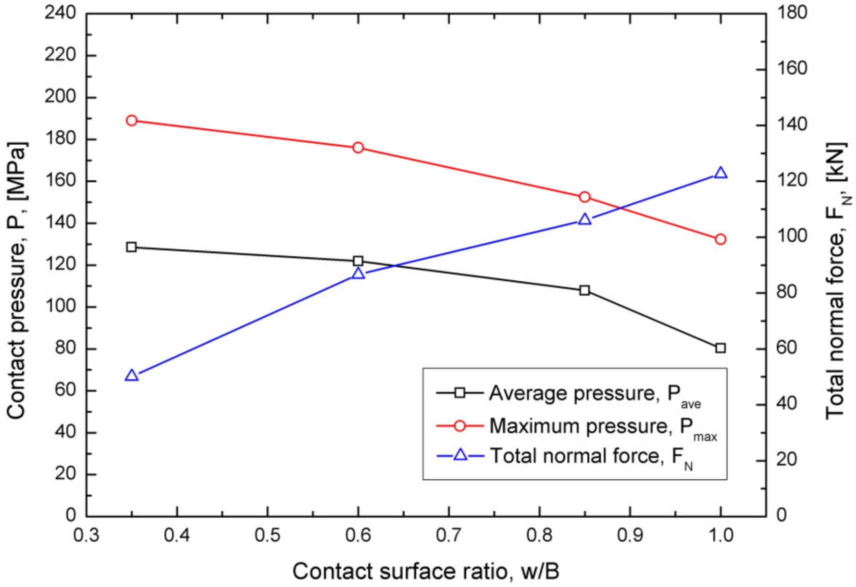

Fig. 6.16. Maximum pressure (P_{max}), average pressure (P_{ave}) and total normal force (F_N) as a function of the contact surface ratio (*w*/*B*)

6.7 Leak tightness performance calculation

The leak tightness performance of the couplings in Table 6.1 were calculated by the conductance model described in Section 5.5.3. Figure 6.17 illustrates the sealing parameter (*S*) (see Eq. 5.16) as a function of the contact surface ratio (*w*/*B*) for aluminum gaskets. In Fig. 6.17, the parameter *S* was calculated using the average pressure values obtained from numerical simulations (see Fig. 6.16). The effects of the effective sealing width ($0.1 \leq \xi \leq 1$, where $\xi = w_e/w$) and of the sealing factor *R* were analyzed. Lower and upper bounds for *R* equal to 30 MPa (soft Al) and 60 MPa (hard Al), respectively, were considered, as recommended in literature (Roth, 1972).

As expected, Fig. 6.17 shows that *R* plays a very important role in the leak tightness performance of the coupling. In fact, the sealing parameter *S* increases by about a factor of 10^3 when decreasing *R* from 60 to 30 MPa. Therefore, a fully annealed aluminum alloy should be used for gasket manufacturing. Furthermore, the sealing performance increases when the effective sealing width, w_e, increases, as shown in Eq. 5.15)

Finally, Fig. 6.17 shows that coupling configurations with w/B=1 never provide the best performance. On the contrary, couplings with w/B=0.35 (Type #7) represent the best choice in terms of leak tightness (*i.e.*, *S* is maximized when *R*=30 MPa), but limited differences are observed with respect to the configuration with w/B=0.60 (Type #6). This latter coupling type becomes the best solution when increasing the sealing factor *R* to 60 MPa.

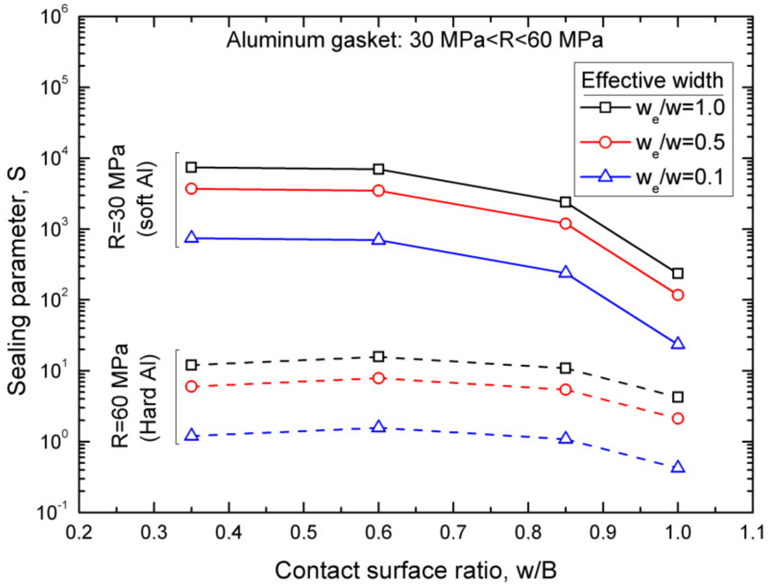

Fig. 6.17. Sealing parameter (*S*) for aluminum gaskets as a function of the contact surface ratio (w/B) for different values of the effective sealing width w_e ($0.1 \leq \xi \leq 1$, $\xi = w_e/w$) and of the sealing factor *R* (30 and 60 MPa)

The data reported in Fig. 6.17 does not take into account the effective pressure distribution along the contact surface, because they were obtained from average pressure values (P_{ave}). Further, the use of average pressures would result in significant underestimation of the sealing performance. In fact, the leak rate exhibits an exponential decrease with the contact pressure *P* and, therefore, local pressure increases are expected to play a significant role in the leak tightness capabilities of the couplings.

To overcome this limitation, the sealing parameter *S* was calculated by a numerical integration of the effective pressure distribution along the contact surface. In particular, a linear integration rule was adopted, according to the element used for the mesh:

$$S = (\xi/\pi d_e) \int_0^w \exp(3\,P/R) ds \cong (\xi/\pi d_e) \sum_{i=1}^{n} \exp(3(P_{i+1} + P_i)/2R)\,(s_{i+1} - s_i), \quad (6.1)$$

where ξ is the effective width ratio ($\xi = w_e/w$), s_i is the coordinate of the *i*th node along the contact line (see Fig. 6.11), P_i is the nodal contact pressure and *n* is the total number of elements on the contact line.

Figure 6.18 reports a comparison between the sealing parameters *S* obtained from the average pressure values and those obtained from the effective pressure distribution (Eq. 6.1) for the case ξ=w_e/*w*=1. As expected, the method based on the effective pressure profile gives higher estimates of the parameter *S*, up to a factor of around 50 for *R*=30 MPa. In addition, it was found that couplings with *w*/*B*=0.6 always give the best results in terms of the sealing parameter *S*.

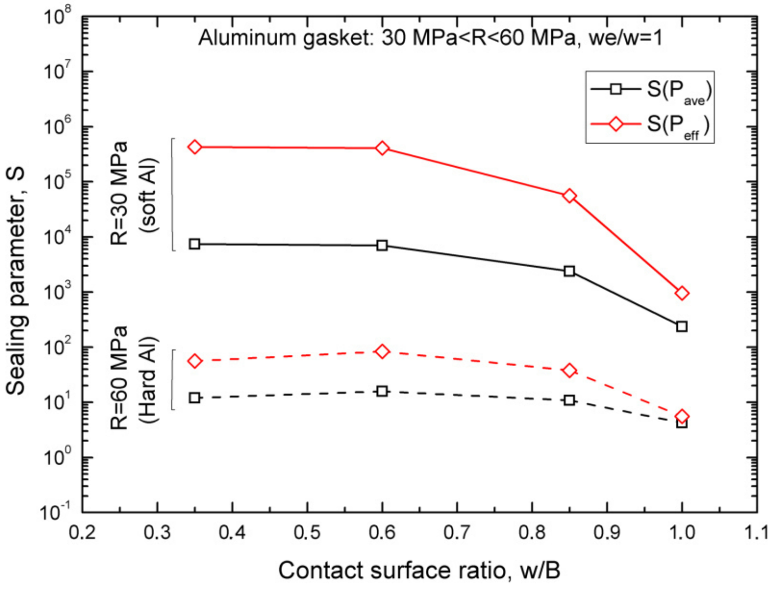

Fig. 6.18. Sealing parameter (*S*) for aluminum gaskets (ξ=w_e/*w*=1, *R*= 30 and 60 MPa) as a function of the contact surface ratio (*w*/*B*): comparison between data obtained using the average pressure and that using the effective pressure distribution.

Figure 6.19 illustrates a comparison between the sealing parameter *S* of aluminum and copper gaskets, obtained using the effective pressure distribution.

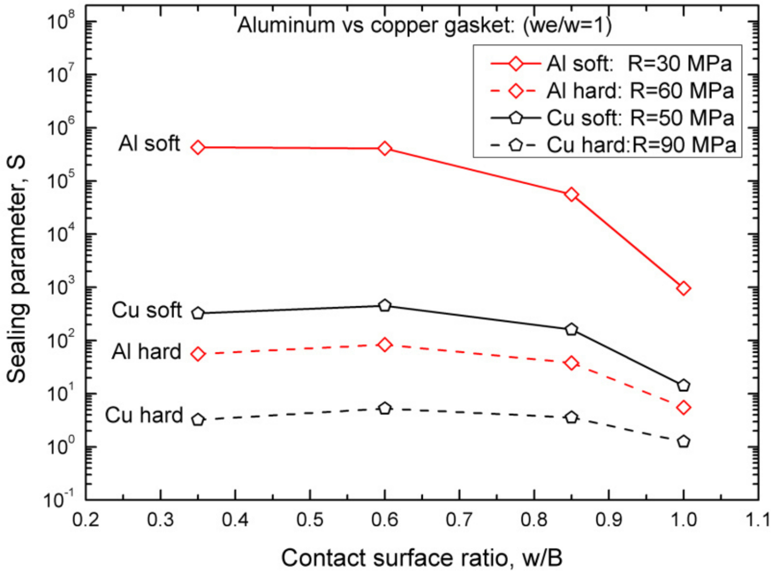

Fig. 6.19. Sealing parameter (*S*) ($\xi = w_e/w = 1$) as a function of the contact surface ratio (*w*/*B*): comparison between aluminum (*R*=30 and 60 MPa) and copper (*R*=50 and 90 MPa) gaskets.

The lower and upper bounds for *R*=50 MPa (soft Cu) and 90 MPa (Hard Cu) were considered for the copper gaskets, as recommended in literature (Roth ,1972). It was found that soft aluminum gaskets give the best sealing performance, with very high differences in the parameter *S* (a factor of around 10^3 with respect to soft Cu).

6.8 Leak tightness performance measurement

The leak tightness values of couplings types #1, 2, 3 4, 5, 6 in Table 6.1 were assessed using a prototype vacuum chamber, as described in Section 5.6. As shown in Table 6.2, the tests were carried out under three different conditions:

a) immediately after the clamping and bake-out cycle, to assess the effectiveness of the coupling process owing to the OW-SME;
b) after 1 year of aging at room temperature, to verify the leak-tightness evolution of the assembly owing to possible creep-like mechanisms occurring in SMA rings;
c) after complete thermal cycles comprising cooling below M_f (−170°C), re-heating above T_{max} (200°C) and cooling again to T_{op} (20°C), to assess the effectiveness of the TW-SME.

Table 6.2 summarizes the results of the leak tightness tests. It was found that all analyzed conditions were tight, and that the leak rate was always smaller than the standard requirement for UHV applications in particle accelerators (less than 10^{-10} mbar l s^{-1}).

Table 6.2. Results of leak tightness tests under different testing conditions

Coupling #	**Testing conditions**	**Leak rate** (mbar·l·s^{-1})
1	1.a: After clamping	$<10^{-10}$
1	1.b: After 1 year aging	$<10^{-10}$
1	1.c: After complete thermal cycle (aged samples)	$<10^{-10}$
2	2.a: After clamping	$<10^{-10}$
2	2.b: After 1 year aging	$<10^{-10}$
2	2.c: After complete thermal cycle (aged samples)	$<10^{-10}$
3	3.a: After clamping	$<10^{-10}$
3	3.b: After complete thermal cycle	$<10^{-10}$
4	4.a: After clamping	$<10^{-10}$
4	4.b: After complete thermal cycle	$<10^{-10}$
5	5.a: After clamping	$<10^{-10}$
5	5.b: After complete thermal cycle	$<10^{-10}$
6	6.a: After clamping	$<10^{-10}$
6	6.b: After complete thermal cycle	$<10^{-10}$

Figures 6.18 and 6.19 illustrate that couplings with w/B=1 (Types #1 and 2) always exhibit the worst sealing performance in terms of the sealing parameter S. In addition, Fig. 6.19 clearly shows that the copper layer in coupling type #1 exhibits a marked decrease of the parameter S (a factor of around 10^3) with respect to aluminum gaskets. This is a noticeable result because it was found that these coupling types are leak-tight (see Table 6.2.) even after aging and complete reactivation. The configurations with the best sealing performance, *i.e.*, those with w/B=0.6, are expected to provide the highest reliability levels. For these reasons, the latter configurations are mainly exploited in NiTi based-connectors, widely investigated in chapter 6.

7. NiTi-BASED COUPLERS FOR ULTRA-HIGH VACUUM PIPES

7.1 Introduction

The proposed NiTiNb-based systems, described in chapter 6, were demonstrated to be viable devices for beam-pipe couplings in particle accelerators. Their functional properties coped with the CERN operational constraints (mounting and dismounting obtainable by temperature variation) and their leak tightness were verified even after multiple activation cycles. Furthermore NiTiNb-based couplers represent a reliable solution; NiTiNb rings can guarantee a full clamping force over a wide thermal range (-70°C/200°C). The only limitation of such couplings is related to the low dismounting temperature (-150°C) which is intrinsically related to the martensitic TT of the NiTiNb alloy investigated.

On the contrary, binary NiTi alloys have higher martensitic TT and lower thermal hysteresis (A_s-M_f) than ternary NiTiNb ones; unfortunately, this implies a lower thermal range with full clamping force but also a faster disconnection owing to higher dismounting temperatures. The latter feature represents a crucial benefit in view of the HL-LHC project that will increase radiation doses by a factor of 16 in some selected areas of particle accelerators.

Following the optimization studies carried out on NiTiNb couplers (see chapter 6), NiTi-based coupler were proposed. Non-commercial NiTi rings (Ni55Ti45 wt%) *ad-hoc* developed by Intrinsic Devices Inc. based on CERN technical constraints, were used for this purpose (see section 5.2). These rings are properly trained to exhibit two-way behavior (see section 4.2.5). Experimental analyses of *ad-hoc* developed NiTi rings and NiTi/steel couplings are reported in the following sections. NiTi-based couplers clearly represent the optimized version of the proposed SMA-based couplers.

7.2 NiTi characterization

Based on the constraints described in section 5.2, non-commercial NiTi rings, manufactured by Intrinsic Devices Inc., were properly selected and analyzed. The main thermo-mechanical properties of the selected alloy (Ni55Ti45 wt.%) were measured by thermal cycles and tensile tests of NiTi rods (3.2 mm diameter) as described in section 5.3.

Figure 7.1.a shows the curve true strain *vs* temperature (ε-T) obtained from the first stress-free heating stage (=3*10^{-2} °C*s^{-1}) above the austenite finish temperature of the pre-strained rod ($T>A_{f1}$), giving the OW-SME. Furthermore, TW-SME obtained from a subsequent thermal cycle between the TTs ($T<M_f$ and $T>A_f$) is also shown. A marked reduction (about 45 °C) of the austenite transformation temperature (A_{s2} and A_{f2}) after the first thermal activation was observed. The figure shows that M_S (-22 °C) in stress free condition is sufficiently lower than T_{op} (20 °C). Furthermore, the constraints on austenite TTs are also satisfied because A_{s1}(40 °C) is higher than the mounting temperature T_M (35 °C).

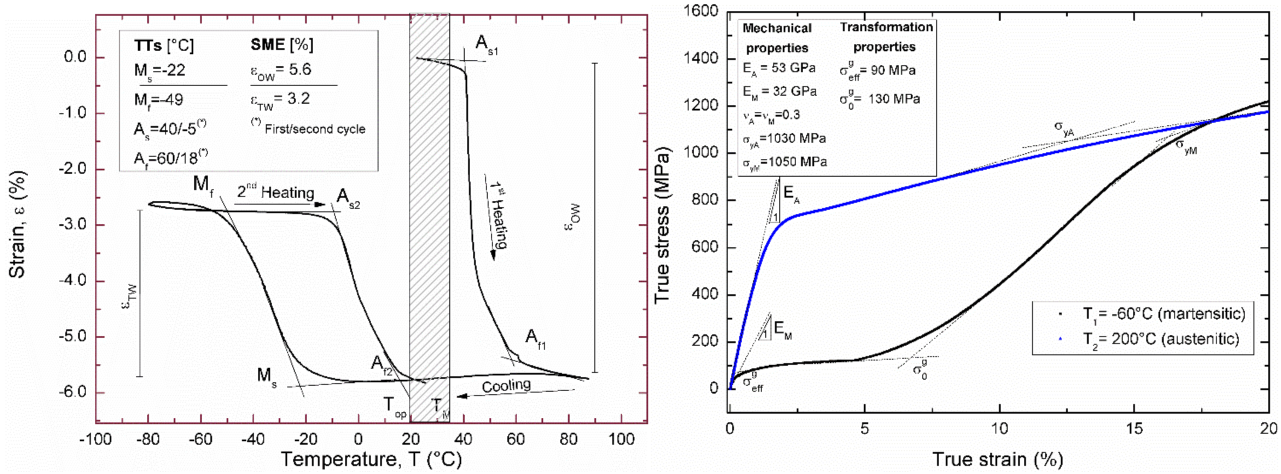

Figure 7.1: Thermo-mechanical properties of the investigated NiTi alloy: a) true strain vs temperature (ε-T) obtained from a stress-free thermal cycle between the TTs and b) Isothermal uniaxial true stress *vs* true strain response (σ-ε) for three different values of the testing temperature.

Figure 7.1.b illustrates the isothermal true stress-true strain (σ–ε) response of the alloy (=5*10^{-4} s^{-1}) at three different temperatures: T_1=-65 °C, T_2= 200 °C. As shown in Fig.7.1b, the temperature T_1 corresponds to fully martensitic condition (the rod was previously cooled down to M_f) while T_2 corresponds to fully austenitic conditions ($T_2>A_{f1}$). However, the alloy exhibits an elastic plastic behavior at $T=T_2$, *i.e.* with no evidence of stress-induced transformation (see Fig.7.2b). This denotes that T_2 is higher than the martensite desist temperature ($T_2>M_D$).

7.3 Stress-free and stress-applied tests of NiTi rings

The free recovery capabilities of the NiTi rings were studied, in terms of both OW-SME and TW-SME as described in sections 5.3. Figure 7.2 shows the normal circumferential strain (ε_θ) at the internal diameter of the SMA ring, together with the diameter variation ($\Delta D=\varepsilon_\theta D_i$), as a function of the temperature (T). A OW recovery strain (ε_{OW}) of about 5.2% was observed, corresponding to an internal diameter variation ΔD of about 2.4 mm. The TW strain (ε_{TW}) is about 2.2%, corresponding to ΔD=1.25 mm. Furthermore, a direct comparison between Figs. 7.1.a and 7.2 reveals a similar behavior between NiTi rods and rings. Very similar values of both TTs and OW/TW strains were found, as well as the same drop in the austenite transformation temperatures after the first thermal activation. This is a relevant result that confirms that the material was properly selected in order to cope to the constraint of beam-pipe coupling applications. In fact, the *ad-hoc* developed NiTi ring are suitable for CERN purposes ($T_M < A_{s1}$ and $T_{op} > M_s$).

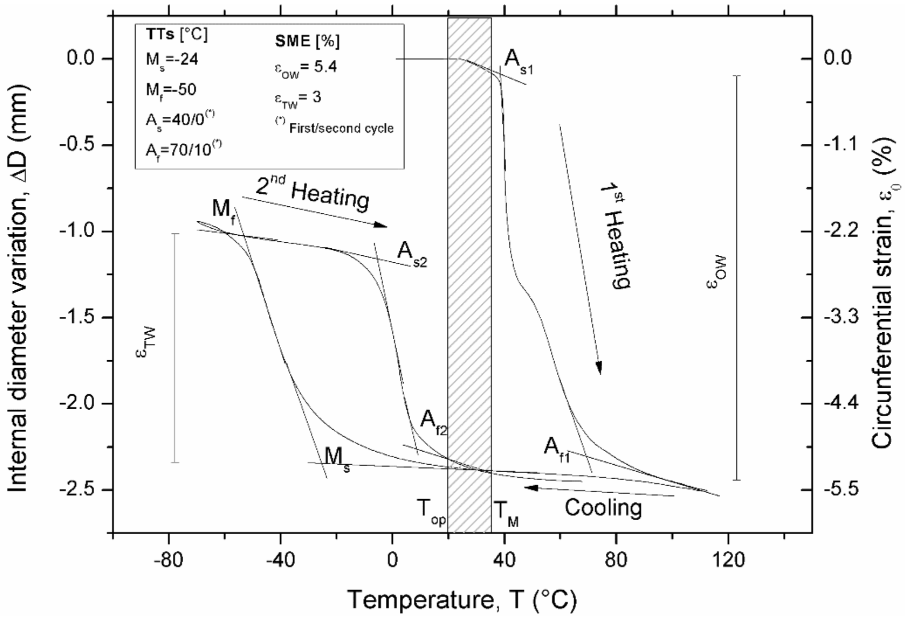

Figure 7.2: Stress free One Way and Two Way shape memory recovery capabilities of a NiTi ring together with the values of the main functional parameters.

Furthermore, the recovery force of the SMA ring against a steel ring was measured by strain gauges, as described in section 5.4.1. The initial SMA/steel clearance value, ΔD in Fig. 5.5, was 0.15 mm corresponding to the minimum clearance configuration which maximize the clamping pressure as previously assessed (see section 6.3).

In particular, a stainless steel with high yield strength was chosen (UNS S20910) to avoid plastic deformation at the inner diameter during thermal activation of the SMA ring. The selected steel has identical coefficient of thermal expansion (16.5 $*10^{-6}$ °C^{-1}) to the 316LN steel normally used for the UHV chambers at CERN. This is an important issue, because the mismatch between the CET of SMA and steel significantly affect the contact pressure at the interface (*P*) during thermal cycling. The contact pressure *P* was calculated starting from the strain measurements, based on theory of elasticity (see equation 5.1)

The evolution of *P* during two subsequent thermal cycles was studied. The temperature-time path of the two cycles is reported in Fig.7.3. Each cycle includes a thermal activation by heating the assembly slowly ($\dot{T}$=0.033 °C/s) to a temperature T_{max} of about 200°C, a subsequent cooling down to $T_{min} \approx M_f$ to verify relaxation effects and dismounting, and a second heating from T_{min} to the operative temperature T_{op}. Finally, at the end of the second cycle, the assembly was heated up to a temperature, T_f = 95°C, above the stabilized austenite finish temperature under stress of the SMA ring ($T > A^{\sigma}_{f2}$). The clamping pressure vs temperature curve of the NiTi/steel assembly is shown in Fig. 7.4.

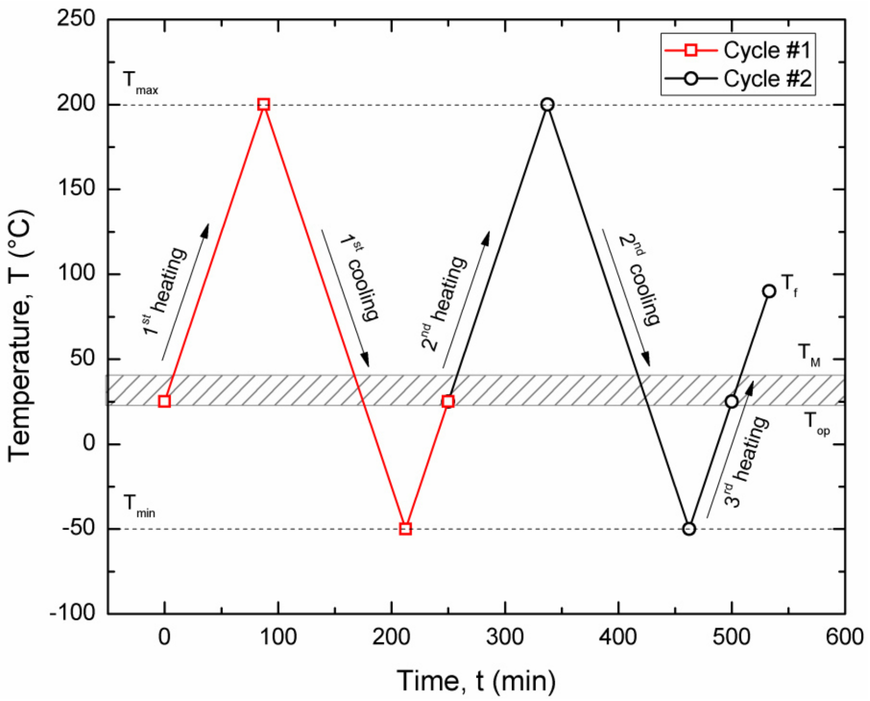

Figure 7.3: Temperature-time path of the assembly for the investigated thermal cycles

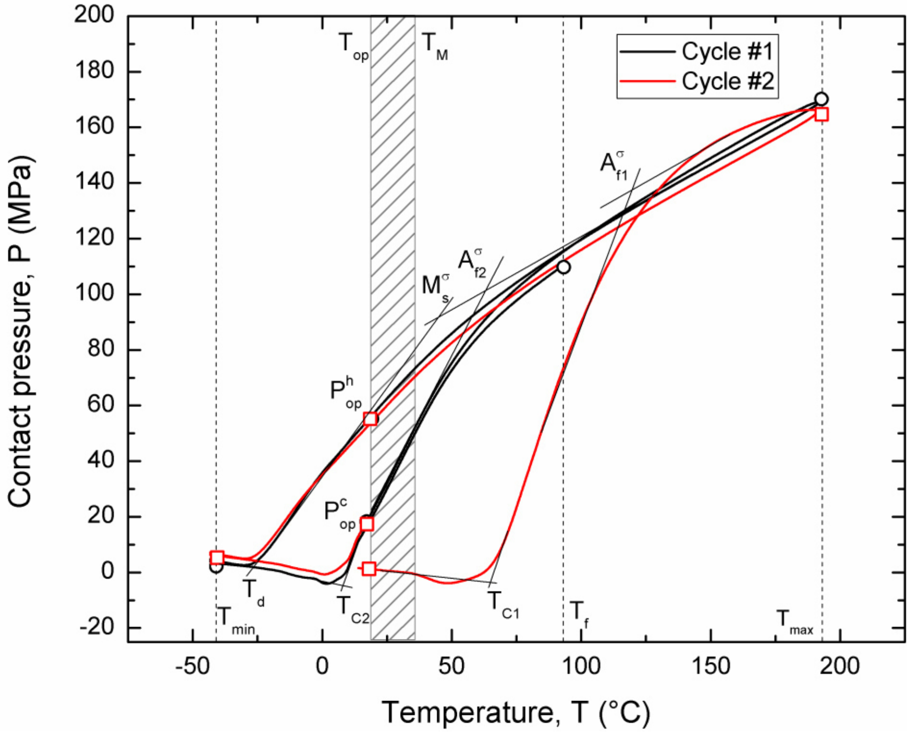

Figure 7.4: Evolution of the contact pressure at the SMA-steel interface as a function of the temperature (*P vs T*) for the two investigated thermal cycles

The red curve in Fig.7.4 shows the P-T evolution of the 1st thermal cycle (cycle #1 in Fig.7.3). The different steps of thermal activation and further dismounting are clearly identifiable: the ring start to contract at $T= A_{s1}$ (see Fig.6.2) and ring-pipe uniform contact occurs at $T=T_{c1}$. In fact, as discussed in section 6.3, A_{s1} is slightly lower than T_{c1} due to the initial assembly clearance between SMA and steel rings. As expected, a marked increase of the contact pressure is observed when increasing the temperature between T_{c1} and A_{f1}^{σ}, as a consequence of the thermally induced OW recovery mechanisms. As discussed in section 6.5, A_{f1}^{σ} corresponds to the temperature at which the SMA ring, under stress, becomes fully austenitic *i.e.* without thermally induced or stress induced martensitic variants. However, an increase of the pressure is observed with further increase the temperature above A_{f1}^{σ}, up to a maximum pressure P_{max} at $T=T_{max}$. This is attributed to several mechanisms, as discussed in section 4.3.2, including the mismatch of the thermal expansion coefficients between the two materials ($11*10^{-6}$ °C^{-1} for SMA and $16.5*10^{-6}$ °C^{-1} for steel) and the variation of the SMA stiffness with the temperature. Consequently, a decrease of the contact pressure is observed when cooling down to the operative temperature (T_{op}=20 °C) where a final operative pressure P_{op}^{h} of about 55 MPa was measured.

Observing the P-T curve in cycle #1, it is evident that T_{op} is slightly lower than martensite start temperature under stress ($M_s^{\sigma} \approx 40°\mathrm{C}$) but, although the presence of thermally induced martensitic variants in the SMA, a significant clamping pressure has been recorded at T_{op}, confirming the effectiveness of the chosen material. In fact, even if P_{op}^{h} is lower than that obtained with NiTiNb rings (see section 6.5), it has been demonstrated to be sufficient to obtain leak-tight joints (see section 7.4). A further cooling to T_d =-30°C leaded to zero contact pressure. T_d is higher than M_f; in fact, NiTi rings continue to enlarge with further cooling (see Fig. 7.2). The martensitic transformation occurs in a wide temperature range during cooling, as demonstrated by the pressure gradient variations around M_s^{σ} similarly to NiTiNb/steel assemblies (section 6.5). The first cycle ended with a reheating up to T_{op}. A noticeable increase of the pressure starts at T_{c2} (about 10°C) which is higher than A_{s2} (see Fig. 7.2), owing to the TW-SME of the rings. It is worth noting that the contact pressure measured at T_{op}, namely P_{op}^{c}, is considerably lower than that resulting from the first activation (P_{op}^{h}). As discussed for NiTiNb/steel assemblies (see section 6.5), this indicates that the thermally induced austenite transformation is not complete.

In cycle #2 (see black curves in Fig.7.4), the further heating induces a fully austenitic structure in the SMA. At temperatures higher than A_{f2}^{σ} (about 60°C) the recorded clamping pressure becomes almost identical to that measured for cycle #1 and its trends and values during the subsequent temperature cycles (from T_{max} to T_{min} and from T_{min} to T_f) are very similar to those corresponding to the cycle #1. In fact, P_{op}^{h} and P_{op}^{c} are almost identical for the two investigated thermal cycles.

These results demonstrate that, these *ad hoc*-developed NiTi-based coupling can guarantee almost identical performance in terms of clamping pressure for at least 3 subsequent activations (heating stage at temperatures above T_{max}) following 2 dismounting (cooling stages) at temperatures below T_d.

This is a remarkable result as it demonstrates that coupling can be dismounted and re-mounted without pre-straining the SMA rings thanks to effective TW-SME occurring for at least three subsequent thermal cycles. The only practical limitations that should be taken into account in coupling designing are related to the shift of the austenitic TT between the first and the other thermal activation cycles with a consequent decrease of the contact temperature (T_{c2}) and the austenite finish temperature under stress (A_{f2}^{σ}) of about 40-50°C. In particular, mounting processes at subsequent cycles have to be carried out at temperatures lower than T_{op} ($T<0°C$).

7.4 Leak tightness measurement and assembly dismounting

Figure 7.5 illustrates a schematic depiction of the investigated NiTi–steel pipe coupling assembly for UHV systems, together with the main characteristic dimensions. The assembly comprises steel pipes (AISI 316LN), the SMA ring ($Ni_{49.9}Ti_{50.1}$), and an aluminum (EN AW-6082-O) or a copper (C10100-O) gasket.

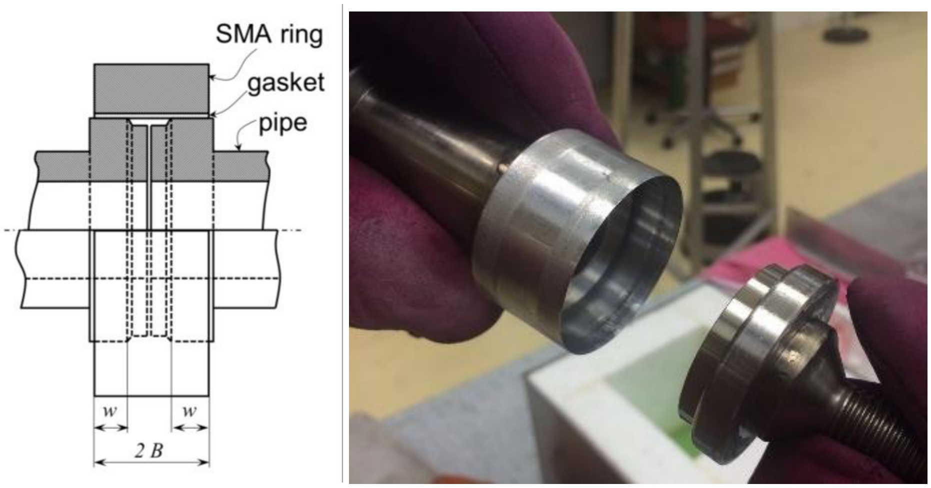

Figure 7.5. Schematic depiction and photography of the proposed SMA–pipe coupling assembly for UHV systems comprising steel pipes (AISI 316LN), SMA ring (Ni55Ti45 wt.%), and aluminum (EN AW-6082-O) or copper (C10100-O) gasket

The effects of different coupling configurations, obtained by varying the gasket thickness and the contact surface ratio (w/B), are analyzed and discussed in the following sections.

Different configurations with three different clearance, ΔD, ranging from 0.15 mm to 1.60 were experimentally investigated in order to verify that the leak rate, similarly to the contact pressure (see section 6.5), is not significantly affected by the SMA/steel assembly initial clearance. The gasket thickness has been kept fixed at t=0.3 in order to limit the thermal stresses (due to the thermal expansion coefficient mismatch) occurring in the chamber/gasket assembly when it is cooled down *to* T_d, for the dismounting.

Table 7.1. Main geometrical parameters of the investigated coupling configurations used for leak tightness tests

Coupling type #	**Gasket material**	**Gasket thickness, *t* (mm)**	**Coupling ratio, *w/B***	**Initial SMA/gasket clearance**
1	Copper	0.3	1.00	0.15
2	Copper	0.3	1.00	0.85
3	Copper	0.3	1.00	1.60
4	Copper	0.3	0.6	0.15
5	Copper	0.3	0.6	1.60
6	Aluminum	0.3	1.00	0.15
7	Aluminum	0.3	1.00	0.85
8	Aluminum	0.3	1.00	1.60
9	Aluminum	0.3	0.6	0.15
10	Aluminum	0.3	0.6	1.6

The leak tightness of the couplings in Table 7.1 were assessed using prototype vacuum chambers similarly to those described in Section 5.6. Both optimized (w/B=0.6) and non-optimized (w/B=1) chamber geometries were investigated (see section 5.5.4). As shown in Table 7.2, the tests were carried out under three different conditions:

d) immediately after the clamping and bake-out cycle, to assess the effectiveness of the coupling process owing to the OW-SME;
e) after 6 month of aging at room temperature, to verify the leak-tightness evolution of the assembly owing to possible creep-like mechanisms occurring in SMA rings;
f) after two complete thermal cycles. Each of them comprised a cooling below M_f (−50°C), re-heating at T_{max} (200°C) and cooling again to T_{op} (20°C), to assess the effectiveness of the TW-SME in case of multicycle applications.

Table 7.2summarizes the results of the leak tightness tests. It was found that all analyzed assemblies, in all the investigated conditions were tight, and that the leak rate was always smaller than the standard requirement for UHV applications in particle accelerators (less than 10^{-10} mbar l s^{-1}).

Table 7.2 Results of leak tightness tests on NiTi-based couplers under different testing conditions

Coupling #	**Testing conditions**	**Leak rate** (mbar·l·s^{-1})
1,2,3,4,5	a: After clamping	$<10^{-10}$
1,2,3,4,5	b: After 6 month aging	$<10^{-10}$
5,6,7,8,9,10	a: After clamping	$<10^{-10}$
5,6,7,8,9,10	b: After 6 month aging	$<10^{-10}$
5,6,7,8,9,10	c: After two complete thermal cycles	$<10^{-10}$

It is important to underline that the unclamping after cooling below $T=T_d$ (see Fig. 7.6) have been verified for all the investigated configurations after the leak tests and both the NiTi ring and the gaskets have been disassembled easily. Liquid nitrogen was used to cool the rings down to T_d for removal and different methods were assessed. Firstly, dismounting was obtained by immersing the parts in liquid nitrogen. This method provided very quick cooling and dismounting (<2min) but it cannot be applied in service. As a consequence, dismounting was also analyzed by other methods: a felt collar covering the SMA ring (see Fig. 7.6) soaked with liquid nitrogen and a jet of pressurized (20 bar) nitrogen. Both methods provided easy dismounting of all assemblies for removal with a recorded cooling time (from T_{op} to T_d) of about 3.5 minutes.

Fig.7.6. Prototype NiTi-based connector wrapped with wool felt wicking liquid nitrogen

7.5 Outgassing measurements of NiTi alloys

As well known, material outgassing in vacuum environment limits the lowest attainable pressure and, therefore it is a key issue for the materials used in particle accelerators (see chapter 2). In fact, low material outgassing is crucial for achieving and preserving extremely low pressures in ultra high vacuum regions. As a consequence, all the material used for vacuum systems at CERN need to comply with strict outgassing constraints. The steel (316 LN), copper (C10100-O) and the aluminum (EN AW-6082-O) used in the proposed SMA coupling devices are widely used within the CERN accelerator complex and all of them show an intrinsic outgassing rate compatible with the CERN UHV constraints. However, if the SMA material becomes a part of the vacuum envelope, for example in prototype chamber #1 in Table 6.1, outgassing properties of such material become a critical issue.

To this aim the outgassing tests were carried out using nearly equiatomic NiTi samples obtained from commercial NiTi sheets provided by Memry (www.saesgetters.com) with chemical composition close to the investigated alloy used in the proposed NiTi-based couplers. Two different materials where selected: one in austenitic state a room temperature, namely Type S (A_f around 0 °C), and the other one in martesitic state, namely Type H (A_f around 100 °C). This was done to analyze the outgassing response of the two crystallographic structure of the alloy, since SMA rings undergo phase temperature and/or stress –induced transformation during mounting and the final structure could be a mixture of the two phases.

The accumulation method (see section 2.8.1) was chosen for the tests. In fact, this method is considered to be the most effective for the proposed application as it gives the near-isothermal intrinsic outgassing properties of the material.

The cylindrical vacuum chamber used for the accumulation test had a diameter of 30 mm and was 70 mm long. It was made of a vacuum fired AISI 316 LN steel. The volume was about $5*10^4$ mm^3 while the surface area was approximately $8*10^3$ mm^2. Four rectangular-shaped samples (15*60*0.5 mm^3) where used for outgassing measurements in order to increase the total exposed surface to about $7.2*10^3$ mm^2. NiTi samples were treated to clean the material surface in order to remove actual or potential contaminants. The cleaning process results in several steps. Fig.7.7 depicts the standard procedure used at CERN (Chiggiato, 2013).

The sample outgassing was measured after baking the system for 24h at 250°C. The chamber outgassing, namely background, was previously evaluated and subtracted from the measurements. Five different measurements were made for a total accumulation time of 336 h.

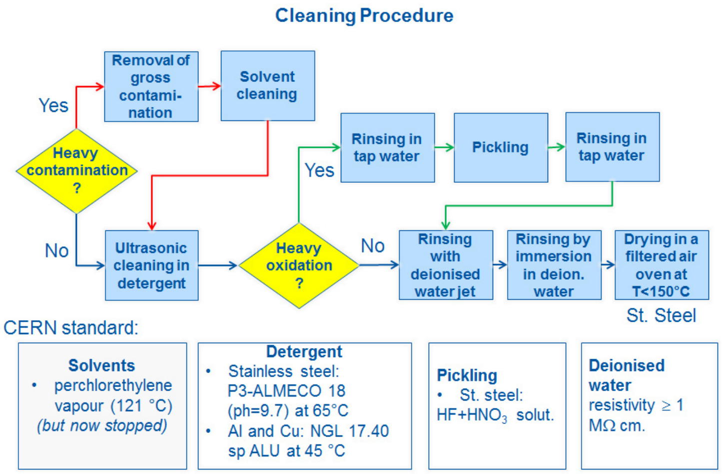

Figure 7.7: General cleaning procedure used at CERN.

Figure 7.8 shows the interpolation of gas quantities accumulated over different times for sample S. Table 7.3 lists the outgassing rates measured for both sample S and H.

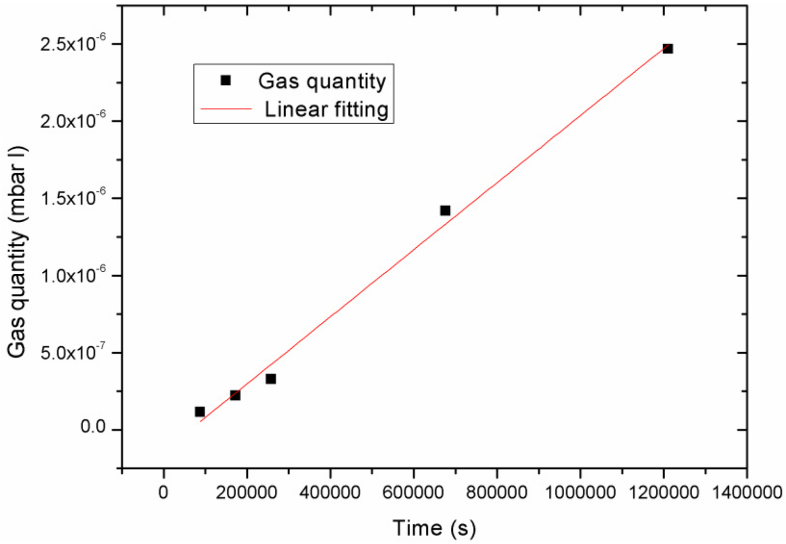

Figure 7.8: Interpolation of gas quantities accumulated over different times for sample S

The outgassing rate found for the investigated NiTi samples are extremely low and with the same order of magnitude of the background outgassing. These values are in the range of acceptability for application in particle accelerators. This enlarge the number of possible applications of NiTi-based devices at CERN and gives further flexibility in the SMA coupler design.

Table 7.3: Specific outgassing measured for sample S and H

Material	N samples	Specific Outgassing (mbar l s^{-1} cm^{-2})
Alloy S	4	1.53E-13

Alloy H	4	8.90E-14

7.6 Irradiation on SMA prototype vacuum chambers: post-irradiation results

Three SMA-based prototype vacuum chambers were used for the irradiation tests performed at CHARM, as shown in the picture in Fig. 7.9. The prototype chambers were equipped with detachable handle, for better post-radiation handling/processing.

Table 7.4 reports a description of the three analyzed couplings. As shown in the table, sample S1 and S2 were made with NiTi rings while sample S3 was obtained by a NiTiNb one. In addition, while sample S1 and S3 were irradiated after the first thermal activation of the SMA ring, sample S2 was subjected to a full mounting and dismounting process, *i.e.* irradiation was performed at the second thermal activation. This allows to analyze the performance of the coupling under multi-cycle applications.

Figure 7.9. SMA-based prototype chambers used for irradiation test.

Table 7.4 Prototype chambers used for irradiation tests at CHARM

Coupling type #	SMA Ring	SMA Installation condition	Sealing element	Gasket thickness *t* (mm)	Coupling ratio, *w*/*B*	Initial clearance ΔD (mm)
S1	NiTi	1^{st} activation	Aluminum gasket	0.3	1.00	0.85

S2	NiTi	Thermally cycled	Aluminum gasket	0.3	1.00	1.60
S3	NiTiNb	1st activation	Copper coating	0.3	1.00	0.15

FLUKA simulations were performed for the set of the three samples. They were aimed to define the proper positioning of the three samples in proximity of the CHARM target area in order to achieve the aimed dose (about 100kGy) in a limited amount of time. The predicted dose distribution in the samples and in area in proximity of the copper target is illustrated in Fig 7.10. Results are then normalized over primary protons on target (POT) to allow a scaling of the dose according to beam and target parameters. The indicative value of the absorbed dose for the three samples was 1kGy per day of exposure. In fact, the exposure time was defined in 100 days (to have an integrated dose of about 100 kGy).

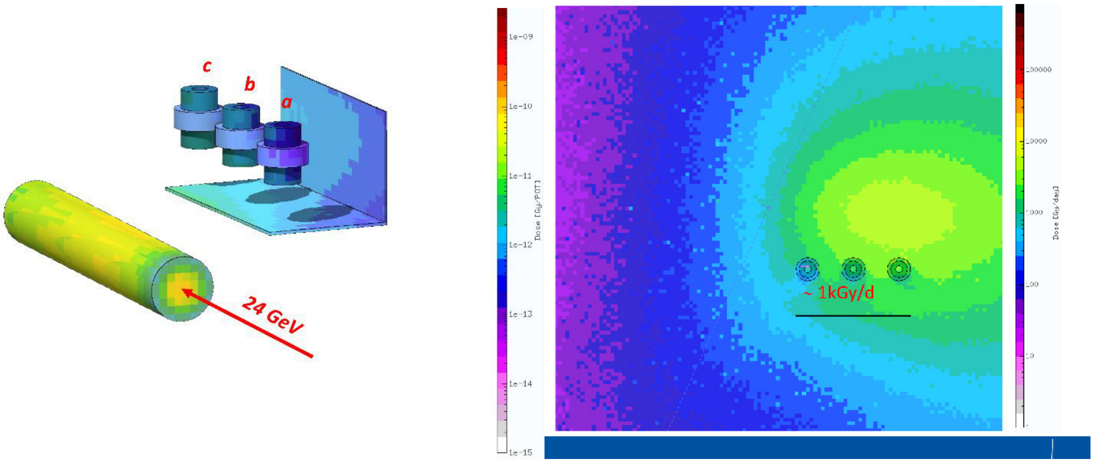

Figure 7.10. Dose (Gy/POT) maps in (a) the SMA-based chambers and in (b) the CHARM target area (courtesy of A. Infantino)

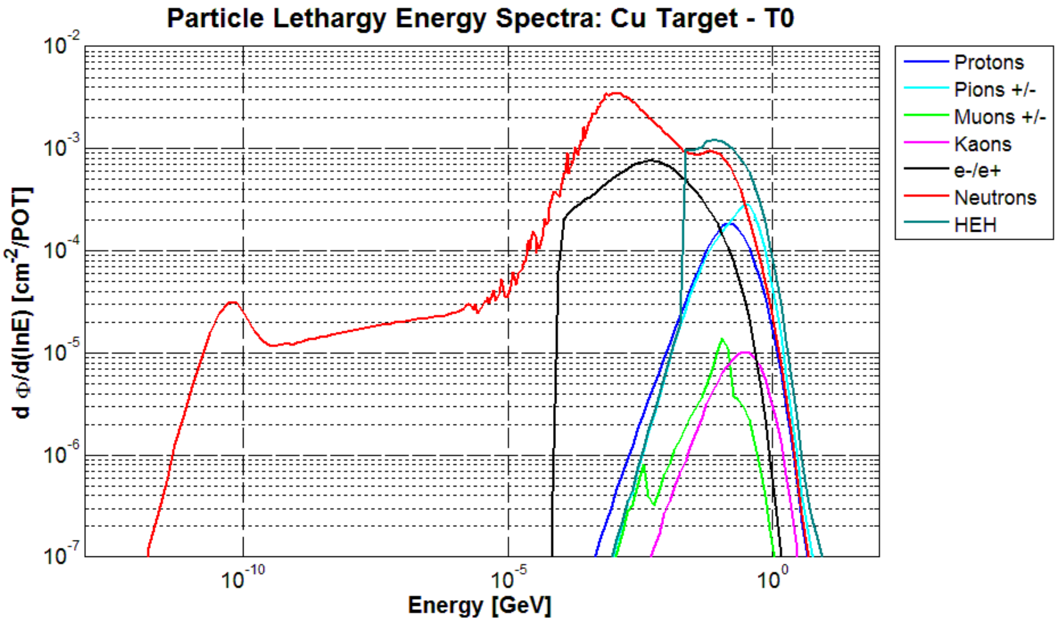

Figure 7.11. Particles Lethargy Energy with Cu target in correspondence of the SMA position. (courtesy of Chiara Cangialosi & A. Infantino).

The particle energy spectra from FLUKA simulations is shown in Fig. 7.11. The spectra are expressed in lethargy form. Lethargy is defined as the differential flux times the geometrical mean of the bin energy and is often used to represent neutron spectra (Greenwood, 1994). The spectra are representative of the actual particle field present in the installation zones for the SMA connectors. Two Radio Photo Luminescence (RPL) glass dosimeters were installed on each SMA chamber (see Fig.7.12). One on the front (beam side) and one on the back (shielding side).

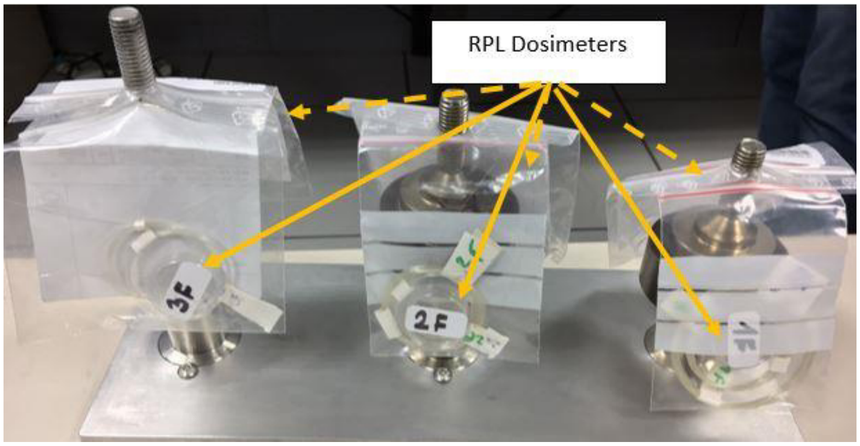

Figure 7.12. SMA assembly with mounted RPL dosimeters, ready for installation at CHARM facility.

The irradiation took place at ambient temperature. After a cool down period (of about three months) aimed to reduce the residual dose rate of the samples to values in agreement with the radiation protection regulations, the following tests were performed on the 3 irradiated assemblies in chronological order:

1. Leak test immediately after the radiation exposure
2. Leak test after reactivation by heating to T_{max}= 200°C and cooling to T_{op}=20°C
3. Dismounting of the SMA connectors by means of liquid nitrogen (only NiTi rings) at $T< T_d$

The dose rate measured at a distance of 10 cm from the center of the irradiated SMA-based chambers and the integrated dose measured by the RPL dosimeters are reported in Table 7.5. The maximum error between FLUKA simulations and the RPL measurements was 45%. The numerical/experimental data mismatch is in agreements with previous tests performed at CHARM. Due to the strong radiation dose gradient in the proximity of the copper target and the possible errors in sample positioning, these results are totally consistent and the best achievable.

Table 7.5. RPL and personnel dosimetry measurements.

SAMPLE	#S1	#S2	#S3
Dose rate at 10cm (µSv/h)	250	180	180
RPL Dosimetry Front (kGy)	140	150	100
RPL Dosimetry Back (kGy)	90	75	55

The leak tests and the dismounting tests were performed in a radioactive workshop. The post radiation tests results are reported in Table 7.6. Sample S1 and S3 were leak tight after irradiation (leak rate < 10^{-10} mbar l s^{-1}).

Table 7.6. Post radiation results: leak rate and dismounting assessment.

Coupling type #	SMA ring	Leak rate After exposure	Leak rate After reactivation (200°C)	Dismounting
#S1	NiTi	<10^{-10} mbar l s^{-1}	<10^{-10} mbar l s^{-1}	OK
#S2	NiTi	<10^{-7} mbar l s^{-1}	<10^{-10} mbar l s^{-1}	OK
#S3	NiTiNb	<10^{-10} mbar l s^{-1}	<10^{-10} mbar l s^{-1}	-

Sample S2 showed a small leak (leak rate < 10^{-7} mbar l s^{-1}) probably coming from a slight unexpected overcooling before or after the irradiation that disappeared by subsequent heating to 200°C. The NiTi assemblies were easily dismounted after 2-3 minutes of immersion in liquid nitrogen (see Fig. 7.13b).

Figure 7.13: Leak tests (a) and dismounting operations (b) performed in a radioactive workshop at CERN

These preliminary results demonstrate that the OW/TW Shape Memory behavior are not significantly affected by the irradiation (up to 140kGy) even in the worst-case scenario represented by steel chambers with non-optimized flat interface (w/B = 1) and large initial clearance (ΔD=1.6 mm for sample S2). In fact, the functional behavior of the proposed SMA-based connections was guaranteed up to a significant absorbed dose, representative of the HL-LHC operations in the next years.

Further irradiation tests are mandatory (on line/off line measurements) in order to better analyze the evolution of mechanical and functional properties of the SMA during/after irradiation. Furthermore, the SMA-based assemblies behavior need to be assessed for higher radiation doses in order to widen their possible application areas within the CERN accelerator complex.

8. CONCLUSIONS AND PERSPECTIVES

Beam-pipe coupling in particle accelerators is nowadays provided by metallic flanges that are tightly connected by several screws or large and heavy collars. Their installation or dismounting in radioactive area contributes to the radioactivity dose received by the technical personnel. Remote interventions are being considered at CERN, in particular in the framework of the High-Luminosity LHC project (Bruning and Rossi, 2015). Owing to the increased proton-beam intensity and luminosity of the HL-LHC, at some points, radioactivity will be sixteen times higher than in the present LHC in the next 20 years of operations. The duration of the technical personnel presence in these areas will be strictly controlled and minimized.

The activities reported in the present thesis focused on the analysis and design of Shape Memory Alloy (SMA)-based, dismountable and thermally activated connection devices for Ultra High Vacuum (UHV) chambers. They could be used as beam-pipe couplers in high-energy particle accelerators, especially in radioactive areas, where thermally induced mounting and dismounting operations can be activated remotely. The proposed coupling system consists of a SMA ring and a sealing element to be placed at the SMA-vacuum chambers interface *i.e.* a copper coating or a thin cylindrical aluminum/copper gasket.

The SMA-based beam-pipe couplers can be installed without using any connection flange. They are smaller and lighter than the traditional and quick connection Conflat® systems currently used in UHV systems at CERN. The bolt-free SMA-based connectors could provide significant benefits in terms of installation/dismounting time, space occupancy, bi-material joining and, above all, possible remote thermal activation, obtainable, for example, with removable heating/cooling collars.

Commercial NiTiNb and *ad-hoc* developed NiTi rings were properly selected and investigated. SMA characterization was carried out. The tightening performance of SMA rings, was studied for different values of the initial clearance between the SMA ring and the vacuum pipe. Contact pressure was estimated by both strain gauge (SG) measurements and by Digital Image Correlation (DIC), by means of an *ad-hoc* developed numerical procedure. A novel design method was proposed that involves numerical results, obtained from Finite Element (FE) simulations, and a vacuum sealing model (Roth, 1972). Leak tightness tests were carried out to assess the sealing performance of the of SMA-based prototype UHV chambers even after ageing at room temperature and repeated thermal cycles. The predicted integrated dose absorbed by a SMA connector after a year of possible operation in some CERN restricted access areas (in correspondence of the HL-LHC beam focusing/defocusing quadrupole magnets) is about 100 kGy; three SMA-based prototype vacuum chambers were exposed to a radiation field representative of the aforementioned operative condition (similar particle spectra and fluence) in order to absorb a comparable dose in a limited amount of time. The irradiation was performed at CHARM (Cern High energy AcceleRator Mixed field) facility (Mekki *et al*., 2016) and the functional and leak tightness performance of the couplings was verified afterwards.

The main results, partially reported in two scientific papers (Niccoli *et al.*, 2017a; Niccoli *et al.*, 2017b), can be summarized as follows:

- Mounting operations can be performed remotely by heating the junction unit (exploiting possible bakeout processes). This is a very important feature especially for SMA installation in restricted access areas of particle accelerators as the radiation doses absorbed by the operators could be significantly reduced.
- Clamping pressure is not significantly affected by the initial ring-pipe clearance. As a consequence, large assembly tolerances (several hundreds of microns in case of SMA ring with internal diameter of about 45 mm) can be adopted for beam pipe coupling. This represents a relevant benefit as the larger the clearance, the easier and faster the assembly operations. The clamping pressure-temperature curves obtained by SG, FE and DIC data (analyzed by the proposed procedure) were in good agreement.
- Thermal dismounting of beam-pipe couplings is always obtained upon cooling. This allows remote interventions in particle accelerators. An easier and faster disconnection of the SMA sleeve is obtained with NiTi-based couplers which allow higher dismounting temperatures (about -30°C) if compared with NiTiNb alloys (about -150°C). Liquid nitrogen can be used to cool rings for removal. Several mechanical solutions for the cooling are considered *e.g.* a wool felt collar wrapped around the SMA ring and soaked with liquid nitrogen or a nitrogen jet (from portable pressurized dewars). In both cases the disassembly is obtained after a cooling stage (from room temperature) of 2/3 minutes. These quick dismounting operations could be easily performed by workers and/or robots; certainly, the duration of technical personnel presence is minimized.
- Gasket thickness, ranging from 0.3 to 0.9 mm, does not play an important role on the pressure distribution at the gasket/pipe interface. This is a very interesting result because gaskets with customized thickness can be manufactured to fill the initial assembly gaps between the pipe and SMA ring. In fact, the dimensional tolerances of the SMA ring internal diameter are not particularly tight owing to the complex mechanisms occurring during mechanical pre-strain.
- Coupling types with different ratios of the contact surface width (w) and coupling surface width (B) were analyzed by modifying the contact geometry. A significant effect of the ratio w/B on the pressure distribution was observed.

- The proposed design method was used to select the best coupling configurations among the investigated ones. In particular, coupling types with *w*/*B* values around 0.6 exhibited the best calculated sealing performance.
- The aluminum or copper gaskets as well as the copper coating on the pipe external surface represent viable and effective solutions as sealing elements for SMA-based pipe connectors. In fact, leak tightness tests of both non-optimized (*w*/*B*=1) and optimized (*w*/*B*=0.6) couplings revealed that the leak rate is always lower than the sensitivity of the leak detectors and therefore below the standard value required for UHV applications in particle accelerators (10^{-10} mbar·l·s^{-1}).
- Although their proved leak tightness, couplings with *w*/*B*=1 always exhibit the worst calculated sealing performance based on the proposed conductance model. This is a remarkable result because the other configurations with better calculated sealing performance (*i.e.*, those with *w*/*B* around 0.6) are expected to be significantly more reliable.
- Thermal re-activation of the coupling can be exploited, thanks to the two-way shape memory capabilities of the SMA rings. In fact, repeated mounting/dismounting operations can be carried out without mechanically pre-straining the SMA element. Leak tightness of NiTi-based couplers was verified after two complete thermal cycles imposed after the first heating (thermal activation). Each of them comprised a cooling below M_f (−50°C), re-heating at T_{max} (200°C) and cooling again to T_{op} (20°C). As a result, SMA-based couplers can be used for multicycle applications; nevertheless, in this case, the re-mounting has to be performed at sub-zero temperatures.
- In order to assess possible creep-like effects occurring in service due to the high values of internal stress in SMA rings, leak tightness was repeated after one year ageing at room temperature. UHV constraints were always satisfied in all aged couplings.
- Preliminary investigations about SMA radiation resistance demonstrated that the functional behavior (One Way/Two Way Shape Memory effect) of the SMA couplers were not significantly affected by the irradiation (up to 140kGy). Even In worst case scenario represented by the use of steel chambers with non-optimized interface (w/B = 1) and SMA rings installed without minimum initial clearance, the leak tightness of the SMA-based joints was guaranteed up to a significant absorbed dose, representative of radiation field occurring in some critical areas of the future HL-LHC accelerators.
- The intrinsic thermal outgassing rate of NiTi alloys is in the range of acceptability for UHV systems in particle accelerators. This enlarge the number of possible applications of NiTi-based devices at CERN and gives further flexibility in the SMA coupler design.

Future studies related on SMA-based connectors should include:

- The definition of the final optimized design of SMA/pipes assemblies for different pipe materials and geometries according to CERN needs by means of the developed design and experimental assessment methods. In the present thesis, the vacuum beam pipe has been considered in steel; the study of SMA assemblies based on other vacuum chamber materials *e.g.* brittle or soft materials would be of interest.
- The selection/design of removable heating-cooling collars to be used in selected areas in order to ensure full remote control of the SMA junction unit.
- The development and numerical implementation of a constitutive model for SMA able to better capture all the complex mechanisms occurring during SMA training procedure and biaxial constrained recovery stage. This model would be able to simulate the evolution of the transformation temperatures, elastic moduli, yielding stress, Clausius-Clapeyron coefficients, plastic strains, One Way and Two Way shape memory capabilities during different thermo-mechanical loading paths representative of the training and operative cycles.
- The design of special loading frames and experimental setups for online mechanical/leak tightness measurements aimed to better analyze the evolution of SMA behavior during and after the radiation exposure (to verify possible strain and/or stress relaxation).
- The realization and validation of full-scale SMA-based prototypes: leak rate assessment, functional behavior during bake out cycling, long term reliability in highly radioactive environments (up to 2 MGy of absorbed dose).

Possible applications in CERN accelerators have been already identified:

- A first use has been proposed for the ISOLDE facility, the Isotope Separator On Line DEvice at CERN. Radioactive nuclides are produced via spallation, fission, or fragmentation reactions in a thick target (Koster, 2001), irradiated with a proton beam at an energy of 1.4 GeV and an intensity up to 2 μA. The access to the target equipment is restricted; the use of SMA could be beneficial to avoid contamination and irradiation of technical personnel.
- A second application is the vacuum system of the Large Hadron Collider (LHC) between the two high luminosity experiments (ATLAS and CMS) (ATLAS Collaboration, 1999; LHC Experiments Committee, 1997) and the beam focusing/defocusing quadrupoles (inner triplets). In these areas, particle debris generated by the 14 TeV proton-proton collisions induce radioactivity doses higher than 5 mSv h-1 so that stringent access regulations are applied. The possibility of remote clamping/unclamping would reduce the personnel collected dose.
- Particle collimators are other critical pieces of accelerator equipment (Redaelli, 2013). The main role of particle collimator is to intercept out of orbit high-energy particles in dedicated materials and location instead of being dispersed along the whole ring. Here again, the application of SMA rings would be welcomed for a simplified design and increased personnel safety.

- The Compact Linear Collider (CLIC) study is an international collaboration working on a concept for a machine to collide electrons and positrons (antielectrons) head-on at energies up to several teraelectronvolts (TeV). This energy range is similar to the LHC's, but using electrons and their antiparticles rather than protons, physicists will gain a different perspective on the underlying physics. The particle radiation loads in linear electron/positron accelerators are very limited when compared with high energy proton machines like the LHC and the use of the proposed UHV connectors in these facilities does not require any further investigation about the actual radiation resistance of SMAs. In fact, SMA coupling installations are already planned in the CLEAR test facility at CERN, which provides the electron beam for the studies. The main advantage of the SMA connectors would be the limited space requirements in this very compact machine.
- Moreover, SMA couplers can be used for joining dissimilar materials in particle accelerators because bi-material welding represents a remarkable engineering issue. For example, SMA couplings could be used for joining high transparent beryllium pipes, around collision points, with standard metallic alloys (Veness, 2011). The use of SMA-based connectors could result in significant material and cost savings; preliminary studies in this direction are ongoing.
- A radiofrequency (RF) cavity, which is widely used in particle accelerator technology, is a metallic chamber that contains an electromagnetic field. Its primary purpose is to accelerate charged particles. Another advantage of the SMA-based connections is the lack of gap between the two aligned vacuum pipes; this would be of interest for applications where RF losses are a limitation or an issue.

BIBLIOGRAPHY

Abrahamsson, P., Bjiimemo, R. (1994). The need for product design tools in shape memory technology. *Proceedings of the 3rd IUMRS international conference on advanced materials*,1171–1174.

Anderson, P., Sangesland, S. (1999). Detailed study of shape memory alloys in oil well applications. *Sintef petroleum research, Trondheim, Norway.*

Andreasen, G., Hilleman, T. (1971). An evaluation of 55 cobalt subsituted nitinol wire for use in orthodontics. *Journal of the American Dental Association*, 82, 1373–1375.

ATLAS Collaboration. (1999). Detector and physics performance technical design report. Volume 1. CERN-LHCC-99-14, ATLAS-TDR-14.

Barbarino, S., Saavedra Flores, E.L., Ajaj, R.M., Dayyani, I., Friswell, M.I. (2014). A review on shape memory alloys with applications to morphing aircraft. *Smart Materials and Structures*, 23 (6).

Barnes, B., Luntz, D. B. J., Browne, A., Strom, K. (2006). Panel deployment using ultrafast SMA latches, *proceedings of ASME International Mechanical Engineering*.

Baz, A., Imam, K., McCoy, J. (1990). Active vibration control of flexible beams using shape memory actuators. *Journal of sounds and vibrations*, 140, 437–56.

Bellini, A., Colli, M., Dragoni, E. (2009). Mechatronic design of a shape memory alloy actuator for automotive tumble flaps: A case study. *IEEE Transactions on Industrial Electronics,* 56(7), 2644-2656.

Benvenuti C. (1998). Non-evaporable getters: from pumping strips to thin film coatings. Proceedings of *European Particle Accelerator Conference.*

Besseghini, S., Businaro, T.V., Ceresara, S. Tuissi, A. (1996). Development of a NiTi shape memory alloy vacuum tight flange for JET In-Vessel Inspection System. *Fusion Technology*, 2, 1645-1648.

Bhattacharya, K. (2003). Microstructure of martensite: why it forms and how it gives rise to the shape-memory effect, *Oxford University Press.*

Birman, V. (1997). Review of mechanics of shape memory alloy structures. *Applied Mechanics Reviews,* 50 (11), 629–645.

Borden, T. (1991). Shape-Memory Alloys: Forming a Tight Fit. *Mechanical Engineering*, 113(10), 67–72.

Bozzolo, G., Noebe, R.D., Mosca, H.O. (2005). Site preference of ternary alloying additions to NiTi: Fe, Pt, Pd, Au, Al, Cu, Zr and Hf. *Journal of Alloys and Compounds*, 389(1-2), 80-94.

Bozzolo, G., Mosca, H.O., Noebe, R.D. (2007). Phase structure and site preference behavior of ternary alloying additions to PdTi and PtTi shape-memory alloys. *Intermetallics* 15(7), 901-911.

Brüning, O., Rossi L. (2015). The High Luminosity Large Hadron Collider: The New Machine for Illuminating the Mysteries of Universe, *Advanced Series on Directions in High Energy Physics*, 24.

Brüning, O., Collier, P., Lebrun, P., Myers, S., Ostojic, R., Poole, J., Proudlock, P. (2004). LHC Design Report. CERN-2004-003-V-1, 548 pp.

Buchter, H. H. (1979). Industrial Sealing Technology, J. Wiley & Sons.

Buehler, W. J., Gilfrich, J.V. & Wiley, R.C. (1963). Effect of Low-Temperature Phase Changes on the Mechanical Properties of Alloys near Composition TiNi. Journal of Applied Physics, 34 (5), 1475.

Butera, F. (2008). Shape memory actuators for automotive applications. *Advanced Materia and Processes*, 166, 37.

Byun, T.S, Farrell K. (2004). Plastic instability in polycrystalline metals after low temperature irradiation. *Acta Materialia* 52 (6), 1597-1608,

Byun, T.S, Farrell K. (2004). Irradiation hardening behavior of polycrystalline metals after low temperature irradiation. *Journal of Nuclear Materials* 326, 86-96.

Carpenter, B., Lyons J. (2001). EO-1 technology validation report: Lightweight flexible solar array experiment. NASA report.

Carroll, M.C., Somsen C., Eggeler G. (2004). Multiple-Step Martensitic Transformations in Ni-rich NiTi Shape Memory Alloys. *Scripta Materialia*, 50, 187-192.

CERN technical specification No. 525 - Ed. 3 - 02.08.1999, Sheets and tubing for special cryogenic applications, stainless steel type X2CrNiMo17-12-2 (1.4404, AISI 316L)

CERN technical specification No. 1002 - Ed. 3 - 02.08.1999, Sheet steel for vacuum applications, stainless steel type X2CrNiMoN17-13-3 (1.4429, AISI 316LN).

CERN technical specification No. 1004 - Ed. 3 - 02.08.1999, Sheet steel for vacuum applications, stainless steel type X2CrNi19-11 (1.4306, AISI 304L).

Chang, L. C., Read, T. A. (1951). Plastic deformation and diffusionless phase changes in metals - the gold-Cadmium beta phase. *Transactions of the American Institute of Mining, Metallurgical and Petroleum Engineers,* 191, 47–52.

Chiggiato, P. (2013). Surface treatments for vacuum systems of particle accelerators. *Proceedings of the 19th International Vacuum Conference.*

Chiggiato P. (2016). Vacuum technology for particle accelerators, JUAS notes. https://indico.cern.ch/event/471931/contributions/1149644/attachments/1226014/1794769/JUAS-Notes_Vacuum_Tech-Chiggiato.pdf

Choi, E., Park, S.H., Cho, B.S., Hui, D. (2013). Lateral reinforcement of welded SMA rings for reinforced concrete columns. *Journal of Alloys and Compounds*, 577(1), 756-759.

Choudhry, S., & Yoon, J. W. (2004). A General Thermo-Mechanical Shape Memory Alloy Model : Formulation and Applications, 1589(1), 1589–1594.

Clausing, P. (1971). The flow of highly rarefied gases through tubes of arbitrary length. *Journal of Vacuum Science & Technology*, 8(5),636-646.

Contardo, L., Guenin, G. (1990). Training and two way memory effect in Cu- Zn-Al alloy, *Acta Metallurgica,* 38 (7), 1267–1272.

Cragg, A., Lund G., Rysavy, J., Castaneda, F., Castaneda-Zuniga, W., and Amplatz, K. (1983). Nonsurgical placement of arterial endoprostheses: a new technique using nitinol wire. *Radiology*, 147, 261-263.

Cross, W. Kariotis Anthony. H, and. Stimler F.J. (1969), Cr- 1433. Nitinol Characterization Study. NASA Report: GER 14188.

Davis, D. H. (1960). Monte carlo calculation of molecular ow rates through a cylindrical elbow and pipes of other shapes. *Journal of Applied Physics*, 31(7), 1169-1176.

Delaey, L., Krishnan R.V., Tas H., and Warlimont H. (1974). Thermoelasticity, pseudoelasticity and the memory effects associated with martensitic transformations. Part 1. Structural and microstructural changes associated with the transformations. *Journal of Materials Science*, 9, 1521-1535.

Dlouhy, A., Kahalil-Allafi J., Eggeler G. (2004). On the Determination of the Volume Fraction of Ni4Ti3 Precipitates in Binary Ni-rich NiTi Shape Memory Alloys, *Zeitschrift fur Metallkunde*, 95 (6), 518-524.

Hoffman, D., Singh B., Thomas John H. (1998). Handbook of Vacuum Science and Technology, *Elsevier Inc.*

Dotter, C.T., Buschmann R.W., McKinney M.K., and Rosch J. (1983). Transluminal expandable nitinol coil stent grafting: preliminary report. *Radiology*, 147, 259-260.

Duerig, T., Pelton A., Stockel D. (1997). Superelastic nitinol for medical devices. *Medical Plastics and Biomaterials,* 31–42.

Duerig, T. and Melton, K. (1989) a. Designing with the shape memory effect, *proceedings of the Mrs international meeting on advanced materials*, 9, 581-597.

Duerig, T. and Melton, K. (1989) b. Wide Hysteresis NiTiNb Alloys. In Hornbogen, E., Jost, N., The Martensitic Transformation in Science and Technology, 191-198.

Duerig, T., Melton K., Stöckel D., Wayman C., (1990). Engineering Aspects of Shape Memory Alloys. *Butterworth-Heinemann Ltd.*

Duerig, T. (1995). Present and future applications of shape memory and superelastic materials. *Materials*

Research Society Symposium Proceedings, Materials Research Society (MRS).

Duerig, T., Stoeckel D., and Pelton A. (1999). An overview of nitinol medical applications. *Materials Science and Engineering A,* 273, 149-160.

Dylla, H. F., Manos D. M., and LaMarche P. H. (1993). Correlation of outgassing of stainless steel and aluminum with various surface treatments. *Journal of Vacuum Science & Technology A*, 11(5), 2623-2636,

Edwards D., McCafferty D., Rios L. (1979). Sealing of knife-edge flanges after a high temperature vacuum firing. *Journal of Vacuum Science and Technology A,* 16(6), 2114.

Edwards T.J., Budge J.R., Hauptli W. (1977). Thin-film polyimide gasket seals for ultrahigh vacuum. *Journal of Vacuum Science and Technology* 14(2), 740.

Elsey R.J. (1975). Outgassing of vacuum materials-ii. *Vacuum*, 25(8), 347-361.

Espe W. (1966). Materials for High Vacuum Technology, *Pergamon, Oxford.*

Evans J., Brei D., Luntz J., (2006). Preliminary experimental study of SMA knitted actuation architectures. *Proceedings of ASME International Mechanical Engineering Congress and Exposition.*

Fend H. (1996). Progress in metal sealing techniques. *Vacuum*, 47 (6–8), 527-529

Forkel-Wirth, D., Roesler, S., Silari, M., Streit-Bianchi, M., Theis, C., Vincke, H., et al. (2011). Radiation protection at CERN. CERN Report CERN-2013-001, 415-436.

Frick, C.P., Ortega, A.M., Tyber, J., A., Maksound, A., Maier, H.J., Liu, Y., Gall, K. (2005). Thermal Processing of Polycrystalline NiTi Shape Memory Alloys, Material Science and Engineering A, 405, 34-49.

Friend C.M. (1986). The effect of applied stress on the reversible strain in CuZnAl shape memory alloys. Scripta Metallurgica, 20 (7), 995-1000.

Funakubo H. (1987). Shape Memory Alloys, *Gordon and Breach Science Publishers.*

Gall K., Sehitoglu H., Chumlyakov Y.I., Kireeva I.V. (1999). Tension-compression Asymmetry of the Stress-strain response in Aged Single Crystal and Polycrystalline NiTi. Acta Materialia. 47, 1203-1217.

Garton D., (2011). Vacuum Technology and Vacuum Design Handbook for Accelerator Technicians, *Australian Nuclear Science and Technology Organisation.*

Ghosh G., Olson G.B. (1994), Kinetics of F.C.C-B.C.C. Heterogeneous Martensitic Nucleation—I. The Critical Driving Force for Athermal Nucleation. *Acta Metallurgica et Materialia*, 42, 3361- 3370.

General Motors. (2013). Chevrolet Debuts Lightweight ‘Smart Material’ on corvette. *General Motors News*

Godard O., Lagoudas M., Lagoudas D., Design of space systems using shape memory alloys, *Proceedings of SPIE, Smart Structures and Materials*, 5056, 545–558.

Greenwood, R. L. (1994). Neutron interactions and atomic recoil spectra, *Journal of Nuclear Materials*, 216, 29–44.

Gröbner, O. (1999). Dynamic outgassing, CERN report, CERN-1999-005, 127-138. DOI 10.5170/CERN-1999-005.127

Hartl, D. J., Lagoudas D.C. (2007). Aerospace applications of shape memory alloys. *Proceedings of the Institution of Mechanical Engineers, Part G: Journal of Aerospace Engineering*.

He, X. M. and Rong, L. J. (2004). DSC analysis of reverse martensitic transformation in deformed Ti–Ni–Nb shape memory alloy. *Scripta Materialia*, 51 (1), 7–11.

Hilleret, N. (1999). Leak detection. CAS: Vacuum Technology, CERN Report, CERN-OPEN-2000-280.

Hirose, S., Ikuta, K., Umetani, Y. (2012). Development of shape-memory alloy actuators. Performance assessment and introduction of a new composing approach. Advanced Robotics, 3, 3–16.

Holden J., Holland L., Laurenson L. (1959). Bakeable vacuum seals using aluminium-wire gaskets. *Journal of Scientific Instruments,* 36(6), 281-283.

Hoshiya, T., Ohmia, M., Matsuia, Y., Nishikawa M. (1998). Shape memory characteristics of neutron irradiated Ti–Ni shape memory alloy couplers. *Journal of Nuclear Materials*, 258–263, 2036–2040

Hoshiya, T., Sekino H. Matsui Y., Sakurai F, Enami K. (1996). Effects of residual strain on deformation processes of neutron-irradiated Ti-Ni and Ti-Pd shape memory alloys*, Journal of Nuclear Materials*, 233–237, 599-603.

Huang W. (2002). On the selection of shape memory alloys for actuators. *Material and Design*, 23, 11–9.

Humbeeck, J.V., Shape memory alloys: A material and a technology. Advanced Engineering Materials, 2001. 3(11): p. 837-850.

Jackson, C. M., Wagner H. J., Wasilewski R. J. (1972), 55-Nitinol-the Alloy With a Memory: Its Physical Metallurgy, Properties, and Applications, NASA Report.

Jacot A., Ruggeri R., Clingman D. (2006). Shape memory alloy device and control method, *U.S. Patent 7,037,076*.

Jani, J.M., Leary, M., Subic, A., Gibson M.A. (2014). A review of shape memory alloy research, applications and opportunities, *Material and Design*, 56, 1078–1113.

Jiang, S., Liang Y., Zhang Y., Zhao Y., Zhao C. (2016). Influence of Addition of Nb on Phase Transformation, Microstructure and Mechanical Properties of Equiatomic NiTi SMA. *Journal of Material Engineering Performance*; 25(10), 4341-4351

Jousten, K. (2016). Handbook of Vacuum Technology, *Wiley-VCH Verlag GmbH & Co. KGaA*. DOI: 10.1002/9783527688265

Kanazawa K. (1989). Analysis of pumping down process. *Journal of Vacuum Science & Technology A*, 7(6), 3361-3370.

Karhu, M., Lindroos, T. (2010). Long-term behaviour of binary Ti–49.7 Ni (at.%) SMA actuators – the fatigue lives and evolution of strains on thermal cycling. *Smart Materials and Structures* 19 (11).

Kauffman, G., Mayo, I. The story of Nitinol: the serendipitous discovery of the memory metal and its applications. *The Chemical Educator,* 1997, 2, 1–21

Kersevan R. and Pons J.-L. (2009). Introduction to MOLFLOW+: new graphical processing unit-based monte carlo code for simulating molecular flows and for calculating angular coefficients in the compute unified device architecture environment. *Journal of Vacuum Science & Technology A*, 27(4), 1017-1023.

Kershaw, K., Feral, B., Grenard, J. L., Feniet, T., De Man, S., Hazelaar-Bal, C., … Ingo, R. (2013). Remote inspection, measurement and handling for maintenance and operation at CERN*. International Journal of Advanced Robotic Systems*, 10. https://doi.org/10.5772/56849

Khalil-Allafi J., Eggeler G., W.Schmahl W., Sheptyakov D. (2006). Quantitative phase analysis in microstructures which display multiple step martensitic transformations in Ni-rich NiTi Shape Memory Alloys, Material Science and Engineering A, 438-440, 593-596.

Kitamura, K., Itoh K., Uchida T., Kondoh M., Obara K., Nakamura K., and Murakami Y. (1994). *Journal of Vacuum Science & Technology A* 12, 3217.

Kornfeldt, H., Mahnberg, M., Stribeck, J., Scott, P., Kilinski, T., Rudland, D., Olson, R,. Djerfh, T. (1997). Demonstration of piping integrity with SMA technology. *Nuclear Engineering and Design*, 172 (3), 367-371.

Kosel, F., Videnic, T., (2007). Generalized Plasticity and Uniaxial Constrained Recovery in Shape Memory Alloys, *Mechanics of Advanced Materials and Structures*, 14 (1), 3-12.

Koster, U. (2001). ISOLDE target and ion source chemistry. *Radiochimica Acta*, 89 (11), 77777 – 7775.

Krishnan, R.V., Delaey L., Tas H., and Warlimont H. (1974). Thermoplasticity, pseudoelasticity and the memory effects associated with martensitic transformations. Part 2. The macroscopic mechanical behavior. *Journal of Materials Science*, 9, 1536-1544.

Kumar, P.K., Lagoudas D.C. (2008). Introduction to shape memory alloys. In: Shape memory alloys. *US: Springer,* 1–51.

Kurokouchi, S., Shinoda S., Morita H. (2003). Dependence of the seal property of ConFlat-type flanges on the final dimensions of th knife edge. *Journal of Vacuum Science and Technology A*, 21(2) 438-448.

Kusagawa, M., Nakamura T., Asada Y., (2001). Fundamental Deformation and Recovery Behaviors of NiTiNb Shape Memory Alloy, *JSME International Journal Series A Solid Mechanics and Material Engineering*, 44 (1),57–63.

Lafferty, J. M. (1998). Foundations of vacuum science and technology. *Wiley, New York.*

Lagoudas D., Vandygriff E. (2002). Processing and characterization of NiTi porous SMA by elevated pressure sintering, *Journal of intelligent material system and structures*, 13, 837–850.

Lagoudas DC., 2008 Shape Memory Alloys: Modeling and Engineering Applications,

LHC Experiments Committee. (1997). LHCC. The CMS muon project Technical Design Report. CERN Report, CERN-LHCC-97-032; CMS-TDR-3,1997.

Li, M. and Dylla, H. F. (1993). Model for the outgassing of water from metal surfaces. *Journal of Vacuum Science & Technology A*, 11(4), 1702-1707.

Li, W., Zhou, Z.X., Xiao, H., Zhang, B. (2015). Design and evaluation of a high-speed and precision microspindle. *International Journal of Advanced Manufacturing Technology,* 78 (5-8): 997-1004.

Sun, L., Wu K. (1994). Two-way memory effect (TWME) in NiTi-Pd high-temperature shape memory alloys. Proceedings of SPIE, Smart Structures and Materials: Smart Materials, 298, doi:10.1117/12.174067

Lin, S. (2015). Strain Measurement by Digital Image Correlation, DESY Report.

Liu, Y. and Favier, D. (2000). Stabilisation of martensite due to shear deformation via variant reorientation in polycrystalline NiTi. Acta Materialia, 48, 3489–3499.

Liu, Y. and Galvin S. P. (1997). Criteria for pseudoelasticity in near-equiatomic NiTi shape memory alloys. Acta Materialia, 45, 114431–4439.

Liu, Y. and Xie Z. (2007). Detwinning in shape memory alloy, *In: Progress in Smart Materials and Structures ISBN: 1-60021-106-2*, 29-66.

Liu, Y., Liu, Y., Van Humbeeck J. (1998). Two-way shape memory effect developed by martensite deformation in NiTi, *Acta Materialia*, 47(1), 199–209.

Loewy R. (1997). Recent developments in smart structures with aeronautical applications. *Smart Materials and Structures*, 6 (5).

Lu, H. and Cary, P.D. (2000). Deformation measurement by digital image correlation: implementation of a second-order displacement gradient. *Experimental Mechanics*, 40, 393–400

Luo, H.Y. and Abel E.W. (2007). A comparison of methods for the training of NiTi two-way shape memory alloy, *Smart Materials and Structures*, 16, 2543–2549. doi:10.1088/0964-1726/16/6/058

Mabe, J., Cabell, R., Butler, G. (2005). Design and control of a morphing chevron for takeoff and cruise noise reduction, *Proceedings of the 26th Annual AIAA Aeroacoustics Conference*, 1–15.

Machado, L., Savi. M. (2003). Medical applications of shape memory alloys, *Brazilian Journal of Medical and Biological Research*,36, 683– 691.

Malukhin, K., Sung, H., & Ehmann, K. (2012). A shape memory alloy based tool clamping device. *Journal of MaterialsProcessing Technology*, *212*(4), 735–744. https://doi.org/10.1016/j.jmatprotec.2011.10.026

Mani, R., Lagoudas D., Rediniotis O. (2003). MEMS based active skin for turbulent drag reduction. *Proceedings of SPIE, Smart Structures and Materials*, 5056, 9–20.

Mantovani, D. (2000). Shape memory alloys: properties and biomedical applications. *Journal of the Minerals, Metals and Materials Society*, 52, 36–44.

Mapes, M. (2001). Summary of quick disconnect vacuum flanges. *Journal of Vacuum Science & Technology A: Vacuum, Surfaces, and Films*, *19*(4), 1693–1698. https://doi.org/10.1116/1.1359540

Matsukawa, Y., Suda, T., Ohnuki, S., Namba, C. (1999). Microstructure and mechanical properties of neutron irradiated TiNi shape memory alloy. *Journal of Nuclear Materials*, 271(1-3), 106-110.

McCormick N. and Lord J. D., (2012). Digital Image Correlation, *Materials Today*, 13 (12), 52-54.

McWilliams, A. (2011). Smart materials and their applications: technologies and global markets. *BCC Research Advanced Materials Report*, 161.

Mekki, J., Brugger, M., Alia, R. G., Thornton, A., Mota, N. C. D. S., & Danzeca, S. (2016). CHARM: A Mixed Field Facility at CERN for Radiation Tests in Ground, Atmospheric, Space and Accelerator Representative Environments. *IEEE Transactions on Nuclear Science*, *63*(4), 2106–2114.

Meng, Q., Yang, H., Liu, Y., Nam, T., & Chen, F. (2011). Thermal arrest analysis of thermoelastic martensitic transformations in shape memory alloys. *Journal of Materials Research*, *26*(10), 1243–1252. https://doi.org/10.1557/jmr.2011.54

Meng, X., Chen, F., Cai, W., Wang, L., & Zhao, L. (2006). Two-Way Shape Memory Effect and Its Stability in a Ti – Ni – Nb Wide Hysteresis Shape Memory Alloy Heating position Spring back position. *Materials Transactions*, *47*(3), 724–727.

Miller D.A., Lagoudas D.C. (2000). Thermo-mechanical characterization of NiTiCu and NiTi SMA actuators: Influence of plastic strains, *Smart Materials and Structures* 9 (5), 640–652.

Milleron N. and Wolgas R. C. (1980). Metal vacuum systems and components. *Methods in experimental physics* (*vacuum physics and technology)* 14, 275–311.

Moore B.C. (1965). Vacuum sealing rough surfaces. *Journal of Vacuum Science and Technology* 2(3), 160-161

Niccoli, F., Garion, C., Maletta, C., Sgambitterra, E., Furgiuele, F. and Chiggiato, P. (2017a). Beam-pipe coupling in particle accelerators by shape memory alloy rings. *Materials and Design*, 114, 603–611.

Niccoli, F., Garion, C., Maletta, C., and Chiggiato, P. (2017b). Shape memory alloy-based pipe couplers for ultra-high vacuum applications in particle accelerators: design and experimental assessment. *Journal of Vacuum Science and Technology A*, 35 (3).

Nishikawa M., Narikawa T., Iwamoto M., Watanabe K. (1986). Conceptual Design of a Cassette Compact Toroid Reactor (The Zero-Phase Study) — Quick Replacement of the Reactor Core*. Fusion Science and Technology*, 9 (1), 101-115.

Nishikawa M., Toda S., Tachibana E., Hoshiya T., Kawai M., Goto S., and Watanabe K. (1989). Application of shape memory alloys to compacting and element-quickly replaceable design in high-power density fusion reactors. *Fusion Engineering and Design*, 10, 509. https://doi.org/10.1016/0920-3796(89)90099-9

Noebe, R., Biles T., and PadulaII S.A. (2006). NiTi-based high-temperature shape memory alloys: properties, prospects, and potential applications. *in Advanced Structural Materials*, Soboyojo W.O., *CRC Press* LLC, 145-186.

Okita, K., Okabe, N., Sato, T., & Nakao, T. (2005). Appearance of two-way strain in shape memory effect of Ti-Ni-Nb alloy: influence of applied strain on two-way strain. *Nippon Kinzoku Gakkaishi/Journal of the Japan Institute of Metals*, *69*(8), 622–627. https://doi.org/10.2320/jinstmet.69.622

Otsuka, K., & Ren, X. (2005). Physical metallurgy of Ti-Ni-based shape memory alloys. *Progress in Materials Science*, *50*(5), 511–678.

Otuska, K., Wayman, C.M. (1998). Shape Memory Materials, *Cambridge University Press*.

Ozbulut, O.E., Hamilton, R.F., Sherif, M.M., Lanba, A. (2015).Feasibility of self-pre-stressing concrete members using shape memory alloys A. *Journal of Intelligent Material System and Structures,* 26(18), 2500-2514.

Rodriguez P., Guenin G., (1990). Stability of the two way memory effect during thermal cycling of a high Ms temperature Cu-Al-Ni alloy, *Materials Science Forum* 56–58 (2),541–546.

Paine J., C. Rogers, (1994). High velocity impact response of composites with surface bonded nitinol-SMA hybrid layers, *Journal of Intelligent Material Systems and Structures*,5 (4), 530–535.

Peacock R.N. (1980). Practical selection of elastomer material for vacuum seal, *Journal of Vacuum Science and Technology A,* 17(1).

Pelton, A., DiCello J., and Miyazaki S. (2000). Optimization of processing and properties of medical-grade nitinol wire. *In Proceedings of the International Conference on Shape Memory and Superelastic Technologies* (SMST).

Peltonen M, Lindroos T., Kallio M. (2008). Effect of Ageing on Transformation Kinetics and Internal Friction on Ni-rich Ni-Ti Alloys, Journal of Alloy and Compounds, 460, 237-245.

Perkins J., (1975), Shape Memory Effects in Alloys, *Springer.*

Perkins W.G. (1973). Permeation and outgassing of vacuum materials, *Journal of Vacuum Science and Technology* 10(4).

Petrini, L., and Migliavacca, F. (2011). Biomedical Applications of Shape Memory Alloys. *Journal of Metallurgy,* 2011 (2011), Article ID 501483.

Piao, M., Miyazaki, S., Otsuka, K., Nishida, N. (1992a). Effect of Nb addition on the microstructure of Ti-Ni alloys. *Material Transaction JIM*, 33(4), 337-345.

Piao, M., Otsuka, K., Miyazaki, S., Horikawa, H. (1993). Mechanism of the As temperature increase by pre-deformation in thermoelastic alloys. *Material Transaction JIM*, 34, 919-929.

Piao M., Miyazaki S., and Otsuka K., (1992b). Characteristics of Deformation and Transformation in Ti44Ni47Nb9 Shape Memory Alloy, *Material Transaction JIM*, 33, 4, 346–353,

Piotrowski, B., Ben Zineb, T., Patoor, E., & Eberhardt, A. (2011). A finite element-based numerical tool for Ni47Ti44Nb9 SMA structures design: Application to tightening rings. *Journal of Intelligent Material Systems and Structures*, 23(2), 141–153.

Piotrowski, B., Ben Zineb, T., Patoor, E., & Eberhardt, A. (2012). Modeling of niobium precipitates effect on the Ni47Ti44Nb9 Shape Memory Alloy behavior. *International Journal of Plasticity*, 36, 130–147. https://doi.org/10.1016/j.ijplas.2012.03.004

Pitt D., Dunne J., White E., Garcia E. (2001). SAMPSON smart inlet SMA powered adaptive lip design and static test, *Proceedings of the 42nd AIAA Structures, Structrual Dynamics, and Materials Conference*, 1–11.

Popov, E.P. (1998). Engineering Mechanics of Solids*, second ed. Prentice-Hall.*

Press, W. H. (2003). C++ Numerical Algorithms. *Beijing: Publishing House of Electronics Industry*

Purser, M.F., Richards, A.L., Cook, R.C., Osborne, J.A., Cormier, D.R., Buckner G.D. (2011). A novel shape memory alloy annuloplasty ring for minimally invasive surgery: design, fabrication, and evaluation. *Annals of Biomedical Engineering*. 39(1), 367-77.

Veness, R. Simmons G., and Dorn C., (2011). Development of beryllium vacuum chamber technology for the LHC. CERN Report, CERN-ATS-2011- 263.

Raj, S.V., Noebe, R.D. (2013). Low temperature creep of hot-extruded near-stoichiometric NiTi shape memory alloy part I: Isothermal creep*. Materials Science and Engineering: A*, 581, 145–153.

Razov A. and Cherniavsky A. (2003). Application of SMAs in modern spacecraft and devices. *Journal de Physique IV*, 112, 1173–1176.

Redaelli S. (2013). The collimation system: defence against beam loss. CERN COURIER 2013.

Redhead P. A. (1995a). Modeling the pumpdown of a reversibly adsorbed phase. i. monolayer and submonolayer initial coverage. *Journal of Vacuum Science & TechnologyA*, 13(2), 467-475.

Redhead P. A. (1995b). Modeling the pump-down of a reversibly adsorbed phase. ii. Multilayer coverage. *Journal of Vacuum Science & Technology A*, 13(6), 2791-2796.

Ren X., Otsuka K. (2000). Universal symmetry property of point defects in crystals, *Physical Review Letters,* 85 (5), 1016–1019.

Rosing, D. et al., (2005); Temperature-Controlled Clamping and Releasing Mechanism. *Technical Support Package NASA Tech Briefs NPO-40541*

Roth, A. (1983). Sealing mechanisms in bakeable vacuum seals. *Journal of Vacuum Science and Technology,*1, 211.

Roth, A., (1972). The interface-contact vacuum sealing processes. *Journal of Vacuum Science and Technology* 9(1), 14-23.

Roth A., (1994). Vacuum sealing techniques, *Springer-Verlag, New York*.

Saadat, S., Salichs, J., Noori, M., Hou, Z., Davoodi, H., Baron, I. (2002). An overview of vibration and seismic applications of NiTi shape memory alloy, *Smart Materials and Structures*, 11, 218–229.

Saeedvafa, M. and Asaro, R.J. (1995). Transformation Induced Plasticity. Los Alamos National Laboratory, Report Number LA-UR-95-482.

Santeler, D. (1986). Exit loss in viscous tube flow. *Journal of Vacuum Science & Technology A*, 4(3), 348-352.

Schreier, H.W. and Sutton, M.A. (2002). Systematic errors in digital image correlation due to under matched subset shape functions. *Experimental Mechanics*, 42(3), 303-310.

Schuchman, J.C. (1965). Metal vacuum seals for the AGS, Brookhaven National Laboratory internal report.

Badescu, M., Bao, X., Bar-Cohen, Y. (2014). Shape Memory Alloy (SMA)-based launch lock. *Proc. SPIE 9061, Sensors and Smart Structures Technologies for Civil, Mechanical, and Aerospace Systems*, 90613L.

Shi, H., Frenzel, J., Martinez, G.T., Van Rompaey, S., Bakulin, A., Kulkova, S., Van Aert, S., Schryvers, D. (2014). Site occupation of Nb atoms in ternary Ni–Ti–Nb shape memory alloys. *Acta Materialia*, 74, 85–95.

Shi, H., Frenzel J., and Schryvers D., (2013). EM Characterization of Precipitates in as-Cast and Annealed Ni45.5Ti45.5Nb9 Shape Memory Alloys. *Materials Science Forum*, 738–739, 113–117.

Shi, H., Pourbabak, S., Van Humbeeck J., and Schryvers D. (2012). Electron microscopy study of Nb-rich nanoprecipitates in Ni – Ti – Nb and their influence on the martensitic transformation, *Scripta Materialia*, 67, 939–942.

Shimizu, K., Tadaki, T. (1984). Shape Memory Effect: Mechanism. *Funakubo, H. (Ed.): Shape Memory Alloys, Gordon and Breach Science Publishers,* 1, 1–60.

Siegert, W., Neuking, K., Mertmann, M., Eggeler, G. (2003). First cycle shape memory effect in the ternary NiTiNb system. *Journal of Physics IV*, 112, 739-742.

Sittner, P.R., Vokoun, D., Dayananda, G.N., Stalmans, R. (2000). Recovery stress generation in shape memory Ti50Ni45Cu5 thin wires, *Materials Science and Engineering A,* 286, 298–31.

Spinella, I., Scirè Mammano, G., Dragoni, E. (2009). Conceptual design and simulation of a compact shape memory actuator for rotary motion. *Journal of Materials Engineering and Performance* 18(5-6), 638-648.

Stalmans, R., Van Humbeeck, J., Delaey, L. (1995). Thermodynamic Modelling of Shape Memory Behaviour, Some Examples. *Journal de Physique IV*, 05 (C8), 203-208.

Stepina, V., Vesely, V. (1992). Lubricants and Special Fluids, *Elsevier*.

Stoeckel, D., Waram T. (1992). Use of Ni–Ti shape memory alloys for thermal sensoractuators. *Proceedings of SPIE, Active and adaptive optical components*, 382–387.

Strittmatter, J., Gümpel, P. (2011). Long-time stability of Ni–Ti-shape memory alloys for automotive safety systems. *Journal of Materials Engineering and Performance*, 20, 506–10.

Stroz, D. (2002). Studies of the R-phase Transformation in a Ti-51 at.%Ni Alloy by Transmission Electron Microscopy, *Scripta Materialia*, 47, 363-369.

Such C.R. (1974). The Characterization of the Reversion Stress for NiTi, Thesis at Naval Postgraduate School.

Sun, L., Huang, W.M., Ding, Z., Zhao, Y., Wang, C.C., Purnawali, H., et al. (2012). Stimulus responsive shape memory materials: a review. Material and Design, 33, 577–640.

Tabesh, M., Atli, K. C., Rohmer, J., Franco, B. E., Karaman, I., Boyd, J. G., & Lagoudas, D. C. (2012). Design of shape memory alloy pipe couplers: Modeling and experiments. *Proceedings of SPIE - The International Society for Optical Engineering*, 8343.

Tuissi, A., Besseghini, S., Businaro, T.V., Musazi, S., Paganini, E. (1998). A Vacuum Tight Shape Memory Flange Prototype For The Joint European Torus (JET) Fusion Machine. *SMST-97 Proceedings, Ed. A.R. Pelton, D.E. Hodgson, S.M. Russell, and T.W. Duerig*, 355- 360.

Tuissi A., Biffi C.A., Ruella S., Casati R. (2015). High Performance Shape Memory Effect (HP-SME) for New Shape Memory Devices: A Diamond-like Actuator. *Materials Today: Proceedings* 2, S975-S978.

Turner T., Buehrle, R., Cano, R., Fleming, G. (2006). Modeling, fabrication, and testing of a SMA hybrid composite jet engine chevron concept. *Journal of Intelligent Material Systems and Structures*, 17, 483–497.

Uchida, K., Shigenaka, N., Sakuma, T., Sutou, Y., & Yamauchi, K. (2007). Effect of Nb Content on Martensitic Transformation Temperatures and Mechanical Properties of Ti-Ni-Nb Shape Memory Alloys for Pipe Joint Applications. *Materials Transactions*, 48(3), 445–450.

Unterlerchner, W. (1977). The influence of the mechanical properties of gasket materials on the reliability of bakeable ultrahigh vacuum flanges. *Proceedings of the 7th International Vacuum Congress & 3rd International Conference of Solid Surfaces*.

Unterlerchner, W. (1987). Some improvement work on ConFlat joints and their limit of reliability in large-size ultrahigh vacuum systems. *Journal of Vacuum Science and Technology A* 5(4).

Unterlerchner, W. (1990). Nonstandard vacuum hardware for an accelerator vacuum system. *Vacuum*, 41, 7-9.

Valiev, R., Gunderov, D., Prokofiev E., Pushin V., Zhu Y. (2008). Nanostructuring of TiNi Alloy by SPD Processing for Advanced Properties. *Materials Transactions*, 49, 97-101.

Valiev, R., Zhu, Y.T., Gunderov, D.V., Klourov, N.I., Kuntsevich, T.E., Uksusnikov, A.N., Yurchenko, L.I. (2006). Effect of Severe Plastic Deformation on the Behavior of Ti-Ni Shape Memory Alloys. *Materials Transactions,* 47, 694-697.

Van Humbeeck J. (1999). Non-medical applications of shape memory alloys. *Materials Science and Engineering A*, 273–275, 134–148.

Varian, (1967). The Varian vacuum views, the Varian company prospect.

Videnic, T., Kosel, F., Sajn, V., & Brojan, M. (2007). Biaxial Constrained Recovery in Shape Memory Alloy Rings. *Journal of Intelligent Material Systems and Structures*, *19*(8), 861–874.

Wang, M. juan, Jiang, M. yuan, Liao, G. Y., Guo, S., & Zhao, X. qing. (2012). Martensitic transformation involved mechanical behaviors and wide hysteresis of NiTiNb shape memory alloys. *Progress in Natural Science:Materials International*, *22*(2), 130–138.

Wang, F. E. & Buehler, W.J. (1963). A Summary of Recent Research on the NiTiNOL Alloys and Their Potential Application in Ocean Engineering, *Journal of Applied Phisics*, 34.

Warlimont, H., Delaey L., Krishnan R.V., and Tas H. (1974). Thermoelasticity, pseudoelasticity and the memory effects associated with martensitic transformations. Part 3. Thermodynamics and kinetics. *Journal of Materials Science*, 9, 1545-1555.

Weston, G. F., (1985). Ultrahigh vacuum practice. *Butterworth & Co. (Publishers) Ltd*

Wheeler W.R. (1977). The design of large vacuum seals for nuclear fusion machines, *Proceedings of the 7th International Vacuum Congress & 3rd International Conference of Solid Surfaces*.

Wikberg T. and Dodelin E. (1990). FEM calculations of UHV all-metal demountable joints for LEP. *Vacuum*. 41 (7-9), 2082–2085

Wikberg T. (1968). Improvements of UHV copper gaskets. *Journal of Vacuum Science and Technology,* 5(6).

Willey C., Huettl B., Hill S. (2001). Design and development of a miniature mechanisms tool-kit for micro spacecraft. *Proceedings of the 35th Aerospace Mechanisms Symposium*, 1–14.

Yamamoto, T., Sakuma, T., Uchida, K., Sutou Y., Yamauchi, K. (2008). Effects of Pre-Strain and Heat Treatment Temperature on Phase Transformation Temperature and Shape Recovery Stress of Ti-Ni-Nb Shape Memory Alloys for Pipe Joint Applications. *Materials Transactions*, 49(7), 1650-1655.

Yoshimura N., (1989). Water vapour permeation through Viton O-ring seals. *Journal of Vacuum Science and Technology A*, 7(1).

Zapfe, K. (2007). Leak detection. *Preprint from CERN Accelerator School on Vacuum in Accelerators*.

Zhang, C. S., Zhao, L. C., Duerig, T. W., and Wayman, C. M. (1990). Effects of Deformation on the Transformation Hysteresis and Shape Memory Effect in a Ni47Ti44Nb9 Alloy," *Scripta Metallurgica et Materialia*, 24, 1807–1812.

Zhao,X., Yan, X., Yang, Y., and Xu, H. (2006). Wide hysteresis NiTi(Nb) shape memory alloys with low Nb content (4.5at.%). *Material Science and Engineering A*, 438–440, 575–578.

Zheng, Y., Cai, W., Luo, Y., and Zhao, L. (1997). Effects of heat treatment on tensile properties and shape memory effects of Ni-Ti-Nb alloy, *Transactions of Nonferrous Metals Society of China*, 7, 4, 92–96.

Zheng, Y, Cai, W., Wang, Y., Luo, Y., and Zhao, L.. (1998). "Effects of heat treatment on the transformation temperature and the microstructure of Ni-Ti-Nb shape memory alloy," *Journal of Materials Science Technology*, 14, 37–40.

Zheng, Y., Jiang, F., Li, L., Yang H., Liu Y. (2008). Effect of ageing treatment on the transformation behavior of Ti–50.9 at. % Ni alloy. *Acta Materialia*, 56 (4), 736–745.

ANNEX

Some of the results reported in the present dissertation were published on peer-reviewed journals or presented at national and international conferences. A list of the publications of the author is reported below:

- **Journal papers**
  - Niccoli F., Garion C., Maletta C., and Chiggiato P., “Shape memory alloy-based pipe couplers for ultra-high vacuum applications in particle accelerators: design and experimental assessment”, Journal of Vacuum Science and Technology A, 2017, Vol. 35 (3).
  - Niccoli F., Garion C., Maletta C., Sgambitterra E., Furgiuele F. and Chiggiato P., “Beam-pipe coupling in particle accelerators by shape memory alloy rings”, Materials and Design, 2017, Vol. 114, pp. 603–611.
  - Maletta C., Sgambitterra E., Niccoli F., “Temperature dependent fracture properties of shape memory alloys: novel findings and a comprehensive model”, Scientific Reports - Nature, 2016, Vol.6 (17).
  - Maletta C., Niccoli F., Sgambitterra E., Furgiuele F. “Analysis of fatigue damage in Shape Memory Alloys by Nanoindentation”, Materials Science & Engineering A, 2017, Vol. 684, pp. 335–343.
  - Niccoli F., Maletta C., Furgiuele F., Sgambitterra E. “A thermo-mechanical model for SMA-based crank heat engines”, Journal of Intelligent Material Systems and Structures, 2015, Vol. 26(6).
  - Niccoli F., Maletta C., Furgiuele F., Alfano M., Bruno L. “Mechanical and Functional Properties of Nickel Titanium Adhesively Bonded Joints”, Journal of Materials Engineering and Performance, 2014, Vol. 23(7).

- **Conference proceedings**
  - Furgiuele F., Maletta C., Niccoli F., Sgambitterra E., “Analisi del danneggiamento a fatica di leghe a memoria di forma mediante nano indentazione strumentata”, in proceedings of the AIAS 2015, Associazione Italiana per l’Analisi delle Sollecitazioni 44° convegno nazionale, September 2-7 ,2015, Messina, Italy.
  - Furgiuele F., Maletta C., Niccoli F., Canto S., Luciani L., “Stima dei parametri che determinano la rottura di raccordi oleodinamici durante la fase di curvatura”, in proceedings of the AIAS 2014, Associazione Italiana per l’Analisi delle Sollecitazioni 43° convegno nazionale, September 9-12, 2014, Bologna, Italy.
  - Furgiuele F., Maletta C., Niccoli F., Sgambitterra E. “A thermo-mechanical model for SMA-based crank heat engines”, in proceedings of the ASME 2013 Conference on Smart Materials, Adaptive Structures and Intelligent Systems (SMASIS 2013), pp. SMASIS2013-3329, September 16-18, 2013, Salt Lake City, Utah, USA.

- **Other pubblications**
  - Schaeffer A., Pandolfi S. “Shape Memory material provides a solution for the High-Luminosity LHC”, CERN Bullettin, Issue No. 15-16, 2016.
    (https://cds.cern.ch/journal/CERNBulletin/2016/15/News%20Articles/2144535?ln=en)